Chair of Automatic Control

Technical University of Munich

Design and Experimental Validation of Output Feedback Tracking Controllers for a Pneumatic System with Distributed Parameters

Richard Michael Kern

Vollständiger Abdruck der von der Fakultät für Maschinenwesen der Technischen Universität München zur Erlangung des akademischen Grades eines

Doktor-Ingenieurs

genehmigten Dissertation.

Vorsitzender:	Prof. Wolfgang Polifke, Ph.D.
Prüfer der Dissertation:	1. Prof. Dr.-Ing. habil. Boris Lohmann
	2. Prof. Dr.-Ing. habil. Dr. h. c. Oliver Sawodny

Die Dissertation wurde am 06.06.2019 bei der Technischen Universität München eingereicht und durch die Fakultät für Maschinenwesen am 01.10.2019 angenommen.

Abstract

Pneumatic systems often comprise a tank and a valve, which are connected via a long tube. Their high-performance and efficient operation requires fast and accurate pressure changes in the tank, which are to be achieved by manipulating the mass flow rate through the valve. However, the significant tube length complicates this objective since the tube notably delays the system response and alters the airflow characteristics. This thesis presents model-based controller designs, which explicitly consider the dynamics of the airflow in the tube. For that, a plant model, describing the air in the system, is derived by the conservation laws of mass, momentum, and energy, resulting in quasilinear hyperbolic partial differential equations for the tube, nonlinear ordinary differential equations for the tank, and static relations for the valve. The validity of the model is verified by experimental studies performed at a test bench. By making use of this rather elaborate system description, models of successively decreasing complexity are derived by introducing additional assumptions. The models are thoroughly discussed and three of them are selected for the subsequent controller design. Based on a linear distributed-parameter model, using a collocated pressure measurement downstream of the valve, output feedback controllers are derived, which comprise a state feedback and a state observer. The first design makes use of a novel backstepping approach for hyperbolic partial differential equations. The resulting output feedback controller is augmented by a flatness-based feedforward controller and implemented at the test bench, providing the first-ever experimental validation of the newly developed backstepping method. In addition, by nature of its infinite-dimensional character, such a control law is very rare for pneumatic systems. The backstepping-based controller is compared to another late-lumping and to two state-of-the-art early-lumping controllers. The infinite-dimensional state feedback and observer are derived from a flatness-based parametrization of the system quantities. For the design of the early-lumping controllers, the linear distributed-parameter model of the test bench is approximated by a lumped-parameter one. Classical methods using pole placement and optimality are applied to derive the two finite-dimensional output feedback tracking controllers. The performance of all output feedback tracking controllers is assessed at the test bench. Experimental data confirms that the controllers track fast pressure changes in the tank nearly perfectly. In particular, the evaluation of these results as well as a comparison in terms of design and implementation aspects underline the excellent performance and practicability of the backstepping-based controller.

Acknowledgements

This thesis is the result of my research over the last five years at Technical University of Munich. During this time, I had the notable pleasure to get to know many unique people who supported me and enriched my life on innumerable levels. While I am deeply thankful to all of them, I want to use this opportunity to especially mention the ones who contributed the most to this thesis.

First of all, I want to express my profound gratitude to my supervisor Univ.-Prof. Dr.-Ing. habil. Boris Lohmann for trusting in my skills and abilities as well as for giving me his unlimited support. I also want to thank Univ.-Prof. Dr.-Ing. habil. Dr. h. c. Oliver Sawodny for his interest in my work and his kindness in agreeing to be the second examiner. Naturally, I would also like to thank Univ.-Prof. Wolfgang Polifke, Ph.D. for accepting to chair the examining committee.

My sincere thanks go to Prof. Dr.-Ing. habil. Joachim Deutscher for his sophisticated academic advise and for the inspiring scientific collaboration we had. Moreover, I am deeply grateful to Dr.-Ing. Nicole Gehring for being not only an advisor and colleague but also a friend to me. Both, Joachim and Nicole, contributed a lot to this work. Furthermore, I want to thank all of my colleagues, especially Dr.-Ing. Paul Kotyczka, Klaus Albert, M.Sc., and Philipp Niermeyer, M.Sc., for sharing their expert knowledge. Thanks go to Dr. David Bou Saba and all of the Laboratoire Ampère in Lyon for the magnificent time we spent together and for the fruitful discussions we had. I sincerely thank Dr. Klaus-Dieter Reinsch for several insightful mathematical dialogues. In sharing their knowledge and code with me, Jakob Gabriel, M.Sc. and Simon Kerschbaum, M.Sc. facilitated some of my own implementations, for which I am very grateful. It should not go unmentioned that this thesis was supported in part by all the students I had the pleasure to work with. In addition, I want to thank Oliver Licht, ass. iur., M.A., LL.M., MPA for his helpful comments in proofreading of this thesis.

My special thanks go to my family for their unconditional love.

Contents

Chapter 1

Introduction

Pneumatic applications, such as pneumatic actuators, are extensively used in the industry since they have low investment costs and a high power density, e.g., [Bea07; Pfe18]. Their operation requires a compressed medium, with air commonly used for its both safe and simple production and handling. In turn, generating compressed air usually requires electricity, whereby the generation accounts for approximately 10 % of the overall industrial electricity consumption in developed countries, e.g, [Rad01; MKK14]. However, according to [SRH10], only 19 % of the energy needed for the production of compressed air is usable, rendering the operational costs of pneumatic systems relatively high. One way to alleviate these costs is to increase the efficiency in order to reduce the amount of compressed air consumed. This can be achieved, e.g., by deriving a suitable mathematical description of the respective pneumatic process for its analysis and optimization. In addition, the development of a sophisticated control strategy can increase the efficiency even further.

1.1 Motivation

Typically, pneumatic actuators are essential components of pneumatic systems, e.g., [JK03]. They are driven by compressed air that is provided via valves. Such a set-up is depicted in Fig. 1.1. Therein, the actuator is a double-acting cylinder, consisting of two chambers and a piston. The valves are fed by a large storage tank, which is in turn connected to the air supply. By adjusting the mass flow rate through the valve, the corresponding chamber pressure in the cylinder is regulated and accordingly the motion and position of the piston.

However, often it is desirable or even inevitable to adjust the set-up in Fig. 1.1 by installing long tubes between the valves and the actuator, depicted in Fig. 1.2. As stated in [Yan+11; KS13; RNM16], such a setting can be more cost effective since less electrical wiring is needed and the compressed air storage tank, providing a more constant supply pressure to the valve, might not be necessary. Because of the shorter cables, wire breaks and signal disturbances can be reduced, resulting in a more reliable system. As the long tubes allow to install the actuator and the valves at different positions, it might be easier to comply with constructive restrictions. For example, when multiple actuators are utilized, the valves can be centrally clustered. Furthermore, in some applications, the environmental conditions limit the use of electrical devices and/or metallic materials,

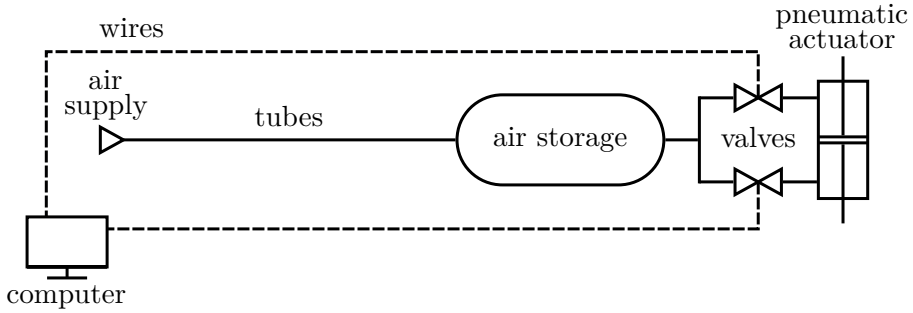

Figure 1.1: A typical pneumatic set-up with short tubes connecting the valves and the actuator

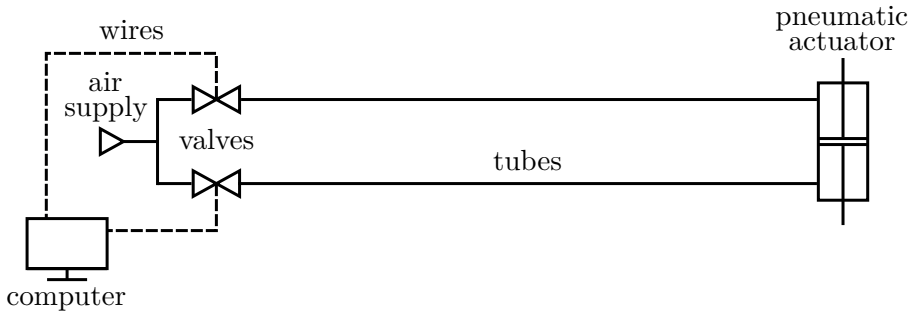

Figure 1.2: A typical pneumatic set-up with long tubes connecting the valves and the actuator

rendering long tubes unavoidable. An example is the strong magnetic field in a magnetic resonance imaging scanner. Further possible limitations are extreme temperatures or environments with an explosive atmosphere.

Apart from the above mentioned benefits, the use of the long tubes can cause drawbacks as they affect the system response from the input, i.e. the mass flow rate through the valve, to the output, i.e. the chamber pressure. In general, signals in pneumatic systems propagate only with the speed of sound, approximately. Thus, the long tubes introduce a delay, depending on their length. In addition, they significantly alter the characteristics of the flow, for example, the pressure drops because of friction, e.g., [RH00a]. These effects increase the complexity of the system and may render a controller design relatively involved, e.g., [TU18].

To investigate this problem, the author of this thesis laid out and built the test bench depicted Fig. 1.3, which is inspired by the set-up in [KS13] and [RNM15]. It basically consists of a long tube, connecting a proportional directional control 5/3-way[1] valve and a tank. Its components are listed in Appx. A. Therefore, the test bench essentially comprises the three main components in Fig. 1.2, where the tank stands in place of one of the cylinder chambers. Since the control objective in Fig. 1.2 is the respective chamber pressure, the controlled variable of the test bench in Fig. 1.3 is the tank pressure. While the regulation of the latter is an important issue on its own, e.g., [AF16; RNM16], it is also a crucial step towards the control of pneumatic actuators.

[1] As one working port of the valve is blocked and both exhaust ports discharge to the ambient pressure via silencers, the valve is treated as a 3/3-way valve in the following.

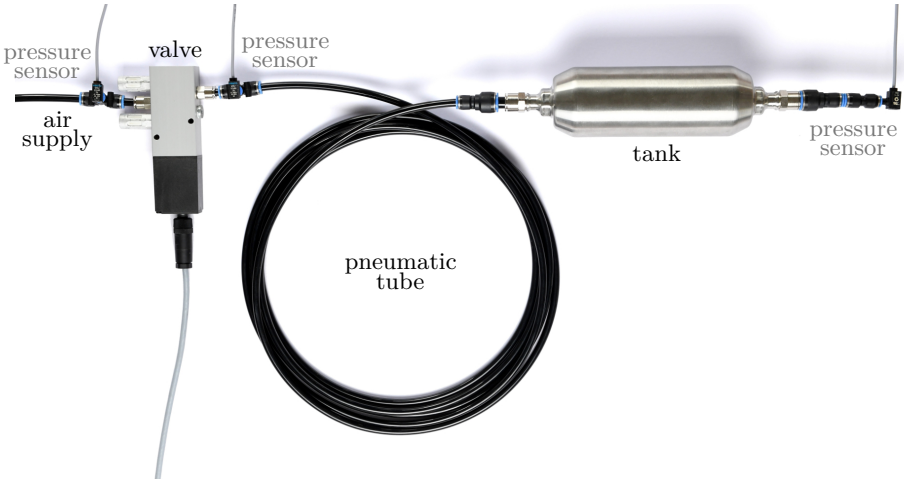

Figure 1.3: A photo of the essential components of the test bench

Naturally, a controller, which achieves a desired tank pressure by manipulating the mass flow rate through the valve, can be designed based on a mathematical description of the set-up, e.g., [Bea07]. For that, its components are modeled by making use of the corresponding laws of physics. Subsequently, the models are interconnected. Often, the valve is described by a static relation since its dynamics is negligible compared to the remaining plant dynamics, e.g., [Bru+99]. While the tank is modeled by ordinary differential equations (ODEs), e.g., [RNM15], hyperbolic partial differential equations (PDEs) might be necessary to adequately capture the spatially distributed character of the tube, depending on, e.g., its length.

If the tube between the valve and the tank is sufficiently short, its dynamics, i.e. the dynamics of the airflow through the tube, can be neglected, rendering the resulting model for the controller design finite-dimensional. Still, a satisfying control performance can be achieved, e.g., [LB88]. In contrast to that, if the tube length is significant as in Fig. 1.3, where a tube of five meters is installed, it might be necessary to consider its dynamics, e.g., [RH00b]. From the combination of the tube model with the models of the valve and the tank, a PDE-ODE system is obtained. The design of controllers and observers based on such an infinite-dimensional model is the scope of this thesis.

1.2 State of the Art

In the literature, there exists a variety of approaches on how to deal with long tubes. Often, to avoid additional complexity in the controller design, their dynamics is simply neglected, e.g., [RNM16]. One example is [Yu+08], where the set-up consists of two valves, connected to a cylinder via tubes with a length of 5 m. Although the authors incorporate the additional tube volume in the model, they neglect the tube dynamics. Based on this system description, two first-order controllers, regulating the corresponding pressure in the cylinder chambers, are designed and validated in experiments. A very similar set-up can be found in [Yan+11]. Therein, the tubes with a length of 9 m are described by PDEs and the effects thereby induced discussed. Still, these dynamics are not taken into account in the subsequently designed finite-dimensional sliding mode

controller, which is validated in experiments. The authors justify their approach by defining rather slow dynamics of the closed-loop system.

In contrast to that, some researchers consider the dynamics of the tube in their controller design. An early example is from 1972 and can be found in [Föl72] (in German). Therein, the set-up consists of a long tube, connecting a valve and a pneumatic resistance, where the pressure at the unactuated end is controlled. For that, the system is modeled and the tube described by PDEs, where friction is neglected, reducing the complexity. Based on the resulting infinite-dimensional model, finite-dimensional controllers up to the order three are derived by the frequency response method and investigated in simulations. Another relatively early example is [PKS91], where the chamber pressures in a cylinder are regulated by a valve via tubes. The latter have a length of approximately 0.2 m and 0.3 m, respectively. The effects, caused by the tubes, are discussed and described by an infinite-dimensional model. However, while some system components can be adequately modeled by physical laws, the authors state that such an approach is not suitable to obtain a holistic model caused by the system's complexity. Instead, a simplified first-order transfer function is derived by measuring the frequency response. Based on that, P as well as PD controllers are designed and validated in experiments.

One of the first contributions which systematically investigated controller designs neglecting and considering the tubes in terms of the resulting performance is [RH00a]. In their previous work [RH00b], a model was derived from a set-up, consisting of a valve and a cylinder, connected via tubes with a length of 0.5 m and 2 m, respectively. First, the tubes are modeled by PDEs. These are simplified in order to avoid distributed delays and subsequently solved. The solution is included in the mathematical description of the entire system, rendering it a model comprising delay differential equations. Based on that, [RH00b] presents the design of two sliding mode controllers: The first one is derived from this infinite-dimensional model, rendering the resulting control law infinite-dimensional, too. The second controller is designed based upon a simplified system description. For that, the valve dynamics and the delays induced by the tubes are neglected. Hence, caused by the latter simplification, the resulting control law is finite-dimensional. The controllers are tested in simulations and experiments. It was shown that the first controller, incorporating the tube model, performed significantly better for actuator frequencies above 20 Hz and/or in configurations with the tubes of 2 m.

A common method to consider the tube dynamics in the controller design is the so-called early-lumping approach: First, the tubes are modeled by PDEs. The resulting infinite-dimensional model is approximated by a finite-dimensional one, comprised of ODEs. The controller is derived based on this reduced model. Such an approach can be found in, e.g., [TRB01]. Therein, a controller is designed for a hydraulic aircraft brake system[2], consisting of a valve, a tube of considerable length, and a brake cavity, approximated by a constant volume. The model of the set-up takes the distributed dynamics of the tubes as well as the nonlinearities of the valve into account. For the design of the controller, regulating the pressure in the cavity, this model is simplified: The nonlinearities are eliminated and the infinite-dimensional tube dynamics is reduced to a second-order model by making use of a modal approximation. Utilizing H_∞ methods, a finite-dimensional robust controller is obtained and validated in simulations.

[2] Although the working fluid is oil, the approach in [TRB01] can also be applied in the context of pneumatic systems as the compressibility of the medium is taken into account.

It can be summarized that all so far existing[3] controller designs for pneumatic systems involving long tubes are not directly based on PDEs and/or the resulting control law is finite-dimensional.

This fact might be surprising, given that the control of hyperbolic PDEs attracted the attention of researchers relatively early because this class of systems typically emerges if conservation laws are employed, e.g., [Rus73] from 1973. Thereby, physical phenomena, such as the flow of fluids through channels or pipelines, the transport of electricity in transmission lines, and the flow of traffic, can be modeled, e.g., [BC16]. However, the existing controller designs for hyperbolic PDEs, so-called late-lumping approaches since they are derived from an infinite-dimensional system description, may not be applicable to pneumatic systems for multiple reasons: For example, the design might require a distributed input along the tube, e.g., [Chr01], which is a rather unusual set-up. Even most of the methods developed for hyperbolic systems with boundary control, e.g., [PWB08], cannot be applied directly. The reason for this is caused by the fact that models for pneumatic systems involving long tubes usually consist not only of PDEs but of ODEs, too, necessitating new design approaches which are applicable in practice.

Remark 1.1. Since this thesis covers modeling as well as late-lumping and early-lumping controller design, a more comprehensive state of the art of each topic can be found at the beginning of the corresponding chapter. △

1.3 Subject and Outline of the Thesis

This thesis bridges the aforementioned gap and presents a late-lumping controller design based on a distributed-parameter model of the set-up in Fig. 1.3. The resulting infinite-dimensional output feedback tracking controller, i.e. a state feedback based on an observer and augmented by a feedforward controller, is validated in experiments and compared to existing approaches.

First, an infinite-dimensional model of the test bench is derived in Chap. 2 by applying conservation laws to the components in Fig. 1.3. This so-called plant model is comprised of quasilinear hyperbolic PDEs, describing the tube, bidirectionally coupled to nonlinear ODEs, modeling the tank. The valve is characterized by static relations. To obtain a system description amenable for the subsequent controller design, the plant model is successively simplified by making use of suitable assumptions. Each step is discussed regarding its physical meaning and validity. Thereby, four additional models are obtained. Simulation data of all five models is compared to each other and to measurement data. Three of these models are essential in the following: the plant model for simulations, the isothermal model for the design of the feedforward controller, and the linear model for the design of the state feedback and observer.

Chap. 3 presents the derivation of the feedforward controller, allowing for a defined transition between desired constant pressure levels in the tank. It is based on the flatness-based approach in [Knü15] (in German). While it achieves an almost excellent performance in simulations, the results in an experimental study are rather poor, emphasizing the necessity of a state feedback.

[3] Further contributions dealing with the control of pneumatic systems involving long tubes will be discussed in Chap. 6.

Motivated by that, an output feedback controller is designed in Chap. 4 by making use of the backstepping approaches in [DGK17] and [DGK18]. The resulting control law, i.e. the state feedback combined with the observer, is augmented by the feedforward controller. This output feedback tracking controller is validated in simulations and experiments.

In addition to the backstepping approach, a flatness-based state feedback and a state observer are designed in Chap. 5. These are based on the methods in [Woi13a] as well as [Woi13b] and investigated in simulations.

To compare these late-lumping approaches to the state-of-the-art early-lumping approach, Chap. 6 presents the design of finite-dimensional output feedback tracking controllers. For that, the linear model of the test bench is approximated by two selected methods: the finite-volume method in [KS13] and the modal approximation in [RNM15]. Based on the resulting lumped-parameter models, output feedback tracking controllers are derived by making use of well-known design methods for finite-dimensional systems. The controllers are tested in simulations and experiments.

Finally, in Chap. 7, the design approaches are discussed in terms of a comparative analysis and the results summarized. The chapter is concluded by an outlook for possible further research in this context.

Chapter 2

Modeling of the Test Bench

There exists a large variety of mathematical models, describing the dynamics of compressible fluids in tubes. Usually, they are based on PDEs and range from relatively simple linear one-dimensional models, e.g., [SB59], to very sophisticated nonlinear three-dimensional ones, e.g., [Nik94]. Although complex models can be a more accurate description, they might be difficult to analyze, computationally inefficient, and render a controller design very involved. Since easy-to-use models can be essential in order to increase the efficiency of a pneumatic system, suitable simplifications are required. For that, additional assumptions are introduced, depending on the intended use. If these are based on physical reasoning, the effect of each assumption regarding the validity range of the model is generally more transparent.

While [SD86a] presents an overview of models with varying complexity and their underlying assumptions, it may not always be obvious which physical effects are taken into account and which are neglected. Furthermore, authors, studying differently complex models for compressible flow, usually substantiate their results with numerical simulations but without experimental data, e.g., [HMS09]. On the other hand, those who validate their model based on experiments, may not consider other modeling approaches, e.g., [RNM15]. To alleviate the choice of a proper model, for example, in the context of an industrial application, it might be beneficial to discuss the underlying assumptions and compare the model with other models as well as its simulation data to experimental data. Such a comparison can be found in [SD86b] for an almost incompressible fluid with laminar flow. However, air is a highly compressible fluid and the flow in pneumatic systems is often turbulent. These aspects are considered in [KS13], where existing modeling approaches for an airflow in a long tube are discussed and the corresponding simulation data is compared with measurement data.

In this chapter, the plant model, describing the test bench in Fig. 1.3, is presented. It is obtained from applying the conservation laws of mass, momentum, and energy to the airflow through the system. First, a mathematical description of the tube is derived, which considers friction and heat transfer. Thereby, a system of quasilinear hyperbolic[1] first-order PDEs results, generally represented by

$$\frac{\partial}{\partial t}\boldsymbol{x}(z,t) + \frac{\partial}{\partial z}\boldsymbol{g}(\boldsymbol{x}(z,t)) = \boldsymbol{c}(\boldsymbol{x}(z,t)), \tag{2.1}$$

[1]The PDEs (2.1) are termed hyperbolic if the eigenvalues of the Jacobian $\frac{\partial \boldsymbol{g}}{\partial \boldsymbol{x}}(\boldsymbol{x})$ are real and if $\frac{\partial \boldsymbol{g}}{\partial \boldsymbol{x}}(\boldsymbol{x})$ is diagonalizable, cf. [Tan92].

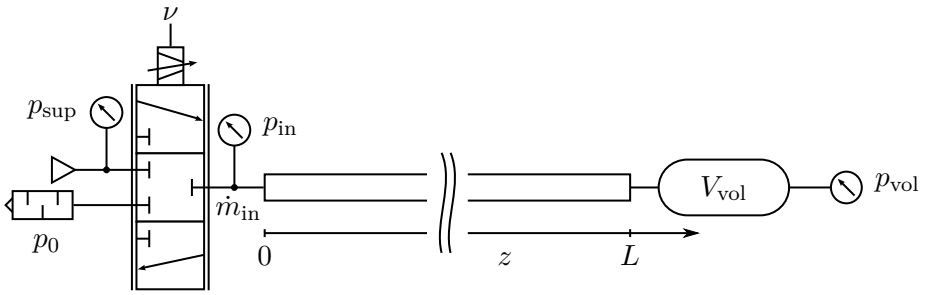

Figure 2.1: A schematic of the test bench

where the state $\boldsymbol{x}(z,t) = [x_1(z,t), \ldots, x_k(z,t)]^T \in \mathbb{R}^k$ comprises k quantities, depending on the spatial coordinate $z \in [0, L]$ in the axial direction of the tube and time $t > 0$. The initial condition is denoted by $\boldsymbol{x}(z,0)$. The function $\boldsymbol{g}(\boldsymbol{x}(z,t)) \in \mathbb{R}^k$ represents the flux and $\boldsymbol{c}(\boldsymbol{x}(z,t)) \in \mathbb{R}^k$ sources and sinks. Subsequently, the valve at $z = 0$ and the tank at $z = L$ are modeled, giving rise to the boundary conditions of (2.1). For that, the valve is considered to be static and the tank is described by nonlinear ODEs.

While the plant model is a very accurate description of the test bench, it might be too complex for a controller design. Thus, it is successively simplified, resulting in a linear model of the test bench. Thereby, four additional models with decreasing complexity result. All involved assumptions are clearly stated. Simulation data of each of the five models is compared with one another and to experimental data of the test bench. The effects of the assumptions and the resulting model uncertainties are discussed. Finally, three models, relevant for the following controller designs, are chosen.

This chapter is based on [Ker17], a contribution by the author of this thesis, which is enhanced with new results. These are, e.g., the valve model and further experimental studies to validate the models.

2.1 Preliminary Considerations

Fig. 2.1 depicts a schematic representation of the photo in Fig. 1.3. Therein, the tube with the length L, connecting the valve at $z = 0$ and the tank with the fixed volume V_{vol} at $z = L$, can be seen. The pressure sensors measure the supply pressure $p_{\text{sup}}(t)$ upstream and the working pressure $p_{\text{in}}(t)$ downstream of the valve, as well as the pressure $p_{\text{vol}}(t)$ in the tank. The constant ambient pressure is denoted by p_0 and the mass flow rate through the valve by $\dot{m}_{\text{in}}(t)$. The supplied voltage $\nu(t)$ specifies the position of the spool inside of the valve.

To model the flow of air through the system, the medium is characterized by the density ρ, the specific total energy e, the velocity v in the axial direction, and the specific internal energy u. These quantities are related by the state equation

$$\rho e = \frac{1}{2}\rho v^2 + \rho u. \tag{2.2}$$

It decomposes the total energy density ρe into the kinetic and the internal energy density, $\rho v^2/2$ and ρu, respectively, e.g., [LeV92]. For air at or near standard conditions, the ideal gas law

$$p = \rho R_{\text{s}} T \tag{2.3}$$

with the specific gas constant R_s and the temperature T is valid[2], e.g., [And11]. In addition, the air can be treated as a calorically perfect gas[3]. Thereby, the specific internal energy becomes proportional to the temperature, i.e. $u = c_V T$ holds, where $c_V = c_p - R_\mathrm{s}$ denotes the specific heat capacity at constant volume and c_p is the specific heat capacity at constant pressure, e.g., [Mun13]. As a consequence, the state equation (2.2) reads

$$\rho e = \frac{1}{2}\rho v^2 + \frac{1}{\gamma - 1} p, \tag{2.4}$$

where $\gamma = c_p / c_V$ is the ratio of specific heats. For air, $\gamma = 1.4$ holds, e.g., [And11].

2.2 An Infinite-Dimensional Model of the Tube

To model the flow of a compressible fluid in a duct with a constant geometry along the axis, often, the following assumptions are made:

i) The flow is inviscid. Therefore, no friction, thermal conduction or diffusion occurs, e.g., [And11].

ii) The system is adiabatic. Hence, the transfer of heat and matter between the system and its surroundings is negligible, e.g., [And11].

iii) The spatial gradients of the flow quantities normal to the streamline direction are insignificant compared to the ones parallel to the streamlines. Therefore, the flow is considered to be one-dimensional, e.g., [And03].

iv) The flow quantities are averaged over the cross section of the duct and thus depend only on the axial coordinate z (and time), e.g., [Dan76].

v) The flow is assumed to be perpendicular to the direction of the gravitational acceleration. Hence, gravity is neglected, e.g., [And11].

By that, the one-dimensional Euler equations in conservative form can be employed to describe the dynamics of the flow. These read

$$\frac{\partial}{\partial t}\rho + \frac{\partial}{\partial z}(\rho v) = 0 \tag{2.5a}$$

$$\frac{\partial}{\partial t}(\rho v) + \frac{\partial}{\partial z}\left(\rho v^2 + p\right) = 0 \tag{2.5b}$$

$$\frac{\partial}{\partial t}(\rho e) + \frac{\partial}{\partial z}\left(v(\rho e + p)\right) = 0, \tag{2.5c}$$

where the arguments z and t are neglected. Therein, the density ρ, the momentum density ρv, and the total energy density ρe are conserved.

[2] The compressibility factor Z of air, defined as $Z = p/(\rho R_\mathrm{s} T)$, modifies the ideal gas law to account for the real gas behavior. For pressures and temperatures usually occurring in a pneumatic system, i.e. $p \in [1\,\mathrm{bar}, 10\,\mathrm{bar}]$ and $T \in [250\,\mathrm{K}, 350\,\mathrm{K}]$, it is essentially equal to one, i.e. $Z \in [0.9992, 1.0004]$ [RHC98].

[3] A calorically perfect gas is an ideal gas, where the specific heat capacity is assumed to be constant. This is a valid approximation for air at moderate temperatures as its specific heat capacity at constant pressure reads $c_p \in \left[1.0044 \cdot 10^3\,{}^{\mathrm{J}}/_{\mathrm{kg\cdot K}}, 1.0104 \cdot 10^3\,{}^{\mathrm{J}}/_{\mathrm{kg\cdot K}}\right]$ for $T \in [250\,\mathrm{K}, 350\,\mathrm{K}]$ [RHC98].

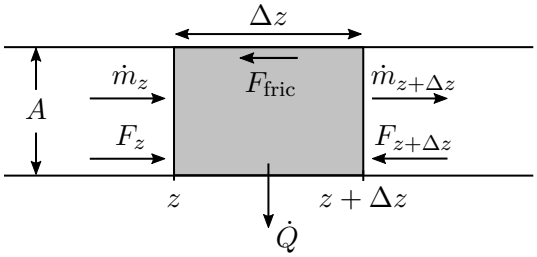

Figure 2.2: Finite tube volume with mass transfer, forces, and heat transfer

If the medium air flows through a tube as in Fig. 2.1, where the diameter compared with the tube's length is relatively small, the accuracy of the Euler equations (2.5) is substantially improved by taking friction effects, arising from the viscosity of the medium air, as well as the heat transfer between the fluid and the inner tube wall into account, cf. [Dan76; Tho99]. In the following, such a model is derived by applying the conservation laws to the finite tube volume in Fig. 2.2, where the width of the volume is denoted by Δz and $f_{z+\Delta z} = f(t, z + \Delta z)$ holds.

Remark 2.1. The subsequent derivation is based on straight tubes, where the geometry along z is constant. Still, the resulting model is valid for slightly elastic tubes with a relatively large bending radius as in Fig. 1.3, cf. [Bea07]. Thus, assumption iii) holds, which can be verified by experiments. △

2.2.1 Conservation of Mass

The change of mass in the finite volume equals its net mass flow rate:

$$A \int_z^{z+\Delta z} \frac{\mathrm{d}}{\mathrm{d}t} \rho(\zeta, t) \, \mathrm{d}\zeta = \dot{m}(z, t) - \dot{m}(z + \Delta z, t),$$

where $A = \pi D^2/4$ is the cross section area of the tube and D the inner tube diameter. By making use of the definition of the mass flow rate $\dot{m} = A\rho v$ and the mean value theorems,

$$A\Delta z \frac{\partial}{\partial t} \rho(z + \theta_1 \Delta z, t) = -A\Delta z \frac{\partial}{\partial z} (\rho v)(z + \theta_2 \Delta z, t), \qquad \theta_{1,2} \in (0, 1)$$

follows. Dividing by $A\Delta z$ and letting $\Delta z \to 0$ results in

$$\frac{\partial}{\partial t} \rho + \frac{\partial}{\partial z} (\rho v) = 0. \tag{2.6}$$

2.2.2 Conservation of Momentum

To account for the pressure drop caused by friction, arising from the viscosity of the fluid and the no slip condition at the inner tube wall, assumption i) is eased. Thus, the conservation law of momentum for the finite volume in Fig. 2.2 reads

$$\begin{aligned} A \int_z^{z+\Delta z} \frac{\mathrm{d}}{\mathrm{d}t} (\rho v)(\zeta, t) \, \mathrm{d}\zeta = (\dot{m}v)(z, t) - (\dot{m}v)(z + \Delta z, t) \\ + F(z, t) - F(z + \Delta z, t) - F_{\text{fric}}(z, \Delta z, t), \end{aligned} \tag{2.7}$$

where $\dot{m}v$ is the momentum transported with the flow and $F = pA$ is the pressure force acting on the corresponding boundary of the finite volume. The friction force caused by shear stress is defined by $F_{\text{fric}} = A\Delta p$, where Δp is the pressure drop over the length Δz induced by friction. According to [Ide94], Δp can be calculated by the Darcy-Weisbach equation

$$\Delta p = f_{\text{c}} \frac{\Delta z}{D} \frac{\rho v|v|}{2} \tag{2.8}$$

for fully-developed steady-state compressible flow. Therein, f_{c} is the compressible friction factor, which depends on ρ, v, and e. By applying a similar procedure as in Sec. 2.2.1 to (2.7),

$$\frac{\partial}{\partial t}(\rho v) + \frac{\partial}{\partial z}(\rho v^2 + p) = -f_{\text{c}} \frac{\rho v|v|}{2D} \tag{2.9}$$

is obtained.

The relationship between the friction factor f_{c} for compressible flow and the friction factor f for incompressible flow is stated in [Ide94] as

$$f_{\text{c}} = f \left(1 + \frac{\gamma - 1}{2} Ma^2\right)^{-0.47}, \tag{2.10}$$

where $Ma = v/a$ is the Mach number in the flow and $a = \sqrt{\gamma p/\rho}$ the speed of sound in a calorically perfect gas, e.g., [And11]. The friction factor f depends on the flow regime and is characterized by the Reynolds number

$$Re = \frac{D\rho|v|}{\mu},$$

where μ is the temperature dependent dynamic viscosity. For laminar flow, where $Re < Re_{\text{crit,min}}$, f is defined by

$$f = \frac{64}{Re}, \tag{2.11}$$

e.g., [Ide94]. For $Re > Re_{\text{crit,max}}$, the flow is turbulent and several empirical correlations can be used to determine f. In this thesis, the Haaland equation

$$\frac{1}{\sqrt{f}} = -1.8 \log \left[\left(\frac{\varepsilon/D}{3.7} \right)^{1.11} + \frac{6.9}{Re} \right] \tag{2.12}$$

is chosen since it is explicit and valid for the entire turbulent regime, e.g., [Mun13]. Therein, ε is the average height of the roughness elements at the inner tube wall. Values of ε for different materials can be found, for example, in [VDI10]. In the transition regime, where $Re_{\text{crit,min}} < Re < Re_{\text{crit,max}}$, the friction factor f is determined by a spline interpolation between (2.11) and (2.12). The critical values of the Reynolds number $Re_{\text{crit,min}}$ and $Re_{\text{crit,max}}$ differ in the literature. This thesis makes use of the formulas

$$Re_{\text{crit,min}} = \begin{cases} 754\, \mathrm{e}^{\left(\frac{0.0065}{0.007}\right)}, & \varepsilon/D \leq 0.007 \\ 754\, \mathrm{e}^{\left(\frac{0.0065}{\varepsilon/D}\right)}, & \varepsilon/D > 0.007 \end{cases} \tag{2.13a}$$

$$Re_{\text{crit,max}} = 2090 \left(\frac{1}{\varepsilon/D} \right)^{0.0635} \tag{2.13b}$$

in [Ide94].

2.2.3 Conservation of Energy

For the derivation of the augmented energy equation, assumption ii) is alleviated, allowing for heat transfer between the fluid and the inner tube wall. In addition, the energy loss caused by friction is taken into account. The change of energy inside the finite volume in Fig. 2.2 reads

$$A\int_z^{z+\Delta z}\frac{\mathrm{d}}{\mathrm{d}t}(\rho e)(\zeta,t)\,\mathrm{d}\zeta = (\dot{m}e)(z,t) - (\dot{m}e)(z+\Delta z,t) + (Fv)(z,t) \\ - (Fv)(z+\Delta z,t) + \dot{Q}(z,\Delta z,t) - (F_{\mathrm{fric}}v)\,(z,\Delta z,t),$$

where $\dot{m}e$ is the energy transported with the flow and Fv is the mechanical power, resulting from the forces acting on the moving particles, e.g., [And03]. The heat flow from the fluid to the tube wall over the length Δz is denoted by $\dot{Q}$ and $F_{\mathrm{fric}}v$ accounts for the energy loss caused by friction, cf. [ETO03]. The steady-state heat flux from the fluid to the tube wall is defined by

$$\dot{Q} = \frac{1}{R}(T_{\mathrm{w}} - T), \tag{2.14}$$

where T_{w} is the inner wall temperature and R the thermal resistance, e.g., [VDI10]. For pneumatic applications, the heat capacity C_{w} of the tube wall is usually much greater[4] than the heat capacity C of the fluid air. Hence, T_{w} is assumed to be constant and equal to the ambient temperature T_0. As a result, the thermal resistance reads $R = 1/(\alpha D\pi\Delta z)$, e.g., [VDI10], where α is the heat transfer coefficient, which depends on ρ, v, and e. Thereby, $\dot{Q} = \alpha\pi D\Delta z(T_0 - T)$ follows from (2.14). Finally, by a similar procedure as for the conservation of mass and momentum,

$$\frac{\partial}{\partial t}(\rho e) + \frac{\partial}{\partial z}(v(\rho e + p)) = \frac{4}{D}\alpha(T_0 - T) - f_{\mathrm{c}}\frac{\rho v^2|v|}{2D} \tag{2.15}$$

is derived.

In order to compute the heat transfer coefficient α between the fluid and the inner tube wall, the Nusselt number

$$Nu = \alpha D/\lambda, \tag{2.16}$$

where λ is the temperature dependent thermal conductivity of the fluid, has to be determined. For laminar flow and a constant wall temperature, the Nusselt number reads $Nu = 3.6568$, e.g., [VDI10]. In the transient and turbulent regime, the correlation by Gnielinski in [RHC98] is chosen to compute the Nusselt number since it is valid for a large range of the Reynolds number and the Prandtl number $Pr = c_p\mu/\lambda$, i.e. $Re_{\mathrm{crit,min}} \leq Re \leq 5{\cdot}10^5$ and $0.5 \leq Pr \leq 2000$. The correlation is slightly adjusted by using f_{c} instead of f to be consistent with the friction model for compressible flow, resulting in

$$Nu = \frac{\frac{f_{\mathrm{c}}}{8}(Re - 1000)Pr}{1 + 12.7\left(\frac{f_{\mathrm{c}}}{8}\right)^{\frac{1}{2}}\left(Pr^{\frac{2}{3}} - 1\right)}.$$

Thereby, α in (2.15) follows from (2.16).

[4] A tube of polyurethane as used in this thesis has an inner radius of $r_{\mathrm{i}} = 2.85\,\mathrm{mm}$, an outer radius of $r_{\mathrm{o}} = 4\,\mathrm{mm}$, a density of $\rho_{\mathrm{w}} = 1200\,{}^{\mathrm{kg}}/_{\mathrm{m}^3}$, and a specific heat capacity of $c_{\mathrm{w}} = 1800\,{}^{\mathrm{J}}/_{\mathrm{kg\cdot K}}$. Air at $T = 300\,\mathrm{K}$ and $p = 6\,\mathrm{bar}$ has a density of $\rho = 6.97\,{}^{\mathrm{kg}}/_{\mathrm{m}^3}$ and a specific heat capacity of $c_V = 719.38\,{}^{\mathrm{J}}/_{\mathrm{kg\cdot K}}$ [VDI10]. The resulting heat capacities are $C_{\mathrm{w}} = c_{\mathrm{w}}\rho_{\mathrm{w}}\pi\left(r_{\mathrm{o}}^2 - r_{\mathrm{i}}^2\right) = 53.46\,{}^{\mathrm{J}}/_{\mathrm{m\cdot K}}$ and $C = c_V\rho\pi r_{\mathrm{i}}^2 = 0.25\,{}^{\mathrm{J}}/_{\mathrm{m\cdot K}}$.

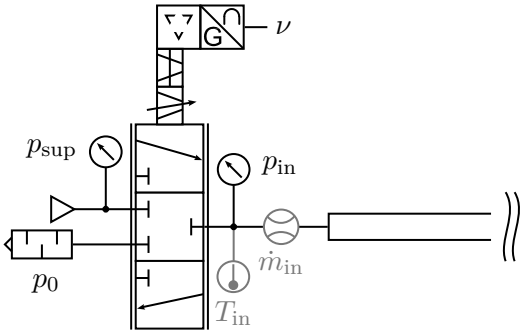

Figure 2.3: Detailed schematic of the valve with optional measurements in gray

2.3 A Static Model of the Valve

At $z = 0$, the tube is attached to the valve, which in turn is connected to the compressed air supply with an almost constant pressure of $p_{\text{sup}}(t) \approx 9\,\text{bar}$. A schematic is depicted in Fig. 2.3, where the valve's control mechanism is displayed in detail. Therein, the symbols are in accordance with [Int12]. While the supply pressure $p_{\text{sup}}(t)$ and the working pressure $p_{\text{in}}(t)$ are measured in all experiments, additional sensors are considered in this section, measuring the mass flow rate $\dot{m}_{\text{in}}(t)$ at $z = 0$ downstream of valve and the corresponding flow temperature $T_{\text{in}}(t)$. Both, $\dot{m}_{\text{in}}(t)$ and $T_{\text{in}}(t)$, mainly depend on $p_{\text{in}}(t)$ and $p_{\text{sup}}(t)$ as well as on the size of the valve orifice area, which is defined by the position of the spool.

In the following, it is assumed that static relations[5] are sufficient to model the pneumatic behavior of the valve adequately, cf. [Bru+99]. As depicted in Fig. 2.3, the valve in this thesis is a proportional directional control valve, where the position of the spool is proportional to the supplied voltage $\nu(t)$, e.g., [Bea07]. Hence, the electrical and mechanical parts of the valve can be neglected in the model. As $\nu(t) \in [0, 10\,\text{V}]$, the mass flow rate is bounded by $\dot{m}_{\text{in}}(t) \in [\dot{m}_{\text{in}}^{\min}(t), \dot{m}_{\text{in}}^{\max}(t)]$. The minimal mass flow rate $\dot{m}_{\text{in}}^{\min}(t)$, discharging the test bench, results for $\nu(t) = 0$ and the maximal mass flow rate $\dot{m}_{\text{in}}^{\max}(t)$, charging the test bench, corresponds to $\nu(t) = 10\,\text{V}$. While $\dot{m}_{\text{in}}^{\min}(t)$ is primarily defined by $p_{\text{in}}(t)$, $\dot{m}_{\text{in}}^{\max}(t)$ depends additionally on $p_{\text{sup}}(t)$. The valve is designed such that

$$\dot{m}_{\text{in}}^{\min}(t) \leq \dot{m}_{\text{in}}(t) < 0 \qquad \text{for} \qquad 0 \leq \nu(t) < 5\,\text{V} \tag{2.17a}$$

$$\dot{m}_{\text{in}}(t) = 0 \qquad \text{for} \qquad \nu(t) = 5\,\text{V} \tag{2.17b}$$

$$0 < \dot{m}_{\text{in}}(t) \leq \dot{m}_{\text{in}}^{\max}(t) \qquad \text{for} \qquad 5\,\text{V} < \nu(t) \leq 10\,\text{V} \tag{2.17c}$$

hold at a specific operating point (cf. [Fes18]). However, to operate the valve under varying conditions, the voltage corresponding to $\dot{m}_{\text{in}}(t) = 0$, which depends on $p_{\text{in}}(t)$ as well as $p_{\text{sup}}(t)$, has to be determined experimentally.

Modeling of the Mass Flow Rate Since the voltage $\nu(t) \in [0, 10\,\text{V}]$ can be continuously specified, the mass flow rate through the valve can be manipulated by adjusting the voltage. To achieve a desired $\dot{m}_{\text{in}}(t)$ in terms of $\nu(t)$, a relation between $\dot{m}_{\text{in}}(t)$ and

[5] Dynamic valve models are stated in, e.g., [RH00a; XW04].

the voltage $\nu(t)$, depending on the pressures $p_{\text{in}}(t)$ and $p_{\text{sup}}(t)$, is needed. For that, the function

$$\dot{m}_{\text{in}}(t) = f_{\dot{m}}\left(r(t), \nu(t)\right) \tag{2.18}$$

is derived based on steady-state measurements, where it is assumed that $\dot{m}_{\text{in}}(t)$ can be defined by the pressure ratio $r(t) = p_{\text{in}}(t)/p_{\text{sup}}(t)$ and the voltage $\nu(t)$. Inverting (2.18) w.r.t. $\nu(t)$ yields the inverse mass flow rate model of the valve:

$$\nu(t) = f_{\nu}\left(r(t), \dot{m}_{\text{in}}(t)\right). \tag{2.19}$$

Therefore, if $r(t)$ and a desired mass flow rate $\dot{m}_{\text{in}}(t)$ are known, $\nu(t)$ results from (2.19) and can be fed to the valve, providing the desired mass flow rate.

Existing approaches in the literature, modeling the mass flow rate by assuming a static relation, can be roughly classified into two categories, depending if the approach is based on the ISO 6358 in [Int13] or not. Therein, a description of the mass flow rate through a valve is derived based on a nozzle model, containing two unknown functions: the sonic conductance and the critical pressure, both depending on the spool displacement. These functions have to be identified through experiments, e.g., [Ola+05; FG11]. However, some authors argue that this model is not accurate enough and propose other approaches, for example, based on a curve fitting without a physical model, e.g., [BM98; WRB09].

In the context of this thesis, several of the aforementioned approaches were tested and the most suitable model, a direct lookup table, was chosen to describe the pneumatic behavior of the valve. To obtain the lookup table, the test bench set-up in Fig. 2.1 is modified: As depicted in Fig. 2.3, a mass flow sensor is installed at $z = 0$ downstream of the valve. Furthermore, the long tube and the tank are replaced by a proportional pressure regulator valve, serving as a throttle to discharge the system to p_0. Next, steady-state experiments are performed, where the voltage $\nu(t)$ and the pressure ratio $r(t)$ are successively varied. From each variation, the corresponding mass flow rate $\dot{m}_{\text{in}}(t)$ is obtained. The measured values of $\nu(t)$, $r(t)$, and $\dot{m}_{\text{in}}(t)$ are stored.

Prior to the derivation of the functions $f_{\dot{m}}\left(r(t), \nu(t)\right)$ and $f_{\nu}\left(r(t), \dot{m}_{\text{in}}(t)\right)$ in (2.18) and (2.19), respectively, the following aspect needs to be considered: For the unique existence of its inverse $f_{\nu}\left(r(t), \dot{m}_{\text{in}}(t)\right)$, $f_{\dot{m}}\left(r(t), \nu(t)\right)$ needs to be strictly monotonic in $\nu(t)$. This is guaranteed if the following condition is imposed on the measured data: For any but fixed r_0 and for all $\nu_1 < \nu_2$, $f_{\dot{m}}\left(r_0, \nu_1\right) < f_{\dot{m}}\left(r_0, \nu_2\right)$ holds. In addition, it is required that for all $r_1 < r_2$ and for any but fixed ν_0, $f_{\dot{m}}\left(r_1, \nu_0\right) > f_{\dot{m}}\left(r_2, \nu_0\right)$ holds. Although these criteria are reasonable from a physical perspective, they are violated by some of the data points caused by measurement noise and/or hysteresis effects of the valve. These points are discarded and the remaining measured data is depicted in the left-hand plot of Fig. 2.4. By a linear interpolation, the function $f_{\dot{m}}\left(r(t), \nu(t)\right)$ is derived and shown in the right-hand plot of Fig. 2.4. From that, the inverse function $f_{\nu}\left(r(t), \nu(t)\right)$ is directly obtained since any pair $\left(r(t), \dot{m}_{\text{in}}(t)\right)$ uniquely defines $\nu(t)$.

Remark 2.2. As it is shown in Sec. 3.4, the prediction of the voltage $\nu(t)$ by the inverse mass flow rate model (2.19) of the valve, i.e. the function $f_{\nu}\left(r(t), \dot{m}_{\text{in}}(t)\right)$, is relatively inaccurate, caused by model uncertainties. These result from measurement noise, hysteresis effects, and the limited accuracy of the sensors. Especially for $\dot{m}_{\text{in}}(t) = 0$, the predicted $\nu(t)$ is prone to errors since the precision of the mass flow rate sensor further diminishes for small mass flow rates. In addition, the gradients of $\nu(t)$ w.r.t. $\dot{m}_{\text{in}}(t)$ are the steepest around $\dot{m}_{\text{in}}(t) = 0$. Still, as shown later on, the model seems to be adequate for the purpose intended in this thesis. △

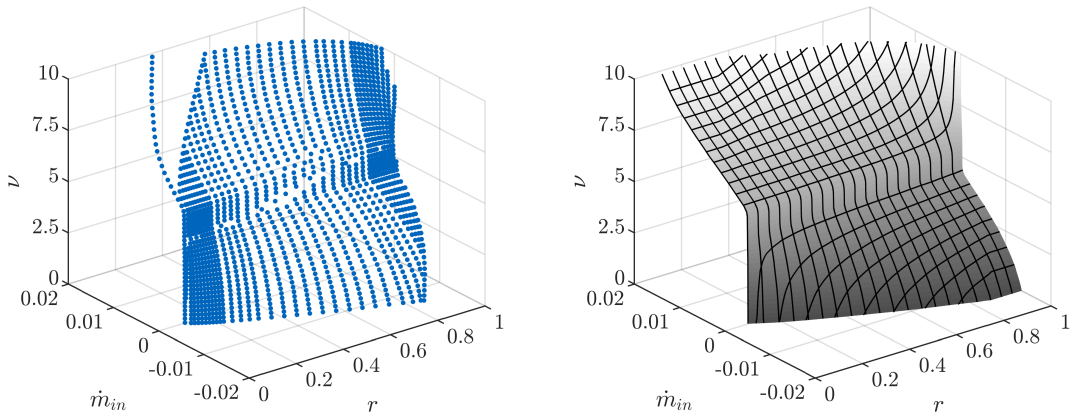

Figure 2.4: The mass flow rate $\dot{m}_{\text{in}}(t)$ (in kg/s) depending on the voltage $\nu(t)$ (in V) and the pressure ratio $r(t)$ (dimensionless): The blue dots show the measured data and the function $f_{\dot{m}}\left(r(t), \nu(t)\right)$ on the right-hand side results from interpolating between these data points

Modeling the Flow Temperature The air transported by the mass flow rate $\dot{m}_{\text{in}}(t)$ through the valve is characterized in terms of the quantities $p_{\text{in}}(t)$, $\rho_{\text{in}}(t)$, and $T_{\text{in}}(t)$, related by the ideal gas law (2.3). In this thesis, $p_{\text{in}}(t)$ results from measurements, necessitating a model for $\rho_{\text{in}}(t)$ or $T_{\text{in}}(t)$. Since $T_{\text{in}}(t)$ is easier to measure compared with $\rho_{\text{in}}(t)$, the function

$$T_{\text{in}}(t) = f_T\left(p_{\text{in}}(t), \dot{m}_{\text{in}}(t)\right) \tag{2.20}$$

is derived in the following. By making use of (2.20), the temperature can be calculated from the quantities $p_{\text{in}}(t)$ and $\dot{m}_{\text{in}}(t)$, resulting from, e.g., measurements and/or simulation data. Still, transient temperature measurements are often inaccurate, e.g., [Gio+08]. Therefore, $f_T\left(p_{\text{in}}(t), \dot{m}_{\text{in}}(t)\right)$ is obtained from steady-state experiments, where the effect of small variations in $p_{\text{sup}}(t)$ are neglected and a constant flow temperature upstream of the valve is assumed.

The function $f_T\left(p_{\text{in}}(t), \dot{m}_{\text{in}}(t)\right)$ is derived in a similar manner as $f_{\dot{m}}\left(r(t), \nu(t)\right)$ in (2.18). Likewise, the long tube and the tank are replaced by a mass flow rate sensor and a pressure regulator valve. In addition, a Pt1000 temperature sensor is installed at $z = 0$ downstream of the valve (cf. Fig. 2.3), measuring the relative temperature $\Delta T(t) = T_{\text{in}}(t) - T_0$. From that, since the ambient temperature is assumed to be constant, $T_{\text{in}}(t) = \Delta T(t) + T_0$ follows. Next, steady-state experiments are performed for varying pressures $p_{\text{in}}(t)$ and positive[6] mass flow rates $\dot{m}_{\text{in}}(t)$. For $\dot{m}_{\text{in}}(t) = 0$, the condition $T_{\text{in}}(t) = T_0$ is imposed, derived from physical reasoning. The results are depicted in the left-hand plot of Fig. 2.5. By linearly interpolating between these measured data points, the surface in the right-hand plot of Fig. 2.5 is obtained. From that, the function $f_T\left(p_{\text{in}}(t), \dot{m}_{\text{in}}(t)\right)$ in (2.20) follows since $T_{\text{in}}(t) = \Delta T(t) + T_0$ holds.

[6]It will be discussed in Sec. 2.5 that the temperature model is only required for positive mass flow rates.

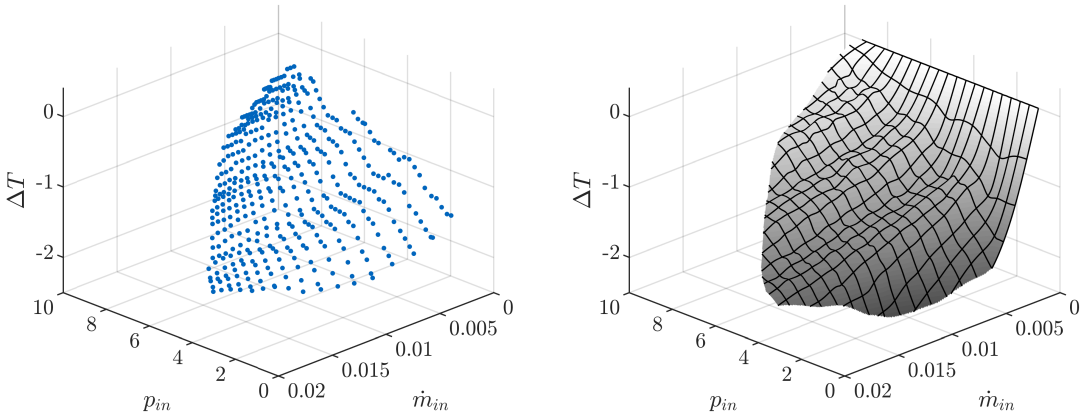

Figure 2.5: The relative temperature $\Delta T(t) = T_{\text{in}}(t) - T_0$ (in K) depending on the mass flow rate $\dot{m}_{\text{in}}(t)$ (in $^{\text{kg}}/_{\text{s}}$) and the pressure $p_{\text{in}}(t)$ (in bar): The blue dots show the measured data and the surface on the right-hand side results from interpolating between these data points

2.4 A Finite-Dimensional Model of the Tank

The model of the tank at $z = L$ (cf. Fig. 2.1) follows from the conservation of mass and energy[7]. Assuming the air in the tank to be perfectly mixed, the ODEs

$$V_{\text{vol}} \frac{\mathrm{d}}{\mathrm{d}t} \rho_{\text{vol}}(t) = \dot{m}(L,t) \tag{2.21a}$$

$$V_{\text{vol}} \frac{\mathrm{d}}{\mathrm{d}t} (\rho e)_{\text{vol}}(t) = (\dot{m}e)(L,t) + (Fv)(L,t) + \dot{Q}_{\text{vol}}(t) \tag{2.21b}$$

are obtained, where the heat flux $\dot{Q}_{\text{vol}}$ is defined as in (2.14) with the constant[8] thermal resistance R_{vol}. By making use of (2.4) and taking $v_{\text{vol}} = 0$ as well as $p_{\text{vol}}(t) = p(L,t)$ into account, the tank model

$$\frac{\mathrm{d}}{\mathrm{d}t} \rho_{\text{vol}}(t) = \frac{A}{V_{\text{vol}}} (\rho v)(L,t) \tag{2.22a}$$

$$\frac{\mathrm{d}}{\mathrm{d}t} p_{\text{vol}}(t) = A \frac{\gamma - 1}{V_{\text{vol}}} \left[\frac{1}{2} (\rho v^3)(L,t) + \frac{\gamma}{\gamma - 1} p_{\text{vol}}(t) v(L,t) + \frac{1}{A R_{\text{vol}}} \left(T_0 - \frac{p_{\text{vol}}(t)}{R_{\text{s}} \rho_{\text{vol}}(t)} \right) \right] \tag{2.22b}$$

follows from (2.21).

Remark 2.3. In general, the cross-section A_{vol} of the tank's pneumatic connection is greater than or equal to the cross-section A of the tube. Hence, $\dot{m} = A\rho v$ holds in (2.21). Otherwise, $\dot{m} = A_{\text{vol}} \rho v$ has to be utilized. △

[7] The kinetic energy is omitted since the position of the tank is fixed.

[8] In order to reduce complexity, R_{vol} is assumed to be constant for a specific tank and is identified experimentally.

2.5 Plant Model

The so-called augmented Euler equations, describing the dynamics of the airflow in the tube, read

$$\frac{\partial}{\partial t}\rho + \frac{\partial}{\partial z}(\rho v) = 0 \tag{2.23a}$$

$$\frac{\partial}{\partial t}(\rho v) + \frac{\partial}{\partial z}(\rho v^2 + p) = -f_\mathrm{c}\frac{\rho v|v|}{2D} \tag{2.23b}$$

$$\frac{\partial}{\partial t}(\rho e) + \frac{\partial}{\partial z}(v(\rho e + p)) = \frac{4}{D}\alpha(T_0 - T) - f_\mathrm{c}\frac{\rho v^2|v|}{2D} \tag{2.23c}$$

and follow from the combination of (2.6), (2.9), and (2.15). By interconnecting this tube model with the models of the valve and the tank in terms of the boundary conditions of (2.23), the plant model is obtained.

Since (2.23) constitutes a system of quasilinear hyperbolic PDEs, these boundary conditions have to be chosen according to the direction and the velocity of the flow. For the test bench set-up in Fig. 2.1, the flow is subsonic, where $Ma < 1$ holds. Thus, two boundary conditions at an inlet, where air flows into the tube, and one at an outlet, where air flows out of the tube, are needed. The boundary conditions can be imposed by the conservative variables ρ, ρv, ρe, and, in addition, in form of the so-called primitive variables ρ, p, v, e.g., [Hir90].

First, the boundary conditions resulting from the valve at $z = 0$ are introduced: If air flows into the tube, i.e. $(\rho v)(0,t) \geq 0$, the test bench is charged and the valve is an inlet. Therefore, two boundary conditions are needed. In this thesis, one of the following two pairs, depending on the intended purpose of the plant model, are imposed. The first pair reads

$$\rho(0,t) = \rho_\mathrm{in}(t) \tag{2.24a}$$

$$(\rho e)(0,t) = \frac{1}{2}\rho_\mathrm{in}(t)v^2(0,t) + \frac{1}{\gamma - 1}p_\mathrm{in}(t) \tag{2.24b}$$

while the second is defined as

$$\rho(0,t) = \rho_\mathrm{in}(t) \tag{2.25a}$$

$$(\rho v)(0,t) = \frac{1}{A}\dot{m}_\mathrm{in}(t). \tag{2.25b}$$

If air flows out of the tube, i.e. $(\rho v)(0,t) < 0$, the test bench is discharged and the valve is an outlet. Hence, only one boundary condition is needed at $z = 0$. In this case, the first pair reduces to

$$(\rho e)(0,t) = \frac{1}{2}(\rho v)^2(0,t) + \frac{1}{\gamma - 1}p_\mathrm{in}(t) \tag{2.26}$$

and the second pair to

$$(\rho v)(0,t) = \frac{1}{A}\dot{m}_\mathrm{in}(t). \tag{2.27}$$

In this thesis, the pair (2.24) is imposed if simulation data from the plant model is compared to measured data from the test bench. For that, $p_\mathrm{in}(t)$ serves as an input to

the simulation. By making use of temperature model (2.20), where $\dot{m}_{\text{in}}(t) = A(\rho v)(0,t)$ follows from the numerical solution of (2.23), $T_{\text{in}}(t)$ is obtained. As $p_{\text{in}}(t)$ and $T_{\text{in}}(t)$ are known, $\rho_{\text{in}}(t)$ in (2.24) results from the ideal gas law (2.3). In contrast to that, the pair (2.25) is utilized in the context of controller design since $\dot{m}_{\text{in}}(t)$ is usually the control input if the valve is considered to be static, e.g., [RNM16].

Remark 2.4. The choice of the pair (2.24) arises from the fact that a measurement of the pressure is generally easier to obtain compared with the measurement of the transient mass flow rate. In general, mass flow rate sensors are expensive, the measurements are prone to errors, and/or the measurement equipment disturbs the flow, e.g., [RNM15]. △

Next, the coupling between the tube and the tank at $z = L$ is discussed. If $(\rho v)(L,t) \leq 0$, the tank is an inlet to the tube. In this case, $(\rho v)(L,t)$ is an input to the tank model (2.22) while $p_{\text{vol}}(t)$ and $\rho_{\text{vol}}(t)$ are outputs of the tank. Thus, the two necessary boundary conditions read

$$\rho(L,t) = \rho_{\text{vol}}(t) \tag{2.28a}$$

$$(\rho e)(L,t) = \frac{1}{2}\rho_{\text{vol}}(t)v^2(L,t) + \frac{1}{\gamma - 1}p_{\text{vol}}(t), \tag{2.28b}$$

where it is assumed that the density in the tube at $z = L$ equals the density in the tank. For $(\rho v)(L,t) > 0$, the tank represents an outlet of the tube. Thus, $\rho(L,t)$ as well as $(\rho v)(L,t)$ are inputs to the tank model (2.22) while $p_{\text{vol}}(t)$ is an output of the tank. Thereby, the boundary condition

$$(\rho e)(L,t) = \frac{1}{2}(\rho v^2)(L,t) + \frac{1}{\gamma - 1}p_{\text{vol}}(t) \tag{2.29}$$

follows from (2.28b). As a consequence of the boundary conditions (2.28) and (2.29), connecting the quasilinear PDE subsystem (2.23) with the nonlinear ODE subsystem (2.22), the plant model is a bidirectionally coupled hyperbolic PDE-ODE system.

2.6 Simplified Models of the Test Bench

In this section, the plant model is successively simplified. For that, additional assumptions are imposed on the model (2.23) of the tube dynamics, eventually resulting in a linear system description. Thereby, the temperature model of the valve becomes superfluous and the tank model and the boundary conditions simplify. The stated assumptions and the corresponding names of the five resulting models are listed in Tab. 2.1. Their derivation is discussed in the following.

2.6.1 Isothermal Model

To obtain the isothermal model, it is assumed that the flow temperature is constant at $T = T_0$, a simplification common in the literature, cf. [OC01; AC08; Cha10]. It is valid if the pressure variations are sufficiently slow and, compared to that, the air in the tube is almost immediately in thermal equilibrium with its surroundings.

The derivation of the isothermal model, presented in the following, is based on the assumption that the entropy

$$S = c_V \ln\left(\frac{p}{\rho^\gamma}\right) + k \tag{2.30}$$

Table 2.1: Models and their corresponding additional assumptions

model	isothermal flow	linear flux	laminar flow	linear friction term
plant				
isothermal	×			
semilinear	×	×		
laminar	×	×	×	
linear	×	×	×	×

remains constant along the particle path, where $k \in \mathbb{R}$. Hence, to derive the isothermal model, friction and heat transfer in the augmented Euler equations (2.23) are initially neglected. Consequently, since the flow is assumed to be subsonic, i.e. it is smooth and no shocks occur, S is constant, resulting in isentropic flow, e.g., [LeV92]. Rearranging (2.30) yields

$$p = f_p(\rho) = \mathrm{e}^{\left(\frac{S-k}{c_V}\right)}\rho^\gamma, \tag{2.31}$$

where the pressure p is a function of density only. Expanding $f_p(\rho)$ by a Taylor series around the ambient density ρ_0 and making use of (2.30) yields

$$f_p(\rho) = f_p(\rho_0) + \frac{\gamma}{\rho_0} f_p(\rho_0)(\rho - \rho_0) + \frac{\gamma^2 - \gamma}{\rho_0^2} f_p(\rho_0)(\rho - \rho_0)^2 + \cdots . \tag{2.32}$$

By assuming relatively small changes in the pressure, the variations in the density are small, too. Thereby, the higher order terms in (2.32) can be neglected. Considering isothermal flow and by making use of the ideal gas law (2.3), the function $f_p(\rho)$ can be approximated by

$$f_p(\rho) = f_p(\rho_0) + \gamma R_\mathrm{s} T_0(\rho - \rho_0).$$

Hence, the Euler equations in (2.23) without friction and heat transfer simplify to

$$\frac{\partial}{\partial t}\rho + \frac{\partial}{\partial z}(\rho v) = 0 \tag{2.33a}$$

$$\frac{\partial}{\partial t}(\rho v) + \frac{\partial}{\partial z}(\rho v^2 + a_\mathrm{iso}^2 \rho) = 0, \tag{2.33b}$$

where the constant $a_\mathrm{iso} = \sqrt{\gamma R_\mathrm{s} T_0}$ denotes the isothermal speed of sound. The energy equation (2.23c) is neglected since it becomes redundant as the continuum equation (2.33a) as well as the momentum equation (2.33b) can be solved independently of (2.23c), e.g., [LeV92]. Finally, (2.33b) is augmented by the friction term in (2.23b). Thereby, the quasilinear system of two PDEs

$$\frac{\partial}{\partial t}\rho + (\rho v)_z = 0 \tag{2.34a}$$

$$\frac{\partial}{\partial t}(\rho v) + \frac{\partial}{\partial z}(\rho v^2 + a_\mathrm{iso}^2 \rho) = -f_\mathrm{c}\frac{\rho v|v|}{2D} \tag{2.34b}$$

is obtained.

Remark 2.5. Usually, in the context of isothermal flow, $\gamma = 1$ holds, e.g., [LeV92]. However, this value does no longer represent the ratio of specific heats and would decrease the accuracy of the model (2.34). Thus, the derivation of the isothermal model in this thesis, where $\gamma = 1.4$ in a_iso holds, differ from the literature. △

2.6.2 Semilinear Model

According to, e.g., [MPE00; HMS09], the nonlinear term ρv^2 in the flux of the momentum equation (2.34b) is often negligible in the context of pneumatic tubes. This assumption is motivated by the fact that the velocity of the medium air in the tube is generally much smaller than the speed of sound, resulting in Mach numbers of $Ma < 0.3$. Hence, $a_{\text{iso}}^2 \rho \gg \rho v^2$ follows and the term ρv^2 can be dropped, rendering the flux linear. Furthermore, $f \approx f_{\text{c}}$ holds, where an error of less than 1 % for $Ma < 0.3$ results from (2.10). Thus, the effect of compressibility on the friction factor is neglected. Based on (2.34), these additional assumptions yield the following semilinear system of two PDEs:

$$\frac{\partial}{\partial t}\rho + \frac{\partial}{\partial z}(\rho v) = 0 \tag{2.35a}$$

$$\frac{\partial}{\partial t}(\rho v) + a_{\text{iso}}^2 \frac{\partial}{\partial z}\rho = -f\frac{\rho v|v|}{2D}. \tag{2.35b}$$

2.6.3 Laminar Model

Assuming laminar flow, where f is defined as in (2.11), the friction term in (2.35b) reads

$$f\frac{\rho v|v|}{2D} = \frac{32\mu_0}{D^2}v$$

with the constant dynamic viscosity μ_0 at ambient conditions. To improve the accuracy of the model in case of turbulent flow, the constant friction amplification

$$k_{\text{fric}}\frac{32\mu_0}{D^2}v \quad \text{with} \quad k_{\text{fric}} \geq 1$$

is introduced, compensating underestimated friction effects. Thereby, the semilinear system

$$\frac{\partial}{\partial t}\rho + \frac{\partial}{\partial z}(\rho v) = 0 \tag{2.36a}$$

$$\frac{\partial}{\partial t}(\rho v) + a_{\text{iso}}^2 \frac{\partial}{\partial z}\rho = -k_{\text{fric}}\frac{32\mu_0}{D^2}v \tag{2.36b}$$

is obtained from (2.35).

2.6.4 Linear Model

For relatively slow fluid velocities, the changes of the density along the tube are small and the flow can be seen as almost incompressible, e.g., [And11]. According to [SB59], this assumption is valid for pneumatic tubes. Hence, the friction term

$$k_{\text{fric}}\frac{32\mu_0}{D^2}v = k_{\text{fric}}\frac{32\mu_0}{D^2}\frac{\rho v}{\rho}$$

in (2.36b) can be simplified by assuming $v = (\rho v)/\rho_0$, where ρ_0 is the constant density at ambient conditions. By that, (2.36) results in the linear system

$$\frac{\partial}{\partial t}\rho + \frac{\partial}{\partial z}(\rho v) = 0 \tag{2.37a}$$

$$\frac{\partial}{\partial t}(\rho v) + a_{\text{iso}}^2 \frac{\partial}{\partial z}\rho = -k_{\text{fric}}\frac{32\mu_0}{D^2}\frac{1}{\rho_0}\rho v. \tag{2.37b}$$

2.6.5 Boundary Conditions of the Simplified Models

Since all simplified models consist of two PDEs, caused by the assumption of isothermal flow, only one boundary condition at each end of the tube is needed, independent of the flow direction.

The boundary condition arising from the valve at $z = 0$ for the simplified models reads

$$\rho(0,t) = \rho_{\mathrm{in}}(t), \tag{2.38}$$

which follows from (2.24), if $p_{\mathrm{in}}(t) = \rho_{\mathrm{in}}(t) R_{\mathrm{s}} T_0$ is the imposed variable and

$$(\rho v)(0,t) = \frac{1}{A}\dot{m}_{\mathrm{in}}(t), \tag{2.39}$$

resulting from (2.25), if $\dot{m}_{\mathrm{in}}(t)$ is chosen. Furthermore, because of the assumption of isothermal flow, the temperature model (2.20) of the valve becomes superfluous as $T_{\mathrm{in}}(t) = T_0$.

The boundary condition following from the tank at $z = L$ results from (2.28) and reads

$$\rho(L,t) = \rho_{\mathrm{vol}}(t). \tag{2.40}$$

As only the lumped state $\rho_{\mathrm{vol}}(t)$ is needed, the energy equation (2.22b) of the tank model is dropped. Hence, the simplified tank model reads

$$\frac{\mathrm{d}}{\mathrm{d}t}\rho_{\mathrm{vol}}(t) = \frac{A}{V_{\mathrm{vol}}}(\rho v)(L,t). \tag{2.41}$$

2.7 Simulation Studies and Measurement Results

In this section, the simulation data of the different models is compared with each other as well as to measurements of the test bench and the underlying assumptions as well as their effects on the accuracy of the models are discussed. To cover a wide range of possible applications, the tube length and diameter as well as the tank volume are varied. The chosen configurations, i.e. long, thin tube and a large tank as well as short, thick tube and small tank, render the different experiments as distinct as possible. Both, the charging and discharging process is investigated. In addition to the standard test bench set-up depicted in Fig. 2.1, another one is utilized. For that, the tank at $z = L$ is removed and the air flows into the ambience. Thus, the tube models can be investigated without the interference of the tank model. The results are stated in terms of a qualitative and quantitative assessment.

At the beginning of each experiment, the air in the system is at rest and in equilibrium with its surroundings, i.e. $v = 0$, $p = p_0$, and $T = T_0$. Next, the test bench is charged by feeding a voltage of $\nu(t) = 10\,\mathrm{V}$ to the hitherto closed valve. Thereby, the excitation resembles a step input[9], limited by the capacities of the valve. After the charged system has reached steady-state conditions at the constant pressure level[10] $p = p_{\mathrm{sup}}$, the test bench is discharged to the ambient pressure p_0 by supplying a voltage of $\nu(t) = 0$ to

[9] Sinusoidal inputs with a frequency of approximately 16 Hz can be found in [Ker17].

[10] To shorten the duration of the experiments, the supply pressure is reduced to $p_{\mathrm{sup}}(t) \approx 7\,\mathrm{bar}$ in this section.

Table 2.2: Fixed parameters of the test bench

p_0	ambient pressure	$1.01\,\mathrm{bar}$	
T_0	ambient temperature	$293.15\,\mathrm{K}$	
R_s	specific gas constant of air	$287.05\,{}^{\mathrm{J}}/_{\mathrm{kg\cdot K}}$	[IG81]
γ	ratio of specific heats of air	1.4	[And11]
ε	height of roughness elements	$1.5 \cdot 10^{-6}\,\mathrm{m}$	[VDI10]
R_{vol}	thermal resistance	$4 \cdot 10^{-3}\,{}^{\mathrm{K}}/_{\mathrm{W}}$	

the valve. During the experiment, two pressures[11] are measured: the working pressure $p_{\mathrm{in}}(t)$ downstream of the valve as well as a reference pressure, for example, the tank pressure $p_{\mathrm{vol}}(t)$ in case of the standard test bench set-up. As stated subsequently, these measurements are utilized to assess the models.

Next, the models are simulated. For that, the measured pressure $p_{\mathrm{in}}(t)$ serves as input to the simulation. Hence, the boundary conditions at $z = 0$ are (2.24) as well as (2.26) for the plant model and (2.38) for the simplified models. The initial conditions read $\rho(z,0) = \rho_0$, $(\rho v)(z,0) = 0$, $(\rho e)(z,0) = (\rho e)_0$, $\rho_{\mathrm{vol}}(0) = \rho_0$, and $p_{\mathrm{vol}}(0) = p_0$.

The computed pressures are compared with each other and to the measured reference pressure. A quantitative assessment is given in form of two criteria: The first one is the L^1-norm of the relative errors[12], generally defined as

$$L^1_{\mathrm{r,err}} = \frac{100\,\%}{t_{\mathrm{f}}} \int_0^{t_{\mathrm{f}}} \left| \frac{p^{\mathrm{r}}(t) - p(t)}{p^{\mathrm{r}}(t)} \right| \mathrm{d}t, \tag{2.42}$$

where $p^{\mathrm{r}}(t) = p_{\mathrm{meas}}(t)$ is the measured reference pressure and $p(t) = p_{\mathrm{sim}}(t)$ the corresponding simulated pressure. The considered period of time is defined by the interval $[0, t_{\mathrm{f}}]$. The second criterion is the L^∞-norm of the error, defined as

$$L^\infty_{\mathrm{err}} = \sup_{t \in [0,t_{\mathrm{f}}]} \left| p^{\mathrm{r}}(t) - p(t) \right|. \tag{2.43}$$

Tab. 2.2 lists the parameters which are constant throughout this thesis and utilized in the simulations unless mentioned otherwise. The temperature dependent quantities η, λ, c_p, and c_V are approximated by the polynomials in T, which are stated in [RHC98]. Furthermore, the discretization schemes, necessary for the numerical implementation of the models, as well as the chosen time and spatial step size Δt and Δz, respectively, are stated in Appx. B.1. A detailed description of the test bench's software framework, implemented in Simulink Real-Time, is given in [MK19].

Remark 2.6. The match of the simulation data with the experimental data might be slightly enhanced by using other correlations for friction and heat transfer. Furthermore, numerical optimizations could be performed to identify the parameters which cannot be directly measured, e.g., R_{vol}, ε, and k_{fric}. While such an approach can improve the accuracy of the models for a specific set-up, a new optimization might be necessary if, e.g., the tube is replaced by another one with a different diameter. Therefore, in order to keep the models general and straightforward, an optimization approach is not pursued in

[11] Naturally, apart from pressure measurements, measurements of the mass flow rate could be used to validate the models, too. However, as discussed in Rem. 2.4, a measurement of the pressure is often preferable.

[12] Hence, the measure resembles the mean absolute percentage error, e.g., [HK06].

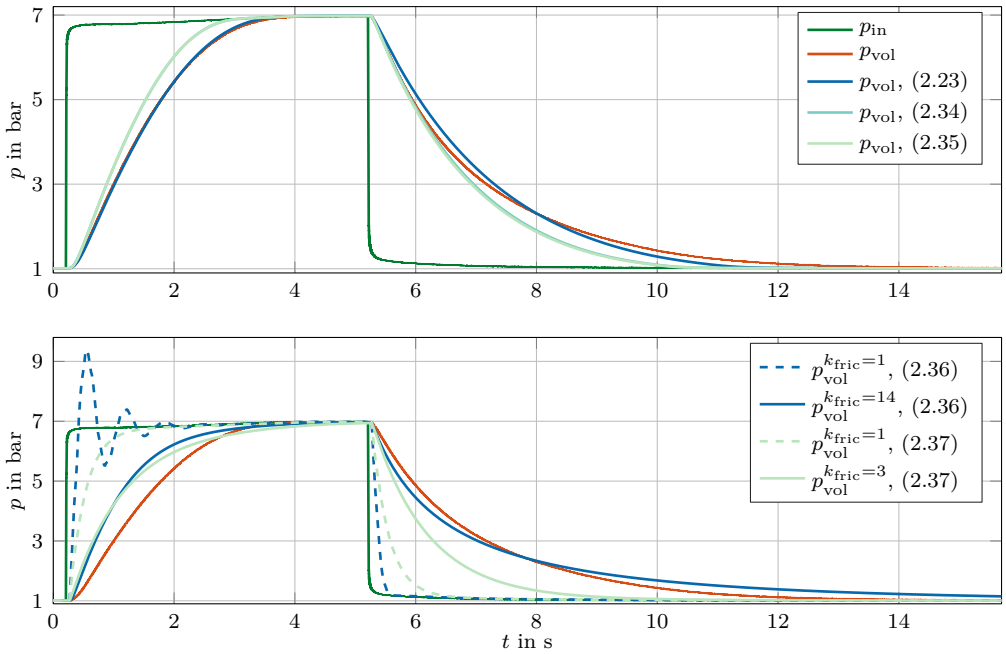

Figure 2.6: Flow into the tank: Measurement and simulation data for $L = 20\,\mathrm{m}$, $D = 4\,\mathrm{mm}$ and $V_{\mathrm{vol}} = 0.64 \cdot 10^{-3}\,\mathrm{m}^3$

Table 2.3: Flow into the tank: Deviations of the measurement and simulation data for $L = 20\,\mathrm{m}$, $D = 4\,\mathrm{mm}$, and $V_{\mathrm{vol}} = 0.64 \cdot 10^{-3}\,\mathrm{m}^3$

model	plant	isothermal	semilinear	laminar ($k_{\mathrm{fric}} = 14$)	linear ($k_{\mathrm{fric}} = 3$)
$L^1_{\mathrm{r,err}}$	3.951 %	8.887 %	9.240 %	13.273 %	16.859 %
L^∞_{err}	0.298 bar	0.629 bar	0.629 bar	1.287 bar	1.291 bar

this thesis. Still, for each test bench configuration, the value of k_{fric} is roughly adjusted by trial and error to facilitate the discussion of the laminar and the linear model. △

2.7.1 Standard Set-Up: Flow into the Tank

Test bench configuration with a long, thin tube and a large tank For this experiment, a test bench configuration with $L = 20\,\mathrm{m}$, $D = 4\,\mathrm{mm}$, and $V_{\mathrm{vol}} = 0.64 \cdot 10^{-3}\,\mathrm{m}^3$ is utilized. In both plots of Fig. 2.6, the measured pressure $p_{\mathrm{in}}(t)$ downstream of the valve as well as the reference pressure, i.e. the measured tank pressure $p_{\mathrm{vol}}(t)$, are displayed. Furthermore, in the upper plot, the tank pressures, resulting from the simulation of the plant model (2.23), the isothermal model (2.34), and the semilinear model (2.35) are shown. The lower plot additionally depicts the laminar model (2.36) with $k_{\mathrm{fric}} = 1$ as well as $k_{\mathrm{fric}} = 14$ and the linear model (2.37) with $k_{\mathrm{fric}} = 1$ as well as $k_{\mathrm{fric}} = 3$. The corresponding errors $L^1_{\mathrm{r,err}}$ and L^∞_{err} in (2.42) and (2.43), respectively, are stated in Tab. 2.3.

Based on Fig. 2.6, it can be concluded that the simulation data of the plant model in the upper plot shows the best match with the experimental data from the test bench. For

the charging process, the fit is almost perfect. During the discharge process, only a slight mismatch between the simulated and measured pressure curves occurs. The increased deviations of the isothermal and the semilinear model are caused by the assumption of no heat transfer. Thereby, the transient tank pressure is overestimated during charging and underestimated during discharging. As the results of the isothermal and the semilinear model are essentially the same, it can be deduced that the neglect of the nonlinear flux term ρv^2 in the momentum equation (2.35b) of the semilinear model has virtually no effect in this experiment.

The lower plot of Fig. 2.6 illustrates the effect of the assumptions of laminar and linear flow, only valid for $Re \leq Re_{\text{crit,min}}$. With $k_{\text{fric}} = 1$, both, the laminar and the linear model, underestimate the increased influence of friction induced by the turbulent flow. Since $Re_{\text{crit,min}} = 1.9 \cdot 10^3$ in (2.13a) is much smaller as the maximum Reynolds number $Re_{\text{max}} = 2.2 \cdot 10^5$ occurring in this experiment, the assumption of laminar flow is violated. As the flow velocity v in the friction term in the momentum equation (2.36b) of the laminar model is defined in terms of the conserved quantities ρ and ρv, i.e. $v = \rho v / \rho$, the effect of friction decreases at higher densities ρ. In contrast to that, the friction term in the momentum equation (2.37b) of the linear model is proportional to ρv since $v = \rho v / \rho_0$ is utilized therein. As a consequence, the reflections of weakly damped waves become visible in the simulation data of the laminar model. By adjusting the respective friction factor k_{fric}, the accuracy of both models is improved.

Test bench configuration with a short, thick tube and a small tank Fig. 2.7 displays the results for a test bench configuration with $L = 5\,\text{m}$, $D = 8\,\text{mm}$, and $V_{\text{vol}} = 0.10 \cdot 10^{-3}\,\text{m}^3$. Because the pneumatic connection of the tank has a smaller diameter than the tube, $\dot{m}(L,t) = A_{\text{vol}}(\rho v)(L,t)$ with $A_{\text{vol}} = 1.26 \cdot 10^{-5}\,\text{m}^2$ is used in (2.21) (cf. Rem. 2.3). In addition, caused by the reduced inner tank surface, the thermal resistance is decreased. Its value $R_{\text{vol}} = 1 \cdot 10^{-1}\,\text{K/W}$ is identified by trial and error, i.e. by comparing experimental data from the test bench to the simulation data of the plant model. The simulation data of the laminar model with $k_{\text{fric}} = 1$ is not depicted in Fig. 2.7 because of severe oscillations but is shown separately in Fig. 2.8. These are mainly caused by non-physical negative densities which occur during the discharge process. Thereby, the friction term in (2.36b) excites the system as its induced force acts in the direction of the flow velocity since the signs of v and ρv differ in this case.

Caused by the increased flow velocities compared to the prior experiment, the neglect of the nonlinear flux term ρv^2 in the momentum equation (2.35b) of the semilinear model has a larger effect. Consequently, the semilinear model is less accurate than the isothermal model, which is especially apparent during the discharge process in the upper plot of Fig. 2.7. Apart from that, the results are relatively similar to these shown in Fig. 2.6. While the simulation data of the plant model matches the measured data best, each simplification induces deviations. The corresponding errors[13] are quantified in Tab. 2.4.

[13] Since the value of k_{fric} is chosen by trial and error, the errors measures of the linear model with $k_{\text{fric}} = 12$ are slightly smaller compared to the ones of the laminar model with $k_{\text{fric}} = 50$.

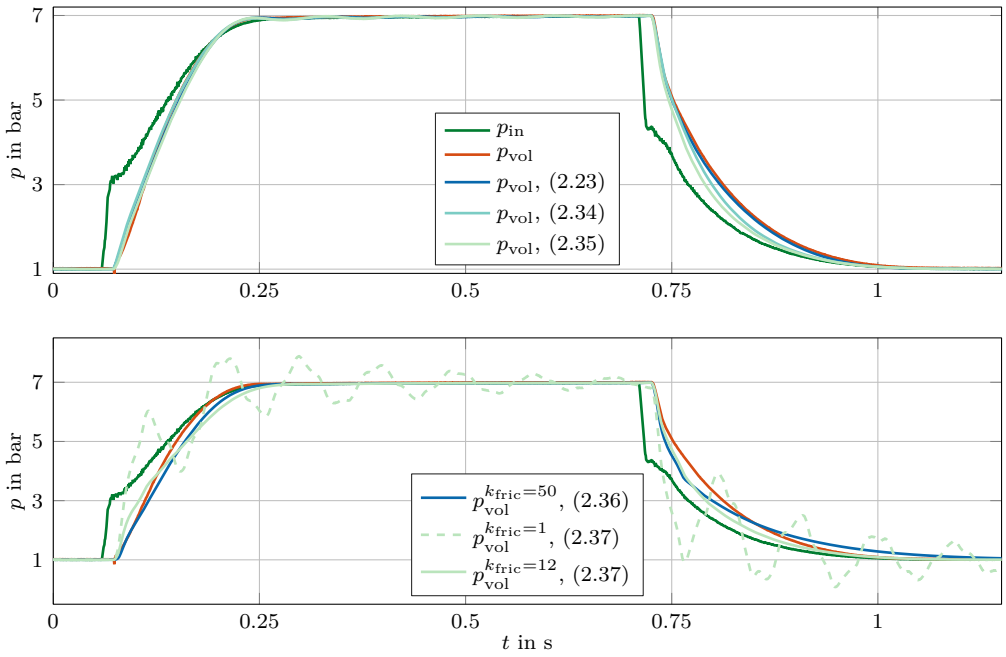

Figure 2.7: Flow into the tank: Measurement and simulation data for $L = 5\,\mathrm{m}$, $D = 8\,\mathrm{mm}$ and $V_{\mathrm{vol}} = 0.10 \cdot 10^{-3}\,\mathrm{m}^3$

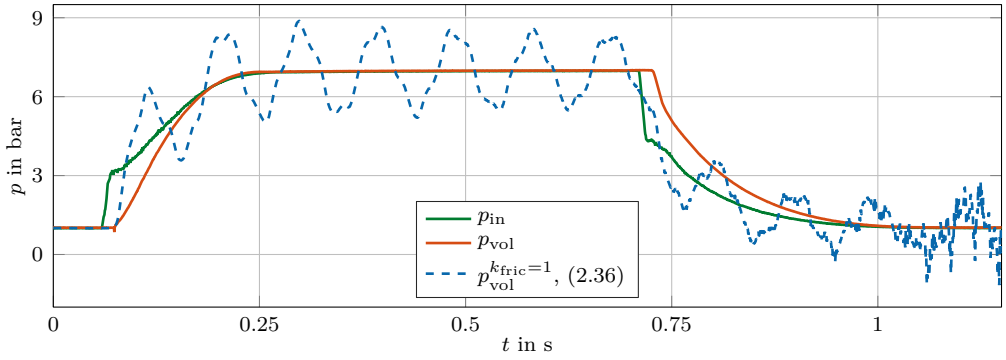

Figure 2.8: Oscillations of the laminar model (2.36) induced by negative densities

Table 2.4: Flow into the tank: Errors between the measurement and simulation data for $L = 5\,\mathrm{m}$, $D = 8\,\mathrm{mm}$ and $V_{\mathrm{vol}} = 0.10 \cdot 10^{-3}\,\mathrm{m}^3$

model	plant	isothermal	semilinear	laminar ($k_{\mathrm{fric}} = 50$)	linear ($k_{\mathrm{fric}} = 12$)
$L^1_{\mathrm{r,err}}$	1.626 %	3.066 %	3.717 %	4.819 %	3.850 %
L^∞_{err}	0.240 bar	0.370 bar	0.601 bar	0.732 bar	0.611 bar

2.7.2 Alternative Set-Up: Flow into the Ambience

For the following experiments, the test bench set-up in Fig. 2.1 is modified by removing the tank at $z = L$. Thus, the air flows from the tube into the ambience. From that, the boundary condition $p(L,t) = p_0$ at $z = L$ follows, replacing the tank dynamics (2.22). Furthermore, an additional sensor is installed, measuring the pressure $p_{L/2}(t) = p(L/2,t)$ at $z = L/2$, i.e. in the middle of the tube. The models are simulated, where the measured pressure $p_{\text{in}}(t)$ serves as input. Subsequently, the computed pressures $p_{L/2}(t)$ are compared to the measured reference pressure $p_{L/2}(t)$.

Test bench configuration with a long, thin tube Fig. 2.9 displays the results for a test bench configuration with $L = 20\,\text{m}$, $D = 4\,\text{mm}$. In the upper plot, it can be seen that the simulation data of the plant model has the best fit with the measurement data while the isothermal and semilinear model are still relatively accurate. Fig. 2.10 depicts the increase of the pressure during the charging process in detail for these three models. Therein, their different propagation speeds and the neglect of heat transfer become apparent. The pressure waves of the plant and the isothermal model are propagated in the positive z direction with a maximum speed[14] of $v + a$ and $v + a_{\text{iso}}$, respectively. In contrast to that, the maximum propagation speed of the semilinear model is a_{iso} since the nonlinear term ρv^2 is not included in its momentum equation (2.35b). Therefore, the increase of the pressure is delayed. Shortly after the initial rise, the pressure gradients (w.r.t. time) of the isothermal and the semilinear model are steeper than the one of the plant model: While the plant model dissipates energy because of friction and heat transfer, the isothermal and the semilinear model dissipate energy because of friction only. As a consequence, the increase of pressure is overestimated by the latter models.

The lower plot of Fig. 2.9 shows the simulation data of the remaining models. However, the laminar model with $k_{\text{fric}} = 1$ is not depicted because of severe oscillations. While the simulated pressure $p_{L/2}(t)$ of the laminar model with $k_{\text{fric}} = 25$ matches the measured pressure under steady-state conditions, the simulated pressure of the linear model does not, independently of the chosen friction amplification factor. The reason for this is the fact that the friction term of the laminar model is proportional to v while the one of the linear model is proportional to ρv. Since $\rho v = \text{const.}$ holds under steady-state conditions, $\frac{\partial}{\partial z}\rho = \text{const.}$ follows from the momentum equation (2.37b) of the linear model. Hence, the pressure gradient of the linear model is constant over the spatial variable z, depicted in Fig. 2.11, where the distributed pressure $p(z,t)$ at $t = 0.79\,\text{s}$ over the spatial variable z for the plant model, the laminar model, and the linear model is shown. Consequently, since the density at $z = 0$ and $z = L$ is defined by the boundary conditions, the steady-state deviation between the measured and simulated pressure $p_{L/2}(t)$, occurring for the linear model, cannot be reduced by tuning k_{fric}.

The corresponding errors in this experiment are stated in Tab. 2.5. By comparing the measures of this experiments with the ones in Tab. 2.3, where the tank is attached to the tube, it can be concluded that the tank model does not significantly alter the tendency of the results.

[14] The maximum propagation speed is defined by the maximum absolute eigenvalue of the matrix $\boldsymbol{B}(\boldsymbol{x})$, defined in (2.49), e.g., [LeV92].

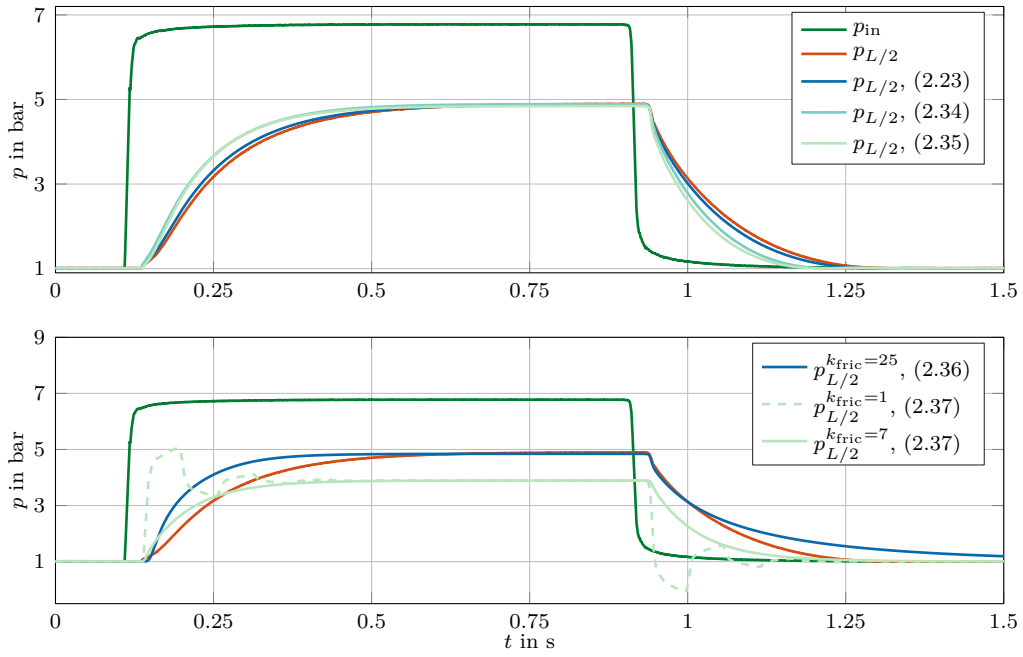

Figure 2.9: Flow into the ambience: Measurement and simulation data for $L = 20\,\mathrm{m}$ and $D = 4\,\mathrm{mm}$

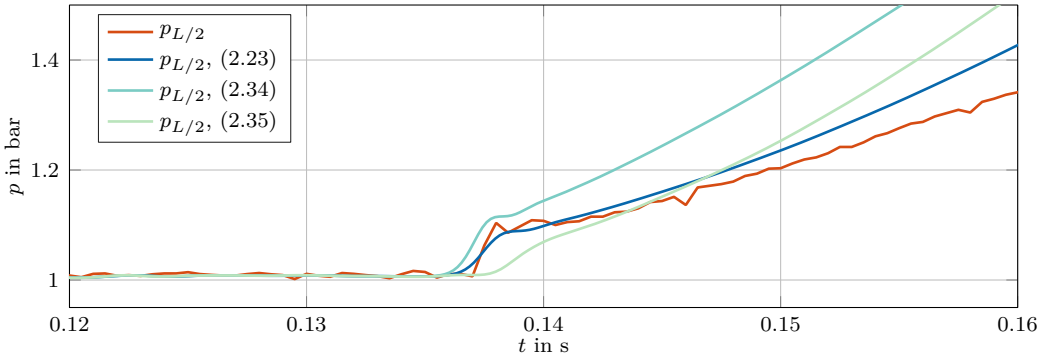

Figure 2.10: Detailed depiction of the measured pressure $p_{L/2}(t)$ compared to the simulated pressure $p_{L/2}(t)$, resulting from the plant model (2.23), the isothermal model (2.34) and the semilinear model (2.35)

Table 2.5: Flow into the ambience: Errors between the measurement and simulation data for $L = 20\,\mathrm{m}$ and $D = 4\,\mathrm{mm}$

model	plant	isothermal	semilinear	laminar ($k_{\mathrm{fric}} = 25$)	linear ($k_{\mathrm{fric}} = 7$)
$L^1_{\mathrm{r,err}}$	1.980 %	5.808 %	6.275 %	13.310 %	12.680 %
L^∞_{err}	0.177 bar	0.543 bar	0.576 bar	1.063 bar	1.011 bar

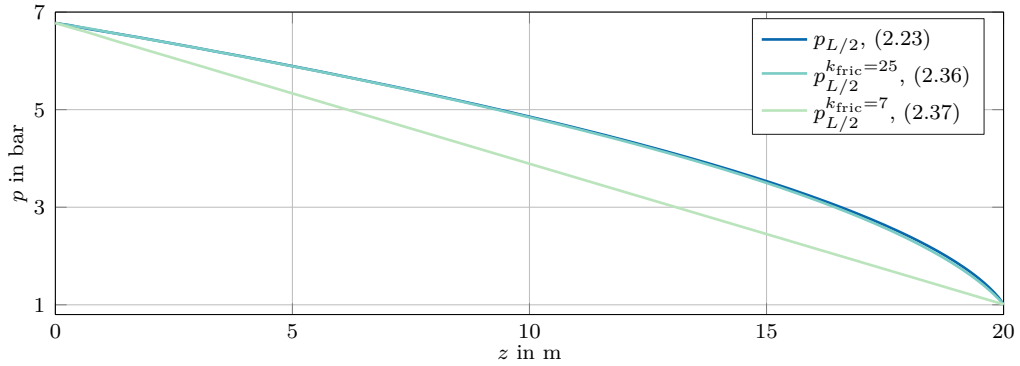

Figure 2.11: Comparison of the distributed pressure $p(z,t)$ at $t = 0.79\,\text{s}$ of the plant model (2.23), the laminar model (2.36) with $k_{\text{fric}} = 25$, and the linear model (2.37) with $k_{\text{fric}} = 7$

Table 2.6: Flow into the ambience: Errors between the measurement and simulation data for $L = 5\,\text{m}$ and $D = 8\,\text{mm}$

model	plant	isothermal	semilinear	laminar ($k_{\text{fric}} = 90$)	linear ($k_{\text{fric}} = 40$)
$L^1_{\text{r,err}}$	1.589 %	2.053 %	3.455 %	4.023 %	10.339 %
L^∞_{err}	0.376 bar	0.507 bar	0.493 bar	0.427 bar	0.671 bar

Test bench configuration with a short, thick tube Fig. 2.12 shows the experimental results, where a short, thick tube with $L = 5\,\text{m}$ and $D = 8$ mm is installed at the test bench. Again, the laminar model with $k_{\text{fric}} = 1$ is not depicted. Caused by this test bench configuration, and since the tube is unconnected at $z = L$, the flow velocities and accelerations are relatively high in this experiment. While the maximum Mach number, obtained from the simulation data of the plant model, reads $Ma \approx 0.64$ for the experiment where a long, thin tube and a large tank are installed (cf. Fig. 2.6), here, its value is $Ma \approx 0.87$. Therefore, more turbulences occur, rendering the pressure measurements in Fig. 2.12 noisy. The measured working pressure $p_{\text{in}}(t)$ is even noisier compared to the measured pressure $p_{L/2}(t)$ since the flow downstream of the valve is not fully developed. As a consequence of the noisy measurements, the simulation data is noisy, too, and the numerical errors are increased. The latter induce the oscillations visible for the linear model with $k_{\text{fric}} = 1$ in the lower plot of Fig. 2.12. Furthermore, induced by the higher flow velocity and acceleration, the entrance length, i.e. the length the flow travels before it becomes fully developed, is increased.

In the upper plot of Fig. 2.12, it can be seen that the simulation and the measurement data considerably deviate during the charging process. This mismatch most probably results from the fact that the assumption of fully developed flow conditions in the Darcy-Weisbach equation (2.8), modeling the pressure drop caused by friction, is violated. Furthermore, the computed pressures in Fig. 2.12, resulting from the simulation of the models which neglect the nonlinear flux term ρv^2, deviate from the measured pressure in steady state. The mismatch arises from the incorrect assumption of a small Mach number, rendering the models without the nonlinear flux term less accurate in this experiment. The resulting errors are given in Tab. 2.6.

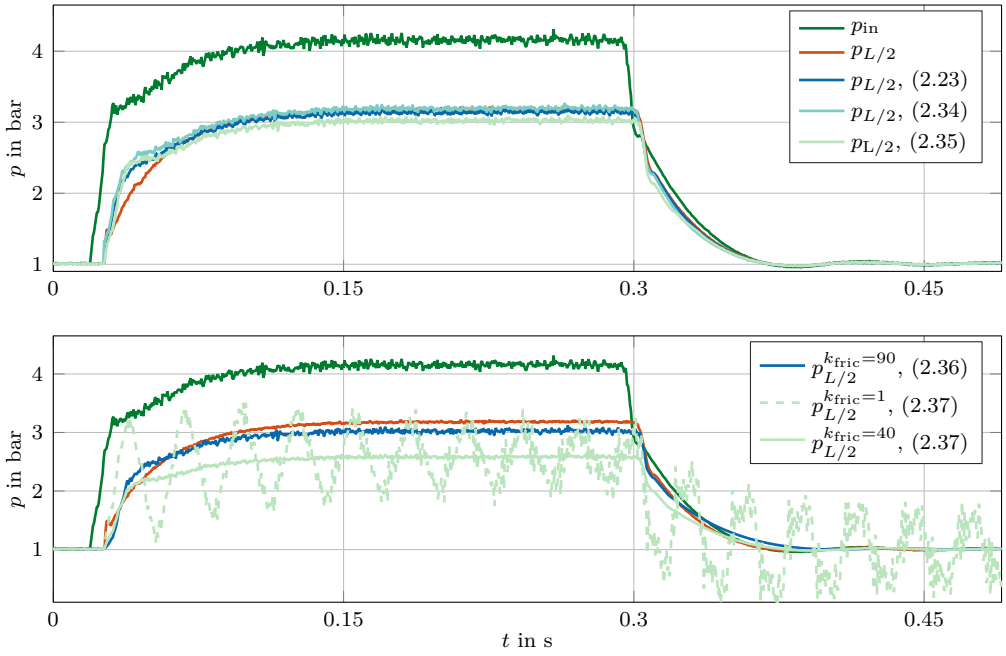

Figure 2.12: Flow into the ambience: Measurement and simulation data for $L = 5\,\mathrm{m}$ and $D = 8\,\mathrm{mm}$

Remark 2.7. Naturally, the accuracy of the models, e.g., expressed in terms of the error measures $L^1_{\mathrm{r,err}}$ and L^∞_{err} in (2.42) and (2.43), respectively, depends on the chosen excitation. A highly dynamic input will increase the deviations between the measured data and the simulation data because, for example, the assumption of fully developed flow is significantly violated and the temperature of the tube wall cannot be considered constant anymore. △

2.8 Summary of the Relevant Models

In the following chapters, several controller designs are presented which enable fast changes between desired pressure levels in the tank by manipulating the mass flow rate through the valve. In the context of these designs, three models are essential: the plant model, the isothermal model, and the linear model. They are briefly restated in a compact form, taking into account the controlled input and the measured output.

The plant model is the most accurate mathematical description of the test bench, verified by the experimental data. Thus, if simulations are performed instead of actual experiments at the test bench, e.g, to validate controllers in the absence of actuator and sensor errors, these simulations are based on the plant model. While the linear model is less precise, it is suited for the late-lumping state feedback and observer design approaches, presented in Chap. 4 and Chap. 5. Furthermore, the linear model is used in the context of the early-lumping controller design in Chap. 6 as this approach is based on a finite-dimensional approximation of the linear model. Since the flatness-based feedforward controller design in Chap. 3 can be applied to quasilinear systems[15], the feedforward

[15]Obviously, the plant model is quasilinear, too. However, as discussed in Sec. 3.5, it is not suited for the approach used in Chap. 3.

controller is derived from the isothermal model as it is more accurate compared with, e.g., the semilinear model.

Prior to the statement of the models, the controlled input is defined. While the actual input to the test bench is the voltage $\nu(t)$, defining the position of the spool, the static inverse mass flow rate model (2.19) of the valve allows to choose the mass flow rate $\dot{m}_{\mathrm{in}}(t)$ as the controlled input $U(t)$. Hence,

$$U(t) = \dot{m}_{\mathrm{in}}(t) \tag{2.44}$$

is defined, where the corresponding voltage $\nu(t)$, fed to the test bench, is obtained from the desired $\dot{m}_{\mathrm{in}}(t)$ and the measured pressure ratio $r(t)$ by making use of (2.19). Consequently, the inverse mass flow rate model can be neglected in the controller design. By inserting (2.44) in the boundary conditions at $z = 0$,

$$\rho(0,t) = \begin{cases} \rho_{\mathrm{in}}(t), & (\rho v)(0,t) > 0 \\ \rho(0,t), & (\rho v)(0,t) \leq 0 \end{cases} \tag{2.45a}$$

$$(\rho v)(0,t) = \frac{1}{A} U(t) \tag{2.45b}$$

results from (2.25) for the plant model and

$$(\rho v)(0,t) = \frac{1}{A} U(t) \tag{2.46}$$

from (2.39) for the simplified models.

With regard to an industrial application, it might be preferable to avoid a pressure sensor in the tank. Thereby, for example, less electrical wiring is needed (cf. Sec. 1.1). Hence, the measured output $Y(t)$ is the collocated measurement of the working pressure $p_{\mathrm{in}}(t)$ downstream of the valve at $z = L$:

$$Y(t) = p_{\mathrm{in}}(t). \tag{2.47}$$

The pressure sensor in the tank, measuring $p_{\mathrm{vol}}(t)$, serves for validation only.

Finally, for the sake of simplicity, the scaled spatial variable

$$\bar{z} = \frac{L - z}{L}$$

with $\bar{z} \in [0,1]$ is introduced. To ease the notation, the scaled spatial variable is denoted by $z \in [0,1]$ in the following. Furthermore, the quantities defined on $z \in [0,1]$ are denoted by their original symbol, e.g., the left-hand side of $\bar{\rho}(\bar{z},t) = \rho(z,t)$ is subsequently denoted by $\rho(z,t)$.

The compact form of the plant model, consisting of the augmented Euler equations (2.23), the tank dynamics (2.22), the temperature model (2.20) of the valve, the boundary conditions (2.28), (2.29) at $z = 0$ as well as (2.45) at $z = 1$, and the measurement (2.47), reads

$$\frac{\partial}{\partial t}\rho = \frac{1}{L}\frac{\partial}{\partial z}(\rho v) \tag{2.48a}$$

$$\frac{\partial}{\partial t}(\rho v) = \frac{1}{L}\frac{\partial}{\partial z}(\rho v^2 + p) - f_{\mathrm{c}}\frac{\rho v|v|}{2D} \tag{2.48b}$$

$$\frac{\partial}{\partial t}(\rho e) = \frac{1}{L}\frac{\partial}{\partial z}(v(\rho e + p)) + \frac{4}{D}\alpha(T_0 - T) - f_\mathrm{c}\frac{\rho v^2|v|}{2D} \tag{2.48c}$$

$$\rho(0,t) = \begin{cases} \rho_\mathrm{vol}(t), & (\rho v)(0,t) \leq 0 \\ \rho(0,t), & (\rho v)(0,t) > 0 \end{cases} \tag{2.48d}$$

$$(\rho e)(0,t) = \begin{cases} \frac{1}{2}\rho_\mathrm{vol}(t)v^2(0,t) + \frac{1}{\gamma-1}p_\mathrm{vol}(t), & (\rho v)(0,t) \leq 0 \\ \frac{1}{2}(\rho v^2)(0,t) + \frac{1}{\gamma-1}p_\mathrm{vol}(t), & (\rho v)(0,t) > 0 \end{cases} \tag{2.48e}$$

$$\rho(1,t) = \begin{cases} \rho_\mathrm{in}(t), & (\rho v)(1,t) \geq 0 \\ \rho(1,t), & (\rho v)(1,t) < 0 \end{cases} \tag{2.48f}$$

$$(\rho v)(1,t) = \frac{1}{A}U(t) \tag{2.48g}$$

$$\frac{\mathrm{d}}{\mathrm{d}t}\rho_\mathrm{vol}(t) = \frac{A}{V_\mathrm{vol}}(\rho v)(0,t) \tag{2.48h}$$

$$\frac{\mathrm{d}}{\mathrm{d}t}p_\mathrm{vol}(t) = A\frac{\gamma-1}{V_\mathrm{vol}}\left[\frac{1}{2}(\rho v^3)(0,t) + \frac{\gamma}{\gamma-1}p_\mathrm{vol}(t)v(0,t) + \frac{1}{AR_\mathrm{vol}}\left(T_0 - \frac{p_\mathrm{vol}(t)}{R_\mathrm{s}\rho_\mathrm{vol}(t)}\right)\right] \tag{2.48i}$$

$$Y(t) = p(1,t). \tag{2.48j}$$

Therein, $p_\mathrm{in}(t) = p(1,t)$ is utilized in (2.48j) and $\rho_\mathrm{in}(t)$ in (2.48f) follows from the temperature model of the valve. The PDEs (2.48a)–(2.48c) are defined on $(z,t) \in (0,1) \times \mathbb{R}^+$, the boundary conditions (2.48d)–(2.48g) and the ODEs (2.48h), (2.48i) for $t > 0$, and the measurement (2.48j) for $t \geq 0$.

For the calculations in the subsequent chapters, it is convenient to rewrite the isothermal and the linear model in terms of the distributed state $\boldsymbol{x}(z,t) = [x_1(z,t), x_2(z,t)]^T = [\rho(z,t), (\rho v)(z,t)]^T$ and the lumped state $\xi(t) = \rho_\mathrm{vol}(t)$. In addition, the PDEs are stated in the quasilinear form

$$\frac{\partial}{\partial t}\boldsymbol{x}(z,t) = \boldsymbol{B}(\boldsymbol{x}(z,t))\frac{\partial}{\partial z}\boldsymbol{x}(z,t) + \boldsymbol{c}(\boldsymbol{x}(z,t)), \tag{2.49}$$

where the matrix $\boldsymbol{B}(\boldsymbol{x}) = -\frac{\partial \boldsymbol{g}}{\partial \boldsymbol{x}}(\boldsymbol{x})$ is the negative Jacobian of $\boldsymbol{g}(\boldsymbol{x}(z,t))$ in (2.1).

Thereby, the isothermal model follows from (2.34), (2.40), (2.41), (2.46), (2.47) and reads

$$\frac{\partial}{\partial t}\boldsymbol{x} = \underbrace{\begin{bmatrix} 0 & \frac{1}{L} \\ -\frac{1}{L}\frac{x_2^2}{x_1^2} + \frac{a_\mathrm{iso}^2}{L} & \frac{2}{L}\frac{x_2}{x_1} \end{bmatrix}}_{=\boldsymbol{B}(\boldsymbol{x})}\frac{\partial}{\partial z}\boldsymbol{x} + \underbrace{\begin{bmatrix} 0 \\ -f_\mathrm{c}(\boldsymbol{x})\frac{x_2\left|\frac{x_2}{x_1}\right|}{2D} \end{bmatrix}}_{=\boldsymbol{c}(\boldsymbol{x})} \tag{2.50a}$$

$$x_1(0,t) = \xi(t) \tag{2.50b}$$

$$x_2(1,t) = \frac{1}{A}U(t) \tag{2.50c}$$

$$\frac{\mathrm{d}}{\mathrm{d}t}\xi(t) = \frac{A}{V_\mathrm{vol}}x_2(0,t) \tag{2.50d}$$

$$Y(t) = R_\mathrm{s}T_0x_1(1,t). \tag{2.50e}$$

The linear model, consisting of (2.37), (2.40), (2.41), (2.46), (2.47), is stated as

$$\frac{\partial}{\partial t}\boldsymbol{x} = \underbrace{\begin{bmatrix} 0 & \frac{1}{L} \\ \frac{a_{\mathrm{iso}}^2}{L} & 0 \end{bmatrix}}_{=\boldsymbol{B}} \frac{\partial}{\partial z}\boldsymbol{x} + \underbrace{\begin{bmatrix} 0 & 0 \\ 0 & -k_{\mathrm{fric}} \frac{32\mu_0}{D^2} \frac{1}{\rho_0} \end{bmatrix}}_{=\boldsymbol{C}} \boldsymbol{x} \tag{2.51a}$$

$$x_1(0,t) = \xi(t) \tag{2.51b}$$

$$x_2(1,t) = \frac{1}{A} U(t) \tag{2.51c}$$

$$\frac{\mathrm{d}}{\mathrm{d}t}\xi(t) = \frac{A}{V_{\mathrm{vol}}} x_2(0,t) \tag{2.51d}$$

$$Y(t) = R_{\mathrm{s}} T_0 x_1(1,t). \tag{2.51e}$$

The equations (2.50a), (2.51a) are defined on $(z,t) \in (0,1) \times \mathbb{R}^+$, (2.50b)–(2.50d), (2.51b)–(2.51d) for $t > 0$, and (2.50e), (2.51e) for $t \geq 0$. The measurement $Y(t)$ in (2.50e), (2.51e) results from $p_{\mathrm{in}}(t) = R_{\mathrm{s}} T_0 \rho(1,t)$.

2.9 Chapter Highlights

In this chapter, a model of the test bench in Fig. 1.3 was derived based on conservation laws. Thereby, all assumptions were clearly stated and substantiated by literature references. The resulting plant model comprises quasilinear hyperbolic PDEs and nonlinear ODEs. The model was successively simplified by considering additional assumptions, resulting in a linear model. Representative quantities, obtained from the numerical solution of the models, have been compared with each other as well as to those from experiments. Thereby, it was shown that the plant model is a very accurate mathematical description of the test bench. Furthermore, the deviations resulting from the additional assumptions were quantified and discussed with respect to their physical effects.

The transparency of the proposed modeling allows to easily choose a suitable model, depending on its intended use, its mathematical complexity, its necessary accuracy, and/or the application. For each model, the corresponding assumptions and their effects are made clear. Such a systematic modeling approach is rather rare in the context of pneumatic systems.

In connection with this chapter, the journal paper [Ker17] was published. In addition, the talks [Ker15; Ker16] were given. The supervised student theses [Sei15; Gün16; Zah16; Ngu17; Gra18] have contributed to the development of the chapter's results.

Chapter 3

Feedforward Controller Design Using Flatness

In the following, a flatness-based feedforward controller is designed. Such a design is motivated by the possibly insufficient performance of feedback controllers without a feedforward part, e.g., when applied to pneumatic systems in industrial applications. While a feedback controller stabilizes a desired equilibrium, its ability to allow for specified transitions between desired pressure levels in the tank is limited. Furthermore, the resulting control input might violate the test bench's physical capacities, e.g., [KG17]. Consequently, this chapter presents the design of a feedforward controller, enabling specified transitions and allowing to comply with physical limitations.

The subsequent feedforward controller design makes use of a flat output, parametrizing all quantities of the system. In contrast to flatness-based designs for lumped-parameter models, such a feedforward controller for hyperbolic distributed-parameter models usually involves lumped as well as distributed delays and predictions in addition to derivatives of the flat output, e.g., [PR01]. Still, flatness-based methods for distributed-parameter models have been successfully applied to a variety of systems, ranging from quasilinear parabolic PDEs, e.g., [Rud03], to linear hyperbolic PDEs, e.g., [PR01].

Although the ideas presented in [PR01; Rud03] can be applied to the linear model (2.51) of the test bench, this thesis makes use of the more recent method introduced in [Knü15] (in German, see [KW15] for a reference in English). Therein, a flatness-based feedforward controller design is presented by generalizing the results in the aforementioned references to quasilinear hyperbolic PDEs coupled to nonlinear ODEs at the boundary. Hence, it allows a design based on the more accurate isothermal model[1] (2.50).

To derive such a feedforward controller, first, all lumped and distributed quantities of the unactuated, differentially flat boundary system at $z = 0$ are parametrized in terms of a desired reference trajectory of the flat output. The resulting Cauchy problem, consisting of the PDEs defined on $z \in (0, 1)$ and subject to the parametrized quantities at $z = 0$, is solved by the method of characteristics. A coordinate transformation is introduced, which turns the PDEs into ODEs along the so-called characteristic curves. For that, the PDEs are rewritten as ODEs which are evaluated along the characteristic curves. The

[1] Although the plant model (2.48) is quasilinear, too, it does not apply in this context, discussed in Sec. 3.5.

characteristic curves propagate the solution from the parametrized boundary at $z = 0$ to the actuated boundary at $z = 1$ in finite time, defined by the propagation speed of the hyperbolic system. By integrating along the characteristic curves (forward and backward in time), the distributed state of the PDE subsystem on $z \in (0, 1)$ as well as the input at $z = 1$ are parametrized in terms of the flat output. Thereby, the feedforward controller is obtained.

In the following, first, it is shown that the tank density is a flat output of the boundary system at $z = 0$ of the isothermal model, i.e. the tank model and the corresponding boundary conditions. Subsequently, the isothermal model is transformed into diagonal form, a convenient representation in order to apply the method of characteristics. By specifying a suitable reference trajectory of the flat output, the transition between two constant pressure levels is defined. Finally, from the solution of the Cauchy Problem, the feedforward controller results, which is investigated in simulations and experiments.

This chapter is based on the results in [KG17], a contribution by N. Gehring and the author of this thesis. In contrast to that, here, the design of the feedforward controller is presented in more mathematical detail. In addition to simulations, the resulting feedforward controller is implemented at the test bench and experiments are performed. Furthermore, it is shown that the plant model is unsuited for the design approach.

Remark 3.1. While other feedforward controller design methods for hyperbolic systems have been tested, e.g., [KS08b], this thesis makes use of the flatness-based approach in [Knü15] as it allows a straightforward design based on the relatively accurate quasilinear model. △

3.1 Preliminary Considerations

Since the flat output $y(t) = \xi(t)$, where $\xi(t)$ is the tank density, differentially parametrizes all quantities of the unactuated boundary system (2.50b), (2.50d) at $z = 0$, i.e.

$$\xi(t) = y(t), \quad x_1(0,t) = y(t), \quad x_2(0,t) = \frac{V_{\mathrm{vol}}}{A}\frac{\mathrm{d}}{\mathrm{d}t}y(t), \tag{3.1}$$

the boundary system is differentially flat in the sense of [Fli+95]. As $p_{\mathrm{vol}}(t) = \xi(t)R_{\mathrm{s}}T_0$ holds, resulting from the ideal gas law (2.3), the flat output $y(t)$ is proportional to the tank pressure, i.e. the controlled output.

Next, to facilitate the application of the method of characteristics, the PDE subsystem (2.50a) of the isothermal model is transformed into the diagonal form

$$\frac{\partial}{\partial t}\bar{\boldsymbol{w}}(z,t) = \underbrace{\begin{bmatrix} \bar{\lambda}_1(\bar{\boldsymbol{w}}(z,t)) & 0 \\ 0 & \bar{\lambda}_2(\bar{\boldsymbol{w}}(z,t)) \end{bmatrix}}_{=\bar{\boldsymbol{\Lambda}}(\bar{\boldsymbol{w}}(z,t))} \frac{\partial}{\partial z}\bar{\boldsymbol{w}}(z,t) + \bar{\boldsymbol{c}}(\bar{\boldsymbol{w}}(z,t)), \tag{3.2}$$

where $\bar{\boldsymbol{w}}(z,t) = \left[\bar{w}_1(z,t), \bar{w}_2(z,t)\right]^T \in \mathbb{R}^2$ and $\bar{\boldsymbol{c}}(\bar{\boldsymbol{w}}(z,t)) = \left[\bar{c}_1(\bar{\boldsymbol{w}}(z,t)), \bar{c}_2(\bar{\boldsymbol{w}}(z,t))\right]^T \in \mathbb{R}^2$. For the derivation of the coordinate transformation

$$\bar{\boldsymbol{w}} = \boldsymbol{s}(\boldsymbol{x}), \tag{3.3}$$

mapping (2.50a) into the diagonal form (3.2), the eigenvalue problem $\boldsymbol{l}_i^T(\boldsymbol{x})\boldsymbol{B}(\boldsymbol{x}) = \lambda_i \boldsymbol{l}_i^T(\boldsymbol{x})$, $i = 1, 2$, is solved. Thereby, the matrices in $\boldsymbol{L}^T(\boldsymbol{x})\boldsymbol{B}(\boldsymbol{x}) = \boldsymbol{\Lambda}(\boldsymbol{x})\boldsymbol{L}^T(\boldsymbol{x})$ are obtained, where $\boldsymbol{\Lambda}(\boldsymbol{x}) = \mathrm{diag}(\lambda_1(\boldsymbol{x}), \lambda_2(\boldsymbol{x}))$ is a diagonal matrix containing the eigenvalues

of $\boldsymbol{B}(\boldsymbol{x})$, defined in (2.50a), and $\boldsymbol{L}(\boldsymbol{x}) = [\boldsymbol{l}_1(\boldsymbol{x}), \boldsymbol{l}_2(\boldsymbol{x})]$ is composed of the associated left eigenvectors:

$$\boldsymbol{\Lambda}(\boldsymbol{x}) = \begin{bmatrix} \frac{x_2 - a_{\mathrm{iso}} x_1}{L x_1} & 0 \\ 0 & \frac{x_2 + a_{\mathrm{iso}} x_1}{L x_1} \end{bmatrix}, \quad \boldsymbol{L}^T(\boldsymbol{x}) = \frac{1}{2} \begin{bmatrix} \frac{x_2^2}{a_{\mathrm{iso}} x_1^2} - a_{\mathrm{iso}} & -\frac{x_2}{a_{\mathrm{iso}} x_1} + 1 \\ -\frac{x_2^2}{a_{\mathrm{iso}} x_1^2} + a_{\mathrm{iso}} & \frac{x_2}{a_{\mathrm{iso}} x_1} + 1 \end{bmatrix}.$$

Subsequently, $\boldsymbol{B}(\boldsymbol{x}) = \boldsymbol{L}^{-T}(\boldsymbol{x}) \boldsymbol{\Lambda}(\boldsymbol{x}) \boldsymbol{L}^T(\boldsymbol{x})$ is substituted in (2.50a) and the equation is multiplied with $\boldsymbol{W}(\boldsymbol{x}) \boldsymbol{L}^T(\boldsymbol{x})$ from the left, resulting in

$$\boldsymbol{W}(\boldsymbol{x}) \boldsymbol{L}^T(\boldsymbol{x}) \frac{\partial}{\partial t} \boldsymbol{x} = \boldsymbol{W}(\boldsymbol{x}) \boldsymbol{\Lambda}(\boldsymbol{x}) \boldsymbol{L}^T(\boldsymbol{x}) \frac{\partial}{\partial z} \boldsymbol{x} + \boldsymbol{W}(\boldsymbol{x}) \boldsymbol{L}^T(\boldsymbol{x}) \boldsymbol{c}(\boldsymbol{x}), \tag{3.4}$$

where $\boldsymbol{W}(\boldsymbol{x})$ is an invertible diagonal matrix which commutes with $\boldsymbol{\Lambda}(\boldsymbol{x})$. By that, the degree of freedom in the scaling of the eigenvectors $\boldsymbol{l}_1(\boldsymbol{x})$ and $\boldsymbol{l}_2(\boldsymbol{x})$ is taken into account[2]. The transformation $\boldsymbol{s}(\boldsymbol{x})$ has to satisfy the condition

$$\frac{\partial \boldsymbol{s}}{\partial \boldsymbol{x}}(\boldsymbol{x}) = \boldsymbol{W}(\boldsymbol{x}) \boldsymbol{L}^T(\boldsymbol{x}), \tag{3.5}$$

following from inserting the new coordinates (3.3) into (3.2) and comparing the resulting coefficients to those in (3.4). To allow for a solution of (3.5), an adequate choice is

$$\boldsymbol{W}(\boldsymbol{x}) = \begin{bmatrix} \frac{1}{a_{\mathrm{iso}} x_1 - x_2} & 0 \\ 0 & \frac{1}{a_{\mathrm{iso}} x_1 + x_2} \end{bmatrix}.$$

Hence, the new coordinates (3.3) and the inverse transformation $\boldsymbol{x} = \boldsymbol{s}^{-1}(\bar{\boldsymbol{w}})$ read

$$\boldsymbol{s}(\boldsymbol{x}) = \frac{1}{2} \begin{bmatrix} \frac{1}{a_{\mathrm{iso}}} \frac{x_2}{x_1} - \ln(x_1) \\ \frac{1}{a_{\mathrm{iso}}} \frac{x_2}{x_1} + \ln(x_1) \end{bmatrix} \quad \text{and} \quad \boldsymbol{s}^{-1}(\bar{\boldsymbol{w}}) = \begin{bmatrix} \mathrm{e}^{\bar{w}_2 - \bar{w}_1} \\ a_{\mathrm{iso}} \mathrm{e}^{\bar{w}_2 - \bar{w}_1} (\bar{w}_1 + \bar{w}_2) \end{bmatrix}, \tag{3.6}$$

respectively. Therein, $x_1 > 0$ is ensured as the density $x_1 = \rho$ is always positive. Applying the transformation $\boldsymbol{s}(\boldsymbol{x})$ to the PDE subsystem (2.50a) of the isothermal model results in the diagonal form (3.2), where

$$\bar{\lambda}_1(\bar{\boldsymbol{w}}) = \frac{a_{\mathrm{iso}}(\bar{w}_1 + \bar{w}_2 - 1)}{L}, \quad \bar{\lambda}_2(\bar{\boldsymbol{w}}) = \frac{a_{\mathrm{iso}}(\bar{w}_1 + \bar{w}_2 + 1)}{L} \tag{3.7a}$$

$$\bar{c}_1(\bar{\boldsymbol{w}}) = \bar{c}_2(\bar{\boldsymbol{w}}) = -\bar{f}_{\mathrm{c}}(\bar{\boldsymbol{w}}) \frac{a_{\mathrm{iso}} |\bar{w}_1 + \bar{w}_2| \, (\bar{w}_1 + \bar{w}_2)}{4D} \tag{3.7b}$$

with $\bar{f}_{\mathrm{c}}(\bar{\boldsymbol{w}}) = f_{\mathrm{c}}(\boldsymbol{x})$ holds.

3.2 Design of the Feedforward Controller

Steady-State Regimes The feedforward controller steers the system from the steady-state regime $\bar{\boldsymbol{w}}_{\mathrm{b}}(z)$ at the initial constant pressure level p_{b} to the steady-state regime $\bar{\boldsymbol{w}}_{\mathrm{e}}(z)$ at p_{e} at the desired constant pressure level p_{e}. In general, a steady-state regime is

[2] More precisely, $\boldsymbol{W}(\boldsymbol{x})$ consists of integrating factors which ensure the existence of the transformation (3.3), e.g., [Tan92].

defined by a solution $\boldsymbol{x}^*(z) = \boldsymbol{x}(z,t)$, $\xi^* = \xi(t)$, which is constant w.r.t. time. Inserting $\boldsymbol{x}^*(z)$, ξ^* into the isothermal model (2.50) yields

$$\mathbf{0} = \begin{bmatrix} 0 & \frac{1}{L} \\ -\frac{1}{L}\frac{(x_2^*)^2}{(x_1^*)^2} + \frac{a_{\mathrm{iso}}^2}{L} & \frac{2}{L}\frac{x_2^*}{x_1^*} \end{bmatrix} \frac{\partial}{\partial z}\boldsymbol{x}^* + \begin{bmatrix} 0 \\ -f_{\mathrm{c}}(\boldsymbol{x}^*)\frac{x_2^*\left|\frac{x_2^*}{x_1^*}\right|}{2D} \end{bmatrix} \tag{3.8a}$$

$$x_1^*(0) = \xi^* \tag{3.8b}$$

$$x_2^*(1) = \frac{1}{A}U^* \tag{3.8c}$$

$$0 = \frac{A}{V_{\mathrm{vol}}}x_2^*(0). \tag{3.8d}$$

By taking (3.8d) as well as the first row of (3.8a) into account, $x_2^*(z) = 0$ follows. Hence, caused by (3.8c), $U^* = 0$ holds. From the second row of (3.8a) as well as (3.8b), $x_1^*(z) = \xi^*$ is obtained. Thus, a steady-state regime of the system is defined by its constant density only as the velocity of the flow is zero. Therefore, $\bar{\boldsymbol{w}}(z,t)$ in steady-state reads

$$\bar{\boldsymbol{w}}^*(z) = \frac{1}{2}\begin{bmatrix} -\ln(y^*) \\ \ln(y^*) \end{bmatrix}, \tag{3.9}$$

where $y^* = \xi^*$ follows from the definition of the flat output. Finally, the steady-state regimes $\bar{\boldsymbol{w}}_{\mathrm{b}}(z)$ and $\bar{\boldsymbol{w}}_{\mathrm{e}}(z)$ result from (3.9), where

$$y_{\mathrm{b}} = 1/(R_{\mathrm{s}}T_0)p_{\mathrm{b}} \quad \text{and} \quad y_{\mathrm{e}} = 1/(R_{\mathrm{s}}T_0)p_{\mathrm{e}} \tag{3.10}$$

are inserted in place of y^*.

Trajectory Planning Next, the desired reference trajectory $y^{\mathrm{r}}(t)$ of the flat output, characterizing the transition from the steady-state regime $\bar{\boldsymbol{w}}_{\mathrm{b}}(z)$ to $\bar{\boldsymbol{w}}_{\mathrm{e}}(z)$ is defined. Since $y(t) = 1/(R_{\mathrm{s}}T_0)p_{\mathrm{vol}}(t)$ holds, the choice of $y^{\mathrm{r}}(t)$ implies the specification of a trajectory $p_{\mathrm{vol}}^{\mathrm{r}}(t)$ of tank pressure and vice versa.

As the tank model (2.50d) is a first-order ODE, the required smoothness of the function $t \mapsto y^{\mathrm{r}}(t)$ is $y^{\mathrm{r}} \in C^1([0,\infty))$ in order for $\boldsymbol{x}(0,\cdot) \in C([0,\infty))$, resulting from (3.1). Here, the piecewise defined third-order polynomial

$$y^{\mathrm{r}}(\bar{t}) = \begin{cases} y_{\mathrm{b}}, & \bar{t} \leq 0 \\ y_{\mathrm{b}} - (y_{\mathrm{b}} - y_{\mathrm{e}})\bar{t}^2(3 - 2\bar{t}), & 0 < \bar{t} < 1 \\ y_{\mathrm{e}}, & \bar{t} \geq 1 \end{cases} \tag{3.11}$$

is chosen, where the shortened notation $\bar{t} = (t - t'_{\mathrm{b}})/(t'_{\mathrm{e}} - t'_{\mathrm{b}})$ is utilized. Therein, t'_{b} and t'_{e}, which have to be specified, denote the begin and the end of the pressure change in the tank. Depending on the initial and desired pressure level, the duration $t'_{\mathrm{e}} - t'_{\mathrm{b}} > 0$ has to be long enough to respect the physical capabilities of the test bench, e.g., the limited input $U(t)$ and $Ma < 1$.

Remark 3.2. Several consecutive pressure changes are achieved by successively combining $y_j^{\mathrm{r}}(t)$ in (3.11), where the index j denotes the j-th transition and $y_{\mathrm{e},j} = y_{\mathrm{b},j+1}$ as well as $t_{\mathrm{e},j} \leq t_{\mathrm{b},j+1}$ hold. In the following, for convenience, a reference trajectory with multiple pressure changes is denoted by $y^{\mathrm{r}}(t)$, too. △

Minimum Transition Time Since any (bounded[3]) signal in a hyperbolic system is propagated with finite speed, the transition from $\bar{\boldsymbol{w}}_\mathrm{b}(z)$ to $\bar{\boldsymbol{w}}_\mathrm{e}(z)$ cannot be arbitrarily fast. While the duration $t'_\mathrm{e} - t'_\mathrm{b}$ of the pressure change in the tank is a design parameter of (3.11), the minimum duration $\Delta T_\mathrm{b} + \Delta T_\mathrm{e}$ of the transition follows from

$$\Delta T_\mathrm{b} = \int_0^1 \frac{1}{\bar{\lambda}_2(\bar{\boldsymbol{w}}_\mathrm{b}(\zeta))}\,\mathrm{d}\zeta$$
$$\Delta T_\mathrm{e} = -\int_0^1 \frac{1}{\bar{\lambda}_1(\bar{\boldsymbol{w}}_\mathrm{e}(\zeta))}\,\mathrm{d}\zeta.$$

By making use of (3.7a) and (3.9), $\Delta T_\mathrm{b} = \Delta T_\mathrm{e} = L/a_\mathrm{iso}$ is obtained. Hence, the transition time reads $\Delta T_\mathrm{b} + \Delta T_\mathrm{e} + t'_\mathrm{e} - t'_\mathrm{b}$.

Solution of the Cauchy Problem To derive the feedforward controller $U^\mathrm{r}(t)$, i.e. the input parametrized in terms of a desired reference trajectory $y^\mathrm{r}(t)$ of the flat output, a Cauchy problem (w.r.t. space) has to be solved. The initial data of the Cauchy problem is given by the parametrization (3.1) at $z = 0$. As a consequence, the distributed state $\bar{\boldsymbol{w}}(z,t)$, satisfying the PDE subsystem (3.2) and subject to the initial data, is parametrized in terms of $y(t)$, too. Thus, for a chosen $y^\mathrm{r}(t)$, the reference state $\bar{\boldsymbol{w}}^\mathrm{r}(z,t)$ results from the solution of the Cauchy problem. By making use of the boundary condition (2.50c), the feedforward controller $U^\mathrm{r}(t)$ is obtained.

A convenient tool to solve the Cauchy problem is the method of characteristics. For that, (3.2) is split into

$$\frac{\partial}{\partial t}\bar{w}_i(z,t) = \bar{\lambda}_i(\bar{\boldsymbol{w}}(z,t))\frac{\partial}{\partial z}\bar{w}_i(z,t) + \bar{c}_i(\bar{\boldsymbol{w}}(z,t)) \tag{3.12}$$

with $i = 1, 2$. Next, $\breve{w}_i(s) = \bar{w}_i(\zeta_i(s), \tau_i(s))$ is introduced, where $s \in \mathbb{R}$ is the independent variable. By taking the total derivative of $\breve{w}_i(s)$ with respect to s and comparing the resulting coefficients to those in (3.12), the ODEs

$$\frac{\mathrm{d}}{\mathrm{d}s}\zeta_i(s) = -\bar{\lambda}_i(\breve{\boldsymbol{w}}(s)) \tag{3.13a}$$
$$\frac{\mathrm{d}}{\mathrm{d}s}\tau_i(s) = 1 \tag{3.13b}$$
$$\frac{\mathrm{d}}{\mathrm{d}s}\breve{w}_i(s) = \bar{c}_i(\breve{\boldsymbol{w}}(s)), \tag{3.13c}$$

subject to the initial data at $z = 0$, are obtained, e.g., [Deb12]. Hence, the characteristic curves of (3.2) satisfy (3.13). By solving (3.13) for a given reference trajectory $y^\mathrm{r}(t)$, e.g., numerically, the reference state $\bar{w}_i^\mathrm{r}(\zeta_i(s), \tau_i(s)) = \breve{w}_i^\mathrm{r}(s)$ and, thus, the feedforward controller

$$U^\mathrm{r}(t) = A\left(a_\mathrm{iso}\mathrm{e}^{\bar{w}_2^\mathrm{r}(1,t) - \bar{w}_1^\mathrm{r}(1,t)}(\bar{w}_1^\mathrm{r}(1,t) + \bar{w}_2^\mathrm{r}(1,t))\right) \tag{3.14}$$

in diagonal coordinates result. Fig. 3.1 illustrates the approach. Therein, a few selected characteristic curves of (3.2) are depicted. These propagate the solution from the boundary at $z = 0$, parametrized in terms of $y^\mathrm{r}(t)$, to the actuated boundary at $z = 1$, forward and backward in time. As a consequence of the finite propagation speed, $U^\mathrm{r}(t)$ is non-zero for $t \in (t_\mathrm{b}, t_\mathrm{e})$ while $y^\mathrm{r}(t)$ is non-constant for $t \in (t'_\mathrm{b}, t'_\mathrm{e})$, where $t_\mathrm{b} = t'_\mathrm{b} - \Delta T_\mathrm{b}$ and $t_\mathrm{e} = t'_\mathrm{e} + \Delta T_\mathrm{e}$.

[3] Unbounded signals in quasilinear systems may propagate with infinite speed.

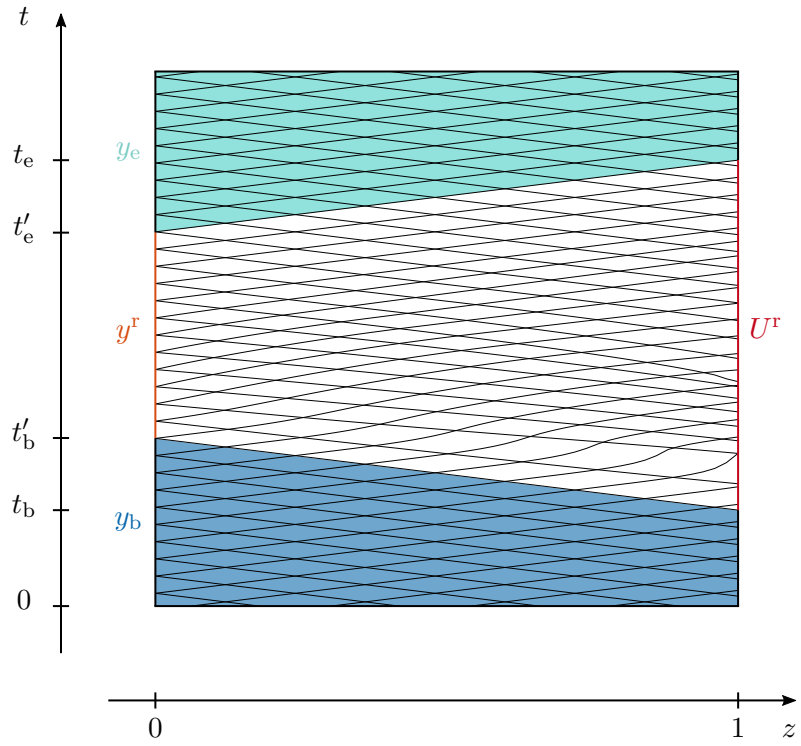

Figure 3.1: Illustration of the solution of the Cauchy problem: The blue and cyan areas define the steady-state regimes $\bar{\boldsymbol{w}}_\mathrm{b}(z)$ and $\bar{\boldsymbol{w}}_\mathrm{e}(z)$, respectively, the white area the transition regime, and the black lines are the characteristic curves of (3.2)

Table 3.1: Test bench parameters of the standard configuration

tube length	$L = 5\,\mathrm{m}$
tube diameter	$D = 5.7\,\mathrm{mm}$
tank volume	$V_\mathrm{vol} = 0.64 \cdot 10^{-3}\,\mathrm{m}^3$

3.3 Simulation Studies

The feedforward controller $U^\mathrm{r}(t)$ is verified in a simulation based on the plant model (2.48) before it is tested in experiments. The parameters of test bench configuration are stated in Tab. 3.1. For the design of the desired tank pressure reference trajectory $p^\mathrm{r}_\mathrm{vol}(t)$, three transitions are specified, each defined separately by (3.11). Thereby, the tank is charged from p_0 to 5 bar, discharged to 3 bar, and finally charged to 6 bar. Here, a maximum tank pressure of 6 bar is chosen since the supply pressure $p_\mathrm{sup}(t) \approx 9\,\mathrm{bar}$ sometimes slightly drops, e.g., if there is a peak demand in the pneumatic network. The rates of change during the transitions read $2.5\,\mathrm{bar/s}$ and $-2.5\,\mathrm{bar/s}$ for the charging and discharging process, respectively. By that choice, fast pressure changes in the tank are performed while the limited capabilities of the test bench are respected. Based on the resulting trajectory $p^\mathrm{r}_\mathrm{vol}(t)$, (3.13) is solved numerically by using the explicit Euler method, where the implementation is stated in Appx. B.2. From that, the flatness-based feedforward controller $U^\mathrm{r}(t)$ is obtained.

The feedforward controller $U^\mathrm{r}(t)$ and the tank pressure $p_\mathrm{vol}(t)$, resulting from the simulation of the plant model (2.48) with $U(t) = U^\mathrm{r}(t)$, are depicted in Fig. 3.2. In addition,

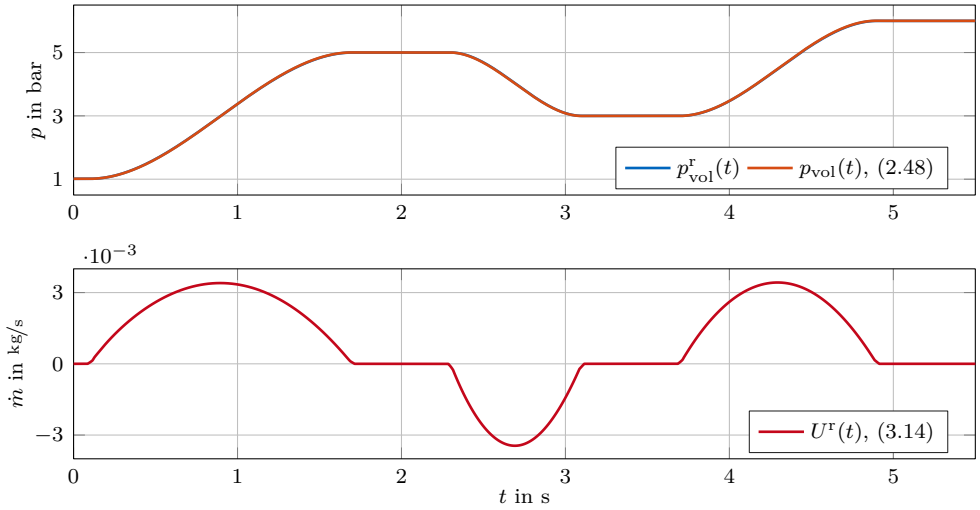

Figure 3.2: Application of the feedforward controller (3.14) to the plant model (2.48): Reference pressure $p^{\mathrm{r}}_{\mathrm{vol}}(t)$ and tank pressure $p_{\mathrm{vol}}(t)$ as well as corresponding control input $U^{\mathrm{r}}(t)$

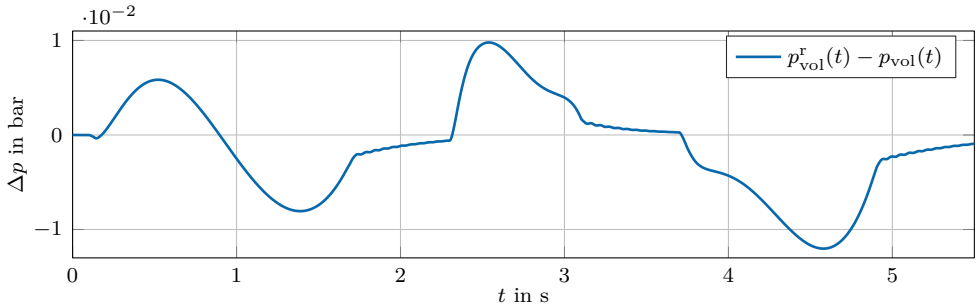

Figure 3.3: Deviations between the reference pressure $p^{\mathrm{r}}_{\mathrm{vol}}(t)$ and the tank pressure $p_{\mathrm{vol}}(t)$ in Fig. 3.2

the reference pressure $p^{\mathrm{r}}_{\mathrm{vol}}(t)$ is shown. Since the match between $p_{\mathrm{vol}}(t)$ and $p^{\mathrm{r}}_{\mathrm{vol}}(t)$ is virtually perfect, the latter cannot be seen. The minor deviations $\Delta p(t) = p^{\mathrm{r}}_{\mathrm{vol}}(t) - p_{\mathrm{vol}}(t)$ are depicted in Fig. 3.3.

The effect of the assumption of isothermal flow becomes visible in Fig. 3.3: Although the feedforward controller guarantees that the isothermal model is immediately in a steady state if $U^{\mathrm{r}}(t) = 0$, the plant model is not since $\Delta p(t)$ is non-constant for $U^{\mathrm{r}}(t) = 0$. However, as indicated in Fig. 3.3 and easily verified by simulations, $\Delta p(t)$ converges to zero if $U^{\mathrm{r}}(t) = 0$. It can be concluded that the deviations $\Delta p(t)$ during the transitions will increase if the assumption of isothermal flow has a more significant effect on the dynamics of the isothermal model compared to the plant model, e.g., if the tube length is increased and/or faster transitions are specified. Still, as soon as the plant model has reached a steady state, $\Delta p(t) = 0$ results.

Remark 3.3. If not stated otherwise, the test bench configuration in Tab. 3.1 as well as the reference trajectory $p^{\mathrm{r}}_{\mathrm{vol}}(t)$ in Fig. 3.2 are utilized for the simulations and experiments in the subsequent chapters. These choices arise from the fact that similar configurations and trajectories are widely used in applications, cf. [AF16; RNM16; TU18]. △

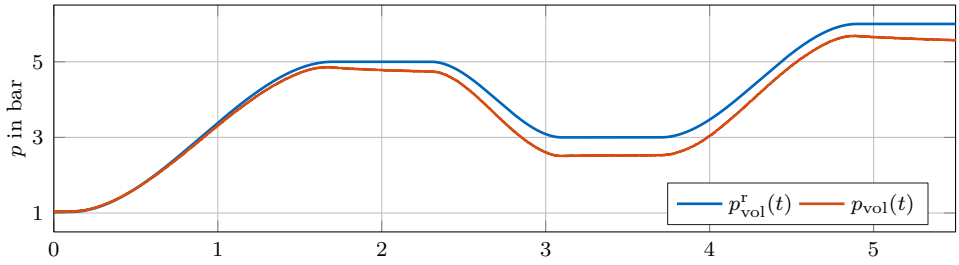

Figure 3.4: Application of the feedforward controller (3.14) to the test bench: Reference pressure $p^{\mathrm{r}}_{\mathrm{vol}}(t)$ and measured tank pressure $p_{\mathrm{vol}}(t)$

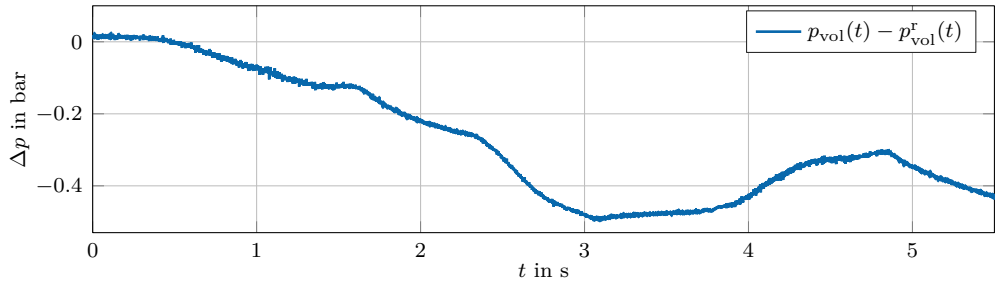

Figure 3.5: Deviations between the reference pressure $p^{\mathrm{r}}_{\mathrm{vol}}(t)$ and the measured tank pressure $p_{\mathrm{vol}}(t)$ in Fig. 3.4

3.4 Experimental Results

Motivated by the perfect simulation results, the same feedforward controller $U^{\mathrm{r}}(t)$ as in Fig. 3.2 is applied to the test bench. The measured tank pressure $p_{\mathrm{vol}}(t)$ is depicted in Fig. 3.4 and the deviations $\Delta p(t)$ in Fig. 3.5.

Obviously, the tank pressure starts to deviate from the reference pressure $p^{\mathrm{r}}_{\mathrm{vol}}(t)$, resulting in a relatively severe mismatch. Furthermore, for $U^{\mathrm{r}}(t) = 0$, $\Delta p(t)$ does not converge to zero. From the latter observation, as there is no leak in the tube or the tank, it can be concluded that the mass flow rate $\dot{m}_{\mathrm{in}}(t)$ through the valve is non-zero and the definition $\dot{m}_{\mathrm{in}}(t) = U(t)$ is violated. This error results from the slightly inaccurate inverse mass flow rate model (2.19) of the valve since it only allows for $\dot{m}_{\mathrm{in}}(t) \approx U(t)$ (cf. Rem. 2.2). Since the inverse mass flow rate model is based on measurements, it could be marginally improved by more accurate and therefore more expensive sensors. However, it is shown in the next chapter that the closed-loop control of the test bench will basically guarantee steady-state accuracy.

3.5 Non-Flatness of the Plant Model

Compared to the isothermal model (2.50), the plant model (2.48) is a slightly more accurate description of the test bench. Thus, it seems natural to design the feedforward controller based on the plant model. While the boundary system at $z = 0$, describing the tank and its coupling with the tube, is differentially flat for $(\rho v)(0, t) > 0$, i.e. when

the tank is charged, this is no longer the case if the tank is discharged and $(\rho v)(0,t) \leq 0$ holds. Then, the boundary system, arising from (2.48d), (2.48e), (2.48h), (2.48i), reads

$$\rho(0,t) = \rho_{\mathrm{vol}}(t) \tag{3.15a}$$

$$(\rho e)(0,t) = \frac{1}{2}\rho_{\mathrm{vol}}(t)v^2(0,t) + \frac{1}{\gamma-1}p_{\mathrm{vol}}(t) \tag{3.15b}$$

$$\frac{\mathrm{d}}{\mathrm{d}t}\rho_{\mathrm{vol}}(t) = \frac{A}{V_{\mathrm{vol}}}(\rho v)(0,t) \tag{3.15c}$$

$$\frac{\mathrm{d}}{\mathrm{d}t}p_{\mathrm{vol}}(t) = A\frac{\gamma-1}{V_{\mathrm{vol}}}\left[\frac{1}{2}(\rho v^3)(0,t) + \frac{\gamma}{\gamma-1}p_{\mathrm{vol}}(t)v(0,t) + \frac{1}{AR_{\mathrm{vol}}}\left(T_0 - \frac{p_{\mathrm{vol}}(t)}{R_{\mathrm{s}}\rho_{\mathrm{vol}}(t)}\right)\right]. \tag{3.15d}$$

In the following, it is shown that (3.15) does not fulfill the ruled manifold criterion, a necessary condition for flatness, e.g., [Fli+95; SA04]. For that, its dynamics is reduced to a single equation, which is required since the representation (3.15) fulfills this necessary condition. First, the definition (3.15b) is neglected as $(\rho e)(0,t)$ does not effect the remaining equations. By making use of (3.15a), $\rho(0,t)$ is replaced by $\rho_{\mathrm{vol}}(t)$ in (3.15c) and (3.15d). From that, the ODE system

$$\frac{\mathrm{d}}{\mathrm{d}t}\rho_{\mathrm{vol}}(t) = \frac{A}{V_{\mathrm{vol}}}\rho_{\mathrm{vol}}(t)v(0,t) \tag{3.16a}$$

$$\frac{\mathrm{d}}{\mathrm{d}t}p_{\mathrm{vol}}(t) = A\frac{\gamma-1}{V_{\mathrm{vol}}}\left[\frac{1}{2}\rho_{\mathrm{vol}}(t)v^3(0,t) + \frac{\gamma}{\gamma-1}p_{\mathrm{vol}}(t)v(0,t) + \frac{1}{AR_{\mathrm{vol}}}\left(T_0 - \frac{p_{\mathrm{vol}}(t)}{R_{\mathrm{s}}\rho_{\mathrm{vol}}(t)}\right)\right] \tag{3.16b}$$

results. Finally, solving (3.16a) for $v(0,t)$ and substituting the result in (3.16b) yields

$$\frac{1}{2}\left(\frac{V_{\mathrm{vol}}}{A}\right)^2\dot{v}_1^3 + \frac{\gamma}{\gamma-1}\dot{v}_1 v_1 v_2 - \frac{1}{\gamma-1}v_1^2\dot{v}_2 + \frac{T_0}{V_{\mathrm{vol}}R_{\mathrm{vol}}}v_1^2 - \frac{1}{V_{\mathrm{vol}}R_{\mathrm{vol}}R_{\mathrm{s}}}v_1 v_2 = 0, \tag{3.17}$$

where $v_1 = \rho_{\mathrm{vol}}$, $\dot{v}_1 = \frac{\mathrm{d}}{\mathrm{d}t}\rho_{\mathrm{vol}}$, $v_2 = p_{\mathrm{vol}}$, $\dot{v}_2 = \frac{\mathrm{d}}{\mathrm{d}t}p_{\mathrm{vol}}$ are introduced. This ODE, describing the dynamics of the boundary system at $z = 0$, is defined by the scalar equation

$$S(\boldsymbol{v}, \dot{\boldsymbol{v}}) = 0, \tag{3.18}$$

where $\boldsymbol{v} = [v_1, v_2]^T$, $\dot{\boldsymbol{v}} = [\dot{v}_1, \dot{v}_2]^T$. By evaluating the function S in terms of the independent variables $\boldsymbol{\xi}_0 = [\xi_{0,1}, \xi_{0,2}]^T$ and $\boldsymbol{\xi}_1 = [\xi_{1,1}, \xi_{1,2}]^T$, (3.18) results in the algebraic equation

$$S(\boldsymbol{\xi}_0, \boldsymbol{\xi}_1) = 0. \tag{3.19}$$

According to [Fli+95], for the existence of a flat output, it is necessary that

$$S(\boldsymbol{\xi}_0, \boldsymbol{\xi}_1 + \kappa\boldsymbol{a}) = 0 \tag{3.20}$$

holds for arbitrary $\kappa \in \mathbb{R}$, where $\boldsymbol{a} = [a_1, a_2]^T \neq \boldsymbol{0}$. By making use of (3.17) and (3.19),

$$\begin{aligned}\frac{1}{2}\left(\frac{V_{\mathrm{vol}}}{A}\right)^2 a_1^3\kappa^3 + \frac{3}{2}\left(\frac{V_{\mathrm{vol}}}{A}\right)^2 \xi_{1,1}a_1^2\kappa^2 \\ + \left(\frac{3}{2}\left(\frac{V_{\mathrm{vol}}}{A}\right)^2 \xi_{1,1}^2 a_1 + \frac{\gamma}{\gamma-1}a_1\xi_{0,1}\xi_{0,2} - \frac{1}{\gamma-1}\xi_{0,1}^2 a_2\right)\kappa = 0\end{aligned} \tag{3.21}$$

results from (3.20). Obviously, (3.21) holds for arbitrary κ only if $\boldsymbol{a} = \boldsymbol{0}$. Therefore, the necessary condition (3.20) is not fulfilled and the boundary system (3.15) not flat.

3.6 Chapter Highlights

In this chapter, the flatness-based approach in [Knü15] was applied to the isothermal model of the test bench. Based on a desired tank pressure trajectory, a feedforward controller was derived. While its performance in simulations was virtually perfect, the experiment emphasized the necessity of a state feedback controller.

Since previous feedforward controller designs for pneumatic systems were based on finite-dimensional models, the novelty of this chapter is the design of a feedforward controller based on an infinite-dimensional model.

The supervised student thesis [Sch17] has contributed to the development of this chapter's results.

Chapter 4

Output Feedback Controller Design Using Backstepping

Well-known for lumped-parameter systems, e.g., [Kha02], the backstepping method for distributed-parameter systems[1] has become a powerful tool since its first introduction in [BK01; BKL01; BK02]. Over the last years, the backstepping-based controller design for PDE-ODE systems attracted increasing research interest. Its effectiveness was first recognized by [KS08a; Krs09b; Krs09a]. Therein, the stabilization of ODE subsystems is considered, where PDEs describe the dynamics of the actuation or sensing path. Subsequently, the results for these PDE-ODE cascades with a unidirectional coupling between the PDE and the ODE were extended in [TX11] and [ZT12] to systems with a bidirectional coupling, where the PDE is represented by a heat equation and a wave equation, respectively.

However, the aforementioned methods cannot be applied to the linear model (2.51) of the test bench. Almost simultaneously, in [Di +18] and [DGK17], two research groups suggested slightly different backstepping-based state feedback designs for this class of systems, i.e. linear heterodirectional 2×2 hyperbolic PDE-ODE systems, where the coupling between the PDE and the ODE is bidirectional. While [Di +18] takes an arbitrary number of transport equations into account and guarantees stability in the L^2-sense, [DGK17], a contribution by J. Deutscher, N. Gehring, and the author of this thesis, covers spatially-varying propagation speeds and utilizes a so-called two-step approach. More precisely, the two-step approach splits the transformation between the original and the target system with the desired dynamics into two separate transformations: the backstepping transformation and the decoupling transformation. The first transformation removes the in-domain coupling of the PDE and only requires the solution of a set of well-known kernel equations, e.g., [Cor+13]. By the second transformation and the choice of the control law, the system is decoupled into a stable PDE-ODE cascade. The transformation kernel essentially follows from the solution of a simple Volterra integral equation of second kind. Furthermore, the choice of the target system ensures the exponential stability of the closed-loop system with a prescribed convergence rate. Based on the results in [DGK17], the two-step approach was extended by the same researchers to derive a state feedback for systems with an arbitrary number of transport equations in [DGK19] and, subsequently, for general bidirectionally coupled ODE-PDE-ODE systems in [DGK18].

[1] In the following, only linear distributed-parameter systems are discussed.

The implementation of the state feedback at the test bench necessitates a state observer. The backstepping-based design of an observer which makes use of a collocated measurement of the distributed state at the actuated boundary is presented in [Aam13] for heterodirectional 2×2 hyperbolic PDE-ODE systems. However, the coupling between the PDE and the ODE is unidirectional, whereas the PDE-ODE system described by the linear model (2.51) is bidirectionally coupled. In [DGK19], an observer design based on an anti-collocated measurement is presented, which takes a bidirectional coupling into account. Still, the design cannot be applied to the linear model since the measurement is collocated at the actuated boundary. Recently, in [DGK18], the researchers presented the design of an observer which is based on such a collocated measurement. Although it considers an additional ODE subsystem at the actuated boundary, the approach can be applied to the linear model, necessitating only minor modifications.

The following section comprises a brief introduction to the concept of backstepping for hyperbolic systems. Subsequently, the standard backstepping form for the considered class of systems is introduced and the linear model is stated in this form. Based on this slightly generalized system description, a state feedback and a state observer are designed. For that, the state feedback[2] and observer design in [DGK17] and [DGK18], respectively, is presented specifically for the considered class of systems. The theoretical part is concluded by the stability analysis of the closed-loop system, controlled by the output feedback controller, i.e. the combined state feedback and observer. Finally, the controller is validated in simulations and experiments. Thereby, its excellent performance is demonstrated.

This chapter is based loosely on [KG17] as well as [Ker+18a], where the former is a contribution of N. Gehring and the author of this thesis and the latter of N. Gehring, J. Deutscher, M. Meißner, and the author of this thesis. Compared to these contributions, the following derivations of the state feedback and observer are based on a more general system description and presented in more mathematical detail. The aspects of stability are discussed thoroughly. In addition, the controller is extensively tested in simulations and experiments.

4.1 The Basic Idea of Backstepping

The idea of backstepping is illustrated in Fig. 4.1. Therein, the original system is a heterodirectional 2×2 hyperbolic system. It can be seen that the system in original coordinates has an in-domain coupling, which is a potential source[3] of instability.

To design a control law, defining the input, the invertible Volterra-type integral transformation $\mathcal{T}$ with the bounded inverse $\mathcal{T}^{-1}$ is applied to the system in original coordinates. By that, it is mapped into the target system with the desired properties. In order to determine the integral kernel, defining the transformation, the corresponding kernel equations have to be derived. In general, to obtain this set of PDEs, the state of the target system is replaced by the transformed original state. From that, the kernel equations follow and are solved subsequently. Naturally, the transformation alone cannot eliminate

[2] Making use of the more general approaches in [DGK19] or [DGK18] would result in the same state feedback.

[3] For PDE-ODE systems, sources of instability might arise from an unstable PDE and/or an unstable ODE subsystem. Even if each subsystem is stable on its own, a bidirectional coupling between the PDE and the ODE can cause instability.

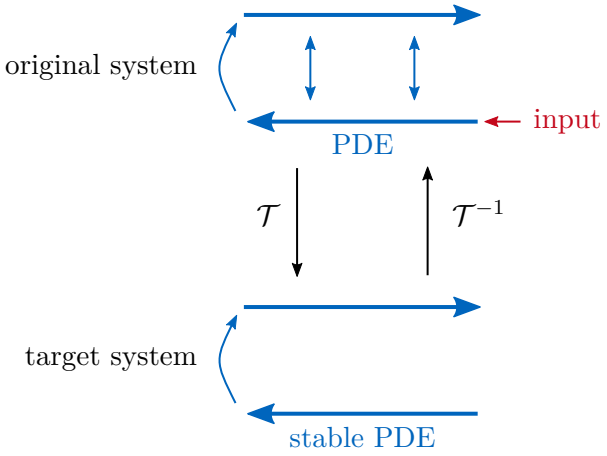

Figure 4.1: Transformations between two equivalent systems descriptions

undesired destabilizing terms but its application to the original system imposes conditions at the actuated boundary of the target system. Thereby, the stabilizing control law, compensating the destabilizing terms, is derived.

Usually, the stability of the target system can be easily shown. From that, the stability of the closed-loop system in original coordinates follows since its dynamics is equivalent to the target system.

4.2 Transformation into Standard Backstepping Form

The controller design in this chapter is based on a general description for 2×2 hyperbolic systems with constant propagation speeds, which are coupled to a first-order ODE, and have a collocated measurement available. This system class in the so-called standard backstepping form reads

$$\frac{\partial}{\partial t}\boldsymbol{w}(z,t) = \boldsymbol{\Lambda}\frac{\partial}{\partial z}\boldsymbol{w}(z,t) + \boldsymbol{A}(z)\boldsymbol{w}(z,t) \tag{4.1a}$$

$$w_1(0,t) = qw_2(0,t) + c\eta(t), \qquad t>0 \tag{4.1b}$$

$$w_2(1,t) = u(t), \qquad t>0 \tag{4.1c}$$

$$\frac{\mathrm{d}}{\mathrm{d}t}\eta(t) = a\eta(t) + bw_2(0,t), \qquad t>0 \tag{4.1d}$$

$$y(t) = w_1(1,t), \qquad t\geq 0. \tag{4.1e}$$

It is chosen as similar representations are widely used in this context, e.g., [Cor+13; Aam13]. The system consists of the two PDEs (4.1a) with the distributed state $\boldsymbol{w}(z,t) = \left[w_1(z,t), w_2(z,t)\right]^T \in \mathbb{R}^2$, where $\boldsymbol{w}$ is defined on $(z,t)\in(0,1)\times\mathbb{R}^+$, the ODE (4.1d) with the lumped state $\eta(t)\in\mathbb{R}$, the input $u(t)\in\mathbb{R}$ and the collocated measurement $y(t)\in\mathbb{R}$. The structure of (4.1) is depicted in Fig. 4.2. The matrix $\boldsymbol{\Lambda}$ is diagonal and $\boldsymbol{A}(z)$ is anti-diagonal, i.e.

$$\boldsymbol{\Lambda} = \begin{bmatrix} -\varepsilon_1 & 0 \\ 0 & \varepsilon_2 \end{bmatrix}, \quad \boldsymbol{A}(z) = \begin{bmatrix} 0 & a_1(z) \\ a_2(z) & 0 \end{bmatrix},$$

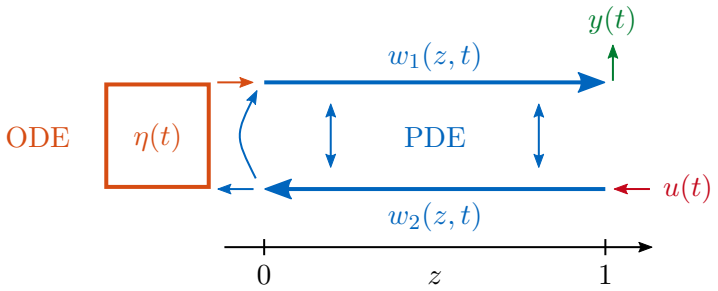

Figure 4.2: Structure of the PDE-ODE system (4.1)

where $\varepsilon_i > 0$, $i = 1, 2$, and

$$a_1(z) = c_2 \mathrm{e}^{-\left(\frac{c_1}{\varepsilon_1}+\frac{c_4}{\varepsilon_2}\right)z}, \quad a_2(z) = c_3 \mathrm{e}^{\left(\frac{c_1}{\varepsilon_1}+\frac{c_4}{\varepsilon_2}\right)z}$$

with $c_j \in \mathbb{R}$, $j = 1, \ldots, 4$. The values of ε_1 and ε_2 are the constant propagation speeds in the positive and negative direction z, respectively. Thus, the system (4.1a)–(4.1c) consists of two coupled heterodirectional transport equations. The function $a_1(z)$ defines the coupling from $w_2(z,t)$ to $w_1(z,t)$ and $a_2(z)$ vice versa. The ODE subsystem is characterized by $a \in \mathbb{R}$ and $b \in \mathbb{R}$. The pairs (a, b) and (a, c) have to satisfy the following conditions:

(A1) (a, b) is controllable and

(A2) (a, c) is observable.

Furthermore, $q \in \mathbb{R}\backslash\{0\}$ holds in (4.1b). The initial conditions are $\boldsymbol{w}(z, 0) = \boldsymbol{w}_0(z) \in \mathbb{R}^2$ and $\eta(0) = \eta_0 \in \mathbb{R}$, where $\boldsymbol{w}_0(z)$ is assumed to be piecewise continuous.

Remark 4.1. It would be sufficient if (a, b) is stabilizable and (a, c) is detectable. Furthermore, $q = 0$ could be covered by minor adaptations of the following target systems (cf. [DGK18; DGK19]). △

To render the linear model (2.51) amenable to a straightforward application of the following state feedback and observer design, the former is mapped into the form (4.1). For that, first, the eigenvalue problem $\boldsymbol{l}_i^T \boldsymbol{B} = \lambda_i \boldsymbol{l}_i^T$, $i = 1, 2$, is solved, where $\boldsymbol{l}_i$ are the left eigenvectors, associated with the eigenvalues λ_i of the matrix $\boldsymbol{B}$, defined in (2.51a). Thereby, $\boldsymbol{L}^T \boldsymbol{B} = \boldsymbol{\Lambda} \boldsymbol{L}^T$ with $\boldsymbol{L} = [\boldsymbol{l}_1, \boldsymbol{l}_2]$ and $\boldsymbol{\Lambda} = \mathrm{diag}(\lambda_1, \lambda_2)$ is obtained. By a procedure similar to the one discussed in Sec. 3.1, the change of coordinates

$$\bar{\boldsymbol{w}}(z,t) = \begin{bmatrix} \bar{w}_1(z,t) \\ \bar{w}_2(z,t) \end{bmatrix} = \boldsymbol{L}^T \boldsymbol{x}(z,t) = \begin{bmatrix} -\frac{a_{\mathrm{iso}}}{2} & \frac{1}{2} \\ \frac{a_{\mathrm{iso}}}{2} & \frac{1}{2} \end{bmatrix} \boldsymbol{x}(z,t) \tag{4.2}$$

results. In addition,

$$\eta(t) = a_{\mathrm{iso}} \xi(t) \tag{4.3}$$

is introduced. Applying (4.2), (4.3) to the linear model (2.51) and defining $\lambda_1 = -\varepsilon_1$, $\lambda_2 = \varepsilon_2$ yield

$$\frac{\partial}{\partial t}\bar{\boldsymbol{w}}(z,t) = \underbrace{\begin{bmatrix} -\varepsilon_1 & 0 \\ 0 & \varepsilon_2 \end{bmatrix}}_{=\boldsymbol{\Lambda}} \frac{\partial}{\partial z}\bar{\boldsymbol{w}}(z,t) + \underbrace{\begin{bmatrix} -\alpha & -\alpha \\ -\alpha & -\alpha \end{bmatrix}}_{=\boldsymbol{L}^T \boldsymbol{C} \boldsymbol{L}^{-T}} \bar{\boldsymbol{w}}(z,t) \tag{4.4a}$$

$$\bar{w}_1(0,t) = q\bar{w}_2(0,t) + c\eta(t) \tag{4.4b}$$
$$\bar{w}_2(1,t) = \frac{1}{A}U(t) - \bar{w}_1(1,t) \tag{4.4c}$$
$$\frac{\mathrm{d}}{\mathrm{d}t}\eta(t) = a\eta(t) + b\bar{w}_2(0,t) \tag{4.4d}$$
$$Y(t) = \frac{R_\mathrm{s}T_0}{a_\mathrm{iso}}\left(\frac{1}{A}U(t) - 2\bar{w}_1(1,t)\right), \tag{4.4e}$$

where

$$\varepsilon_i = \frac{a_\mathrm{iso}}{L}, \quad \alpha = k_\mathrm{fric}\frac{16\mu_0}{D^2}\frac{1}{\rho_0}, \quad a = -a_\mathrm{iso}\frac{A}{V_\mathrm{vol}}, \quad b = 2a_\mathrm{iso}\frac{A}{V_\mathrm{vol}}, \quad c = -1, \quad q = 1.$$

The second transformation

$$\boldsymbol{w}(z,t) = \operatorname{diag}\left(\mathrm{e}^{\alpha\tau_0 z}, \mathrm{e}^{-\alpha\tau_0 z}\right)\bar{\boldsymbol{w}}(z,t), \tag{4.5}$$

where $\tau_0 = L/a_\mathrm{iso}$, maps (4.4) into a system with an anti-diagonal coupling matrix $\boldsymbol{A}(z)$ and, hence, into the desired form (4.1), e.g., [VK14]. Thereby, (4.4) results in

$$\frac{\partial}{\partial t}\boldsymbol{w}(z,t) = \boldsymbol{\Lambda}\frac{\partial}{\partial z}\boldsymbol{w}(z,t) + \boldsymbol{A}(z)\boldsymbol{w}(z,t) \tag{4.6a}$$
$$w_1(0,t) = qw_2(0,t) + c\eta(t) \tag{4.6b}$$
$$w_2(1,t) = \frac{\mathrm{e}^{-\alpha\tau_0}}{A}U(t) - \mathrm{e}^{-2\alpha\tau_0}w_1(1,t) \tag{4.6c}$$
$$\frac{\mathrm{d}}{\mathrm{d}t}\eta(t) = a\eta(t) + bw_2(0,t) \tag{4.6d}$$
$$Y(t) = \frac{R_\mathrm{s}T_0}{a_\mathrm{iso}}\left(\frac{1}{A}U(t) - 2\mathrm{e}^{-\alpha\tau_0}w_1(1,t)\right), \tag{4.6e}$$

where the non-zero elements $a_1(z) = -\alpha\mathrm{e}^{2\alpha\tau_0 z}$ and $a_2(z) = -\alpha\mathrm{e}^{-2\alpha\tau_0 z}$ of $\boldsymbol{A}(z)$ follow from $\varepsilon_i = 1/\tau_0$, $i = 1, 2$, and $c_j = -\alpha$, $j = 1, \ldots, 4$. Finally, inserting the transformed input and measurement

$$u(t) = \mathrm{e}^{-\alpha\tau_0}\left(\frac{1}{A}U(t) - \mathrm{e}^{-\alpha\tau_0}w_1(1,t)\right) \tag{4.7a}$$
$$y(t) = \frac{1}{2}\mathrm{e}^{\alpha\tau_0}\left(\frac{1}{A}U(t) - \frac{a_\mathrm{iso}}{R_\mathrm{s}T_0}Y(t)\right), \tag{4.7b}$$

respectively, in (4.6), the linear model (2.51) is stated in the form (4.1).

4.3 Design of the State Feedback

In the following, a state feedback

$$u(t) = -k_\eta\eta(t) - \int_0^1 \boldsymbol{k}_w^T(z)\boldsymbol{w}(z,t)\,\mathrm{d}z = \mathcal{K}\left[\eta(t), \boldsymbol{w}(\cdot,t)\right] \tag{4.8}$$

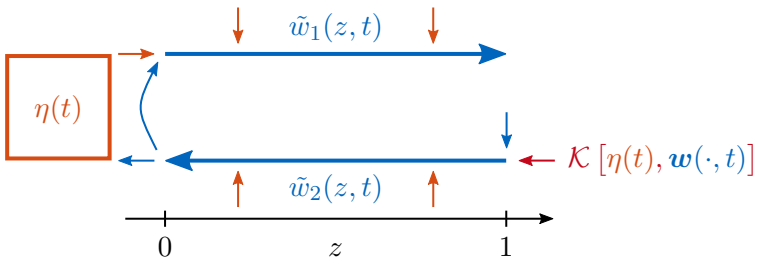

Figure 4.3: Structure of the PDE-ODE system (4.11)

with the formal feedback operator $\mathcal{K}$ is derived. By inserting (4.8) into the system (4.1) in standard backstepping form, the closed-loop system

$$\frac{\partial}{\partial t}\boldsymbol{w}(z,t) = \boldsymbol{\Lambda}\frac{\partial}{\partial z}\boldsymbol{w}(z,t) + \boldsymbol{A}(z)\boldsymbol{w}(z,t) \tag{4.9a}$$
$$w_1(0,t) = qw_2(0,t) + c\eta(t) \tag{4.9b}$$
$$w_2(1,t) = \mathcal{K}\left[\eta(t), \boldsymbol{w}(\cdot,t)\right] \tag{4.9c}$$
$$\frac{\mathrm{d}}{\mathrm{d}t}\eta(t) = a\eta(t) + bw_2(0,t) \tag{4.9d}$$

follows. The measurement $y(t)$ is neglected as it is not relevant in the context of the state feedback design.

4.3.1 Backstepping Transformation

In the first step, the invertible Volterra integral transformation

$$\tilde{\boldsymbol{w}}(z,t) = \boldsymbol{w}(z,t) - \int_0^z \boldsymbol{K}(z,\zeta)\boldsymbol{w}(\zeta,t)\,\mathrm{d}\zeta = \mathcal{T}_1\left[\boldsymbol{w}(\cdot,t)\right](z), \tag{4.10}$$

where $\tilde{\boldsymbol{w}}(z,t) = [\tilde{w}_1(z,t), \tilde{w}_2(z,t)]^T \in \mathbb{R}^2$ and $\boldsymbol{K}(z,\zeta) \in \mathbb{R}^{2\times 2}$, $i,j = 1,2$, is applied to (4.9). It maps the system into the intermediate target system in backstepping coordinates:

$$\frac{\partial}{\partial t}\tilde{\boldsymbol{w}}(z,t) = \boldsymbol{\Lambda}\frac{\partial}{\partial z}\tilde{\boldsymbol{w}}(z,t) + \boldsymbol{g}(z)\eta(t) \tag{4.11a}$$
$$\tilde{w}_1(0,t) = q\tilde{w}_2(0,t) + c\eta(t) \tag{4.11b}$$
$$\tilde{w}_2(1,t) = \mathcal{K}[\eta(t), \boldsymbol{w}(\cdot,t)] - \int_0^1 \boldsymbol{e}_2^T\boldsymbol{K}(1,\zeta)\boldsymbol{w}(\zeta,t)\,\mathrm{d}\zeta \tag{4.11c}$$
$$\frac{\mathrm{d}}{\mathrm{d}t}\eta(t) = a\eta(t) + b\tilde{w}_2(0,t), \tag{4.11d}$$

where $\boldsymbol{e}_i \in \mathbb{R}^2$ denotes the i-th unit vector and $\boldsymbol{g}(z) \in \mathbb{R}^2$. Thereby, the in-domain coupling between the distributed states is removed. The structure of (4.11) is depicted in Fig. 4.3.

Derivation of the Kernel Equations To derive the kernel equations of $\boldsymbol{K}(z,\zeta)$, the distributed state $\tilde{\boldsymbol{w}}(z,t)$ in (4.11a) is replaced by the transformation (4.10). For

that, first, (4.10) is differentiated w.r.t. time. By inserting (4.9a) and making use of an integration by parts as well as of (4.9b),

$$\begin{aligned}\frac{\partial}{\partial t}\tilde{\boldsymbol{w}}(z,t) = \boldsymbol{\Lambda}\frac{\partial}{\partial z}\boldsymbol{w}(z,t) + \left(\boldsymbol{A}(z) - \boldsymbol{K}(z,z)\boldsymbol{\Lambda}\right)\boldsymbol{w}(z,t)\\ + \int_0^z \left(\frac{\partial}{\partial \zeta}\boldsymbol{K}(z,\zeta)\boldsymbol{\Lambda} - \boldsymbol{K}(z,\zeta)\boldsymbol{A}(\zeta)\right)\boldsymbol{w}(\zeta,t)\,\mathrm{d}\zeta\\ + \boldsymbol{K}(z,0)\boldsymbol{\Lambda}(q\boldsymbol{e}_1+\boldsymbol{e}_2)w_2(0,t) + c\boldsymbol{K}(z,0)\boldsymbol{\Lambda}\boldsymbol{e}_1\eta(t)\end{aligned} \tag{4.12}$$

is obtained. The spatial derivative of (4.10) reads

$$\frac{\partial}{\partial z}\tilde{\boldsymbol{w}}(z,t) = \frac{\partial}{\partial z}\boldsymbol{w}(z,t) - \boldsymbol{K}(z,z)\boldsymbol{w}(z,t) - \int_0^z \frac{\partial}{\partial z}\boldsymbol{K}(z,\zeta)\boldsymbol{w}(\zeta,t)\,\mathrm{d}\zeta, \tag{4.13}$$

where the Leibniz integral rule is used. The condition

$$\begin{aligned}0 = \int_0^z \left(\boldsymbol{\Lambda}\frac{\partial}{\partial z}\boldsymbol{K}(z,\zeta) + \frac{\partial}{\partial \zeta}\boldsymbol{K}(z,\zeta)\boldsymbol{\Lambda} - \boldsymbol{K}(z,\zeta)\boldsymbol{A}(\zeta)\right)\boldsymbol{w}(\zeta,t)\,\mathrm{d}\zeta\\ + \left(\boldsymbol{\Lambda}\boldsymbol{K}(z,z) - \boldsymbol{K}(z,z)\boldsymbol{\Lambda} + \boldsymbol{A}(z)\right)\boldsymbol{w}(z,t) + \boldsymbol{K}(z,0)\boldsymbol{\Lambda}(q\boldsymbol{e}_1+\boldsymbol{e}_2)w_2(0,t)\\ + \left(c\boldsymbol{K}(z,0)\boldsymbol{\Lambda}\boldsymbol{e}_1 - \boldsymbol{g}(z)\right)\eta(t)\end{aligned} \tag{4.14}$$

follows from replacing $\tilde{\boldsymbol{w}}(z,t)$ and its derivatives in (4.11a) with (4.10), (4.12), and (4.13). Since (4.14) holds for arbitrary $\boldsymbol{w}(z,t)$, $\eta(t)$, the kernel equations

$$\boldsymbol{\Lambda}\frac{\partial}{\partial z}\boldsymbol{K}(z,\zeta) + \frac{\partial}{\partial \zeta}\boldsymbol{K}(z,\zeta)\boldsymbol{\Lambda} = \boldsymbol{K}(z,\zeta)\boldsymbol{A}(\zeta), \quad 0<\zeta<z<1 \tag{4.15a}$$

$$\boldsymbol{K}(z,0)\boldsymbol{\Lambda}(q\boldsymbol{e}_1+\boldsymbol{e}_2) = \boldsymbol{0} \tag{4.15b}$$

$$\boldsymbol{K}(z,z)\boldsymbol{\Lambda} - \boldsymbol{\Lambda}\boldsymbol{K}(z,z) = \boldsymbol{A}(z), \tag{4.15c}$$

which are well known in the context of backstepping for hyperbolic systems, and $\boldsymbol{g}(z) = c\boldsymbol{K}(z,0)\boldsymbol{\Lambda}\boldsymbol{e}_1$ result. Hence, if $\boldsymbol{K}(z,\zeta)$ satisfies the boundary value problem (BVP) (4.15), the transformation (4.10) maps the system (4.9) into the intermediate target system (4.11). By restating (4.15) in terms of the elements of $\boldsymbol{K}(z,\zeta) = [K_{ij}(z,\zeta)]$, two separate sets of equations follow, one for $K_{11}(z,\zeta)$, $K_{12}(z,\zeta)$ and the other one for $K_{21}(z,\zeta)$, $K_{22}(z,\zeta)$. Each set is a BVP on its own and represents a so-called generalized Goursat problem, e.g., [Cor+13].

Solution of the Kernel Equations In [VK14], an explicit solution of $K_{21}(z,\zeta)$, $K_{22}(z,\zeta)$ is derived. For that, the expressions in the corresponding BVP are expanded by a power series. This leads to an infinite number of Goursat problems, which are transformed into explicitly solvable integral equations. From that, the solutions

$$\begin{aligned}K_{21}(z,\zeta) = \frac{-1}{q(\varepsilon_1+\varepsilon_2)}\exp\left[\left(\frac{c_1}{\varepsilon_1}+\frac{c_4}{\varepsilon_2}\right)\frac{\varepsilon_1 z+\varepsilon_2\zeta}{\varepsilon_1+\varepsilon_2}\right]\Bigg\{\frac{c_2\varepsilon_2}{q\varepsilon_1}I_0\left[\frac{2\sqrt{c_2c_3}}{\varepsilon_1+\varepsilon_2}\sqrt{(z-\zeta)\left(\frac{\varepsilon_1}{\varepsilon_2}z+\zeta\right)}\right]\\ + \sqrt{c_2c_3\frac{z-\zeta}{\frac{\varepsilon_1}{\varepsilon_2}z+\zeta}}I_1\left[\frac{2\sqrt{c_2c_3}}{\varepsilon_1+\varepsilon_2}\sqrt{(z-\zeta)\left(\frac{\varepsilon_1}{\varepsilon_2}z+\zeta\right)}\right]\\ + \frac{c_3q^2\varepsilon_1-c_2\varepsilon_2}{q\varepsilon_1}\Pi\left[\frac{q\varepsilon_1c_3}{\varepsilon_2}\frac{z-\zeta}{\varepsilon_1+\varepsilon_2}, \frac{c_2}{q\varepsilon_1}\frac{\varepsilon_1z+\varepsilon_2\zeta}{\varepsilon_1+\varepsilon_2}\right]\Bigg\}\end{aligned} \tag{4.16}$$

and

$$K_{22}(z,\zeta) = \frac{-1}{\varepsilon_1+\varepsilon_2}\exp\left[\left(\frac{c_1}{\varepsilon_1}+\frac{c_4}{\varepsilon_2}\right)\frac{\varepsilon_1 z-\varepsilon_2\zeta}{\varepsilon_1+\varepsilon_2}\right]\Bigg\{\frac{c_2}{q}I_0\left[\frac{2\sqrt{c_2c_3}}{\varepsilon_1+\varepsilon_2}\sqrt{(z-\zeta)\left(\frac{\varepsilon_1}{\varepsilon_2}z+\zeta\right)}\right] + \sqrt{c_2c_3\frac{\frac{\varepsilon_1}{\varepsilon_2}z+\zeta}{z-\zeta}}I_1\left[\frac{2\sqrt{c_2c_3}}{\varepsilon_1+\varepsilon_2}\sqrt{(z-\zeta)\left(\frac{\varepsilon_1}{\varepsilon_2}z+\zeta\right)}\right] + \frac{c_3q^2\varepsilon_1-c_2\varepsilon_2}{q\varepsilon_2}\Pi\left[\frac{q\varepsilon_1c_3}{\varepsilon_2}\frac{z-\zeta}{\varepsilon_1+\varepsilon_2},\frac{c_2}{q\varepsilon_1}\frac{\varepsilon_1 z+\varepsilon_2\zeta}{\varepsilon_1+\varepsilon_2}\right]\Bigg\} \tag{4.17}$$

are obtained. Therein, $I_k(z)$, $k=0,1$, is the modified Bessel function of the first kind of k-th order and $\Pi(x,y)=\mathrm{e}^{x+y}Q_1(2\sqrt{x},2\sqrt{y})$ holds, where

$$Q_1\left(2\sqrt{x},2\sqrt{y}\right) = 1-y\mathrm{e}^{-x}\int_0^1 \mathrm{e}^{-\sigma y}I_0\left(2\sqrt{\sigma xy}\right)\,\mathrm{d}\sigma$$

denotes the generalized Marcum Q-function of first order, e.g., [VK14]. Because of the similar structure of the two sets for the elements of $\boldsymbol{K}(z,\zeta)$, the solution $K_{11}(z,\zeta)$, $K_{12}(z,\zeta)$ can be derived from the solution

$$K_{21}(z,\zeta) = K_{21}(z,\zeta;\varepsilon_1,\varepsilon_2,c_1,c_2,c_3,c_4,q) \tag{4.18a}$$
$$K_{22}(z,\zeta) = K_{22}(z,\zeta;\varepsilon_1,\varepsilon_2,c_1,c_2,c_3,c_4,q) \tag{4.18b}$$

in (4.16) and (4.17), respectively, by making use of

$$K_{11}(z,\zeta) = K_{22}(z,\zeta;\varepsilon_2,\varepsilon_1,-c_4,-c_3,-c_2,-c_1,1/q)$$
$$K_{12}(z,\zeta) = K_{21}(z,\zeta;\varepsilon_2,\varepsilon_1,-c_4,-c_3,-c_2,-c_1,1/q).$$

4.3.2 Decoupling Transformation

From (4.11a) and (4.11b), it is apparent that the lumped state $\eta(t)$ acts on the PDE. Since the ODE (4.11d) depends on $\tilde{w}_2(0,t)$, the system (4.11) is still a bidirectionally coupled PDE-ODE system. Next, the coupling from the ODE to the PDE is removed by a second transformation and the choice of the control law. For that, the decoupling coordinates

$$\boldsymbol{e}_w(z,t) = \mathcal{T}_2\left[\tilde{\boldsymbol{w}}(\cdot,t)\right](z) - \boldsymbol{n}(z)\eta(t), \tag{4.19}$$

with $\boldsymbol{e}_w(z,t)=[e_{w_1}(z,t),e_{w_2}(z,t)]^T\in\mathbb{R}^2$, $\boldsymbol{n}(z)=\in\mathbb{R}^2$, and

$$\mathcal{T}_2\left[\tilde{\boldsymbol{w}}(\cdot,t)\right](z) = \tilde{\boldsymbol{w}}(z,t) - \int_0^z \boldsymbol{P}(z,\zeta)\tilde{\boldsymbol{w}}(\zeta,t)\,\mathrm{d}\zeta, \tag{4.20}$$

where $\boldsymbol{P}(z,\zeta)\in\mathbb{R}^{2\times2}$, are introduced. The transformation (4.19) maps the intermediate target system (4.11) into the PDE-ODE cascade

$$\frac{\partial}{\partial t}\boldsymbol{e}_w(z,t) = \boldsymbol{\Lambda}\frac{\partial}{\partial z}\boldsymbol{e}_w(z,t) \tag{4.21a}$$
$$e_{w_1}(0,t) = qe_{w_2}(0,t) \tag{4.21b}$$
$$e_{w_2}(1,t) = 0 \tag{4.21c}$$
$$\frac{\mathrm{d}}{\mathrm{d}t}\eta(t) = (a-bk)\,\eta(t) + be_{w_2}(0,t). \tag{4.21d}$$

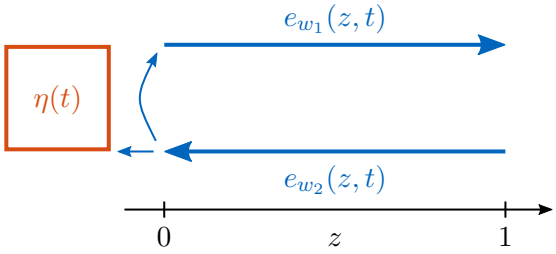

Figure 4.4: Structure of the PDE-ODE cascade (4.21)

Therein, the parameter $k \in \mathbb{R}$ is a degree of freedom in the controller design and chosen such that $a - bk < 0$ holds. As the distributed state $\boldsymbol{e}_w(z,t)$ is decoupled from the lumped state $\eta(t)$, the coupling in the system (4.21) is only unidirectional. Therefore, (4.21) is a PDE-ODE cascade, illustrated in Fig. 4.4.

Derivation of the Decoupling Equations The conditions fulfilled by $\boldsymbol{P}(z,\zeta)$ and $\boldsymbol{n}(z)$ are derived in a similar manner as discussed in Sec. 4.3.1. By replacing $\boldsymbol{e}_w(z,t)$ in (4.21a) with (4.19),

$$\begin{aligned} 0 = &\int_0^z \left(\boldsymbol{\Lambda} \frac{\partial}{\partial z} \boldsymbol{P}(z,\zeta) + \frac{\partial}{\partial \zeta} \boldsymbol{P}(z,\zeta) \boldsymbol{\Lambda} \right) \tilde{\boldsymbol{w}}(\zeta,t)\, \mathrm{d}\zeta \\ &+ \left(\boldsymbol{\Lambda} \boldsymbol{P}(z,z) - \boldsymbol{P}(z,z) \boldsymbol{\Lambda} \right) \tilde{\boldsymbol{w}}(z,t) + \left(\boldsymbol{P}(z,0) \boldsymbol{\Lambda} (q\boldsymbol{e}_1 + \boldsymbol{e}_2) - b\boldsymbol{n}(z) \right) \tilde{w}_2(0,t) \\ &+ \left(\boldsymbol{\Lambda} \frac{\mathrm{d}}{\mathrm{d}z} \boldsymbol{n}(z) - a\boldsymbol{n}(z) + \mathcal{T}_2 \left[\boldsymbol{g} \right](z) + c\boldsymbol{P}(z,0) \boldsymbol{\Lambda} \boldsymbol{e}_1 \right) \eta(t) \end{aligned} \tag{4.22}$$

is obtained, where (4.11a), (4.11b), and (4.11d) are utilized. Furthermore, the boundary conditions of the PDE-ODE cascade are evaluated in terms of the transformation (4.19). By taking (4.11b) and (4.11c) into account,

$$c\eta(t) - \boldsymbol{e}_1^T \boldsymbol{n}(0) \eta(t) = -q \boldsymbol{e}_2^T \boldsymbol{n}(0) \eta(t) \tag{4.23}$$

follows from (4.21b) and

$$\mathcal{K}[\eta(t), \boldsymbol{w}(\cdot,t)] - \int_0^1 \boldsymbol{e}_2^T \left(\boldsymbol{K}(1,z) \boldsymbol{w}(z,t) + \boldsymbol{P}(1,z) \mathcal{T}_1 \left[\boldsymbol{w}(t) \right](z) \right) \mathrm{d}z - \boldsymbol{e}_2^T \boldsymbol{n}(1) \eta(t) = 0 \tag{4.24}$$

from (4.21c). Finally, (4.19) is inserted into the ODE (4.21d), resulting in

$$0 = -bk\eta(t) - b\boldsymbol{e}_2^T \boldsymbol{n}(0) \eta(t), \tag{4.25}$$

where (4.11d) is utilized. From (4.22), the BVP

$$\boldsymbol{\Lambda} \frac{\partial}{\partial z} \boldsymbol{P}(z,\zeta) + \frac{\partial}{\partial \zeta} \boldsymbol{P}(z,\zeta) \boldsymbol{\Lambda} = \boldsymbol{0}, \quad 0 < \zeta < z < 1 \tag{4.26a}$$

$$\boldsymbol{P}(z,0) \boldsymbol{\Lambda} (q\boldsymbol{e}_1 + \boldsymbol{e}_2) = b\boldsymbol{n}(z) \tag{4.26b}$$

$$\boldsymbol{P}(z,z) \boldsymbol{\Lambda} - \boldsymbol{\Lambda} \boldsymbol{P}(z,z) = \boldsymbol{0}, \tag{4.26c}$$

satisfied by $\boldsymbol{P}(z,\zeta)$, follows. Combining the remaining condition in (4.22) with (4.23) and (4.25) results in the initial value problem (IVP)

$$\boldsymbol{\Lambda}\frac{\mathrm{d}}{\mathrm{d}z}\boldsymbol{n}(z) = a\boldsymbol{n}(z) - \mathcal{T}_2\left[\boldsymbol{g}\right](z) - c\boldsymbol{P}(z,0)\boldsymbol{\Lambda}\boldsymbol{e}_1, \qquad z \in (0,1] \tag{4.27a}$$

$$\left(\boldsymbol{e}_1^T - q\boldsymbol{e}_2^T\right)\boldsymbol{n}(0) = c \tag{4.27b}$$

$$\boldsymbol{e}_2^T\boldsymbol{n}(0) = -k, \tag{4.27c}$$

satisfied by $\boldsymbol{n}(z)$. Obviously, caused by (4.26b) and (4.27a), the BVP (4.26) and the IVP (4.27) are coupled. The feedback law

$$\mathcal{K}[\eta(t), \boldsymbol{w}(\cdot,t)] = -k_\eta\eta(t) - \int_0^1 \boldsymbol{k}_w^T(z)\boldsymbol{w}(z,t)\,\mathrm{d}z$$

with the feedback gains

$$k_\eta = -\boldsymbol{e}_2^T\boldsymbol{n}(1) \tag{4.28a}$$

$$\boldsymbol{k}_w^T(z) = -\boldsymbol{e}_2^T\left(\boldsymbol{K}(1,\zeta) + \boldsymbol{P}(1,\zeta) - \int_z^1 \boldsymbol{P}(1,\zeta)\boldsymbol{K}(\zeta,z)\,\mathrm{d}\zeta\right) \tag{4.28b}$$

follows from solving (4.24) for $\mathcal{K}[\eta(t), \boldsymbol{w}(t)]$ and a subsequent change of the order of integration.

Solution of the Decoupling Equations The solutions $\boldsymbol{P}(z,\zeta)$ and $\boldsymbol{n}(z)$ are basically obtained by tracing the decoupling equations (4.26) and (4.27) back to a Volterra integral equation. For that, first, the solution $\boldsymbol{P}(z,\zeta)$ is derived. As a consequence of (4.26a) and (4.26c), the diagonal structure $\boldsymbol{P}(z,\zeta) = \mathrm{diag}\left(P_1(z,\zeta), P_2(z,\zeta)\right)$ follows. Thereby,

$$\frac{\partial}{\partial z}P_i(z,\zeta) + \frac{\partial}{\partial\zeta}P_i(z,\zeta) = 0 \tag{4.29}$$

with $i = 1, 2$ results from (4.26a). Hence, the general solution of (4.29) reads $\boldsymbol{P}(z,\zeta) = \mathrm{diag}(p_1(z-\zeta), p_2(z-\zeta))$, where $p_i(z)$ are piecewise continuous functions that can be determined by, e.g., applying the method of characteristics. By evaluating the boundary condition (4.26b) in terms of this result,

$$\boldsymbol{P}(z,0) = b\boldsymbol{\Lambda}^{-1}\,\mathrm{diag}\left(\frac{1}{q}\boldsymbol{e}_1^T\boldsymbol{n}(z), \boldsymbol{e}_2^T\boldsymbol{n}(z)\right)$$

is obtained. From that, the explicit solution

$$\boldsymbol{P}(z,\zeta) = b\boldsymbol{\Lambda}^{-1}\,\mathrm{diag}\left(\frac{1}{q}\boldsymbol{e}_1^T\boldsymbol{n}(z-\zeta), \boldsymbol{e}_2^T\boldsymbol{n}(z-\zeta)\right) \tag{4.30}$$

results. Next, the solution $\boldsymbol{n}(z)$ of the IVP (4.27) is derived. Since the IVP is linear, the solution follows by means of the matrix exponential:

$$\boldsymbol{n}(z) = \mathrm{e}^{a\boldsymbol{\Lambda}^{-1}z}\begin{bmatrix} c - qk \\ -k \end{bmatrix} + \int_0^z \mathrm{e}^{a\boldsymbol{\Lambda}^{-1}(z-\zeta)}\left(-\boldsymbol{\Lambda}^{-1}\mathcal{T}_2\left[\boldsymbol{g}\right](\zeta) - c\boldsymbol{P}(\zeta,0)\boldsymbol{e}_1\right)\mathrm{d}\zeta. \tag{4.31}$$

Inserting (4.20) and (4.30) in (4.31), substituting the integration variable, and changing the order of integration yields

$$\boldsymbol{n}(z) = \boldsymbol{f}(z) + \int_0^z \boldsymbol{P}(\zeta, 0) \left(-c\mathrm{e}^{a\boldsymbol{\Lambda}^{-1}(z-\zeta)}\boldsymbol{e}_1 + \int_\zeta^z \mathrm{e}^{a\boldsymbol{\Lambda}^{-1}(z-\sigma)}\boldsymbol{\Lambda}^{-1}\boldsymbol{g}(\zeta-\sigma)\,\mathrm{d}\sigma \right) \mathrm{d}\zeta, \tag{4.32}$$

where

$$\boldsymbol{f}(z) = \mathrm{e}^{a\boldsymbol{\Lambda}^{-1}z}\boldsymbol{n}(0) - \int_0^z \mathrm{e}^{a\boldsymbol{\Lambda}^{-1}(z-\zeta)}\boldsymbol{\Lambda}^{-1}\boldsymbol{g}(\zeta)\,\mathrm{d}\zeta.$$

By combining the solutions $\boldsymbol{P}(z,\zeta)$ and $\boldsymbol{n}(z)$, i.e. inserting (4.30) into (4.32), the Volterra integral equation

$$\boldsymbol{n}(z) = \boldsymbol{f}(z) + \int_0^z \boldsymbol{Q}(z-\zeta)\boldsymbol{n}(\zeta)\,\mathrm{d}\zeta \tag{4.33}$$

of the second kind with the convolution kernel

$$\begin{aligned}\boldsymbol{Q}(z-\zeta) = b\boldsymbol{\Lambda}^{-1}\mathrm{e}^{a\boldsymbol{\Lambda}^{-1}(z-\zeta)} \Bigg(& -c\frac{1}{q}\boldsymbol{e}_1\boldsymbol{e}_1^T \\ & + \int_0^{z-\zeta} \mathrm{e}^{-a\boldsymbol{\Lambda}^{-1}\sigma}\boldsymbol{\Lambda}^{-1}\,\mathrm{diag}\left(\frac{1}{q}\boldsymbol{e}_1^T\boldsymbol{g}(-\sigma), \boldsymbol{e}_2^T\boldsymbol{g}(-\sigma)\right)\mathrm{d}\sigma \Bigg)\end{aligned}$$

is obtained. Since $\boldsymbol{f}(z)$ and $\boldsymbol{Q}(z)$ are continuous, there exists a unique and continuous solution $\boldsymbol{n}(z)$ of (4.33), e.g., [Lin85]. Hence, $\boldsymbol{P}(z,\zeta)$ is unique and continuous, too. The Volterra integral equation (4.33) can be solved by, e.g., applying the method of successive approximations. This method can be numerically implemented in a straightforward manner by utilizing a truncated fixed-point iteration.

4.3.3 Stability Analysis

Next, the stability of the PDE-ODE cascade (4.21) is shown. Thereby, the stability of the closed-loop system (4.9) follows since both system descriptions are equivalent. The latter property holds true as the inverse transformations $\mathcal{T}_1^{-1}$ and $\mathcal{T}_2^{-1}$ of (4.10) and (4.19), respectively, exist and are bounded. The existence and boundedness of the inverse $\mathcal{T}_1^{-1}$ of the first transformation $\mathcal{T}_1$ is shown in [Cor+13] by proving that $\mathcal{T}_1^{-1}$ is also a Volterra integral transformation with a unique and continuous kernel, implying its boundedness. Since the kernel $\boldsymbol{P}(z,\zeta)$ of the second transformation $\mathcal{T}_2$ is unique and continuous, likewise, the kernel of $\mathcal{T}_2^{-1}$ is unique and continuous, e.g., [DGK19].

The stability of the PDE-ODE cascade (4.21) can be shown by making use of the solution

$$\begin{aligned} e_{w_1}(z,t) = {} & e_{w_1,0}\left(-\varepsilon_1 t + z\right) h\left(\frac{z}{\varepsilon_1} - t\right) \\ & + q e_{w_2,0}\left(\varepsilon_2 t - \frac{\varepsilon_2}{\varepsilon_1} z\right)\left[h\left(t - \frac{z}{\varepsilon_1}\right) - h\left(t - \frac{1}{\varepsilon_2} - \frac{z}{\varepsilon_1}\right)\right] \end{aligned} \tag{4.34a}$$

$$e_{w_2}(z,t) = e_{w_2,0}\left(\varepsilon_2 t + z\right) h\left(\frac{1-z}{\varepsilon_2} - t\right) \tag{4.34b}$$

of the PDE subsystem (4.21a)–(4.21c), where $e_{w_i,0}(z)$ are the initial values in the decoupled coordinates, resulting from $\boldsymbol{e}_{w,0}(z) = \mathcal{T}_2\mathcal{T}_1[\boldsymbol{w}_0](z) - \boldsymbol{n}(z)\eta_0$, and

$$h(t) = \begin{cases} 0: & t < 0 \\ 1: & t \geq 0 \end{cases} \tag{4.35}$$

denotes the Heaviside step function. The solution (4.34) can obtained by, e.g., the method of characteristics. Evaluating (4.34b) for $t > 1/\varepsilon_2$ yields $e_{w_2}(z,t) = 0$. As a consequence, the asymptotically stable ODE (4.21d) becomes autonomous and its solution reads

$$\eta(t) = \mathrm{e}^{(a-bk)\left(t-\frac{1}{\varepsilon_2}\right)}\eta\left(\tfrac{1}{\varepsilon_2}\right), \quad t > \frac{1}{\varepsilon_2}.$$

Since the initial conditions $\boldsymbol{w}_0(z)$ are assumed to be piecewise continuous, $\eta(1/\varepsilon_2)$ is bounded. Therefore, $\eta(t)$ decays exponentially, specified by the assigned eigenvalue $a - bk$. By evaluating (4.34) for $t > t_\mathrm{c}$, where

$$t_\mathrm{c} = \frac{1}{\varepsilon_1} + \frac{1}{\varepsilon_2}, \tag{4.36}$$

$\boldsymbol{e}_w(z,t) = \boldsymbol{0}$ follows, rendering the PDE subsystem (4.21a) finite-time stable. Thereby, the stability of the PDE-ODE cascade (4.21) is shown. By making use of these results, for $t > t_\mathrm{c}$, the closed-loop solution of the system (4.9) reads

$$\boldsymbol{w}(z,t) = \mathcal{T}_1^{-1}\mathcal{T}_2^{-1}[\boldsymbol{n}](z)\eta(t) \tag{4.37a}$$

$$\eta(t) = \mathrm{e}^{(a-bk)\left(t-\frac{1}{\varepsilon_2}\right)}\eta\left(\tfrac{1}{\varepsilon_2}\right), \tag{4.37b}$$

where (4.37a) results from the application of the inverse transformations $\mathcal{T}_1^{-1}$ and $\mathcal{T}_2^{-1}$ to $\boldsymbol{e}_w(z,t) = \boldsymbol{0}$. Thus, the closed-loop system (4.9) is exponentially stable pointwise in space, i.e., for $t > t_\mathrm{c}$, the convergence of

$$\left\|\boldsymbol{w}(\cdot,t)\right\|_\infty = \sup_{z\in[0,1]} \left\|\boldsymbol{w}(z,t)\right\|_{\mathbb{R}^2}$$

is exponential with a prescribed convergence rate, defined by k.

4.4 Design of the State Observer

The implementation of the state feedback (4.8) at the test bench necessitates an observer. For that, a Luenberger-type observer based on a collocated measurement $y(t)$ is used. It follows from a copy of the system (4.1) with an additional injection of the output error:

$$\frac{\partial}{\partial t}\hat{\boldsymbol{w}}(z,t) = \boldsymbol{\Lambda}\frac{\partial}{\partial z}\hat{\boldsymbol{w}}(z,t) + \boldsymbol{A}(z)\hat{\boldsymbol{w}}(z,t) + \boldsymbol{l}(z)\left(y(t) - \hat{w}_1(1,t)\right) \tag{4.38a}$$

$$\hat{w}_1(0,t) = q\hat{w}_2(0,t) + c\hat{\eta}(t) \tag{4.38b}$$

$$\hat{w}_2(1,t) = u(t) \tag{4.38c}$$

$$\frac{\mathrm{d}}{\mathrm{d}t}\hat{\eta}(t) = a\hat{\eta}(t) + b\hat{w}_2(0,t) + l_\eta\left(y(t) - \hat{w}_1(1,t)\right), \tag{4.38d}$$

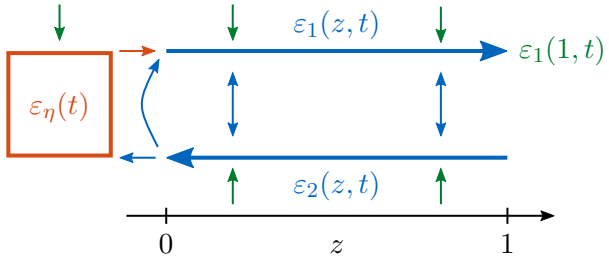

Figure 4.5: Structure of the PDE-ODE system (4.40)

where $\hat{\boldsymbol{w}}(z,t) = [\hat{w}_1(z,t), \hat{w}_2(z,t)]^T \in \mathbb{R}^2$ and $\hat{\eta}(t) \in \mathbb{R}$. The observer gains are $\boldsymbol{l} \in L^2(0,1)^2$ and $l_\eta \in \mathbb{R}$. The initial conditions of the observer read $\hat{\boldsymbol{w}}(z,0) = \hat{\boldsymbol{w}}_0(z) \in \mathbb{R}^2$, assumed to be piecewise continuous, and $\hat{\eta}(0) = \hat{\eta}_0 \in \mathbb{R}$.

By defining the deviation between the actual states of (4.1) and the estimated states of (4.38) in terms of the error states

$$\boldsymbol{\varepsilon}(z,t) = \boldsymbol{w}(z,t) - \hat{\boldsymbol{w}}(z,t), \quad \varepsilon_\eta(t) = \eta(t) - \hat{\eta}(t), \tag{4.39}$$

the dynamics of the observer error reads

$$\frac{\partial}{\partial t}\boldsymbol{\varepsilon}(z,t) = \boldsymbol{\Lambda}\frac{\partial}{\partial z}\boldsymbol{\varepsilon}(z,t) + \boldsymbol{A}(z)\boldsymbol{\varepsilon}(z,t) - \boldsymbol{l}(z)\varepsilon_1(1,t) \tag{4.40a}$$

$$\varepsilon_1(0,t) = q\varepsilon_2(0,t) + c\varepsilon_\eta(t) \tag{4.40b}$$

$$\varepsilon_2(1,t) = 0 \tag{4.40c}$$

$$\frac{\mathrm{d}}{\mathrm{d}t}\varepsilon_\eta(t) = a\varepsilon_\eta(t) + b\varepsilon_2(0,t) - l_\eta\varepsilon_1(1,t), \tag{4.40d}$$

where $\boldsymbol{\varepsilon}(z,t) = [\varepsilon_1(z,t), \varepsilon_2(z,t)]^T \in \mathbb{R}^2$ and $\varepsilon_\eta(t) \in \mathbb{R}$. A schematic of the system (4.40) can be seen in Fig. 4.5. In the following, the gains $\boldsymbol{l}(z)$ and l_η are derived, rendering the system (4.40) asymptotically stable.

Remark 4.2. Although $y(t)$ in (4.40) does not equal the measurement at the test bench, it is a linear combination of the physical input $U(t)$ and the physical measurement $Y(t)$, both input signals to the observer (4.38). Therefore, $y(t)$ represents a transformation of the observer inputs. △

4.4.1 First Backstepping Transformation

In the first step, the in-domain coupling of the distributed states in (4.40a) is removed. For that, the invertible Volterra integral transformation

$$\boldsymbol{\varepsilon}(z,t) = \bar{\boldsymbol{\varepsilon}}(z,t) - \int_z^1 \boldsymbol{J}_I(z,\zeta)\bar{\boldsymbol{\varepsilon}}(\zeta,t)\,\mathrm{d}\zeta = \mathcal{T}_3^{-1}\left[\bar{\boldsymbol{\varepsilon}}(\cdot,t)\right](z) \tag{4.41}$$

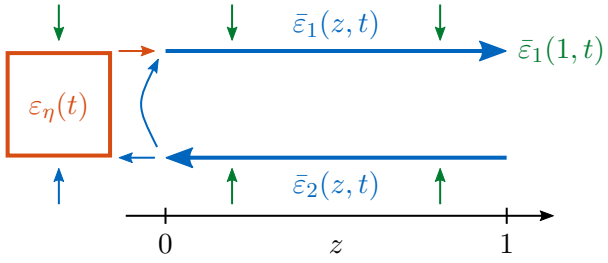

Figure 4.6: Structure of the PDE-ODE system (4.42)

with $\bar{\boldsymbol{\varepsilon}}(z,t) = [\bar{\varepsilon}_1(z,t), \bar{\varepsilon}_2(z,t)]^T \in \mathbb{R}^2$ and the integral kernel $\boldsymbol{J}_I(z,\zeta) \in \mathbb{R}^{2\times 2}$, $i,j = 1,2$, is introduced. Its inverse $\mathcal{T}_3$, likewise a Volterra integral transformation with the kernel[4] $\boldsymbol{J}(z,\zeta) \in \mathbb{R}^{2\times 2}$, maps the system (4.40) into the intermediate target system

$$\frac{\partial}{\partial t}\bar{\boldsymbol{\varepsilon}}(z,t) = \boldsymbol{\Lambda}\frac{\partial}{\partial z}\bar{\boldsymbol{\varepsilon}}(z,t) - \bar{\boldsymbol{l}}(z)\bar{\varepsilon}_1(1,t) \tag{4.42a}$$

$$\bar{\varepsilon}_1(0,t) = q\bar{\varepsilon}_2(0,t) + c\varepsilon_\eta(t) \tag{4.42b}$$

$$\bar{\varepsilon}_2(1,t) = 0 \tag{4.42c}$$

$$\frac{\mathrm{d}}{\mathrm{d}t}\varepsilon_\eta(t) = a\varepsilon_\eta(t) + b\bar{\varepsilon}_2(0,t) - l_\eta\bar{\varepsilon}_1(1,t) - \int_0^1 b\boldsymbol{e}_2^T\boldsymbol{J}_I(0,z)\bar{\boldsymbol{\varepsilon}}(z,t)\,\mathrm{d}z \tag{4.42d}$$

with $\bar{\boldsymbol{l}}(z) \in \mathbb{R}^2$. Fig. 4.6 illustrates the structure of (4.42).

Derivation of the Kernel Equations The kernel equations of $\boldsymbol{J}_I(z,\zeta)$ are derived in a similar manner as in Sec. 4.3.1. However, as (4.41) is an inverse transformation, the error state $\boldsymbol{\varepsilon}(z,t)$ in (4.40) is replaced by the coordinate transformation (4.41). Making use of (4.42a) and (4.42c) results in

$$\begin{aligned} 0 = &\int_z^1 \left(\boldsymbol{\Lambda}\frac{\partial}{\partial z}\boldsymbol{J}_I(z,\zeta) + \frac{\partial}{\partial\zeta}\boldsymbol{J}_I(z,\zeta)\boldsymbol{\Lambda} + \boldsymbol{A}(z)\boldsymbol{J}_I(z,\zeta)\right)\bar{\boldsymbol{\varepsilon}}(\zeta,t)\,\mathrm{d}\zeta \\ &+ \left(\boldsymbol{J}_I(z,z)\boldsymbol{\Lambda} - \boldsymbol{\Lambda}\boldsymbol{J}_I(z,z) - \boldsymbol{A}(z)\right)\bar{\boldsymbol{\varepsilon}}(z,t) \\ &+ \left(-\bar{\boldsymbol{l}}(z) + \int_z^1 \boldsymbol{J}_I(z,\zeta)\bar{\boldsymbol{l}}(\zeta)\,\mathrm{d}\zeta + \boldsymbol{l}(z) - \boldsymbol{J}_I(z,1)\boldsymbol{\Lambda}\boldsymbol{e}_1\right)\bar{\varepsilon}_1(1,t). \end{aligned} \tag{4.43}$$

By evaluating the boundary condition (4.40b) in terms of (4.41) and inserting (4.42b),

$$-\int_0^1 \boldsymbol{e}_1^T\boldsymbol{J}_I(0,\zeta)\bar{\boldsymbol{\varepsilon}}(\zeta,t)\,\mathrm{d}\zeta = -q\int_0^1 \boldsymbol{e}_2^T\boldsymbol{J}_I(0,\zeta)\bar{\boldsymbol{\varepsilon}}(\zeta,t)\,\mathrm{d}\zeta \tag{4.44}$$

follows. Combining (4.43) and (4.44) yields the BVP

$$\boldsymbol{\Lambda}\frac{\partial}{\partial z}\boldsymbol{J}_I(z,\zeta) + \frac{\partial}{\partial\zeta}\boldsymbol{J}_I(z,\zeta)\boldsymbol{\Lambda} = -\boldsymbol{A}(z)\boldsymbol{J}_I(z,\zeta), \quad 0 < z < \zeta < 1 \tag{4.45a}$$

$$\left(\boldsymbol{e}_1^T - q\boldsymbol{e}_2^T\right)\boldsymbol{J}_I(0,\zeta) = \boldsymbol{0}^T \tag{4.45b}$$

$$\boldsymbol{J}_I(z,z)\boldsymbol{\Lambda} - \boldsymbol{\Lambda}\boldsymbol{J}_I(z,z) = \boldsymbol{A}(z), \tag{4.45c}$$

satisfied by $\boldsymbol{J}_I(z,\zeta)$, and the definition

$$\bar{\boldsymbol{l}}(z) = \mathcal{T}_3[\boldsymbol{l}](z) - \mathcal{T}_3[\boldsymbol{J}_I(\cdot,1)](z)\boldsymbol{\Lambda}\boldsymbol{e}_1. \tag{4.46}$$

[4] If $\boldsymbol{J}_I(z,\zeta)$ is a unique and continuous solution, the likewise unique and continuous solution $\boldsymbol{J}(z,\zeta)$ can by obtained from $\boldsymbol{J}_I(z,\zeta)$, e.g., [DGK19].

Solution of the Kernel Equations The kernel equations (4.45) can be traced back to the kernel equations (4.15). For that, the relations

$$\breve{\boldsymbol{K}}(z,\zeta) = \boldsymbol{P}_2\boldsymbol{\Lambda}\boldsymbol{J}_I^T(\zeta,z)\boldsymbol{\Lambda}^{-1}\boldsymbol{P}_2, \qquad \breve{\boldsymbol{\Lambda}} = -\boldsymbol{P}_2\boldsymbol{\Lambda}\boldsymbol{P}_2$$
$$\breve{\boldsymbol{A}}(z) = \boldsymbol{P}_2\boldsymbol{\Lambda}\boldsymbol{A}^T(z)\boldsymbol{\Lambda}^{-1}\boldsymbol{P}_2, \qquad \breve{q} = -q$$

with the permutation matrix

$$\boldsymbol{P}_2 = \begin{bmatrix} 0 & 1 \\ 1 & 0 \end{bmatrix}$$

are applied, which leads to a BVP with the same structure as in (4.15). Thereby, the solution $\breve{\boldsymbol{K}}(z,\zeta) = [\breve{K}_{ij}(z,\zeta)]$ follows from (4.18) since

$$\breve{K}_{11}(z,\zeta) = K_{22}(z,\zeta;\varepsilon_1,\varepsilon_2,-c_1,c_3\varepsilon_1/\varepsilon_2,c_2\varepsilon_2/\varepsilon_1,-c_4,-1/q) \tag{4.47a}$$
$$\breve{K}_{12}(z,\zeta) = K_{21}(z,\zeta;\varepsilon_1,\varepsilon_2,-c_1,c_3\varepsilon_1/\varepsilon_2,c_2\varepsilon_2/\varepsilon_1,-c_4,-1/q) \tag{4.47b}$$
$$\breve{K}_{21}(z,\zeta) = K_{21}(z,\zeta;\varepsilon_2,\varepsilon_1,c_4,-c_2\varepsilon_2/\varepsilon_1,-c_3\varepsilon_1/\varepsilon_2,-c_1,-q) \tag{4.47c}$$
$$\breve{K}_{22}(z,\zeta) = K_{22}(z,\zeta;\varepsilon_2,\varepsilon_1,c_4,-c_2\varepsilon_2/\varepsilon_1,-c_3\varepsilon_1/\varepsilon_2,-c_1,-q). \tag{4.47d}$$

From that, $\boldsymbol{J}_I(z,\zeta) = \boldsymbol{\Lambda}\boldsymbol{P}_2\breve{\boldsymbol{K}}^T(\zeta,z)\boldsymbol{P}_2\boldsymbol{\Lambda}^{-1}$ is obtained.

4.4.2 Decoupling Transformation

The PDE subsystem (4.42a)–(4.42c) is still bidirectionally coupled to the ODE subsystem (4.42d). To render the ODE independent of the PDE, the decoupling transformation

$$\bar{\varepsilon}_\eta(t) = \varepsilon_\eta(t) - \int_0^1 \boldsymbol{r}^T(z)\bar{\boldsymbol{\varepsilon}}(z,t)\,\mathrm{d}z \tag{4.48}$$

with $\bar{\varepsilon}_\eta(t) \in \mathbb{R}$ and $\boldsymbol{r}^T(z) \in \mathbb{R}^{1\times 2}$ is introduced. It maps the system (4.42) into the unidirectional coupled ODE-PDE cascade

$$\frac{\partial}{\partial t}\bar{\boldsymbol{\varepsilon}}(z,t) = \boldsymbol{\Lambda}\frac{\partial}{\partial z}\bar{\boldsymbol{\varepsilon}}(z,t) - \bar{\boldsymbol{l}}(z)\bar{\varepsilon}_1(1,t) \tag{4.49a}$$
$$\bar{\varepsilon}_1(0,t) = q\bar{\varepsilon}_2(0,t) + c\bar{\varepsilon}_\eta(t) + \int_0^1 c\boldsymbol{r}^T(z)\bar{\boldsymbol{\varepsilon}}(z,t)\,\mathrm{d}z \tag{4.49b}$$
$$\bar{\varepsilon}_2(1,t) = 0 \tag{4.49c}$$
$$\frac{\mathrm{d}}{\mathrm{d}t}\bar{\varepsilon}_\eta(t) = (a-\ell c)\,\bar{\varepsilon}_\eta(t). \tag{4.49d}$$

Therein, the design parameter $\ell \in \mathbb{R}$ is chosen such that $a - \ell c < 0$ holds. Hence, the ODE subsystem (4.49d) is asymptotically stable. Fig. 4.7 depicts the structure of (4.49).

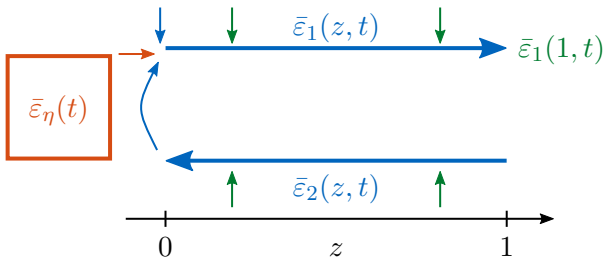

Figure 4.7: Structure of the ODE-PDE cascade (4.49)

Derivation of the Kernel Equations The conditions that have to be fulfilled by $\boldsymbol{r}^T(z)$ are derived by replacing the lumped state $\bar{\varepsilon}_\eta(t)$ in (4.49d) by the transformation (4.48). Thereby,

$$\begin{aligned} 0 = &\int_0^1 \left(\frac{\mathrm{d}}{\mathrm{d}z}\boldsymbol{r}^T(z)\boldsymbol{\Lambda} + (a-\ell c)\,\boldsymbol{r}^T(z) - b\boldsymbol{e}_2^T\boldsymbol{J}_I(0,z) \right) \bar{\boldsymbol{\varepsilon}}(z,t)\,\mathrm{d}z \\ &+ \left(\boldsymbol{r}^T(0)\boldsymbol{\Lambda}\,(\boldsymbol{e}_1 q + \boldsymbol{e}_2) + b \right) \bar{\varepsilon}_2(0,t) + \left(\boldsymbol{r}^T(0)\boldsymbol{\Lambda}\boldsymbol{e}_1 + \ell \right) c\varepsilon_\eta(t) \\ &+ \left(\int_0^1 \boldsymbol{r}^T(z)\bar{\boldsymbol{l}}(z)\,\mathrm{d}z - \boldsymbol{r}^T(1)\boldsymbol{\Lambda}\boldsymbol{e}_1 - l_\eta \right) \bar{\varepsilon}_1(1,t) \end{aligned}$$

is obtained, where (4.42) and an integration by parts are used. From that, the IVP

$$\frac{\mathrm{d}}{\mathrm{d}z}\boldsymbol{r}^T(z)\boldsymbol{\Lambda} = -(a-\ell c)\,\boldsymbol{r}^T(z) + b\boldsymbol{e}_2^T\boldsymbol{J}_I(0,z), \qquad z \in (0,1] \tag{4.50a}$$

$$\boldsymbol{r}^T(0)\boldsymbol{\Lambda}\,(\boldsymbol{e}_1 q + \boldsymbol{e}_2) = -b \tag{4.50b}$$

$$\boldsymbol{r}^T(0)\boldsymbol{\Lambda}\boldsymbol{e}_1 = -\ell \tag{4.50c}$$

and the definition

$$l_\eta = \int_0^1 \boldsymbol{r}^T(z)\bar{\boldsymbol{l}}(z)\,\mathrm{d}z - \boldsymbol{r}^T(1)\boldsymbol{\Lambda}\boldsymbol{e}_1 \tag{4.51}$$

follow.

Solution of the Kernel Equations Since the IVP (4.50) is linear, its solution in terms of the matrix exponential reads

$$\boldsymbol{r}^T(z) = \boldsymbol{r}^T(0)\mathrm{e}^{(\ell c-a)\boldsymbol{\Lambda}^{-1}z} + \int_0^z b\boldsymbol{e}_2^T\boldsymbol{J}_I(0,\zeta)\boldsymbol{\Lambda}^{-1}\mathrm{e}^{(\ell c-a)\boldsymbol{\Lambda}^{-1}(z-\zeta)}\,\mathrm{d}\zeta \tag{4.52}$$

with the initial condition

$$\boldsymbol{r}^T(0) = \begin{bmatrix} \frac{1}{\varepsilon_1}\ell & \frac{1}{\varepsilon_2}(\ell q - b) \end{bmatrix}.$$

Therefore, as $\boldsymbol{J}_I(0,\zeta)$ is continuous, $\boldsymbol{r}^T(z)$ is likewise continuous.

4.4.3 Second Backstepping Transformation

Next, the PDE subsystem (4.49a)–(4.49c) is stabilized by mapping the system (4.49) into a ODE-PDE cascade, where the transport equations of the PDE subsystem are cascaded, too. For that, the inverse transformation

$$\bar{\boldsymbol{\varepsilon}}(z,t) = \tilde{\boldsymbol{\varepsilon}}(z,t) - \int_z^1 \boldsymbol{\Omega}_I(z,\zeta)\tilde{\boldsymbol{\varepsilon}}(\zeta,t)\,\mathrm{d}\zeta = \mathcal{T}_4^{-1}\left[\tilde{\boldsymbol{\varepsilon}}(\cdot,t)\right](z) \tag{4.53}$$

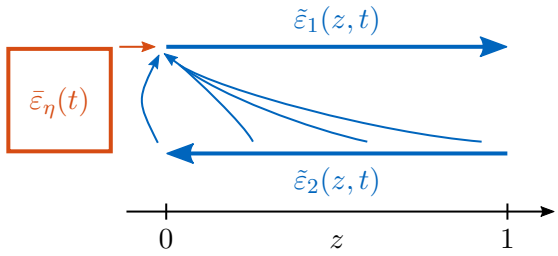

Figure 4.8: Structure of the ODE-PDE cascade (4.54)

with $\tilde{\boldsymbol{\varepsilon}}(z,t) = [\tilde{\varepsilon}_1(z,t), \tilde{\varepsilon}_2(z,t)]^T \in \mathbb{R}^2$ and the kernel $\boldsymbol{\Omega}_I(z,\zeta) \in \mathbb{R}^{2\times 2}$ is introduced. Its inverse $\mathcal{T}_4$ with the kernel[5] $\boldsymbol{\Omega}(z,\zeta) \in \mathbb{R}^{2\times 2}$ maps the system (4.49) into

$$\frac{\partial}{\partial t}\tilde{\boldsymbol{\varepsilon}}(z,t) = \boldsymbol{\Lambda}\frac{\partial}{\partial z}\tilde{\boldsymbol{\varepsilon}}(z,t) \tag{4.54a}$$

$$\tilde{\varepsilon}_1(0,t) = q\tilde{\varepsilon}_2(0,t) + c\bar{\varepsilon}_\eta(t) + \int_0^1 \boldsymbol{s}^T(z)\tilde{\boldsymbol{\varepsilon}}(z,t)\,\mathrm{d}z \tag{4.54b}$$

$$\tilde{\varepsilon}_2(1,t) = 0 \tag{4.54c}$$

$$\frac{\mathrm{d}}{\mathrm{d}t}\bar{\varepsilon}_\eta(t) = (a-\ell c)\,\bar{\varepsilon}_\eta(t), \tag{4.54d}$$

where the vector

$$\boldsymbol{s}^T(z) = \begin{bmatrix} 0 & s(z) \end{bmatrix} \in \mathbb{R}^{1\times 2} \tag{4.55}$$

ensures the cascaded PDE subsystem. A schematic of (4.54) is shown in Fig. 4.8.

Derivation of the Kernel Equations By replacing $\bar{\boldsymbol{\varepsilon}}(z,t)$ in (4.49a) by the transformation (4.53),

$$\begin{aligned} 0 = \int_z^1 \left(\boldsymbol{\Lambda}\frac{\partial}{\partial z}\boldsymbol{\Omega}_I(z,\zeta) + \frac{\partial}{\partial \zeta}\boldsymbol{\Omega}_I(z,\zeta)\boldsymbol{\Lambda}\right)\tilde{\boldsymbol{\varepsilon}}(\zeta,t)\,\mathrm{d}\zeta \\ + \left(\boldsymbol{\Omega}_I(z,z)\boldsymbol{\Lambda} - \boldsymbol{\Lambda}\boldsymbol{\Omega}_I(z,z)\right)\tilde{\boldsymbol{\varepsilon}}(z,t) + \left(\bar{\boldsymbol{l}}(z) - \boldsymbol{\Omega}_I(z,1)\boldsymbol{\Lambda}\boldsymbol{e}_1\right)\tilde{\varepsilon}_1(1,t) \end{aligned}$$

is obtained, where (4.54a) as well as (4.54c) are utilized. The boundary condition (4.49b) is evaluated in terms of (4.53) by making use of (4.54b), resulting in

$$\begin{aligned} \int_0^1 \left(\boldsymbol{s}^T(\zeta) - e_1^T\boldsymbol{\Omega}_I(0,\zeta)\right)\tilde{\boldsymbol{\varepsilon}}(\zeta,t)\,\mathrm{d}\zeta = \int_0^1 \left(c\boldsymbol{r}^T(z) - q\boldsymbol{e}_2^T\boldsymbol{\Omega}_I(0,\zeta)\right)\tilde{\boldsymbol{\varepsilon}}(\zeta,t)\,\mathrm{d}\zeta \\ - \int_0^1 c\boldsymbol{r}^T(\zeta)\int_\zeta^1 \boldsymbol{\Omega}_I(\zeta,\zeta')\tilde{\boldsymbol{\varepsilon}}(\zeta',t)\,\mathrm{d}\zeta'\,\mathrm{d}\zeta. \end{aligned} \tag{4.56}$$

From the condition (4.56), the BVP

$$\boldsymbol{\Lambda}\frac{\partial}{\partial z}\boldsymbol{\Omega}_I(z,\zeta) + \frac{\partial}{\partial \zeta}\boldsymbol{\Omega}_I(z,\zeta)\boldsymbol{\Lambda} = \boldsymbol{0} \tag{4.57a}$$

$$\left(\boldsymbol{e}_1^T - q\boldsymbol{e}_2^T\right)\boldsymbol{\Omega}_I(0,\zeta) = \boldsymbol{s}^T(\zeta) - c\boldsymbol{r}^T(\zeta) + \int_0^\zeta c\boldsymbol{r}^T(\zeta')\boldsymbol{\Omega}_I(\zeta',\zeta)\,\mathrm{d}\zeta' \tag{4.57b}$$

$$\boldsymbol{\Omega}_I(z,z)\boldsymbol{\Lambda} - \boldsymbol{\Lambda}\boldsymbol{\Omega}_I(z,z) = \boldsymbol{0}, \tag{4.57c}$$

[5]The unique and continuous solution $\boldsymbol{\Omega}(z,\zeta)$ follows from the unique and continuous solution $\boldsymbol{\Omega}_I(z,\zeta)$, e.g., [DGK19].

where (4.57a) is defined on $0 < z < \zeta < 1$, and the definition

$$\bar{\boldsymbol{l}}(z) = \boldsymbol{\Omega}_I(z,1)\boldsymbol{\Lambda}\boldsymbol{e}_1 \tag{4.58}$$

follow.

Solution of the Kernel Equations From (4.57a) and (4.57c), the structure $\boldsymbol{\Omega}_I(z,\zeta) = \operatorname{diag}(\Omega_{I,1}(z,\zeta), \Omega_{I,2}(z,\zeta))$ follows, resulting in the general solution $\boldsymbol{\Omega}_I(z,\zeta) = \operatorname{diag}(\omega_1(\zeta - z), \omega_2(\zeta - z))$, where $\omega_i(z)$ are arbitrary piecewise continuous functions. By choosing

$$s(z) = \left(c\boldsymbol{r}^T(z) - \int_0^z c\boldsymbol{r}^T(\zeta)\boldsymbol{\Omega}_I(\zeta,z)\,\mathrm{d}\zeta\right)\boldsymbol{e}_2,$$

$\Omega_{I,2}(0,\zeta) = 0$ follows from (4.55) and (4.57b). Hence, $\Omega_{I,2}(z,\zeta) = \omega_2(\zeta - z) = 0$ holds, which in turn results in $s(z) = c\boldsymbol{r}^T(z)\boldsymbol{e}_2$ and simplifies (4.57b) to

$$\Omega_{I,1}(0,\zeta) = \omega_1(\zeta) = -c\boldsymbol{r}^T(\zeta)\boldsymbol{e}_1 + \int_0^\zeta c\boldsymbol{r}^T(\zeta')\boldsymbol{e}_1\Omega_{I,1}(\zeta',\zeta)\,\mathrm{d}\zeta'.$$

A substitution of the integration variable yields a Volterra integral equation of the second kind:

$$\omega_1(z) = -c\boldsymbol{r}^T(z)\boldsymbol{e}_1 + \int_0^z c\boldsymbol{r}^T(z-\zeta)\boldsymbol{e}_1\omega_1(\zeta)\,\mathrm{d}\zeta. \tag{4.59}$$

Since $\boldsymbol{r}^T(z)$ is continuous, the solution $\omega_1(z)$ of (4.59) is unique and continuous, e.g., [Lin85]. This solution can be obtained, e.g., with the method of successive approximations, allowing for a straightforward numerical implementation.

4.4.4 Stability Analysis

In the following, it is shown that the observer error dynamics (4.40) with the observer gains

$$l_\eta = \int_0^1 \boldsymbol{r}^T(z)\boldsymbol{\Omega}_I(z,1)\boldsymbol{\Lambda}\boldsymbol{e}_1\,\mathrm{d}z - \boldsymbol{r}^T(1)\boldsymbol{\Lambda}\boldsymbol{e}_1 \tag{4.60a}$$

$$\boldsymbol{l}(z) = \mathcal{T}_3^{-1}\left[\boldsymbol{\Omega}_I(\cdot,1)\right](z)\boldsymbol{\Lambda}\boldsymbol{e}_1 + \boldsymbol{J}_I(z,1)\boldsymbol{\Lambda}\boldsymbol{e}_1, \tag{4.60b}$$

resulting from (4.46), (4.51), and (4.58), is asymptotically stable. To facilitate the proof of stability, the transformation

$$\hat{\boldsymbol{\varepsilon}}(z,t) = \tilde{\boldsymbol{\varepsilon}}(z,t) - \boldsymbol{\gamma}(z)\bar{\varepsilon}_\eta(t) \tag{4.61}$$

with $\hat{\boldsymbol{\varepsilon}}(z,t) = [\hat{\varepsilon}_1(z,t), \hat{\varepsilon}_2(z,t)]^T \in \mathbb{R}^2$ and $\boldsymbol{\gamma}(z) \in \mathbb{R}^2$ is introduced. It removes the coupling from the ODE subsystem (4.54d) to the PDE subsystem (4.54a)–(4.54c) by mapping the system (4.54) into two separate subsystems:

$$\frac{\partial}{\partial t}\hat{\boldsymbol{\varepsilon}}(z,t) = \boldsymbol{\Lambda}\frac{\partial}{\partial z}\hat{\boldsymbol{\varepsilon}}(z,t) \tag{4.62a}$$

$$\hat{\varepsilon}_1(0,t) = q\hat{\varepsilon}_2(0,t) + \int_0^1 \boldsymbol{s}^T(z)\hat{\boldsymbol{\varepsilon}}(z,t)\,\mathrm{d}z \tag{4.62b}$$

$$\hat{\varepsilon}_2(1,t) = 0 \tag{4.62c}$$

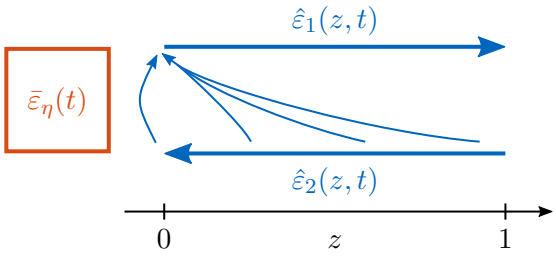

Figure 4.9: Structure of the two separate subsystems (4.62)

and

$$\frac{\mathrm{d}}{\mathrm{d}t}\bar{\varepsilon}_\eta(t) = (a - \ell c)\,\bar{\varepsilon}_\eta(t). \tag{4.62d}$$

The resulting structure of (4.62) is shown in Fig. 4.9.

To derive the conditions that have to be satisfied by $\boldsymbol{\gamma}(z)$, the state $\hat{\boldsymbol{\varepsilon}}(z,t)$ in (4.62a) is replaced by (4.61). In addition, the boundary conditions (4.62b) and (4.62c) are evaluated in terms of (4.61). From that, the BVP

$$\begin{aligned} \boldsymbol{\Lambda}\frac{\mathrm{d}}{\mathrm{d}z}\boldsymbol{\gamma}(z) &= (a - \ell c)\,\boldsymbol{\gamma}(z), & z \in (0,1) \\ \left(\boldsymbol{e}_1^T - q\boldsymbol{e}_2^T\right)\boldsymbol{\gamma}(0) &= \int_0^1 \boldsymbol{s}^T(z)\boldsymbol{\gamma}(z)\,\mathrm{d}z + c \\ \boldsymbol{e}_2^T\boldsymbol{\gamma}(1) &= 0 \end{aligned}$$

is obtained, where (4.54) is taken into account. Its explicit solution reads

$$\boldsymbol{\gamma}(z) = \begin{bmatrix} c\mathrm{e}^{-\frac{1}{\varepsilon_1}(a-\ell c)z} \\ 0 \end{bmatrix}.$$

The stability of (4.62) is shown in a similar manner as in Sec. 4.3.3. For $t > t_\mathrm{o}$, where $t_\mathrm{o} = 1/\varepsilon_1 + 1/\varepsilon_2$, the solution of the PDE subsystem (4.62a)–(4.62c) reads $\hat{\boldsymbol{\varepsilon}}(z,t) = \mathbf{0}$, rendering the PDE subsystem finite-time stable. As a consequence, for $t > t_\mathrm{o}$, the dynamics of the observer error (4.40) is defined by

$$\bar{\varepsilon}_\eta(t) = \mathrm{e}^{(a-\ell c)t}\bar{\varepsilon}_\eta(0). \tag{4.63}$$

Since the initial conditions $\boldsymbol{w}_0(z)$ and $\hat{\boldsymbol{w}}_0(z)$ are piecewise continuous, $\bar{\varepsilon}_\eta(0)$ is bounded. Thus, $\bar{\varepsilon}_\eta(t)$ decays exponentially, defined by the assigned eigenvalue $a-\ell c$. Since $\hat{\boldsymbol{\varepsilon}}(z,t) = \mathbf{0}$ holds, for $t > t_\mathrm{o}$, the solution

$$\boldsymbol{\varepsilon}(z,t) = \mathcal{T}_3^{-1}\mathcal{T}_4^{-1}\left[\boldsymbol{\gamma}\right](z)\bar{\varepsilon}_\eta(t) \tag{4.64a}$$

$$\varepsilon_\eta(t) = \left(1 + \int_0^1 \boldsymbol{r}^T(z)\mathcal{T}_4^{-1}\left[\boldsymbol{\gamma}\right](z)\,\mathrm{d}z\right)\bar{\varepsilon}_\eta(t) \tag{4.64b}$$

of (4.40), where (4.41), (4.48), (4.53), and (4.61) are utilized, is obtained. Therefore, the system (4.40) is exponentially stable pointwise in space, i.e. for $t > t_\mathrm{o}$, the convergence of

$$\left\|\boldsymbol{\varepsilon}(\cdot,t)\right\|_\infty = \sup_{z\in[0,1]}\left\|\boldsymbol{\varepsilon}(z,t)\right\|_{\mathbb{R}^2}$$

is exponential with a prescribed convergence rate, defined by ℓ.

4.5 Stability of the Closed-Loop System

From the combination of the state feedback (4.8) with the state observer (4.38), the output feedback controller

$$\frac{\partial}{\partial t}\hat{\boldsymbol{w}}(z,t) = \boldsymbol{\Lambda}\frac{\partial}{\partial z}\hat{\boldsymbol{w}}(z,t) + \boldsymbol{A}(z)\hat{\boldsymbol{w}}(z,t) + \boldsymbol{l}(z)\left(y(t) - \hat{w}_1(1,t)\right) \tag{4.65a}$$

$$\hat{w}_1(0,t) = q\hat{w}_2(0,t) + c\hat{\eta}(t) \tag{4.65b}$$

$$\hat{w}_2(1,t) = u(t) \tag{4.65c}$$

$$\frac{\mathrm{d}}{\mathrm{d}t}\hat{\eta}(t) = a\hat{\eta}(t) + b\hat{w}_2(0,t) + l_\eta\left(y(t) - \hat{w}_1(1,t)\right) \tag{4.65d}$$

$$u(t) = \mathcal{K}\left[\hat{\eta}(t), \hat{\boldsymbol{w}}(\cdot,t)\right] \tag{4.65e}$$

is obtained. By inserting (4.65e) into (4.1),

$$\frac{\partial}{\partial t}\boldsymbol{w}(z,t) = \boldsymbol{\Lambda}\frac{\partial}{\partial z}\boldsymbol{w}(z,t) + \boldsymbol{A}(z)\boldsymbol{w}(z,t) \tag{4.66a}$$

$$w_1(0,t) = qw_2(0,t) + c\eta(t) \tag{4.66b}$$

$$w_2(1,t) = \mathcal{K}\left[\hat{\eta}(t), \hat{\boldsymbol{w}}(\cdot,t)\right] \tag{4.66c}$$

$$\frac{\mathrm{d}}{\mathrm{d}t}\eta(t) = a\eta(t) + bw_2(0,t) \tag{4.66d}$$

results. In the following, the stability of (4.66) is shown. For that, it is beneficial to apply the transformations (4.10) and (4.19) to the state $\boldsymbol{w}(z,t)$ in (4.66), resulting in

$$\frac{\partial}{\partial t}\boldsymbol{e}_w(z,t) = \boldsymbol{\Lambda}\frac{\partial}{\partial z}\boldsymbol{e}_w(z,t) \tag{4.67a}$$

$$e_{w_1}(0,t) = qe_{w_2}(0,t) \tag{4.67b}$$

$$e_{w_2}(1,t) = \mathcal{K}\left[\hat{\eta}(t), \hat{\boldsymbol{w}}(\cdot,t)\right] - \mathcal{K}\left[\eta(t), \boldsymbol{w}(\cdot,t)\right] \tag{4.67c}$$

$$\frac{\mathrm{d}}{\mathrm{d}t}\eta(t) = (a - bk)\,\eta(t) + be_{w_2}(0,t). \tag{4.67d}$$

Since the feedback operator $\mathcal{K}$ is linear, the boundary condition (4.67c) can be expressed in terms of the errors states (4.39):

$$e_{w_2}(1,t) = -\mathcal{K}\left[\varepsilon_\eta(t), \boldsymbol{\varepsilon}(\cdot,t)\right]. \tag{4.68}$$

By applying the transformations (4.41), (4.48), (4.53), and (4.61), the boundary condition (4.68) reads

$$\begin{aligned} e_{w_2}(1,t) = &\left[k_\eta + \int_0^1 \left(k_\eta \boldsymbol{r}^T(z)\mathcal{T}_4^{-1}\left[\boldsymbol{\gamma}\right](z) + \boldsymbol{k}_w^T(z)\mathcal{T}_3^{-1}\mathcal{T}_4^{-1}\left[\boldsymbol{\gamma}\right](z)\right)\mathrm{d}z\right]\bar{\varepsilon}_\eta(t) \\ &+ \int_0^1 \left(k_\eta \boldsymbol{r}^T(z)\mathcal{T}_4^{-1}\left[\hat{\boldsymbol{\varepsilon}}(t)\right](z) + \boldsymbol{k}_w^T(z)\mathcal{T}_3^{-1}\mathcal{T}_4^{-1}\left[\hat{\boldsymbol{\varepsilon}}(t)\right](z)\right)\mathrm{d}z, \end{aligned} \tag{4.69}$$

where the definition (4.8) of the feedback operator is used. Next, the coupling from the ODE to the PDE in the system (4.67) is removed by eliminating $\bar{\varepsilon}_\eta(t)$ in the boundary condition (4.69). For that, the transformation

$$\bar{\boldsymbol{e}}_w(z,t) = \boldsymbol{e}_w(z,t) - \boldsymbol{\beta}(z)\bar{\varepsilon}_\eta(t) \tag{4.70}$$

with $\bar{\boldsymbol{e}}_w(z,t) = [\bar{e}_{w_1}(z,t), \bar{e}_{w_2}(z,t)]^T \in \mathbb{R}^2$ and $\boldsymbol{\beta}(z) \in \mathbb{R}^2$ is introduced, mapping the system (4.67) into

$$\frac{\partial}{\partial t}\bar{\boldsymbol{e}}_w(z,t) = \boldsymbol{\Lambda}\frac{\partial}{\partial z}\bar{\boldsymbol{e}}_w(z,t) \tag{4.71a}$$

$$\bar{e}_{w_1}(0,t) = q\bar{e}_{w_2}(0,t) \tag{4.71b}$$

$$\bar{e}_{w_2}(1,t) = \int_0^1 \left(k_\eta \boldsymbol{r}^T(z)\mathcal{T}_4^{-1}\left[\hat{\boldsymbol{\varepsilon}}(t)\right](z) + \boldsymbol{k}_w^T(z)\mathcal{T}_3^{-1}\mathcal{T}_4^{-1}\left[\hat{\boldsymbol{\varepsilon}}(t)\right](z)\right)\mathrm{d}z \tag{4.71c}$$

$$\frac{\mathrm{d}}{\mathrm{d}t}\eta(t) = (a-bk)\,\eta(t) + b\bar{e}_{w_2}(0,t) + b\boldsymbol{e}_2^T\boldsymbol{\beta}(0)\bar{\varepsilon}_\eta(t). \tag{4.71d}$$

To derive the conditions that have to be satisfied by $\boldsymbol{\beta}(z)$, the state $\boldsymbol{e}_w(z,t)$ in (4.67a) is replaced with (4.70), using (4.62d) and (4.71a). Furthermore, (4.67b) and (4.69) are evaluated in terms of (4.70), utilizing (4.71b) and (4.71c). From that, the BVP

$$\boldsymbol{\Lambda}\frac{\mathrm{d}}{\mathrm{d}z}\boldsymbol{\beta}(z) = (a-\ell c)\,\boldsymbol{\beta}(z) \tag{4.72a}$$

$$\left(\boldsymbol{e}_1^T - q\boldsymbol{e}_2^T\right)\boldsymbol{\beta}(0) = 0 \tag{4.72b}$$

$$\boldsymbol{e}_2^T\boldsymbol{\beta}(1) = \underbrace{k_\eta + \int_0^1 \left(k_\eta \boldsymbol{r}^T(z)\mathcal{T}_4^{-1}\left[\boldsymbol{\gamma}\right](z) + \boldsymbol{k}_w^T(z)\mathcal{T}_3^{-1}\mathcal{T}_4^{-1}\left[\boldsymbol{\gamma}\right](z)\right)\mathrm{d}z}_{=\boldsymbol{e}_2^T\boldsymbol{\beta}_1}, \tag{4.72c}$$

where (4.72a) is defined on $z \in (0,1)$, is obtained. Its explicit solution reads

$$\boldsymbol{\beta}(z) = \begin{bmatrix} \mathrm{e}^{-(a-\ell c)\left(\frac{1}{\varepsilon_1}z + \frac{1}{\varepsilon_2}\right)} q\boldsymbol{e}_2^T\boldsymbol{\beta}_1 \\ \mathrm{e}^{\frac{1}{\varepsilon_2}(a-\ell c)(z-1)}\boldsymbol{e}_2^T\boldsymbol{\beta}_1 \end{bmatrix}.$$

To show the stability of (4.71), first, $t > t_\mathrm{o}$ is considered. Hence, as discussed in Sec. 4.4.4, $\hat{\boldsymbol{\varepsilon}}(z,t) = \boldsymbol{0}$ holds and the boundary condition (4.71c) reads $\bar{e}_{w_2}(1,t) = 0$. Thus, for $t > t_\mathrm{o} + t_\mathrm{c}$, the solution $\bar{\boldsymbol{e}}_w(z,t) = \boldsymbol{0}$ of (4.71a)–(4.71c) results, rendering the PDE subsystem finite-time stable. As a consequence, for $t > t_\mathrm{o} + t_\mathrm{c}$, the dynamics of (4.71) is defined by the ODEs (4.62d) and (4.71d):

$$\frac{\mathrm{d}}{\mathrm{d}t}\begin{bmatrix}\bar{\varepsilon}_\eta(t) \\ \eta(t)\end{bmatrix} = \begin{bmatrix} a-\ell c & 0 \\ b\boldsymbol{e}_2^T\boldsymbol{\beta}(0) & a-bk\end{bmatrix}\begin{bmatrix}\bar{\varepsilon}_\eta(t) \\ \eta(t)\end{bmatrix}. \tag{4.73}$$

Since the eigenvalues of (4.73) are $a - \ell c < 0$ and $a - bk < 0$, the combined systems (4.65) and (4.66) are exponentially stable pointwise in space for $t > t_\mathrm{o} + t_\mathrm{c}$.

Remark 4.3. As the matrix in (4.73) has a lower triangular structure, its eigenvalues can be specified independently of each other. Therefore, the separation principle holds. △

4.6 Simulation Studies

In the following, first, the backstepping controller, designed in Sec. 4.3, is evaluated in simulations. For that, the feedback law (4.8) is applied to the linear model (2.51) of the test bench, stabilizing a desired constant pressure level. Subsequently, the state feedback is combined with the state observer, resulting in the output feedback controller, and

augmented by the feedforward controller, designed in Chap. 3. From that, the output feedback tracking controller is obtained. Its performance is validated in simulations by means of the linear model and the plant model (2.48). The parameters of the test bench configuration are stated in Tab. 3.1. For the implementation of the controller, the integral in (4.8) is discretized w.r.t. space by the trapezoidal rule and the observer by the methods stated in Appx. B.1.

State Feedback Controller To allow for the application of the feedback law (4.8) to the test bench, it is rewritten as

$$U(t) = A\left(\mathrm{e}^{-\alpha\tau_0} w_1(1,t) + \mathrm{e}^{\alpha\tau_0}\mathcal{K}[\eta(t), \boldsymbol{w}(\cdot,t)]\right), \tag{4.74}$$

resulting from (4.7a). While it guarantees the asymptotic stabilization of the equilibrium $\boldsymbol{x}(z,t) = \boldsymbol{0}$, $\xi(t) = 0$, a pressure of zero is not desirable. In order to stabilize a non-zero constant tank pressure $p_{\mathrm{vol}}^{\mathrm{r}}$, the error states

$$\tilde{\boldsymbol{w}}(z,t) = \boldsymbol{w}(z,t) - \begin{bmatrix} -\dfrac{\mathrm{e}^{\alpha\tau_0 z}}{2a_{\mathrm{iso}}} \\ \dfrac{\mathrm{e}^{-\alpha\tau_0 z}}{2a_{\mathrm{iso}}} \end{bmatrix} y_{\mathrm{e}}, \quad \tilde{\eta}(t) = \eta(t) - a_{\mathrm{iso}} y_{\mathrm{e}},$$

where $y_{\mathrm{e}} = p_{\mathrm{vol}}^{\mathrm{r}}/(R_{\mathrm{s}} T_0)$, are substituted into (4.74), resulting in

$$U^{\mathrm{c}}(t) = A\left(\mathrm{e}^{-\alpha\tau_0}\tilde{w}_1(1,t) + \mathrm{e}^{\alpha\tau_0}\mathcal{K}[\tilde{\eta}(t), \tilde{\boldsymbol{w}}(\cdot,t)]\right). \tag{4.75}$$

The design parameter k is chosen such that the eigenvalue $a \approx -13.61$ in the ODE (4.1d) of the linear model in standard backstepping form is shifted to $a - bk = -20$ in the ODE (4.21d) of the closed-loop system. This choice is motivated by a trade-off between a sufficiently smooth input signal and a adequately fast dynamic behavior. Since the state feedback is initially applied to the linear model (2.51) in a simulation, an adjustment of the friction amplification factor k_{fric} in (2.51a), which can be regarded as an additional freedom of choice in the controller design, is unnecessary. Therefore, it is set to $k_{\mathrm{fric}} = 1$ in the simulation as well as in the design of the feedback gains k_η, $\boldsymbol{k}_w^T(z)$ in (4.28).

Fig. 4.10 shows the application of the state feedback $U^{\mathrm{c}}(t)$ with $p_{\mathrm{vol}}^{\mathrm{r}} = 3\,\mathrm{bar}$ to the linear model. Initially, the system is at rest and in equilibrium with its surroundings, i.e. $x_1(z,0) = \xi(0) = \rho_0$, $x_2(z,0) = 0$. The feedback controller is activated at $t_{\mathrm{on}} = 0.05\,\mathrm{s}$. In the upper plot of Fig. 4.10, for $t > t_1 = 1/\varepsilon_2 + t_{\mathrm{on}} \approx 0.07\,\mathrm{s}$, it can be seen that the tank pressure $p_{\mathrm{vol}}(t)$ exponential converges to the desired value $p_{\mathrm{vol}}^{\mathrm{r}}$. The lower plot depicts the input $U^{\mathrm{c}}(t)$, which converges to zero for $t > t_2 = t_{\mathrm{c}} + t_{\mathrm{on}} \approx 0.08\,\mathrm{s}$, where t_{c} is defined in (4.36). The high frequency oscillations, occurring shortly after t_{on} and t_2, are induced by discontinuities in the solution, resulting in numerical errors.

To demonstrate that the input $U^{\mathrm{c}}(t)$ in Fig. 4.10 guarantees the desired closed-loop dynamics (4.21), the distributed error state $\tilde{\boldsymbol{w}}(z,t)$ of the closed-loop system is transformed into $\tilde{\boldsymbol{e}}_w(z,t)$ by making use of the transformations (4.10) and (4.19). The resulting error state $\tilde{\boldsymbol{e}}_w(z,t)$ is depicted in Fig. 4.11. Therein, it can be seen that, besides numerical inaccuracies, $\tilde{\boldsymbol{e}}_w(z,t)$ satisfies the dynamics of the PDE subsystem (4.21a)–(4.21c): For $t > t_{\mathrm{on}}$, $e_{w,2}(1,t) = 0$ holds. This value propagates along a characteristic curve from $z = 1$ to $z = 0$ in $1/\varepsilon_2 \approx 0.015\,\mathrm{s}$, resulting in $e_{w,2}(z,t) = 0$ and $e_{w,1}(0,t) = 0$. Consequently, after $1/\varepsilon_1 \approx 0.015\,\mathrm{s}$, $e_{w,1}(z,t) = 0$ is obtained. Therefore, for $t > t_2$, $\tilde{\boldsymbol{e}}_w(z,t) = \boldsymbol{0}$ holds.

Fig. 4.12 shows the exponential convergence of the L^∞-norm of the error state $\tilde{\boldsymbol{w}}(z,t)$ to zero. While the solid blue line follows from the simulation of the controlled linear model, the dash-dotted yellow line is calculated for $t > t_2$ based on the analytical solution (4.37). It can be seen that the numerical solution matches the analytical one almost perfectly while the minor deviations shortly after t_2 are caused by numerical errors in $\tilde{\boldsymbol{w}}(z,t)$.

Output Feedback Tracking Controller In view of the implementation of the control law at the test bench, next, the state feedback (4.74) is combined the observer (4.38), resulting in the output feedback controller

$$U^{\mathrm{c}}(t) = A\left(\mathrm{e}^{-\alpha\tau_0}\hat{w}_1(1,t) + \mathrm{e}^{\alpha\tau_0}\mathcal{K}[\hat{\eta}(t), \hat{\boldsymbol{w}}(\cdot,t)]\right), \tag{4.76}$$

where $\hat{\boldsymbol{w}}(z,t)$, $\hat{\eta}(t)$ are the estimated states. The parameter ℓ in the observer design is specified such that the eigenvalue of the ODE (4.49d) reads $a - \ell c = -20$, guaranteeing sufficiently smooth estimates with respect to noise and a fast convergence of the observer error. As discussed in Chap. 3, it is advisable to augment the output feedback controller with a feedforward controller. Hence, $U^{\mathrm{c}}(t)$ is superposed with the feedforward controller $U^{\mathrm{r}}(t)$, resulting in the output feedback tracking controller[6]

$$U(t) = U^{\mathrm{r}}(t) + U^{\mathrm{c}}(t). \tag{4.77}$$

To allow for the stabilization of a desired tank pressure trajectory $p^{\mathrm{r}}_{\mathrm{vol}}(t)$, the feedback part reads

$$U^{\mathrm{c}}(t) = A\left(\mathrm{e}^{-\alpha\tau_0}\tilde{w}_1(1,t) + \mathrm{e}^{\alpha\tau_0}\mathcal{K}[\tilde{\eta}(t), \tilde{\boldsymbol{w}}(\cdot,t)]\right). \tag{4.78}$$

It follows from replacing the estimated states $\hat{\boldsymbol{w}}(z,t)$, $\hat{\eta}(t)$ in (4.76) by the error states

$$\tilde{\boldsymbol{w}}(z,t) = \hat{\boldsymbol{w}}(z,t) - \boldsymbol{w}^{\mathrm{r}}(z,t), \quad \tilde{\eta}(t) = \hat{\eta}(t) - \eta^{\mathrm{r}}(t),$$

where $\boldsymbol{w}^{\mathrm{r}}(z,t)$, $\eta^{\mathrm{r}}(t)$ are the reference states, parametrized by $p^{\mathrm{r}}_{\mathrm{vol}}(t)$. The trajectories $U^{\mathrm{r}}(t)$ and $\boldsymbol{w}^{\mathrm{r}}(z,t)$, $\eta^{\mathrm{r}}(t)$ are obtained by applying a flatness-based feedforward controller design[7] to the linear model since the latter is utilized in the subsequent simulation. The desired tank pressure $p^{\mathrm{r}}_{\mathrm{vol}}(t)$ results from (3.11) and equals the standard reference trajectory in Fig. 3.2.

The simulation results, following from the application of the output feedback tracking controller (4.77) to the linear model (2.51), are depicted in Fig. 4.13. While the system is in equilibrium with its surroundings at $t = 0$, the initial state of the observer is $\hat{x}_1(z,0) = \hat{\xi}(0) = 3\rho_0$, $\hat{x}_2(z,0) = 0$. In the upper plot of Fig. 4.13, the reference tank pressure $p^{\mathrm{r}}_{\mathrm{vol}}(t)$, the estimated tank pressure $\hat{p}_{\mathrm{vol}}(t)$, and the actual tank pressure $p_{\mathrm{vol}}(t)$ can be seen. The lower plot shows the control input $U(t)$ with feedforward part $U^{\mathrm{r}}(t)$ and feedback part $U^{\mathrm{c}}(t)$.

Fig. 4.14 depicts the deviations $\Delta p(t)$ of the pressure trajectories in Fig. 4.13, i.e. $p_{\mathrm{vol}}(t) - \hat{p}_{\mathrm{vol}}(t)$, $p^{\mathrm{r}}_{\mathrm{vol}}(t) - \hat{p}_{\mathrm{vol}}(t)$, and $p^{\mathrm{r}}_{\mathrm{vol}}(t) - p_{\mathrm{vol}}(t)$. At the beginning, the tank pressure starts to deviate from the reference pressure caused by the initial observer error. Since the estimated state converges to the actual state, the actual state converges to the reference

[6] More precisely, the output feedback tracking controller comprises (4.38) and (4.77).

[7] By making use of the results in Chap. 5, the trajectories follow from the flatness-based parametrization (5.15), based on (3.11).

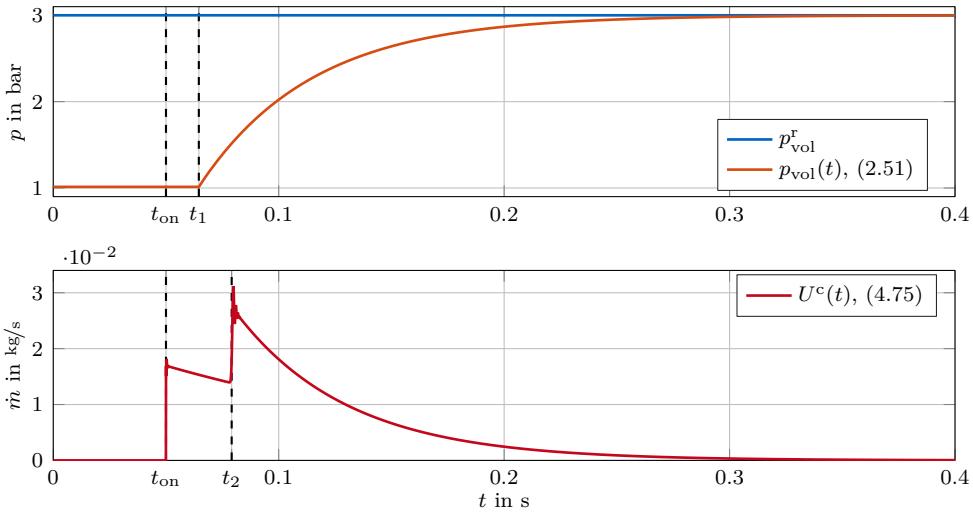

Figure 4.10: Application of the feedback controller (4.75) to the linear model (2.51): Reference pressure $p^{\mathrm{r}}_{\mathrm{vol}}$ and tank pressure $p_{\mathrm{vol}}(t)$ as well as corresponding control input $U^{\mathrm{c}}(t)$

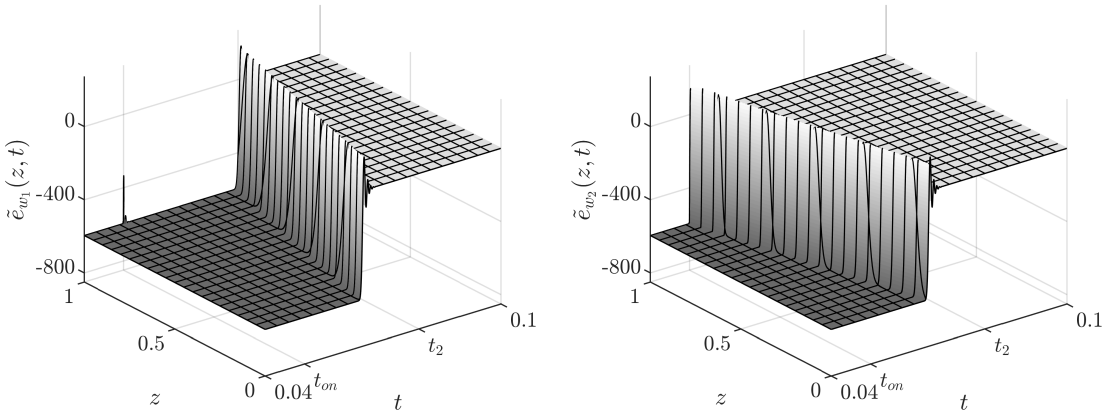

Figure 4.11: Transformed distributed error state $\tilde{\boldsymbol{e}}_w(z,t)$, satisfying the dynamics (4.21a)–(4.21c) for $t > t_{\mathrm{on}}$

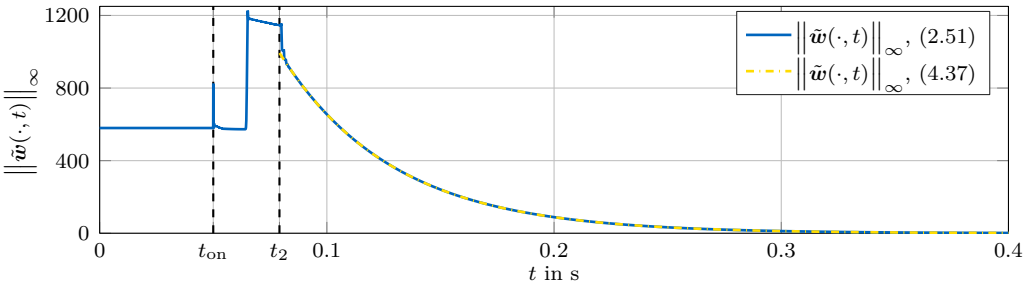

Figure 4.12: Resulting L^∞-norm of the error state $\tilde{\boldsymbol{w}}(z,t)$, calculated based on the simulation data of the closed-loop system and based on the analytical solution (4.37)

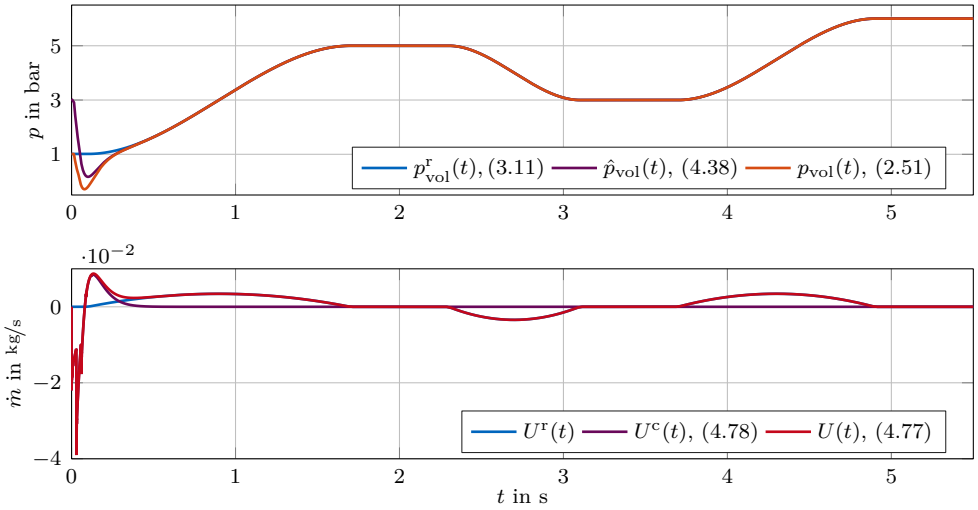

Figure 4.13: Application of the output feedback tracking controller (4.77) to the linear model (2.51): Reference pressure $p^{\mathrm{r}}_{\mathrm{vol}}(t)$, estimated pressure $\hat{p}_{\mathrm{vol}}(t)$, and tank pressure $p_{\mathrm{vol}}(t)$ as well as corresponding control input $U(t)$ with feedforward part $U^{\mathrm{r}}(t)$ and feedback part $U^{\mathrm{c}}(t)$

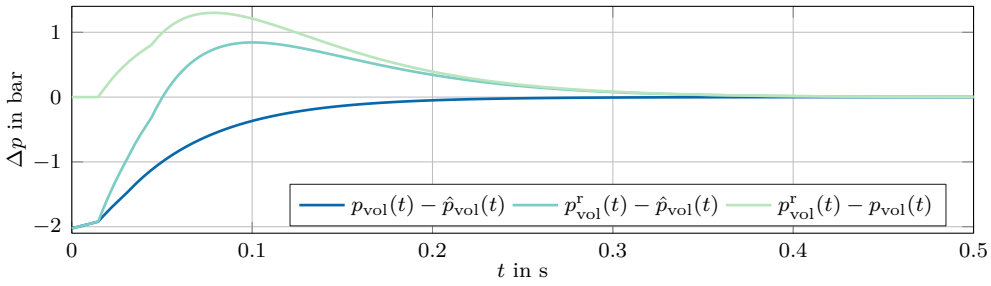

Figure 4.14: Deviations between the reference pressure $p^{\mathrm{r}}_{\mathrm{vol}}(t)$, the estimated pressure $\hat{p}_{\mathrm{vol}}(t)$, and the tank pressure $p_{\mathrm{vol}}(t)$ in Fig. 4.13

state. Consequently, for approximately $t > 0.4\,\mathrm{s}$, the feedback part $U^{\mathrm{c}}(t)$ becomes virtually zero and the system is steered by the feedforward controller $U^{\mathrm{r}}(t)$ only, which can be seen in the lower plot of Fig. 4.13.

Having validated the controller for the linear model, next, it is applied to the plant model in a simulation. Thereby, the discussion of the experimental results in the subsequent section is facilitated. While the other parameters remain unchanged, the friction amplification factor k_{fric} in (2.51a), compensating underestimated friction effects, is tuned by trial and error and set to $k_{\mathrm{fric}} = 4$ for the design of the gains k_η, $\boldsymbol{k}_w^T(z)$ and l_η, $\boldsymbol{l}(z)$ in (4.28) and (4.60), respectively. Naturally, as described in Chap. 3, the design of the flatness-based feedforward controller $U^{\mathrm{r}}(t)$ in (3.14) is now based on the isothermal model (2.50) since the plant model is used in the simulation. Both, the system and the observer, are initialized at ambient conditions. The results are depicted in Fig. 4.15 and the corresponding deviations[8] in Fig. 4.16. In contrast to Fig. 4.13, it can be seen that small deviations occur during the transitions. These arise from the fact that the state

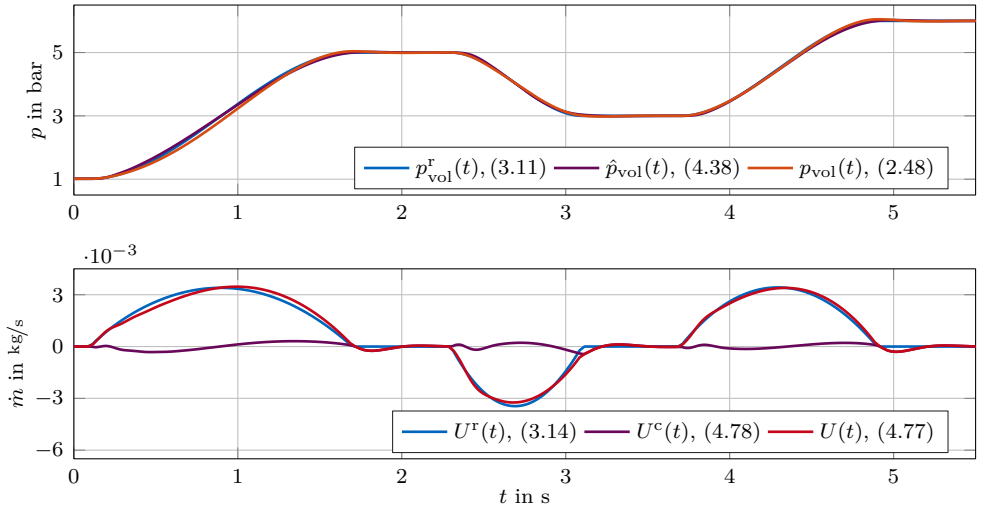

Figure 4.15: Application of the output feedback tracking controller (4.77) to the plant model (2.48): Reference pressure $p^{\mathrm{r}}_{\mathrm{vol}}(t)$, estimated pressure $\hat{p}_{\mathrm{vol}}(t)$, and tank pressure $p_{\mathrm{vol}}(t)$ as well as corresponding control input $U(t)$ with feedforward part $U^{\mathrm{r}}(t)$ and feedback part $U^{\mathrm{c}}(t)$

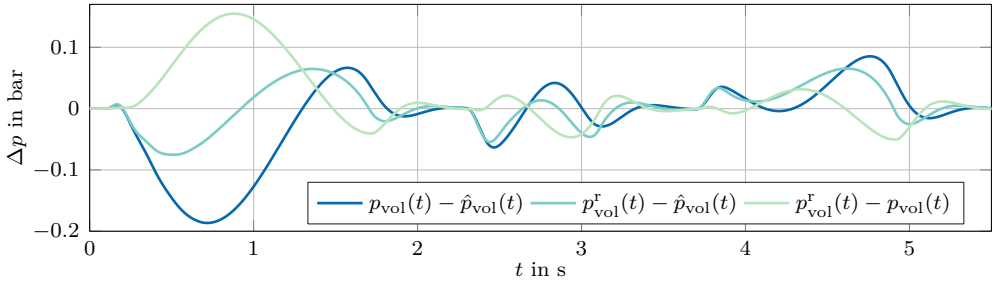

Figure 4.16: Deviations between the reference pressure $p^{\mathrm{r}}_{\mathrm{vol}}(t)$, the estimated pressure $\hat{p}_{\mathrm{vol}}(t)$, and the tank pressure $p_{\mathrm{vol}}(t)$ in Fig. 4.15

feedback as well as the observer are designed based on the linear model but the thereby resulting controller applied to the plant model.

Finally, it should be noted that the performance of the output feedback tracking controller depends on the validity of the isothermal and the linear model and, hence, essentially on four factors: the tube's length as well as its diameter, the volume of the tank, and the transition rate of the reference pressure trajectory (cf. Sec. 2.7). For a test bench configuration with a short, thick tube as well as a small tank and slow transitions, the deviations will be relatively small. Compared to that, the deviations will be increased if a test bench configuration with a long, thin tube as well as a large tank is utilized and fast transitions are specified.

Furthermore, it can be shown by simulations and experiments that the deviations $\Delta p(t)$ are mainly caused by the observer and less by the feedforward or state feedback controller. To achieve a satisfying control performance for a test bench configuration with, e.g., a very long tube, a nonlinear state observer is designed in Appx. C by making use of

[8]The deviations of all essential simulation and experimental results are quantified in terms of the error measures $L^{1}_{\mathrm{r,err}}$ and $L^{\infty}_{\mathrm{err}}$ in (2.42) and (2.43), respectively. They can be found in Chap. 7.

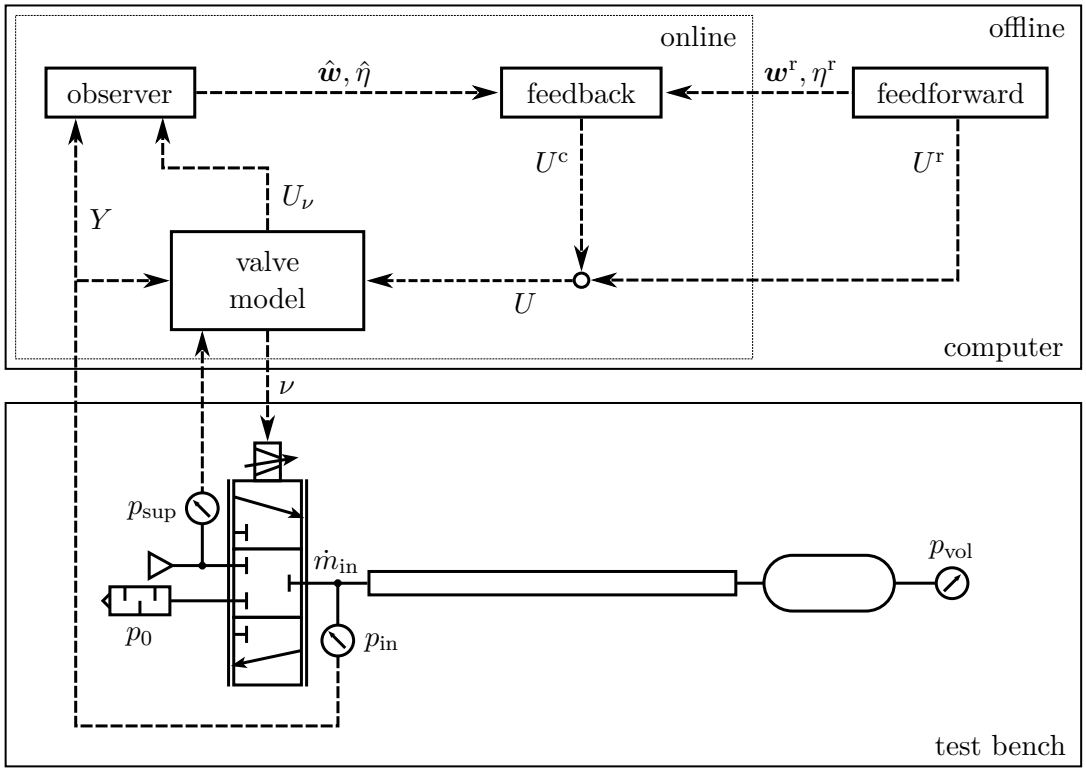

Figure 4.17: A schematic of the implementation of the output feedback tracking controller (4.77) at the test bench

the idea in [RNM16]. Since the nonlinear state observer significantly decreases the estimation error, the tracking behavior is improved. However, as illustrated in Fig. 4.15, the controller performance for the standard test bench configuration in Tab. 3.1 is entirely satisfying. Thus, the nonlinear state observer is not focused on any further.

4.7 Experimental Results

To validate the output feedback tracking controller (4.77) in experiments, it is implemented in Simulink and integrated in the software framework of the test bench. The chosen space step size Δz for the discretization and the sample time Δt of the test bench are given in Appx. B.1.1. A schematic of the implementation and the interface with the test bench is depicted in Fig. 4.17.

Therein, it can be seen that the feedforward controller $U^{\mathrm{r}}(t)$, designed based on the isothermal model (2.50), and the corresponding reference states $\boldsymbol{w}^{\mathrm{r}}(z,t)$, $\eta^{\mathrm{r}}(t)$ are calculated offline. In addition, the controller gains k_η, $\boldsymbol{k}_w^T(z)$ and the observer gains l_η, $\boldsymbol{l}(z)$ are computed prior to the experiment. While the experiment is conducted, the observer estimates the states $\hat{\boldsymbol{w}}(z,t)$, $\hat{\eta}(t)$ based on the pressure measurement $Y(t) = p_{\mathrm{in}}(t)$. These states as well as the reference states are fed to the feedback controller which calculates $U^{\mathrm{c}}(t)$. The input $U(t)$, resulting from the summation of $U^{\mathrm{c}}(t)$ and $U^{\mathrm{r}}(t)$, is passed to the inverse mass flow rate model (2.19) of the valve. Depending on the measured pressures[9] $p_{\mathrm{sup}}(t)$ and $p_{\mathrm{in}}(t)$, the voltage $\nu(t)$, corresponding to $U(t)$, is fed to the valve. Thereby,

[9]The tank pressure $p_{\mathrm{vol}}(t)$ is measured for validation purposes only.

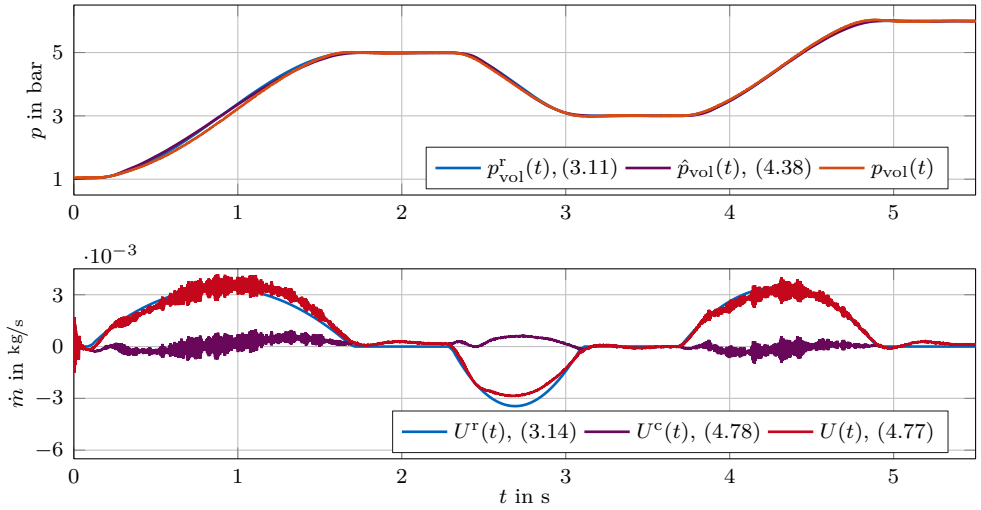

Figure 4.18: Application of the output feedback tracking controller (4.77) to the test bench: Reference pressure $p^{\mathrm{r}}_{\mathrm{vol}}(t)$, estimated pressure $\hat{p}_{\mathrm{vol}}(t)$, and measured tank pressure $p_{\mathrm{vol}}(t)$ as well as corresponding control input $U(t)$ with feedforward part $U^{\mathrm{r}}(t)$ and feedback part $U^{\mathrm{c}}(t)$

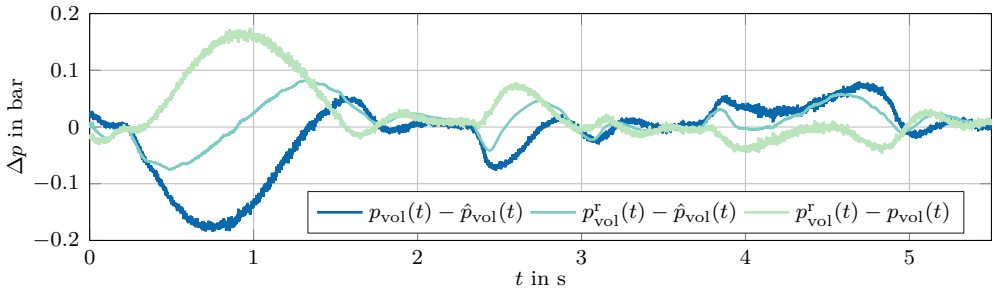

Figure 4.19: Deviations between the reference pressure $p^{\mathrm{r}}_{\mathrm{vol}}(t)$, the estimated pressure $\hat{p}_{\mathrm{vol}}(t)$, and the measured tank pressure $p_{\mathrm{vol}}(t)$ in Fig. 4.18

the position of the spool is defined and, hence, the actual mass flow rate $\dot{m}_{\mathrm{in}}(t)$ at the test bench results[10]. In addition to $\nu(t)$, the inverse mass flow rate model calculates the bounded input

$$U_\nu(t) = \min\left\{\max\{\dot{m}^{\min}_{\mathrm{in}}(t), U(t)\}, \dot{m}^{\max}_{\mathrm{in}}(t)\right\} \tag{4.79}$$

by making use of (2.17). Thus, the minimum and maximum mass flow rates $\dot{m}^{\min}_{\mathrm{in}}(t)$ and $\dot{m}^{\max}_{\mathrm{in}}(t)$, attainable through the valve, are taken into account. The resulting $U_\nu(t)$ is passed to the observer since it resembles the actual input to the test bench.

Remark 4.4. To improve the visualization, some blocks of the Simulink model are not depicted in Fig. 4.17, e.g., two low-pass filters, slightly smoothing the noisy measurements $p_{\mathrm{in}}(t)$ and $p_{\mathrm{sup}}(t)$. A more detailed description of the Simulink Real-Time software framework of the test bench can be found in [MK19]. △

In the first experiment, the controller tracks the standard reference trajectory in Fig. 3.2. The design parameters are chosen as in Sec. 4.6, i.e. $a - bk = a - \ell c = -20$ holds, and

[10] As mentioned in Rem. 2.2, the actual mass flow rate $\dot{m}_{\mathrm{in}}(t)$ matches the desired mass flow rate $U(t)$ only approximately, caused by model uncertainties.

the friction amplification factor in (2.51a) is set to $k_{\text{fric}} = 4$ for the design of the gains k_η, $\boldsymbol{k}_w^T(z)$ and l_η, $\boldsymbol{l}(z)$ in (4.28) and (4.60), respectively. The results of the experiment are depicted in Fig. 4.18. The corresponding pressure deviations are shown in Fig. 4.19.

Obviously, the results of the experiment in Fig. 4.18 and of the simulation in Fig. 4.15 are very similar. However, in the experiment, high frequency oscillations occur in the feedback part $U^{\text{c}}(t)$. These arise from measurement noise in $p_{\text{in}}(t)$ and $p_{\text{sup}}(t)$. Hence, $U_\nu(t)$ and $Y(t)$, both fed to the observer, are noisy, too. In contrast to a lumped-parameter observer, the hyperbolic observer (4.38) does not exhibit such a strong filtering property. As a consequence, the measurement noise is quite significant in the estimates $\hat{\boldsymbol{w}}(z,t)$, $\hat{\eta}(t)$, which leads to the high frequency oscillations in the feedback part $U^{\text{c}}(t)$. Furthermore, in steady-state, $p_{\text{vol}}^{\text{r}}(t) - p_{\text{vol}}(t)$ is not driven to zero entirely. The minor deviations, apparent in Fig. 4.19, result from the fact that the inverse mass flow rate model is less accurate for small mass flow rates. Still, the controller tracks the reference trajectory with a high precision.

In the next experiment, a highly dynamic reference trajectory is chosen for $p_{\text{vol}}^{\text{r}}(t)$ while the test bench configuration and the parameters remain unchanged. For that, two transitions of the tank pressure from 3 bar to 6 bar and back to 3 bar are carried out twice. While the first two transitions have a rate of $7.5\,{}^{\text{bar}}/_{\text{s}}$, the rate of the latter is twice as slow at $3.75\,{}^{\text{bar}}/_{\text{s}}$. The results are presented in Fig. 4.20, where the bounded input $U_\nu(t)$ in (4.79) is depicted instead of the desired input $U(t)$ since the latter partially exceeds the actuation capabilities of the valve. The corresponding pressure deviations are shown in Fig. 4.21.

Compared to the slower transitions, the deviations in Fig. 4.21 during the fast transitions are relatively large and the share of the feedback part $U^{\text{c}}(t)$ in $U_\nu(t)$ is increased. Both effects are caused by the highly dynamic reference trajectory, which induces high flow velocities. Hence, the linear model, used for the state feedback and observer design, is a less accurate description of the test bench (cf. Sec. 2.7). To illustrate the valve's physical capabilities, the voltage $\nu(t)$ is shown in Fig. 4.22. Therein, it can be seen that the signal $\nu(t) = 0$ is fed to the valve for $t \in [2.00\,\text{s}, 2.22\,\text{s}]$. Hence, the test bench is discharged at its fastest rate and $U(t) \leq U_\nu(t) = \dot{m}_{\text{in}}^{\min}(t)$ holds, resulting from (4.79). In contrast to the fast transitions, the slower transitions are tracked with a high precision. Furthermore, as it can be seen in Fig. 4.22, $\nu(t) \in (0, 10\,\text{V})$ holds during the slower transitions. Hence, the desired input equals the bounded input, i.e. $U(t) = U_\nu(t)$, and the valve is operated within its limits.

4.8 Chapter Highlights

This chapter presented the design of a backstepping-based state feedback and state observer for 2×2 hyperbolic systems with constant propagation speeds, which are coupled to a first-order ODE, and have a collocated measurement available. By making use of the two-step approach, all but two integral kernels of the transformations were calculated by explicit expressions. Each of the remaining two kernels followed from the numerical solution of a simple Volterra integral equation. Based on the linear model of the test bench, an output feedback controller was designed, i.e. the combined state feedback and observer, which was augmented by the feedforward controller, derived in Chap. 3. The resulting output feedback tracking controller was investigated in simulations and experiments.

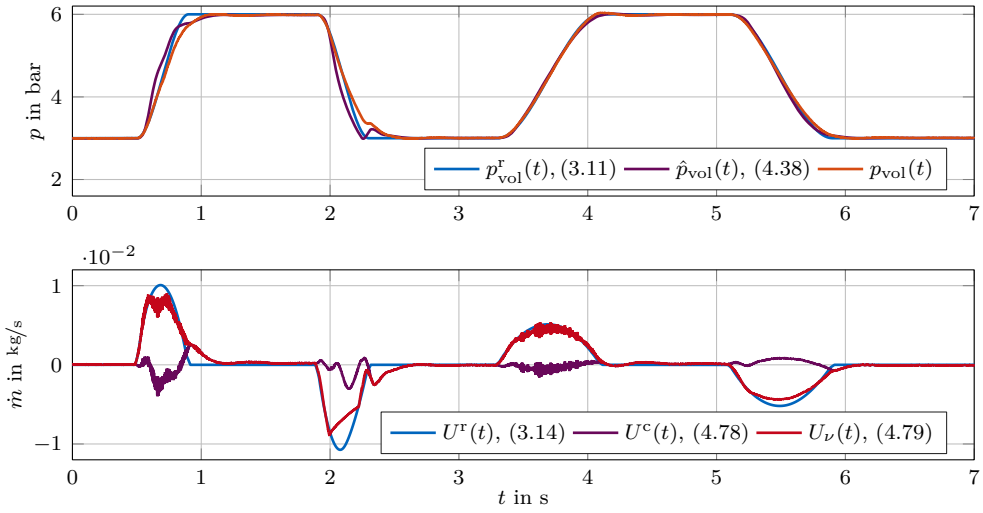

Figure 4.20: Application of the output feedback tracking controller (4.77) to the test bench with faster transitions: Reference pressure $p^{\mathrm{r}}_{\mathrm{vol}}(t)$, estimated pressure $\hat{p}_{\mathrm{vol}}(t)$, and measured tank pressure $p_{\mathrm{vol}}(t)$ as well corresponding bounded control input $U_\nu(t)$ with feedforward part $U^{\mathrm{r}}(t)$ and feedback part $U^{\mathrm{c}}(t)$

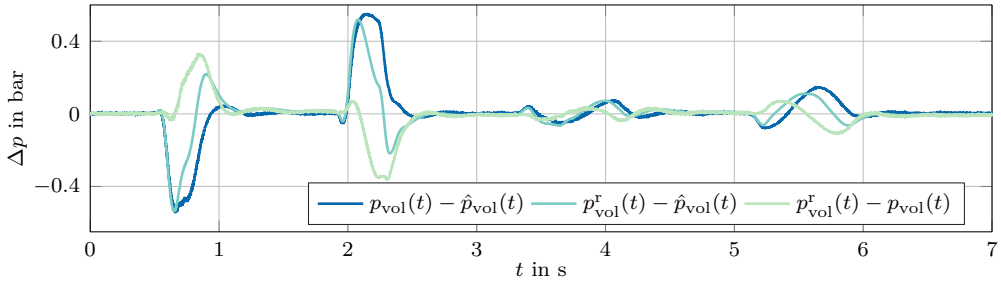

Figure 4.21: Deviations between the reference pressure $p^{\mathrm{r}}_{\mathrm{vol}}(t)$, the estimated pressure $\hat{p}_{\mathrm{vol}}(t)$, and the measured tank pressure $p_{\mathrm{vol}}(t)$ in Fig. 4.20

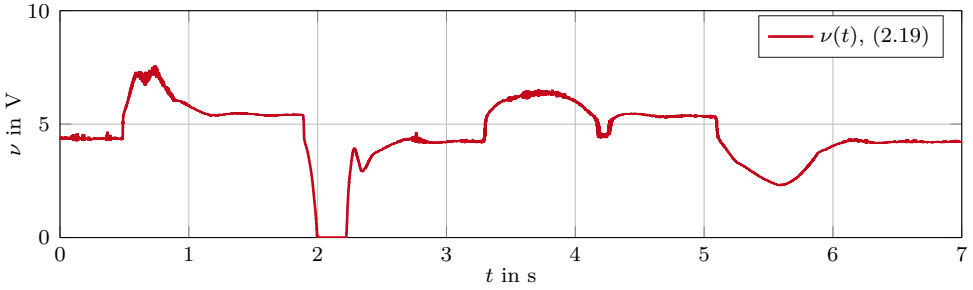

Figure 4.22: The voltage $\nu(t)$, resulting from the inverse mass flow rate model (2.19) and fed to the valve for the experiment in Fig. 4.20

So far, controller designs for pneumatic systems involving tubes, found in the literature, were not directly based on PDEs and/or the resulting control law was finite-dimensional. In contrast to that, the presented infinite-dimensional state feedback and observer are derived based on a PDE-ODE system, describing the test bench. The resulting controller can be implemented in a straightforward manner and its tracking performance in experiments is almost perfect.

In connection with this chapter, the journal papers [DGK18; DGK19] as well as the conference papers [DGK17; KG17; Ker+18a] were published. Furthermore, the talks [GK17; Ker+18b; Ker19] were given. The supervised student theses [Mey16; Mei18; Rot18] have contributed to the development of the chapter's results.

Chapter 5

State Feedback and State Observer Design Using Flatness

As mentioned in Chap. 3, the flatness-based approach has become a viable method for the design of feedforward controllers in the context of distributed-parameter systems. It is shown in [WM10] (in German) and [Woi11] that the parametrization of the system quantities in terms of a flat output is also useful for the controllability analysis of systems described by wave equations. In [Woi12] (in German) and [WR12], these results are generalized to linear hyperbolic PDE systems, coupled to linear ODE systems. Moreover, the hyperbolic controller form (HCF) is introduced, a special system representation, which allows for a straightforward state feedback design.

The HCF essentially consists of a scalar transport equation, where the boundary input acts on its inlet and a chain of integrators is attached at its outlet. The HCF is obtained by making use of a flatness-based parametrization of the input, resulting in a functional differential equation (FDE). This equation involves lumped and distributed delays as well as predictions of the flat output and its time derivatives. If the system is in HCF, it is relatively simple to design a state feedback, similar to the controller canonical form of lumped-parameter systems, e.g., [Oga10]. For that, a desired dynamics of the flat output, e.g., represented by an FDE, is specified. It is shown in [Woi13a] that the explicit transformation of a system into HCF is not necessarily required for the flatness-based state feedback design. Instead, the state feedback can be directly derived in terms of the so-called flat coordinates with a desired dynamics of the flat output.

In [Woi12], the basic idea of the flatness-based state feedback design, where the system quantities are parametrized in terms of the flat output, is adopted for the design of a state observer. For that, the concept of duality is employed. Based on a flat parametrization of the quantities of the dual system, the hyperbolic observer form (HOF) is defined. Similar to the state feedback design, the design of the state observer is relatively straightforward if the system is in the HOF. The convergence of the estimated state towards the actual state is guaranteed by specifying the dynamics of the observation error. It is shown in [Woi13b] that the HOF can also be derived from a specific input-output relation in form of an FDE. This equation is an equivalent description of the system dynamics and involves the input and the measured output as well as their delayed and predicted values and time derivatives.

The output feedback controller follows from the combination of the state feedback with the state observer, e.g., as illustrated in [Woi12], where such a controller is designed based on a wave equation. Since there are currently no general results on the required transformation between the state used in the feedback controller and the one in the HOF, such a combination is not always possible. This also holds true in the context of the pneumatic system in this thesis.

Still, in the following, a state feedback and an observer are designed based on the linear model (2.51) of the test bench by utilizing the flatness-based approaches in [Woi13a] and [Woi13b]. The state feedback in flat coordinates is derived by parametrizing the system quantities in terms of a flat output. The observer in the HOF follows from the input-output relation between $U(t)$ and $Y(t)$. The resulting state feedback and observer are separately validated in simulations since the combination to an output feedback controller would require the aforementioned transformation, which is unknown. Obviously, this prevents an experimental validation of the flatness-based approach, too.

The state feedback design in this chapter follows [GK18], a contribution of N. Gehring and the author of this thesis, and the observer design is based on the unpublished notes [Geh18]. Compared to these references, this chapter presents the state feedback design in more detail. For that, the two-sided Laplace transform is utilized instead of the one-sided. In addition, new theoretical aspects are introduced by discussing both the stability of the closed-loop system and of the observer error dynamics. Furthermore, the state observer investigated in simulations.

5.1 Design of the State Feedback

In the following, first, the system quantities are parametrized in terms of a flat output. By prescribing a desired dynamics of the latter, the state feedback follows, guaranteeing this dynamics and, hence, stabilizing the system. The HCF is not explicitly stated since it is not required, e.g., [Woi13a].

5.1.1 Time-Domain Solution in Terms of a Flat Parametrization

The design of the state feedback is based on the time-domain solution of the linear model (2.51) parametrized in terms of a flat output $y(t)$. In this thesis, it is derived by making use of the two-sided Laplace transform, defined in Appx. D. By transforming $\boldsymbol{x}(z,t)$ and its derivatives[1] into the operational domain, the PDE (2.51a) results in

$$\frac{\mathrm{d}}{\mathrm{d}z}\hat{\boldsymbol{x}}(z,s) = \underbrace{\begin{bmatrix} 0 & \frac{k_3+s}{k_2} \\ \frac{s}{k_1} & 0 \end{bmatrix}}_{\boldsymbol{A}(s)} \hat{\boldsymbol{x}}(z,s) \tag{5.1}$$

with $\hat{\boldsymbol{x}}(z,s) = [\hat{x}_1(z,s), \hat{x}_2(z,s)]^T \in \mathbb{C}^2$, where $\hat{x}_i(z,s) = \mathcal{L}_{II}[x_i(z,\cdot)](s)$, $i = 1,2$, is the image of $x_i(z,t)$. Furthermore,

$$k_1 = \frac{1}{L}, \quad k_2 = \frac{a_{\mathrm{iso}}^2}{L}, \quad k_3 = k_{\mathrm{fric}} \frac{32\mu_0}{D^2} \frac{1}{\rho_0} \tag{5.2}$$

[1] It is assumed that $\boldsymbol{x}(z,t)$, $\xi(t)$ and their derivatives fulfill the necessary conditions for the existence of the following (inverse) Laplace transforms (cf. [vB55; Yos95]).

are introduced for brevity. The explicit solution of the ODE (5.1) in terms of the initial value $\hat{\boldsymbol{x}}(0,s)$ reads

$$\hat{\boldsymbol{x}}(z,s) = \mathrm{e}^{\boldsymbol{A}(s)z}\hat{\boldsymbol{x}}(0,s) \quad \text{with} \quad \mathrm{e}^{\boldsymbol{A}(s)z} = \begin{bmatrix} \cosh(\omega(s)z) & \frac{k_3+s}{k_2}\frac{\sinh(\omega(s)z)}{\omega(s)} \\ \frac{s}{k_1}\frac{\sinh(\omega(s)z)}{\omega(s)} & \cosh(\omega(s)z) \end{bmatrix}, \tag{5.3}$$

the complex function

$$\omega(s) = \tau_0\sqrt{(s+\alpha)^2-\beta^2}, \tag{5.4}$$

and the constants $\tau_0 = 1/\sqrt{k_1k_2} = L/a_{\mathrm{iso}}$ as well as $\alpha = \beta = k_3/2 = 16k_{\mathrm{fric}}\mu_0/(D^2\rho_0)$. Next, the initial value $\hat{\boldsymbol{x}}(0,s)$ in (5.3) is expressed in terms of the flat output. Similar to the isothermal model (2.50), discussed in Sec. 3.1,

$$y(t) = \xi(t)$$

is a flat output of the linear model (2.51). Thus, by making use of (2.51b) and (2.51d), the boundary values at $z = 0$ are parametrized by

$$\hat{x}_1(0,s) = \hat{y}(s), \quad \hat{x}_2(0,s) = \frac{s}{k_4}\hat{y}(s) \quad \text{with} \quad k_4 = A/V_{\mathrm{vol}}, \tag{5.5}$$

where $\hat{\xi}(s) = \mathcal{L}_{II}[\xi](s)$ is replaced by $\hat{y}(s) = \mathcal{L}_{II}[y](s)$. Finally, inserting (5.5) into (5.3) yields the parametrization

$$\hat{x}_1(z,s) = \frac{s(k_3+s)}{k_2k_4}\hat{y}(s)\frac{\sinh(\omega(s)z)}{\omega(s)} + \hat{y}(s)\cosh(\omega(s)z) \tag{5.6a}$$

$$\hat{x}_2(z,s) = \frac{s}{k_4}\hat{y}(s)\cosh(\omega(s)z) + \frac{s}{k_1}\hat{y}(s)\frac{\sinh(\omega(s)z)}{\omega(s)}. \tag{5.6b}$$

To transform the operational solution (5.6) back into the time domain, first, the term

$$\hat{T}_1(z,s) = \hat{y}(s)\frac{\sinh(\omega(s)z)}{\omega(s)} \tag{5.7}$$

is transformed. Although relatively similar calculations can be found in [Doe56; Fod65; Rud03], those are based on the one-sided Laplace transform. Since this thesis makes use of the two-sided Laplace transform, the derivation of the relation $T_1(z,t) = \mathcal{L}_{II}^{-1}[\hat{T}_1(z,\cdot)](t)$ is presented in more detail. Based on this result, the relations required to obtain the time-domain solution of (5.6) follow.

First, by making use of the identity $\sinh(z) = (\mathrm{e}^z - \mathrm{e}^{-z})/2$, the function $\hat{T}_1(z,s) = \hat{f}_1(z,s) + \hat{f}_2(z,s)$ is split, where

$$\hat{f}_i(z,s) = \pm\frac{1}{2\tau_0}\hat{y}(s)\frac{1}{\sqrt{(s+\alpha)^2-\beta^2}}\mathrm{e}^{\pm\tau_0 z\sqrt{(s+\alpha)^2-\beta^2}}.$$

After expanding this fraction with $s(s+\alpha)$, the properties in Tab. D.2 and the transformation in Tab. D.1 (cf. Appx. D) can be directly utilized. From that,

$$\mathcal{L}_{II}^{-1}\left[\hat{f}_i(z,\cdot)\right](t) = \pm\frac{1}{2\tau_0}\int_{-\infty}^{\infty}\mathrm{e}^{-\alpha\tau}h(\tau\pm\tau_0 z)J_0\left(\beta\sqrt{(\tau_0 z)^2-\tau^2}\right)y(t-\tau)\,\mathrm{d}\tau$$

results. Therein, the Bessel function $J_0(z)$ of the first kind of zeroth order follows from $J_0(jz) = I_0(z)$. Thus, the inverse transformation of (5.7) reads

$$\mathcal{L}_{II}^{-1}\left[\hat{T}_1(z,\cdot)\right](t) = \frac{1}{2\tau_0}\int_{-\tau_0 z}^{\tau_0 z} \mathrm{e}^{-\alpha\tau} J_0\left(\beta\sqrt{(\tau_0 z)^2 - \tau^2}\right) y(t-\tau)\,\mathrm{d}\tau. \tag{5.8}$$

Finally, by substituting the integration variable and introducing

$$B(z,\tau) = \frac{1}{2}\mathrm{e}^{-\alpha\tau_0\tau} J_0\left(\tau_0\beta\sqrt{z^2-\tau^2}\right),$$

the relation (5.8) can be stated as

$$\mathcal{L}_{II}^{-1}\left[\hat{T}_1(z,\cdot)\right](t) = \int_{-z}^{z} B(z,\tau) y(t-\tau_0\tau)\,\mathrm{d}\tau. \tag{5.9}$$

Next, by making use of (5.9), the relations for the terms in the operational solution (5.6) are derived. For that, (5.6) is rewritten as

$$\begin{aligned}
\hat{x}_1(z,s) &= \frac{k_3}{k_2 k_4}\hat{T}_2(z,s) + \frac{1}{k_2 k_4}\hat{T}_3(z,s) + \hat{T}_4(z,s)\\
\hat{x}_2(z,s) &= \frac{1}{k_4}\hat{T}_5(z,s) + \frac{1}{k_1}\hat{T}_2(z,s).
\end{aligned}$$

Therein, the terms $\hat{T}_j(z,t)$, $j = 2,\ldots,5$ are defined by means of $\hat{T}_1(z,s)$ in (5.7):

$$\hat{T}_2(z,s) = s\hat{T}_1(z,s) \tag{5.10a}$$
$$\hat{T}_3(z,s) = s\hat{T}_2(z,s) \tag{5.10b}$$
$$\hat{T}_4(z,s) = \hat{y}(s)\cosh(\omega(s)z) = \frac{\mathrm{d}}{\mathrm{d}z}\hat{T}_1(z,s) \tag{5.10c}$$
$$\hat{T}_5(z,s) = s\hat{T}_4(z,s). \tag{5.10d}$$

Consequently, the relations $\hat{T}_j(z,t)$ can be obtained from (5.9). By making use of the differentiation property in Tab. D.2 and an integration by parts,

$$\begin{aligned}
\mathcal{L}_{II}^{-1}\left[\hat{T}_2(z,\cdot)\right](t) = &-\frac{1}{2\tau_0}\mathrm{e}^{-\alpha\tau_0 z} y(t-\tau_0 z) + \frac{1}{2\tau_0}\mathrm{e}^{\alpha\tau_0 z} y(t+\tau_0 z)\\
&+ \int_{-z}^{z} \frac{\frac{\partial}{\partial\tau}B(z,\tau)}{\tau_0} y(t-\tau_0\tau)\,\mathrm{d}\tau
\end{aligned} \tag{5.11}$$

follows. In a similar manner,

$$\begin{aligned}
\mathcal{L}_{II}^{-1}\left[\hat{T}_3(z,\cdot)\right](t) = &-\frac{1}{2\tau_0}\mathrm{e}^{-\alpha\tau_0 z}\frac{\mathrm{d}}{\mathrm{d}t} y(t-\tau_0 z) + \frac{1}{2\tau_0}\mathrm{e}^{\alpha\tau_0 z}\frac{\mathrm{d}}{\mathrm{d}t} y(t+\tau_0 z)\\
&- \frac{1}{4\tau_0^2}(\beta^2\tau_0^2 z - 2\alpha\tau_0)\mathrm{e}^{-\alpha\tau_0 z} y(t-\tau_0 z)\\
&- \frac{1}{4\tau_0^2}(\beta^2\tau_0^2 z + 2\alpha\tau_0)\mathrm{e}^{\alpha\tau_0 z} y(t+\tau_0 z)\\
&+ \int_{-z}^{z} \frac{\frac{\partial^2}{\partial\tau^2}B(z,\tau)}{\tau_0^2} y(t-\tau_0\tau)\,\mathrm{d}\tau
\end{aligned} \tag{5.12}$$

is obtained. In order to derive $\hat{T}_4(z,\cdot)$, (5.9) is differentiated with respect to space, resulting in

$$\mathcal{L}_{II}^{-1}\left[\hat{T}_4(z,\cdot)\right](t) = \frac{1}{2}\mathrm{e}^{-\alpha\tau_0 z}y(t-\tau_0 z) + \frac{1}{2}\mathrm{e}^{\alpha\tau_0 z}y(t+\tau_0 z) + \int_{-z}^{z}\frac{\partial}{\partial z}B(z,\tau)y(t-\tau_0\tau)\,\mathrm{d}\tau, \tag{5.13}$$

where the Leibniz integral rule is applied. The relation

$$\begin{aligned}\mathcal{L}_{II}^{-1}\left[\hat{T}_5(z,\cdot)\right](t) = {}& \frac{1}{2}\mathrm{e}^{-\alpha\tau_0 z}\frac{\mathrm{d}}{\mathrm{d}t}y(t-\tau_0 z) + \frac{1}{2}\mathrm{e}^{\alpha\tau_0 z}\frac{\mathrm{d}}{\mathrm{d}t}y(t+\tau_0 z)\\ &+ \frac{1}{4\tau_0}\beta^2\tau_0^2 z\mathrm{e}^{-\alpha\tau_0 z}y(t-\tau_0 z) - \frac{1}{4\tau_0}\beta^2\tau_0^2 z\mathrm{e}^{\alpha\tau_0 z}y(t+\tau_0 z)\\ &+ \int_{-z}^{z}\frac{\frac{\partial^2}{\partial\tau\partial z}B(z,\tau)}{\tau_0}y(t-\tau_0\tau)\,\mathrm{d}\tau\end{aligned} \tag{5.14}$$

follows from the differentiation property in Tab. D.2 and an integration by parts.

Thereby, the time-domain solution of (5.6), i.e. the solution of the linear model (2.51) in terms of the flat output $y(t)$, follows:

$$\begin{aligned}x_1(z,t) = {}& \frac{1}{2k_2k_4\tau_0}\mathrm{e}^{\alpha\tau_0 z}\frac{\mathrm{d}}{\mathrm{d}t}y(t+\tau_0 z) - \frac{1}{2k_2k_4\tau_0}\mathrm{e}^{-\alpha\tau_0 z}\frac{\mathrm{d}}{\mathrm{d}t}y(t-\tau_0 z)\\ &+ f_1(z;\tau_0)y(t+\tau_0 z) + f_1(z;-\tau_0)y(t-\tau_0 z) + \int_{-z}^{z}g_1(z,\tau)y(t-\tau_0\tau)\,\mathrm{d}\tau\end{aligned} \tag{5.15a}$$

$$\begin{aligned}x_2(z,t) = {}& \frac{1}{2k_4}\mathrm{e}^{\alpha\tau_0 z}\frac{\mathrm{d}}{\mathrm{d}t}y(t+\tau_0 z) + \frac{1}{2k_4}\mathrm{e}^{-\alpha\tau_0 z}\frac{\mathrm{d}}{\mathrm{d}t}y(t-\tau_0 z)\\ &+ f_2(z;\tau_0)y(t+\tau_0 z) + f_2(z;-\tau_0)y(t-\tau_0 z) + \int_{-z}^{z}g_2(z,\tau)y(t-\tau_0\tau)\,\mathrm{d}\tau,\end{aligned} \tag{5.15b}$$

where

$$f_1(z;\tau) = \frac{\mathrm{e}^{\alpha\tau z}}{2}\left(1+\frac{k_3-\beta^2\tau z}{2k_2k_4\tau}\right),\quad g_1(z,t) = \frac{\frac{\partial^2}{\partial t^2}B(z,t) + c\tau_0\frac{\partial}{\partial t}B(z,t)}{k_2k_4\tau_0^2} + \frac{\partial}{\partial z}B(z,t)$$

$$f_2(z;\tau) = \frac{\mathrm{e}^{\alpha\tau z}}{2}\left(\frac{1}{k_1\tau}-\frac{\beta^2\tau z}{2k_4}\right),\qquad g_2(z,t) = \frac{\frac{\partial}{\partial t}B(z,t)}{a\tau_0} + \frac{\frac{\partial^2}{\partial t\partial z}B(z,t)}{k_4\tau_0}.$$

5.1.2 State Transformation and Controller Design

To derive a state feedback as in [Woi13a], the input is expressed in terms of the flat coordinate

$$\bar{y}(\theta,t) = y(t+\theta)\quad\text{with}\quad\frac{\partial}{\partial\theta}\bar{y}(\theta,t) = \frac{\partial}{\partial t}\bar{y}(\theta,t) \tag{5.16}$$

and $\bar{y}(\theta,t)\in\mathbb{R}$, where $\theta\in[-\tau_0,\tau_0]$ holds since $y(\bar{t})$ in (5.15) is evaluated on the interval $\bar{t}\in[t-\tau_0,t+\tau_0]$. By making use of (5.15b) at $z=1$ as well as of (2.51c) and (5.16),

$$\begin{aligned}u_\flat(t) = {}& \frac{1}{2k_4}\mathrm{e}^{\alpha\tau_0}\frac{\partial}{\partial t}\bar{y}(\tau_0,t) + \frac{1}{2k_4}\mathrm{e}^{-\alpha\tau_0}\frac{\partial}{\partial t}\bar{y}(-\tau_0,t)\\ &+ f_2(1;\tau_0)\bar{y}(\tau_0,t) + f_2(1;-\tau_0)\bar{y}(-\tau_0,t) + \int_{-1}^{1}g_2(1,\tau)\bar{y}(-\tau_0\tau,t)\,\mathrm{d}\tau\end{aligned} \tag{5.17}$$

is obtained, where the scaled input $u_\flat(t) = U(t)/A$ is introduced for brevity. To asymptotically stabilize the linear model (2.51), a desired dynamics of the closed-loop system is specified based on $\bar{y}(\theta, t)$. As (5.17) involves first-order time derivatives, the first-order FDE

$$\frac{\mathrm{d}}{\mathrm{d}t}\varepsilon(t) + \kappa_\mathrm{c}\varepsilon(t) = 0 \quad \text{with} \quad \varepsilon(t) = \bar{y}(\tau_0, t) + \gamma_\mathrm{c}\bar{y}(-\tau_0, t) \tag{5.18}$$

is chosen, where $\kappa_\mathrm{c} > 0$ and $\gamma_\mathrm{c} \in (-1, 1)$ ensure the convergence of $\bar{y}(\theta, t)$ to zero, e.g., [Woi13a]. Next, in order to obtain a state feedback, the derivatives in (5.17) have to be replaced. For that, (5.15a) is evaluated at $z = 1$ and expressed in terms of $\bar{y}(\theta, t)$ by making use of (5.16). The resulting equation and (5.18) are solved for $\frac{\partial}{\partial t}\bar{y}(\tau_0, t)$ and $\frac{\partial}{\partial t}\bar{y}(-\tau_0 z, t)$, respectively. By substituting these derivatives into (5.17), the control law

$$u_\flat(t) = k_2\tau_0 k_0 x_1(1, t) + k^+\bar{y}(\tau_0, t) + k^-\bar{y}(-\tau_0, t) + \int_{-1}^{1} k(\tau)\bar{y}(-\tau_0\tau, t)\,\mathrm{d}\tau \tag{5.19}$$

with

$$k_0 = \frac{\gamma_\mathrm{c} - \mathrm{e}^{-2\alpha\tau_0}}{\gamma_\mathrm{c} + \mathrm{e}^{-2\alpha\tau_0}}, \quad k_1 = \frac{\kappa_\mathrm{c}}{2k_4}(k_0 - 1), \quad k^+ = f_2(1; \tau_0) - b\tau_0 k_0 f_1(1; \tau_0) + k_1\mathrm{e}^{\alpha\tau_0} \tag{5.20a}$$

$$k(\tau) = g_2(1, \tau) - b\tau_0 k_0 g_1(1, \tau), \quad k^- = f_2(1; -\tau_0) - b\tau_0 k_0 f_1(1; -\tau_0) + \gamma_\mathrm{c} k_1 \mathrm{e}^{\alpha\tau_0} \tag{5.20b}$$

follows.

To express the state feedback (5.19) by means of the states $\boldsymbol{x}(z, t)$, $\xi(t)$, a transformation from $\boldsymbol{x}(z, t)$, $\xi(t)$ to $\bar{y}(\theta, t)$ is needed. For that, first, (5.15) is rewritten in a vector-based notation in terms of the flat coordinate $\bar{y}$ by substituting (5.16) into (5.15). Thereby,

$$\boldsymbol{x}(z, t) = \boldsymbol{D}^{-1}(z)\begin{bmatrix} \frac{\mathrm{d}}{\mathrm{d}z}\bar{y}(\tau_0 z, t) \\ \frac{\mathrm{d}}{\mathrm{d}z}\bar{y}(-\tau_0 z, t) \end{bmatrix} + \boldsymbol{F}(z)\begin{bmatrix} \bar{y}(\tau_0 z, t) \\ \bar{y}(-\tau_0 z, t) \end{bmatrix} + \int_0^z \boldsymbol{G}(z, \tau)\begin{bmatrix} \bar{y}(\tau_0\tau, t) \\ \bar{y}(-\tau_0\tau, t) \end{bmatrix}\mathrm{d}\tau \tag{5.21}$$

with

$$\boldsymbol{D}(z) = \begin{bmatrix} \mathrm{e}^{-\alpha\tau_0 z} & 0 \\ 0 & \mathrm{e}^{\alpha\tau_0 z} \end{bmatrix}\begin{bmatrix} k_2 k_4 \tau_0^2 & k_4\tau_0 \\ k_2 k_4 \tau_0^2 & -k_4\tau_0 \end{bmatrix} \tag{5.22}$$

and

$$\boldsymbol{F}(z) = \begin{bmatrix} f_1(z; \tau_0) & f_1(z; -\tau_0) \\ f_2(z; \tau_0) & f_2(z; -\tau_0) \end{bmatrix}, \quad \boldsymbol{G}(z, \tau) = \begin{bmatrix} g_1(z, -\tau) & g_1(z, \tau) \\ g_2(z, -\tau) & g_2(z, \tau) \end{bmatrix}$$

are obtained. Solving (5.21) for the derivatives $\frac{\mathrm{d}}{\mathrm{d}z}\bar{y}(\tau_0 z, t)$, $\frac{\mathrm{d}}{\mathrm{d}z}\bar{y}(-\tau_0 z, t)$, integrating over z, and changing the order of integration results in a Volterra integral equation of the second kind for $\bar{y}(\theta, t)$:

$$\begin{bmatrix} \bar{y}(\tau_0 z, t) \\ \bar{y}(-\tau_0 z, t) \end{bmatrix} = \begin{bmatrix} \xi(t) \\ \xi(t) \end{bmatrix} + \int_0^z \boldsymbol{D}(\tau)\boldsymbol{x}(\tau, t)\,\mathrm{d}\tau + \int_0^z \boldsymbol{H}(z, \tau)\begin{bmatrix} \bar{y}(\tau_0\tau, t) \\ \bar{y}(-\tau_0\tau, t) \end{bmatrix}\mathrm{d}\tau, \tag{5.23}$$

defined on $z \in [0, 1]$ and where $\bar{y}(0, t) = \xi(t)$ as well as

$$\boldsymbol{H}(z, \tau) = -\boldsymbol{D}(\tau)\boldsymbol{F}(\tau) - \int_\tau^z \boldsymbol{D}(\bar{\tau})\boldsymbol{G}(\bar{\tau}, \tau)\,\mathrm{d}\bar{\tau} \tag{5.24}$$

are utilized. It is shown in [Woi13a] that the solution $\bar{y}(\theta, t)$ of (5.23) uniquely exists. The integral equation (5.24) can be solved by, e.g., the method of successive approximations.

Remark 5.1. A choice of $\gamma_\mathrm{c} \in (-1,1)\backslash\{0\}$ in (5.18) leads to discontinuities in the solution of $\bar{y}(\theta,t)$ and, hence, in the tank pressure $p_\mathrm{vol}(t)$ since these quantities are proportional. Consequently, in the following, the design parameter is set to $\gamma_\mathrm{c} = 0$ as a non-smooth tank pressure is not desirable. △

5.1.3 Stability Analysis

The closed-loop system results from inserting the state feedback (5.19) into the boundary condition (2.51c) of the linear model (2.51). Since the controller acts on the boundary at $z = 1$ for $t \in (0,\infty)$, the flat output $y(t) = \bar{y}(0,t)$ at $z = 0$ satisfies the desired dynamics (5.18) for $t > \tau_0$. The time τ_0 is needed to propagate a signal from the actuated to the unactuated boundary (and vice versa). Hence, for $t > \tau_0$, the explicit solution of (5.18) in terms of $y(t)$ reads

$$y(t) = \mathrm{e}^{-\kappa_\mathrm{c}(t-\tau_0)} y(\tau_0) \tag{5.25}$$

with $\gamma_\mathrm{c} = 0$. Next, (5.25) is inserted into the time-domain solution (5.15) of $\boldsymbol{x}(z,t)$. Caused by the lumped and distributed delays therein, the resulting solution holds for $t > 2\tau_0$. Replacing $y(t)$ by $\xi(t)$ yields the closed-loop solution

$$\boldsymbol{x}(z,t) = \left[\boldsymbol{D}^{-1}(z) \frac{\mathrm{d}}{\mathrm{d}z} \begin{bmatrix} \mathrm{e}^{-\tau_0\kappa_\mathrm{c} z} \\ \mathrm{e}^{\tau_0\kappa_\mathrm{c} z} \end{bmatrix} + \boldsymbol{F}(z) \begin{bmatrix} \mathrm{e}^{-\tau_0\kappa_\mathrm{c} z} \\ \mathrm{e}^{\tau_0\kappa_\mathrm{c} z} \end{bmatrix} + \int_0^z \boldsymbol{G}(z,\tau) \begin{bmatrix} \mathrm{e}^{-\tau_0\kappa_\mathrm{c}\tau} \\ \mathrm{e}^{\tau_0\kappa_\mathrm{c}\tau} \end{bmatrix} \mathrm{d}\tau \right] \xi(t) \tag{5.26a}$$

$$\xi(t) = \mathrm{e}^{-\kappa_\mathrm{c}(t-\tau_0)} \xi(\tau_0) \tag{5.26b}$$

for $t > 2\tau_0$. Thus, by assuming that $\xi(\tau_0) = y(\tau_0)$ is bounded, for $t > 2\tau_0$, the closed-loop system is exponentially stable pointwise in space, where the convergence rate of

$$\left\| \boldsymbol{x}(\cdot,t) \right\|_\infty = \sup_{z\in[0,1]} \left\| \boldsymbol{x}(z,t) \right\|_{\mathbb{R}^2}$$

is defined by the choice of the design parameter $\kappa_\mathrm{c} > 0$.

Remark 5.2. If $\gamma_\mathrm{c} \neq 0$ holds, still, a solution similar to (5.26) can be obtained explicitly, e.g., based on the (infinitely many) roots of the corresponding characteristic equation. Since these have negative real parts for $\kappa_\mathrm{c} > 0$ and $\gamma_\mathrm{c} \in (-1,1)$, the solution converges to zero asymptotically, e.g., [BC63]. △

5.2 Design of the State Observer

In order to design the flatness-based state observer, first, the input-output equation between $U(t)$ and $Y(t)$ is derived. By making use of this result, the linear model (2.51) is expressed in the HOF. The observer in the HOF essentially follows from prescribing a desired dynamics for the observation error.

5.2.1 Input-Output Equation in the Time Domain

The transformation of the linear model into the HOF is based on a specific system description, consisting of an FDE, relating the (scaled) input $u_\flat(t)$ to the (scaled) measured

output $y_\flat(t) = Y(t)/(R_\mathrm{s}T_0)$ of the linear model (2.51). Based on the general results in [Woi13b], the input-output equation

$$\begin{aligned}0 = {}& \frac{\mathrm{d}}{\mathrm{d}t}y_\flat(t+\tau_0) + c_1\frac{\mathrm{d}}{\mathrm{d}t}y_\flat(t-\tau_0) + c_2\frac{\mathrm{d}}{\mathrm{d}t}u_\flat(t+\tau_0) + c_3\frac{\mathrm{d}}{\mathrm{d}t}u_\flat(t-\tau_0) + c_4 y_\flat(t-\tau_0)\\ &+ \int_{-\tau_0}^{\tau_0}\bar{c}_1(\tau)\frac{\mathrm{d}}{\mathrm{d}t}y_\flat(t+\tau)\,\mathrm{d}\tau + \int_{-\tau_0}^{\tau_0}\bar{c}_2(\tau)\frac{\mathrm{d}}{\mathrm{d}t}u_\flat(t+\tau)\,\mathrm{d}\tau + c_5 u_\flat(t-\tau_0) \end{aligned} \tag{5.27}$$

is derived in [Geh18] for 2×2 linear hyperbolic systems with constant propagation speeds, which are coupled to a first-order ODE. To define the coefficients $c_j \in \mathbb{R}$, $j = 1, \ldots, 5$, and $\bar{c}_i(\tau) \in \mathbb{R}$, $i = 1, 2$, the ODE (5.1) is solved by making use of the initial value $\hat{\boldsymbol{x}}(1, s)$ at the actuated boundary with the measurement $y_\flat(t)$. From that,

$$\hat{\boldsymbol{x}}(z,s) = \begin{bmatrix} \cosh(\omega(s)(1-z)) & -\frac{k_3+s}{k_2}\frac{\sinh(\omega(s)(1-z))}{\omega(s)} \\ -\frac{s}{k_1}\frac{\sinh(\omega(s)(1-z))}{\omega(s)} & \cosh(\omega(s)(1-z)) \end{bmatrix}\hat{\boldsymbol{x}}(1,s)$$

results. Substituting $\hat{x}_1(1,s) = \hat{y}_\flat(s) = \mathcal{L}_{II}[y_\flat](s)$ as well as $\hat{x}_2(1,s) = \hat{u}_\flat(s) = \mathcal{L}_{II}[u_\flat](s)$ and applying the map $z \mapsto 1 - z$ yields

$$\hat{\boldsymbol{x}}(1-z,s) = \begin{bmatrix} \cosh(\omega(s)(z)) & -\frac{k_3+s}{k_2}\frac{\sinh(\omega(s)(z))}{\omega(s)} \\ -\frac{s}{k_1}\frac{\sinh(\omega(s)(z))}{\omega(s)} & \cosh(\omega(s)(z)) \end{bmatrix}\begin{bmatrix}\hat{y}_\flat(s)\\ \hat{u}_\flat(s)\end{bmatrix}, \tag{5.28}$$

parametrizing $\hat{\boldsymbol{x}}(z, s)$ in terms of $\hat{u}_\flat(s)$ and $\hat{y}_\flat(s)$. The time-domain solution of (5.28) is obtained by making use of the relations (5.9) and (5.11)–(5.14). From that,

$$\begin{aligned}\bar{x}_1(1-z,t) = {}& \frac{1}{2}\mathrm{e}^{\alpha\tau_0 z}y_\flat(t+\tau_0 z) + \frac{1}{2}\mathrm{e}^{-\alpha\tau_0 z}y_\flat(t-\tau_0 z) + \int_{-\tau_0 z}^{\tau_0 z}\frac{\frac{\partial}{\partial z}\bar{B}(z,\tau)}{\tau_0}y_\flat(t+\tau)\,\mathrm{d}\tau\\ &- \int_{-\tau_0 z}^{\tau_0 z}\frac{\bar{B}(z,\tau)}{k_2\tau_0}\frac{\mathrm{d}}{\mathrm{d}t}u_\flat(t+\tau)\,\mathrm{d}\tau - \int_{-\tau_0 z}^{\tau_0 z}\frac{k_3\bar{B}(z,\tau)}{k_2\tau_0}u_\flat(t+\tau)\,\mathrm{d}\tau \end{aligned} \tag{5.29a}$$

$$\begin{aligned}\bar{x}_2(1-z,t) = {}& \frac{1}{2}\mathrm{e}^{\alpha\tau_0 z}u_\flat(t+\tau_0 z) + \frac{1}{2}\mathrm{e}^{-\alpha\tau_0 z}u_\flat(t-\tau_0 z)\\ &- \int_{-\tau_0 z}^{\tau_0 z}\frac{\bar{B}(z,\tau)}{k_1\tau_0}\frac{\mathrm{d}}{\mathrm{d}t}y_\flat(t+\tau)\,\mathrm{d}\tau + \int_{-\tau_0 z}^{\tau_0 z}\frac{\frac{\partial}{\partial z}B(z,\tau)}{\tau_0}u_\flat(t+\tau)\,\mathrm{d}\tau, \end{aligned} \tag{5.29b}$$

where $\bar{B}(z,\tau) = B(z,-\tau/\tau_0)$, results after a substitution of the integration variable. Next, (5.29) is evaluated at $z = 1$ and inserted into (2.51d) using (2.51b). Thereby, a second-order time derivative of $u_\flat(t)$ occurs in an integral, which is eliminated by applying an integration by parts in order to obtain the form in (5.27). Finally, by making use of the relations

$$w(t+\tau_0) = w(t-\tau_0) + \int_{-\tau_0}^{\tau_0}\frac{\mathrm{d}}{\mathrm{d}t}w(t+\tau)\,\mathrm{d}\tau \tag{5.30a}$$

$$\int_{-\tau_0}^{\tau_0}f(\tau)w(t+\tau)\,\mathrm{d}\tau = \int_{-\tau_0}^{\tau_0}f(\tau)\,\mathrm{d}\tau w(t-\tau_0) + \int_{-\tau_0}^{\tau_0}\int_{\tau}^{\tau_0}f(\sigma)\,\mathrm{d}\sigma\frac{\mathrm{d}}{\mathrm{d}t}w(t+\tau)\,\mathrm{d}\tau, \tag{5.30b}$$

the input-output equation

$$\begin{aligned}0 = {} & \frac{1}{2}\mathrm{e}^{\alpha\tau_0}\frac{\mathrm{d}}{\mathrm{d}t}y_\flat(t+\tau_0) + \frac{1}{2}\mathrm{e}^{-\alpha\tau_0}\frac{\mathrm{d}}{\mathrm{d}t}y_\flat(t-\tau_0) - \frac{1}{2k_2\tau_0}\mathrm{e}^{\alpha\tau_0}\frac{\mathrm{d}}{\mathrm{d}t}u_\flat(t+\tau_0) \\ & + \frac{1}{2k_2\tau_0}\mathrm{e}^{-\alpha\tau_0}\frac{\mathrm{d}}{\mathrm{d}t}u_\flat(t-\tau_0) + \int_{-\tau_0}^{\tau_0}\frac{k_4\bar{B}(1,\tau)+k_1\frac{\partial}{\partial z}\bar{B}(z,\tau)|_{z=1}}{k_1\tau_0}\frac{\mathrm{d}}{\mathrm{d}t}y_\flat(t+\tau)\,\mathrm{d}\tau \\ & + \int_{-\tau_0}^{\tau_0}\left[\frac{\frac{\partial}{\partial\tau}\bar{B}(1,\tau)-k_3\bar{B}(1,\tau)}{k_2\tau_0} - \frac{k_4}{2}\mathrm{e}^{\alpha\tau_0} - \int_\tau^{\tau_0}\frac{k_4\frac{\partial}{\partial z}\bar{B}(z,\sigma)|_{z=1}}{\tau_0}\,\mathrm{d}\sigma\right]\frac{\mathrm{d}}{\mathrm{d}t}u_\flat(t+\tau)\,\mathrm{d}\tau \\ & - k_4\left[\cosh(\alpha\tau_0) + \int_{-\tau_0}^{\tau_0}\frac{\frac{\partial}{\partial z}\bar{B}(z,\tau)|_{z=1}}{\tau_0}\,\mathrm{d}\tau\right]u_\flat(t-\tau_0) \end{aligned} \tag{5.31}$$

is obtained, equivalent to the system dynamics of the linear model (2.51). A comparison of (5.31) and (5.27) yields

$$c_1 = \mathrm{e}^{-2\alpha\tau_0}, \quad c_2 = -\frac{1}{k_2\tau_0}, \quad c_3 = \frac{1}{k_2\tau_0}\mathrm{e}^{-2\alpha\tau_0}, \quad c_4 = 0 \tag{5.32a}$$

$$c_5 = -2k_4\mathrm{e}^{-\alpha\tau_0}\left[\cosh(\alpha\tau_0) + \int_{-\tau_0}^{\tau_0}\frac{\frac{\partial}{\partial z}\bar{B}(z,\tau)|_{z=1}}{\tau_0}\,\mathrm{d}\tau\right] \tag{5.32b}$$

$$\bar{c}_1(\tau) = 2\mathrm{e}^{-\alpha\tau_0}\frac{k_4\bar{B}(1,\tau)+k_1\frac{\partial}{\partial z}\bar{B}(z,\tau)|_{z=1}}{k_1\tau_0} \tag{5.32c}$$

$$\bar{c}_2(\tau) = 2\mathrm{e}^{-\alpha\tau_0}\frac{\frac{\partial}{\partial\tau}\bar{B}(1,\tau)-k_3\bar{B}(1,\tau)}{k_2\tau_0} - k_4 - 2k_4\mathrm{e}^{-\alpha\tau_0}\int_\tau^{\tau_0}\frac{\frac{\partial}{\partial z}\bar{B}(z,\sigma)|_{z=1}}{\tau_0}\,\mathrm{d}\sigma. \tag{5.32d}$$

5.2.2 Hyperbolic Observer Form

Derived from the general results in [Woi13b], the HOF in [Geh18], associated with the input-output relation (5.31), reads

$$\frac{\mathrm{d}}{\mathrm{d}t}\eta_1(t) = -c_4y_\flat(t) - c_5u_\flat(t) \tag{5.33a}$$

$$\frac{\partial}{\partial t}\eta_2(\theta,t) = -\frac{\partial}{\partial\theta}\eta_2(\theta,t) - \bar{c}_1(\theta)y_\flat(t) - \bar{c}_2(\theta)u_\flat(t) \tag{5.33b}$$

$$\eta_2(-\tau_0,t) = \eta_1(t) - c_1y_\flat(t) - c_3u_\flat(t) \tag{5.33c}$$

$$y_\flat(t) = \eta_2(\tau_0,t) - c_2u_\flat(t). \tag{5.33d}$$

The states, satisfying (5.33), are defined by

$$\eta_1(t) = y_\flat(t+2\tau_0) + c_1y_\flat(t) + c_2u_\flat(t+2\tau_0) + c_3u_\flat(t) \tag{5.34a}$$

$$+ \int_{-\tau_0}^{\tau_0}\bar{c}_1(\tau)y_\flat(t+\tau_0+\tau)\,\mathrm{d}\tau + \int_{-\tau_0}^{\tau_0}\bar{c}_2(\tau)u_\flat(t+\tau_0+\tau)\,\mathrm{d}\tau \tag{5.34b}$$

$$\eta_2(\theta,t) = y_\flat(t+\tau_0-\theta) + c_2u_\flat(t+\tau_0-\theta) + \int_\theta^{\tau_0}\bar{c}_1(\tau)y_\flat(t-\theta+\tau)\,\mathrm{d}\tau \tag{5.34c}$$

$$+ \int_\theta^{\tau_0}\bar{c}_2(\tau)u_\flat(t-\theta+\tau)\,\mathrm{d}\tau, \tag{5.34d}$$

where $\theta \in [-\tau_0, \tau_0]$ holds since the measurement $y_\flat(\bar{t})$ in (5.27) is evaluated on the interval $\bar{t} \in [t-\tau_0, t+\tau_0]$. Obviously, the HOF (5.33) consists of the ODE (5.33a), bidirectionally coupled to the transport PDE (5.33b) with the boundary condition (5.33c) and the output equation (5.33d).

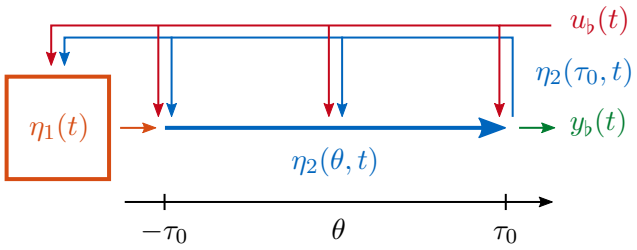

Figure 5.1: Structure of the system (5.33)

Remark 5.3. As the measured output $y_\flat(t)$ acts on (5.33a)–(5.33c), the system description (5.33) may not be considered as a classical state representation. Such a representation could be achieved by substituting $y_\flat(t)$ in (5.33a)–(5.33c) by (5.33d). While this step is unnecessary for the design of the state observer and therefore not explicitly stated, the resulting structure is visualized in Fig. 5.1. △

5.2.3 Observer Error Dynamics and State Observer

The observer in the HOF provides the estimates $\hat{\eta}_1(t)$, $\hat{\eta}_2(\theta,t)$ of the states $\eta_1(t)$, $\eta_2(\theta,t)$. It follows from (5.33) and a desired dynamics for the observation error $\tilde{y}_\flat(t) = \hat{y}_\flat(t) - y_\flat(t)$, where $\hat{y}_\flat(t)$ is the estimated measurement. The desired dynamics of the observation error are defined by the FDE

$$\frac{\mathrm{d}}{\mathrm{d}t}\varepsilon_\flat(t) + \kappa_\mathrm{o}\varepsilon_\flat(t) = 0 \quad \text{with} \quad \varepsilon_\flat(t) = \tilde{y}_\flat(t+\tau_0) + \gamma_\mathrm{o}\tilde{y}_\flat(t-\tau_0), \tag{5.35}$$

where $\kappa_\mathrm{o} > 0$ and $\gamma_\mathrm{o} \in (-1,1)$ guarantee the convergence of $\tilde{y}_\flat(t)$ to zero. To obtain the error dynamics (5.35) in the HOF, (5.35) is rewritten as the input-output equation

$$0 = \frac{\mathrm{d}}{\mathrm{d}t}\tilde{y}_\flat(t+\tau_0) + \gamma_\mathrm{o}\frac{\mathrm{d}}{\mathrm{d}t}\tilde{y}_\flat(t-\tau_0) + \kappa_\mathrm{o}\int_{-\tau_0}^{\tau_0}\frac{\mathrm{d}}{\mathrm{d}t}\tilde{y}_\flat(t+\tau)\,\mathrm{d}\tau + \kappa_\mathrm{o}(1+\gamma_\mathrm{o})\tilde{y}_\flat(t-\tau_0),$$

where (5.30a) is utilized. Thereby, the HOF

$$\frac{\mathrm{d}}{\mathrm{d}t}\tilde{\eta}_1(t) = -\kappa_\mathrm{o}(1+\gamma_\mathrm{o})\tilde{y}_\flat(t) \tag{5.36a}$$

$$\frac{\partial}{\partial t}\tilde{\eta}_2(\theta,t) = -\frac{\partial}{\partial\theta}\tilde{\eta}_2(\theta,t) - \kappa_\mathrm{o}\tilde{y}_\flat(t) \tag{5.36b}$$

$$\tilde{\eta}_2(-\tau_0,t) = \tilde{\eta}_1(t) - \gamma_\mathrm{o}\tilde{y}_\flat(t) \tag{5.36c}$$

$$\tilde{y}_\flat(t) = \tilde{\eta}_2(\tau_0,t) \tag{5.36d}$$

of the observer error dynamics (5.35) with the error states

$$\tilde{\eta}_1(t) = \tilde{y}_\flat(t+2\tau_0) + \gamma_\mathrm{o}\tilde{y}_\flat(t) + \kappa_\mathrm{o}\int_{-\tau_0}^{\tau_0}\tilde{y}_\flat(t+\tau_0+\tau)\,\mathrm{d}\tau \tag{5.37a}$$

$$\tilde{\eta}_2(\theta,t) = \tilde{y}_\flat(t+\tau_0-\theta) + \kappa_\mathrm{o}\int_{\theta}^{\tau_0}\tilde{y}_\flat(t-\theta+\tau)\,\mathrm{d}\tau, \quad \theta \in [-\tau_0,\tau_0] \tag{5.37b}$$

is obtained. By making use of the definitions $\tilde{\eta}_1(t) = \hat{\eta}_1(t) - \eta_1(t)$, $\tilde{\eta}_2(\theta,t) = \hat{\eta}_2(\theta,t) - \eta_2(\theta,t)$, the observer

$$\frac{\mathrm{d}}{\mathrm{d}t}\hat{\eta}_1(t) = -c_4 y_\flat(t) - c_5 u_\flat(t) - \kappa_\mathrm{o}(1+\gamma_\mathrm{o})\tilde{y}_\flat(t) \tag{5.38a}$$

$$\frac{\partial}{\partial t}\hat{\eta}_2(\theta,t) = -\frac{\partial}{\partial\theta}\hat{\eta}_2(\theta,t) - \bar{c}_1(\theta)y_\flat(t) - \bar{c}_2(\theta)u_\flat(t) - \kappa_\mathrm{o}\tilde{y}_\flat(t) \tag{5.38b}$$

$$\hat{\eta}_2(-\tau_0,t) = \hat{\eta}_1(t) - c_1 y_\flat(t) - c_3 u_\flat(t) - \gamma_\mathrm{o}\tilde{y}_\flat(t) \tag{5.38c}$$

$$\hat{y}_\flat(t) = \hat{\eta}_2(\tau_0,t) - c_2 u_\flat(t) \tag{5.38d}$$

in the HOF follows from (5.33) and (5.36).

Remark 5.4. A choice of $\gamma_\mathrm{o} \in (-1,1)\backslash\{0\}$ can lead to an increase of discontinuities in the solution $\hat{\eta}_2$. If a state feedback is based on such a non-smooth estimate, oscillations in the input may result. Therefore, the design parameter is set to $\gamma_\mathrm{o} = 0$ in the following. △

5.2.4 Stability Analysis

The convergence of the observer errors $\tilde{\eta}_1(t)$, $\tilde{\eta}_2(\theta,t)$ to zero can be shown in a manner relatively similar to the stability analysis of the closed-loop system in Sec. 5.1.3. Obviously, (5.37) requires the measurement $y_\flat(\bar{t})$ on $\bar{t} \in [t, t+2\tau_0]$. To avoid these unknown predictions, the time shift $t \mapsto t - 2\tau_0$ is applied to (5.37). Thereby, the states $\tilde{\eta}_1(t)$, $\tilde{\eta}_2(\theta,t)$ are based on the measurement $y_\flat(\bar{t})$ evaluated on $\bar{t} \in [t-2\tau_0, t]$. Since $y_\flat(t)$ is not available for $t < 0$, the states $\tilde{\eta}_1(t)$, $\tilde{\eta}_2(\theta,t)$ of (5.36a)–(5.36c) are defined for $t > 2\tau_0$. As (5.36d) defines $\tilde{y}_\flat(t)$, the desired dynamics (5.35) is achieved for $t > 2\tau_0$. With $\gamma_\mathrm{o} = 0$, the explicit solution

$$\tilde{y}_\flat(t) = \mathrm{e}^{-\kappa_\mathrm{o}(t-2\tau_0)}\tilde{y}_\flat(2\tau_0) \tag{5.39}$$

results.

Inserting (5.39) into (5.37) yields the solution

$$\tilde{\eta}_1(t) = \tilde{y}_\flat(t) \tag{5.40a}$$

$$\tilde{\eta}_2(\theta,t) = \tilde{y}_\flat(t) \tag{5.40b}$$

of the observer errors for $t > 2\tau_0$. Therefore, by assuming that $\tilde{y}_\flat(2\tau_0)$ is bounded, the convergence of $\tilde{\eta}_2(\theta,t)$ is exponential pointwise in space, i.e. for $t > 2\tau_0$,

$$\left\|\tilde{\eta}_2(\cdot,t)\right\|_\infty = \sup_{\theta\in[-\tau_0,\tau_0]}\left\|\tilde{\eta}_2(\theta,t)\right\|_{\mathbb{R}}$$

converges exponentially with a desired convergence rate, specified by $\kappa_\mathrm{o} > 0$.

5.3 Simulation Studies

In the following, the flatness-based state feedback

$$U^\mathrm{c}(t) = A u_\flat(t), \tag{5.41}$$

where $u_\flat(t)$ is defined in (5.19), is investigated in simulations by applying (5.41) to the linear model[2] (2.51) of the test bench. The state $\bar{y}(\theta,t)$ in (5.19) results from the Volterra integral equation (5.23), where $\boldsymbol{x}(z,t)$, $\xi(t)$ are replaced by the error states

$$\tilde{\boldsymbol{x}}(z,t) = \begin{bmatrix} x_1(z,t) \\ x_2(z,t) \end{bmatrix} - \begin{bmatrix} \frac{1}{R_\mathrm{s}T_0} p^\mathrm{r}_\mathrm{vol} \\ 0 \end{bmatrix}$$
$$\tilde{\xi}(t) = \xi(t) - \frac{1}{R_\mathrm{s}T_0} p^\mathrm{r}_\mathrm{vol},$$

allowing for the stabilization of a constant tank pressure $p^\mathrm{r}_\mathrm{vol}$. The observer (5.38) is discussed separately from the feedback by comparing the measurements $Y(t)$, obtained from the simulation of the linear model, to the estimated measurement

$$\hat{Y}(t) = R_\mathrm{s}T_0\hat{y}_\flat(t), \tag{5.42}$$

resulting from (5.38d). For the numerical implementation, the integral in (5.19) is discretized w.r.t. space by the trapezoidal rule. Furthermore, for each time step, the solution of the Volterra integral equation (5.23) is iteratively determined online by utilizing the method of successive approximations. The result from this iteration is used as the initialization in the next time step. Thereby, the computational effort is kept within limits. The state observer is discretized by the methods stated in Appx. B.1.

The application of the state feedback (5.41), stabilizing the desired pressure level $p^\mathrm{r}_\mathrm{vol} = 3\,\mathrm{bar}$, to the linear model (2.51) is shown in Fig. 5.2. The test bench configuration is stated in Tab. 3.1 and $k_\mathrm{fric} = 1$ in (2.51a) holds in the simulation as well as in the computation of the control law (5.19) since the state feedback is applied to the linear model. The design parameters in (5.18) are set to $\kappa_\mathrm{c} = 20$ and $\gamma_\mathrm{c} = 0$. This choice facilitates the comparison between the flatness-based and backstepping-based[3] state feedbacks in Sec. 7.1. Initially, the system is in equilibrium with its surroundings. At $t_\mathrm{on} = 0.05\,\mathrm{s}$, the controller is activated. The exponential convergence of the tank pressure $p_\mathrm{vol}(t)$ to $p^\mathrm{r}_\mathrm{vol}$ for $t > t_1 = \tau_0 + t_\mathrm{on} \approx 0.07\,\mathrm{s}$, defined in (5.25), can be seen in the upper plot of Fig. 5.2. The lower plot depicts the input $U^\mathrm{c}(t) = Ax_2(1,t)$, which converges to zero for $t > t_2 = 2\tau_0 + t_\mathrm{on} \approx 0.08\,\mathrm{s}$, resulting from the convergence of $x_2(1,t)$ in (5.26a). The high frequency oscillations shortly after $t = t_\mathrm{on}$ and $t = t_2$ are induced by numerical inaccuracies caused by discontinuities in the solution.

Fig. 5.3 shows the distributed state $\bar{y}(\theta,t)$, obtained from the numerical solution of the Volterra integral equation (5.23). Since $\bar{y}(\theta,t)$ satisfies the transport equation in (5.16), it can be seen that the boundary values at $\theta = \tau_0$ are propagated along the characteristic curves in the negative direction of θ to the boundary at $\theta = -\tau_0$ with a relative velocity of $1\,{}^1\!/_\mathrm{s}$. In addition, for $t > t_1 - \theta$, the solution $\bar{y}(\theta,t)$ satisfies the desired dynamics (5.18) and thus decays to zero.

The exponential convergence of the L^∞-norm of $\tilde{\boldsymbol{x}}(z,t)$ to zero for $t > t_2$ is depicted in Fig. 5.4. The solid blue line results from the simulation of the closed-loop system and the dash-dotted yellow line is calculated for $t > t_2$ by making use of the analytical solution (5.26). Besides minor deviations shortly after $t = t_2$, induced by numerical oscillations, both lines match perfectly.

[2] A simulation, where the flatness-based feedback controller is applied to the plant model (2.48), is not explicitly stated since these results are very similar to the backstepping-based controller in Sec. 4.6. Still, such simulation data can be found in [GK18].

[3] The design parameter k of the backstepping-based state feedback (4.74) was chosen such that $a - bk = -20$ holds in the ODE (4.21d) (cf. Sec. 4.6).

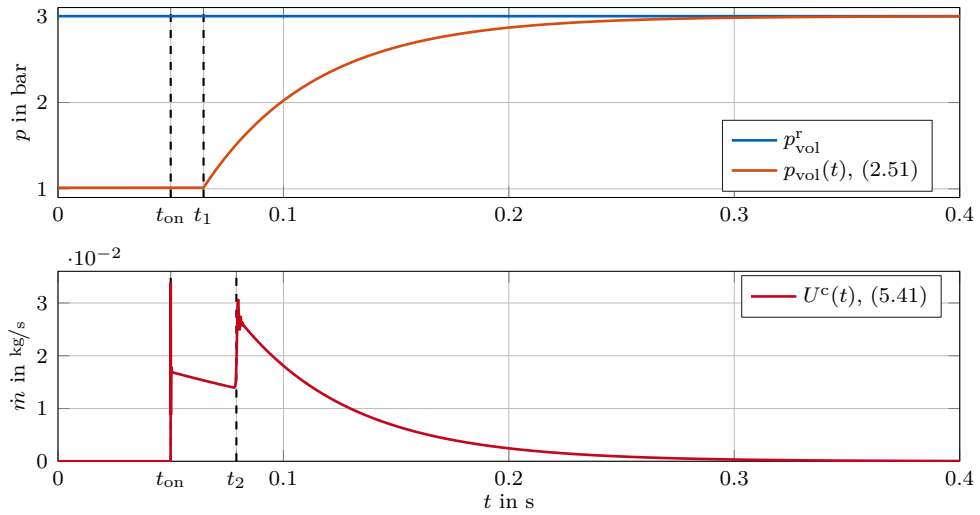

Figure 5.2: Application of the feedback controller (5.41) to the linear model (2.51): Reference pressure $p^{\mathrm{r}}_{\mathrm{vol}}$ and tank pressure $p_{\mathrm{vol}}(t)$ as well as corresponding control input $U^{\mathrm{c}}(t)$

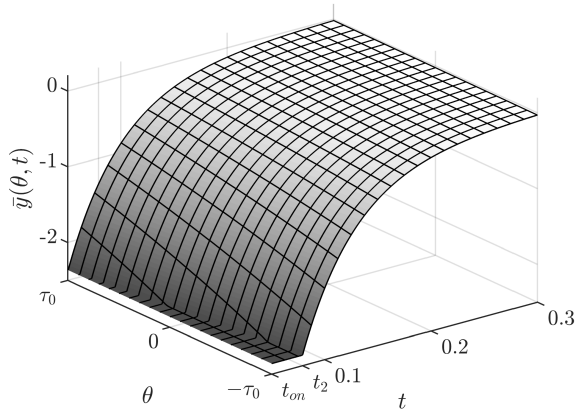

Figure 5.3: Convergence of the state $\bar{y}(\theta, t)$, satisfying the dynamics (5.18) for $t > t_1 - \theta$

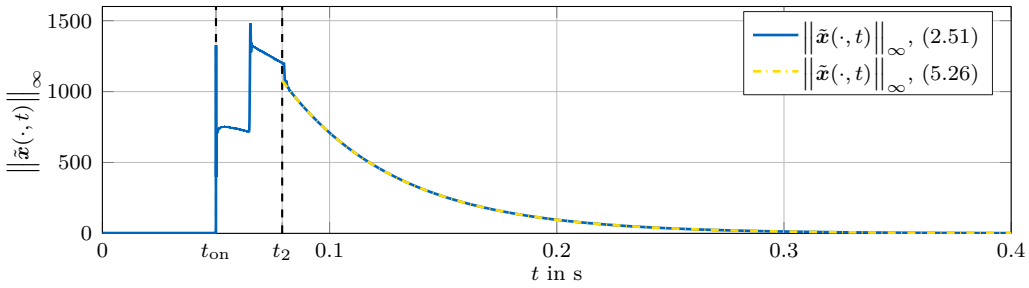

Figure 5.4: Resulting L^∞-norm of the state $\tilde{\boldsymbol{x}}(z, t)$, calculated based on the simulation of the closed-loop system and based on the analytical solution (5.26)

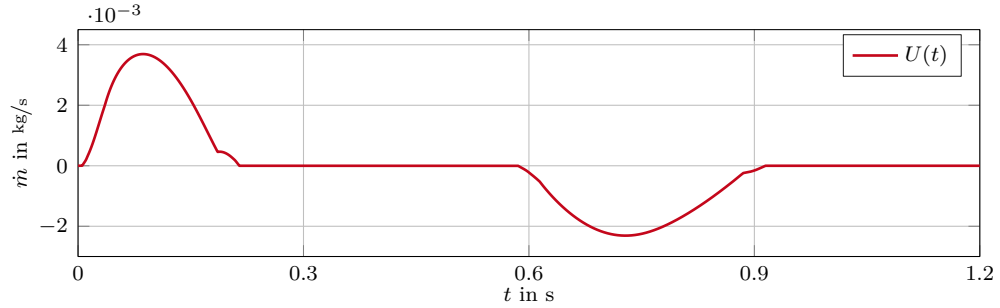

Figure 5.5: The input $U(t)$, corresponding to the simulation depicted in Fig. 5.6

Having discussed the flatness-based state feedback, next, the state observer (5.38) is validated in simulations. As already mentioned, the required transformation between the estimated states $\hat{\eta}_1(t)$, $\hat{\eta}_2(\theta, t)$ and the corresponding estimates of the states $\boldsymbol{x}(z,t)$, $\xi(t)$ is unknown. Still, the observer can be verified in terms of the observation error $\tilde{Y}(t) = \hat{Y}(t) - Y(t)$, following from the measurement $Y(t)$ and the estimation $\hat{Y}(t)$ in (5.42). The measurement $Y(t)$, injected into the state observer (5.38), results from the simulation of the linear model (2.51), which is excited by the input $U(t)$, depicted in Fig. 5.5. While the system is initially at rest and in equilibrium with its surroundings, the initial state of the observer is set to $\hat{\eta}_1(0) = \hat{\eta}_2(\theta, 0) = 0$, allowing to demonstrate the convergence of $\tilde{Y}(t)$. Similar to the choice of the parameters κ_c and γ_c for the design of the state feedback (5.41), the parameters in (5.35) are chosen as $\kappa_\mathrm{o} = 20$ and $\gamma_\mathrm{o} = 0$. The friction amplification factor is set to $k_\mathrm{fric} = 1$ for both, the design of the state observer and the simulation of the linear model.

Remark 5.5. By making use of (5.34), it would be possible to compare the states $\eta_1(t)$, $\eta_2(\theta, t)$ of the linear model or the plant model in the HOF to the estimated states $\hat{\eta}_1(t)$, $\hat{\eta}_2(\theta, t)$ of the observer. As shown in the student thesis [Fri18], this is possible for experimental data, too, but does not grant further insights. △

The upper plot of Fig. 5.6 shows the measured pressure $Y(t)$, resulting from the simulation of the linear model, as well as the pressure[4] $\hat{Y}(t)$, estimated by the state observer (5.38). The lower plot of Fig. 5.6 depicts the exponential convergence of the observation error $\tilde{Y}(t) = \hat{Y}(t) - Y(t)$ to zero. Therein, the solid black line is obtained from the simulation and the dash-dotted yellow line follows from the analytical solution (5.39) for $t > 2\tau_0$. Apart from negligible deviations shortly after $t = 2\tau_0$, it can be seen that the observation error converges with the prescribed convergence rate.

The simulation indicates that the estimates $\hat{\eta}_1(t)$, $\hat{\eta}_2(\theta, t)$ of the observer are reasonable. Still, an experimental validation, where the estimated pressure $\hat{p}_\mathrm{vol}(t)$ is compared to the measured pressure $p_\mathrm{vol}(t)$ necessitates the unknown transformation between the estimated states $\hat{\eta}_1(t)$, $\hat{\eta}_2(\theta, t)$ and the corresponding estimates of the states $\boldsymbol{x}(z,t)$, $\xi(t)$. Recently, an approximation-based approach was suggested, circumventing[5] the explicit transformation and allowing for the design of a flatness-based output feedback controller. Such an approximation of a state feedback, derived for hyperbolic and parabolic systems, respectively, can be found in [WRE17] and of an observer for a parabolic system in [RW18]. The design of an approximation-based output feedback controller for

[4]The negative estimated pressure in Fig. 5.6 is irrelevant for the validation of the observer in a simulation. It can be attributed to the initialization of the observer.

[5]Thereby, the transformation (5.23) from $\boldsymbol{x}(z,t)$, $\xi(t)$ to $\bar{y}(\theta, t)$ becomes unnecessary, too.

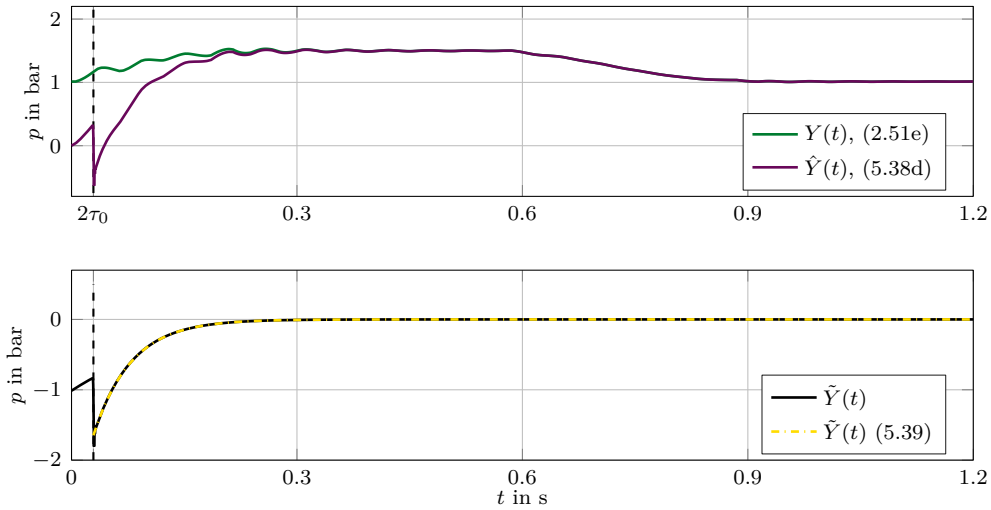

Figure 5.6: Validation of the observer (5.38) with a measurement obtained from the simulation of the linear model (2.51): Pressure $Y(t)$ and estimated pressure $\hat{Y}(t)$ as well as corresponding observation error $\tilde{Y}(t)$, resulting from the simulation and calculated based on the analytical solution (5.39), respectively

hyperbolic systems is currently being developed in cooperation with the author of this thesis and implemented at the test bench.

Remark 5.6. It would be possible to validate the flatness-based state feedback at the test bench by making use of the backstepping-based state observer in Sec. 4.4. In simulations, the resulting controller performs similar to the backstepping-based output feedback controller in Sec. 4.7. Since such a result is expected in experiments, too, this approach is not further investigated. △

5.4 Chapter Highlights

In this chapter, a state feedback and observer were designed based on a parametrization of the quantities of the linear model. The stability of the closed-loop system and of the observer error dynamics were analyzed and the performance of the designs investigated in simulations.

For the first time, the flatness-based state feedback and observer design was applied to a non-academic example. Caused by the dissipation in the linear model of the test bench, as mentioned before, the transformation required to derive the output feedback controller is unknown. However, based on the approximation approach in [WRE17; RW18], a method to circumvent this transformation is currently being developed.

In connection with this chapter, the conference paper [GK18] was published. The supervised student theses [Zof17; Fri18] have contributed to the development of the chapter's results.

Chapter 6

Output Feedback Controller Design Using Early-Lumping

Based on backstepping and flatness, the previous chapters presented novel late-lumping controllers for pneumatic systems involving long tubes. In contrast to that, state-of-the-art controller designs most frequently make use of the early-lumping approach. By this method, in order to derive a control law for a system description involving PDEs, the infinite-dimensional model is approximated by a finite-dimensional one, prior to the controller design, e.g., [CM09]. For the approximation, among others, finite difference, element or volume methods as well as modal or spectral decomposition techniques are employed. Since the resulting models comprise ODEs only, controller designs well-known for lumped-parameter systems can be used. Furthermore, for complex distributed-parameter systems described by, e.g., nonlinear PDEs, there are currently only very few results for a late-lumping controller design, e.g., [Meu13]. In contrast to that, the early-lumping approach might allow for the derivation of a stabilizing control law based on nonlinear ODEs, arising from the approximation of the system dynamics.

Still, the early-lumping approach might have several drawbacks: For example, the appropriate choice of the approximation order n, i.e. the order of the resulting finite-dimensional model, has to be chosen carefully. Choosing a high order for the approximation can lead to problems inherent to the controller design for high-dimensional systems and/or numerical issues, e.g., [Meu13]. On the other hand, controllers designed based on a low-order and, hence, less accurate approximation may result[1] in an unsatisfying performance or even an unstable closed-loop system. This degradation of the performance results from the effects caused by the neglect of dynamics in the early-lumping controller design, the so-called spillover, e.g., [Bal78]. In addition, while one approximation method might work well for a specific class of PDEs, it is not necessarily suited for other classes: For example, according to [CD98], modal decomposition techniques are useful for parabolic PDEs but may be inadequate for hyperbolic systems.

In the context of pneumatic systems involving long tubes, there exists a variety of methods to approximate the infinite-dimensional tube dynamics, e.g., [WT88; Sou+05], and the development of such approaches is still an ongoing research topic, e.g., [Kam17]. In the following, finite-dimensional system descriptions of the test bench are obtained by

[1] Naturally, the approximation order of an infinite-dimensional control law, e.g., (4.77), required for its implementation, also needs to be sufficiently large.

making use of two selected methods, presented in [KS13] and [RNM15], respectively. These relatively recent methods are chosen for two reasons: First, they are specifically developed for pneumatic systems involving long tubes, which are similar to the test bench set-up in Fig. 1.3. Second, state-of-the-art controller designs in this context, discussed in the following, are often based on these approaches.

In [KS13], a tube model similar to the semilinear model (2.35) is considered. Based on [KS11], a nonlinear lumped-parameter model is derived by applying the finite volume method (FVM) to the distributed-parameter model. Thereby, the dynamics of the tube is described by ODEs. The resulting finite-dimensional model with varying approximation order n is validated by comparing simulation data with measurement data from a test bench.

The second approximation approach utilized in this chapter follows [RNM15]. Therein, low-order models are derived by applying modal approximation (MA) techniques to an infinite-dimensional system description, similar to the linear model (2.51). One of the resulting models with $n = 3$ is augmented by a nonlinear friction term, accounting for turbulent friction effects. Simulation data of the finite-dimensional models is compared with each other and to measurement data. It is concluded that the augmented model with $n = 3$ properly describes the dynamics of the considered pneumatic system.

Early-lumping controller designs based on a model derived by the FVM in [KS13] can be found in [TU17] and [TU18]. In both contributions, the set-up mainly consists of a valve, a double-acting pneumatic cylinder, and two long tubes, which are described by the nonlinear finite-dimensional model in [KS13]. By making use of the resulting system description, in [TU17], a cascaded PI controller is designed. To predict the pressures in the cylinder chambers as well as the corresponding mass flow rates, a model with $n = 4$ is utilized. Based on these results, [TU18] designs a control law by applying a multiple sliding surface control method, where the approximated nonlinear dynamics of the tubes are explicitly taken into account. In both references [TU17; TU18], the controllers are validated in experiments.

In addition to the MA, [RNM15] presents a linear controller design by making use of this approximation approach in order to regulate the tank pressure. For that, a feedforward controller is derived, taking into account the approximated tube dynamics explicitly, and combined with a P controller. The linear control law is validated in simulations. These results are extended in [RNM16]. Therein, based on a finite-dimensional model with $n = 3$, an output feedback tracking controller is designed using pole placement. The excellent tracking performance of the controller is demonstrated in experiments.

A further early-lumping controller design based on a model derived by the MA in [RNM15] is presented in [AF16]. The considered pneumatic system consists of two valves, connected to a tank, which is in turn connected to a second tank via a long tube. By making use of the MA, the tube dynamics are approximated by ODEs. Thereby, a third-order model, describing the pneumatic system, results. The proposed explicit model predictive controller, derived from this system description, allows to track a desired reference pressure in the second tank. The very good performance of the controller is validated in simulations.

The tube dynamics of the pneumatic system in [Fal17] (in German) is approximated by the method in [RNM15], too. Based on the resulting model with $n = 3$, an output feedback tracking controller is designed by pole placement. The performance of the

controller is compared to other designs by making use of simulation and experimental data.

In this chapter, two finite-dimensional output feedback tracking controllers are derived by early-lumping. Thereby, the late-lumping approaches in the previous chapters can be related to the aforementioned state-of-the-art controller designs. For that, the linear model (2.51) of the test bench is approximated by the approaches in [KS13] and [RNM15]. Based on the resulting finite-dimensional models, the controllers are designed. The latter are validated in simulations and experiments.

6.1 Two Approximations of the Linear Model

In the following, the FVM and the MA in [KS13] and [RNM15], respectively, are slightly modified and applied to the linear model (2.51) of the test bench. The resulting finite-dimensional models are written in the state-space representation

$$\frac{\mathrm{d}}{\mathrm{d}t}\boldsymbol{X}(t) = \boldsymbol{A}\boldsymbol{X}(t) + \boldsymbol{b}U(t) \tag{6.1a}$$

$$y(t) = (\boldsymbol{c}^y)^T\boldsymbol{X}(t) + d^yU(t), \tag{6.1b}$$

where $\boldsymbol{X}(t) \in \mathbb{R}^n$ denotes the lumped state and $\boldsymbol{A} \in \mathbb{R}^{n\times n}$, $\boldsymbol{b} \in \mathbb{R}^n$, $(\boldsymbol{c}^y)^T \in \mathbb{R}^{1\times n}$ as well as $d^y \in \mathbb{R}$ hold. While the input $U(t)$ is defined in (2.44), the output $y(t) \in \mathbb{R}$ depends on the context and is specified subsequently. The finite-dimensional models, resulting from the approximations, are compared with each other and with the linear model (2.51) in the frequency and time domain, whereby the influence of the approximation order n is investigated.

6.1.1 Finite Volume Method

In contrast to finite difference methods, the FVM is based on the integral formulation of the system dynamics. Hence, a discretization of the spatial domain in terms of a specified grid results in finite volumes. By averaging the distributed quantities over each volume, the dynamics of the respective volume is approximated by ODEs, e.g., [LeV02].

The tube dynamics of the linear model (2.51) is stated in an integral formulation by integrating (2.51a) over space. Subsequently, the spatial coordinate is divided into $\mathbb{N} \ni m \geq 2$ finite segments. Since a staggered grid can be advantageous for the numerical simulation of fluid flows, the segments are separately defined for $x_1(z,t)$ and $x_2(z,t)$, e.g., [Pat80]. From that, $2m$ volumes are obtained. These are centered at the positions z_i^j, where $i = 1,2$ and $j = 1,\ldots,m$. By choosing $z_1^j = j\Delta z$ and $z_2^j = (j-1/2)\Delta z$, where the constant step size $\Delta z = 1/(m+1/2)$ defines the width of each volume, the approximation scheme depicted in Fig. 6.1 results. Thereby, the ODEs

$$\frac{\mathrm{d}}{\mathrm{d}t}\bar{X}_1^j(t) = \frac{1}{L}\frac{x_2(z_2^{j+1},t) - x_2(z_2^j,t)}{\Delta z}$$

$$\frac{\mathrm{d}}{\mathrm{d}t}\bar{X}_2^j(t) = \frac{a_{\mathrm{iso}}^2}{L}\frac{x_1(z_1^j,t) - x_1(z_1^{j-1},t)}{\Delta z} - k_{\mathrm{fric}}\frac{32\mu_0}{D^2}\frac{1}{\rho_0}\bar{X}_2^j(t)$$

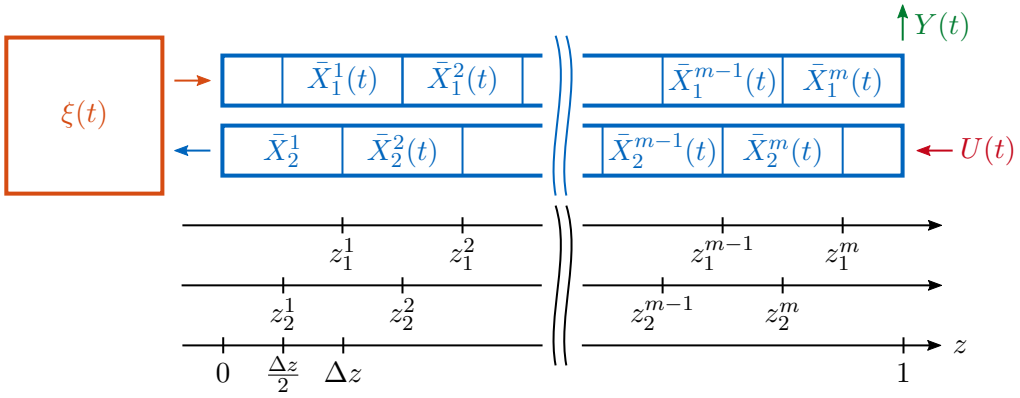

Figure 6.1: Scheme of the FVM

are obtained from the integral formulation of (2.51a), where

$$\bar{X}_1^j(t) = \frac{1}{\Delta z}\int_{z_2^j}^{z_2^{j+1}} x_1(z,t)\,\mathrm{d}z, \quad \bar{X}_2^j(t) = \frac{1}{\Delta z}\int_{z_1^{j-1}}^{z_1^j} x_2(z,t)\,\mathrm{d}z$$

defines the average of each quantity in the corresponding volume. Next, the approximation

$$\bar{X}_i^j(t) \approx x_i(z_i^j, t) \tag{6.2}$$

is introduced. Furthermore, the boundary values $x_2(0,t)$ and $x_1(1,t)$ are defined by means of the first-order extrapolations[2]

$$\frac{3}{2}\bar{X}_2^1(t) - \frac{1}{2}\bar{X}_2^2(t) \approx x_2(0,t), \quad \frac{3}{2}\bar{X}_1^m(t) - \frac{1}{2}\bar{X}_1^{m-1}(t) \approx x_1(1,t). \tag{6.3}$$

From that, the lumped-parameter system

$$\frac{\mathrm{d}}{\mathrm{d}t}\bar{X}_1^j(t) = \frac{1}{L}\frac{\bar{X}_2^{j+1}(t) - \bar{X}_2^j(t)}{\Delta z}, \qquad \text{for } j = 1,\dots,m-1 \tag{6.4a}$$

$$\frac{\mathrm{d}}{\mathrm{d}t}\bar{X}_2^j(t) = \frac{a_{\mathrm{iso}}^2}{L}\frac{\bar{X}_1^j(t) - \bar{X}_1^{j-1}(t)}{\Delta z} - k_{\mathrm{fric}}\frac{32\mu_0}{D^2}\frac{1}{\rho_0}\bar{X}_2^j(t), \quad \text{for } j = 2,\dots,m \tag{6.4b}$$

$$\frac{\mathrm{d}}{\mathrm{d}t}\bar{X}_2^1(t) = \frac{a_{\mathrm{iso}}^2}{L}\frac{\bar{X}_1^1(t) - \xi(t)}{\Delta z} - k_{\mathrm{fric}}\frac{32\mu_0}{D^2}\frac{1}{\rho_0}\bar{X}_2^1(t) \tag{6.4c}$$

$$\frac{\mathrm{d}}{\mathrm{d}t}\bar{X}_1^m(t) = \frac{1}{L}\frac{\frac{1}{A}U(t) - \bar{X}_2^m(t)}{\Delta z} \tag{6.4d}$$

$$\frac{\mathrm{d}}{\mathrm{d}t}\xi(t) = \frac{3}{2}\frac{A}{V_{\mathrm{vol}}}\bar{X}_2^1(t) - \frac{1}{2}\frac{A}{V_{\mathrm{vol}}}\bar{X}_2^2(t) \tag{6.4e}$$

$$\bar{y}(t) = \frac{3}{2}\bar{X}_1^m(t) - \frac{1}{2}\bar{X}_1^{m-1}(t) \tag{6.4f}$$

is derived, approximating the linear model (2.51). The scaled measurement $\bar{y}(t) \approx x_1(1,t) = Y(t)/(R_{\mathrm{s}}T_0)$ in (6.4f) follows from (2.51e) and (6.3).

By introducing the state

$$\bar{\boldsymbol{X}}(t) = \begin{bmatrix}\xi(t) & \bar{X}_2^1(t) & \bar{X}_1^1(t) & \bar{X}_2^2(t) & \bar{X}_1^2(t) & \cdots & \bar{X}_2^m(t) & \bar{X}_1^m(t)\end{bmatrix}^T \in \mathbb{R}^n \tag{6.5}$$

[2] Although [KS13] utilizes zero-order instead of first-order extrapolations, the latter are chosen as they render the model (6.4) a more accurate approximation, which can be verified by simulations.

with $n = 2m + 1$, the system (6.4) in the form (6.1) with $d^y = 0$ is obtained:

$$\frac{\mathrm{d}}{\mathrm{d}t}\bar{\boldsymbol{X}}(t) = \boldsymbol{A}_\mathrm{F}\bar{\boldsymbol{X}}(t) + \boldsymbol{b}_\mathrm{F}U(t) \tag{6.6a}$$

$$y(t) = (\boldsymbol{c}_\mathrm{F}^y)^T\bar{\boldsymbol{X}}(t). \tag{6.6b}$$

Therein, the matrices $\boldsymbol{A}_\mathrm{F}$ and $\boldsymbol{b}_\mathrm{F}$ read

$$\boldsymbol{A}_\mathrm{F} = \begin{bmatrix} 0 & \frac{3}{2}k_4 & 0 & -\frac{1}{2}k_4 & 0 & \cdots & \cdots & 0 \\ -\kappa_2 & -k_3 & \kappa_2 & 0 & 0 & \ddots & \ddots & \vdots \\ 0 & -\kappa_1 & 0 & \kappa_1 & \ddots & \ddots & \ddots & \vdots \\ \vdots & \ddots & -\kappa_2 & -k_3 & \kappa_2 & \ddots & \ddots & \vdots \\ \vdots & \ddots & \ddots & -\kappa_1 & 0 & \kappa_1 & \ddots & \vdots \\ \vdots & \ddots & \ddots & \ddots & \ddots & \ddots & \ddots & 0 \\ \vdots & \ddots & \ddots & \ddots & \ddots & -\kappa_2 & -k_3 & \kappa_2 \\ 0 & \cdots & \cdots & \cdots & \cdots & 0 & -\kappa_1 & 0 \end{bmatrix} \in \mathbb{R}^{n\times n}, \quad \boldsymbol{b}_\mathrm{F} = \begin{bmatrix} 0 \\ \vdots \\ 0 \\ \frac{\kappa_1}{A} \end{bmatrix} \in \mathbb{R}^n,$$

where the abbreviations

$$\kappa_1 = \frac{1}{L\Delta z}, \quad \kappa_2 = \frac{a_\mathrm{iso}^2}{L\Delta z}, \quad k_3 = k_\mathrm{fric}\frac{32\mu_0}{D^2}\frac{1}{\rho_0}, \quad k_4 = \frac{A}{V_\mathrm{vol}} \tag{6.7}$$

are introduced for brevity. The matrix $(\boldsymbol{c}_\mathrm{F}^y)^T$ depends on the choice of the output $y(t)$. For the measurement $\bar{y}(t)$, defined in (6.4f), the output equation (6.6b) reads

$$\bar{y}(t) = (\boldsymbol{c}_\mathrm{F}^{\bar{y}})^T\bar{\boldsymbol{X}}(t) \quad \text{with} \quad (\boldsymbol{c}_\mathrm{F}^{\bar{y}})^T = \begin{bmatrix} 0 & \cdots & 0 & -\frac{1}{2} & 0 & \frac{3}{2} \end{bmatrix} \in \mathbb{R}^{1\times n}. \tag{6.8}$$

Remark 6.1. Obviously, (6.4) is undefined for $m = 1$. Still, by making use of the proposed approximation scheme, the matrices

$$\boldsymbol{A}_\mathrm{F} = \begin{bmatrix} 0 & \frac{3}{2}k_4 & 0 \\ -\kappa_2 & -k_3 & \kappa_2 \\ 0 & -\kappa_1 & 0 \end{bmatrix}, \quad \boldsymbol{b}_\mathrm{F} = \begin{bmatrix} -\frac{1}{2}\frac{k_4}{A} \\ 0 \\ \frac{\kappa_1}{A} \end{bmatrix}, \quad (\boldsymbol{c}_\mathrm{F}^{\bar{y}})^T = \begin{bmatrix} -\frac{1}{2} & 0 & \frac{3}{2} \end{bmatrix}$$

are obtained, resulting in a lumped-parameter model of the order $n = 3$. △

6.1.2 Modal Approximation

According to [CM09], MA techniques in the context of linear single-input-single-output distributed-parameter systems in one spatial dimension can be described as follows: First, the infinite-dimensional model is mapped into the operational domain, e.g., by applying the Laplace transform with the complex variable s. The solution of the resulting ODEs w.r.t. z is obtained in a straightforward manner. From that, the transfer function $G_u^y(s) = \hat{y}(s)/\hat{u}(s)$ is derived, where $\hat{u}(s)$ is the input and $\hat{y}(s)$ the output. Often, the irrational functions in $G_u^y(s)$, arising from the spatial integration, can be expressed in terms of infinite sums or products. These expansions are chosen and subsequently truncated such that the finite-dimensional transfer function $\tilde{G}_u^y(s)$, approximating $G_u^y(s)$, reproduces the lower-order poles of $G_u^y(s)$ exactly.

In the following, a state-space representation (6.1) is derived by means of the MA. First, the state $\hat{\boldsymbol{x}}(z,s)$ of the linear model (2.51) in the operational domain is parametrized in terms of the scaled input $u_\flat(t) = U(t)/A$. By making use of the results in Sec. 5.1.1, the general solution (5.3) in the operational domain is evaluated in terms of the transformed boundary conditions (2.51c) as well as (2.51d), i.e. $s\hat{x}_1(0,s) = k_4\hat{x}_2(0,s)$, $\hat{x}_2(1,s) = \hat{u}_\flat(s)$, resulting in the specific solution

$$\hat{x}_1(z,s) = \frac{k_1\left[(s^2+k_3 s)\frac{\sinh\left(\omega(s)z\right)}{\omega(s)} + k_2 k_4\cosh\left(\omega(s)z\right)\right]}{k_2 s\left[k_4\frac{\sinh\left(\omega(s)\right)}{\omega(s)} + k_1\cosh\left(\omega(s)\right)\right]}\hat{u}_\flat(s) \tag{6.9a}$$

$$\hat{x}_2(z,s) = \frac{k_2 s\left[k_4\frac{\sinh\left(\omega(s)z\right)}{\omega(s)} + k_1\cosh\left(\omega(s)z\right)\right]}{k_2 s\left[k_4\frac{\sinh\left(\omega(s)\right)}{\omega(s)} + k_1\cosh\left(\omega(s)\right)\right]}\hat{u}_\flat(s), \tag{6.9b}$$

where $\omega(s)$ is defined in (5.4) and the coefficients k_j, $j = 1,\dots,4$, in (5.2) and (5.5).

Remark 6.2. Usually, in the context of long tubes described by 2×2 linear hyperbolic systems, the so-called two-port (or four-terminal) network, also known for electrical transmission lines, e.g., [GK68], serves as starting point for the MA, e.g., [GL72]. It maps $\hat{\boldsymbol{x}}(1,s)$ to $\hat{\boldsymbol{x}}(0,s)$ and is independent of the spatial coordinate z. However, this thesis makes use of (6.9) as its dependency on z allows to derive a relation between the distributed state and the lumped state of the approximation, presented in the following. △

There exist multiple methods to approximate the numerators and denominators of (6.9) by suitable rational expression. Two of them are presented in [RNM15], one using truncated infinite products and the other truncated Taylor series. A truncated infinite product of the numerator and denominator preserves the zeros and poles up to the approximation order, e.g., [OG64]. In contrast to that, the truncated Taylor series requires additional terms or coefficients to achieve a similar result, e.g., [Goo70; KS11]. To approximate the denominators of (6.9), this thesis makes use of

$$\begin{aligned} k_4\frac{\sinh\left(\omega(s)z\right)}{\omega(s)} + k_1\cosh\left(\omega(s)z\right) &= (k_4 z + k_1)\prod_{k=1}^{\infty}\left(1+\frac{\left(\omega(s)z\right)^2}{p_k^2}\right) \\ &\approx (k_4 z + k_1)\prod_{k=1}^{m}\left(1+\frac{\left(\omega(s)z\right)^2}{p_k^2}\right), \end{aligned} \tag{6.10}$$

preserving the low-order poles [Goo70], where $p_k > 0$ are the positive real solutions of $\tan(p_k) = -p_k k_1/k_4$. While the numerator of (6.9b) is essentially approximated by (6.10), too, the irrational terms in the numerator of (6.9a) are replaced by[3]

$$\frac{\sinh\left(\omega(s)z\right)}{\omega(s)} = z\prod_{k=1}^{\infty}\left(1+\frac{\left(\omega(s)z\right)^2}{k^2\pi^2}\right) \approx z\prod_{k=1}^{m-1}\left(1+\frac{\left(\omega(s)z\right)^2}{k^2\pi^2}\right) \tag{6.11a}$$

$$\cosh\left(\omega(s)z\right) = \prod_{k=1}^{\infty}\left(1+\frac{4\left(\omega(s)z\right)^2}{(2k-1)^2\pi^2}\right) \approx \prod_{k=1}^{m}\left(1+\frac{4\left(\omega(s)z\right)^2}{(2k-1)^2\pi^2}\right), \tag{6.11b}$$

[3]For $m = 1$, the approximation (6.11a) reads $\sinh\left(\omega(s)z\right)/\omega(s) \approx z$.

e.g., [Goo70], as the author of this thesis is not aware of any infinite product expansion for such an expression. Thereby, the approximation

$$\hat{x}_1(z,s) \approx \underbrace{\frac{k_1\left[(s^2+k_3 s)z\prod_{k=1}^{m-1}\left(1+\frac{(\omega(s)z)^2}{k^2\pi^2}\right)+k_2k_4\prod_{k=1}^{m}\left(1+\frac{4\,(\omega(s)z)^2}{(2k-1)^2\pi^2}\right)\right]}{k_2 s(k_4+k_1)\prod_{k=1}^{m}\left(1+\frac{\omega^2(s)}{p_k^2}\right)}}_{=\tilde{G}_1(z,s)}\hat{u}_\flat(s) \tag{6.12a}$$

$$\hat{x}_2(z,s) \approx \underbrace{\frac{k_2 s\left[(k_4 z+k_1)\prod_{k=1}^{m}\left(1+\frac{(\omega(s)z)^2}{p_k^2}\right)\right]}{k_2 s(k_4+k_1)\prod_{k=1}^{m}\left(1+\frac{\omega^2(s)}{p_k^2}\right)}}_{=\tilde{G}_2(z,s)}\hat{u}_\flat(s). \tag{6.12b}$$

of (6.9) results, where the numerators and denominators are polynomial in s since $\omega^2(s)$ is a rational expression.

While the poles of (6.12) and the zeros of (6.9b) are preserved in (6.12), the preservation of the zeros of (6.9a) would require additional terms in the numerator of (6.12a). For example, such a correction is used in [RNM15], where the approximation of a two-port network follows from (6.11).

Finally, by making use of the approximation

$$\hat{y}(s) = \tilde{G}_i(\tilde{z},s)\hat{u}_\flat(s) \approx \hat{x}_i(\tilde{z},s), \tag{6.13}$$

where $i = 1,2$ and $\tilde{z} \in [0,1]$ is arbitrary but fixed, a proper[4] transfer function of the form

$$\frac{\hat{y}(s)}{\hat{u}_\flat(s)} = \frac{b_n s^n + b_{n-1}s^{n-1} + \cdots + b_1 s + b_0}{s^n + a_{n-1}s^{n-1} + \cdots + a_1 s + a_0} = \tilde{G}_u^y(s) \tag{6.14}$$

for a specified output $\hat{y}(s)$ results. Therein, $n = 2m+1$ denotes the system order. From that, a state-space representation

$$\frac{\mathrm{d}}{\mathrm{d}t}\tilde{\boldsymbol{X}}(t) = \boldsymbol{A}_\mathrm{M}\tilde{\boldsymbol{X}}(t) + \boldsymbol{b}_\mathrm{M}U(t) \tag{6.15a}$$

$$y(t) = (\boldsymbol{c}_\mathrm{M}^y)^T\tilde{\boldsymbol{X}}(t) + d_\mathrm{M}^y U(t) \tag{6.15b}$$

with the state

$$\tilde{\boldsymbol{X}}(t) = \begin{bmatrix}\tilde{X}_1(t) & \cdots & \tilde{X}_n(t)\end{bmatrix}^T \in \mathbb{R}^n, \tag{6.16}$$

[4] For $\hat{y}(s) = \tilde{G}_1(\tilde{z},s)\hat{u}_\flat(s)$, the resulting transfer function is strictly proper. Thus, $d_\mathrm{M}^{x_1} = 0$ holds in (6.17d).

where $n \geq 3$, in controller form is obtained, e.g. [Oga10]. Thus,

$$\boldsymbol{A}_{\mathrm{M}} = \begin{bmatrix} 0 & 1 & 0 & \cdots & 0 \\ \vdots & 0 & \ddots & \ddots & \vdots \\ \vdots & \vdots & \ddots & \ddots & 0 \\ 0 & 0 & \cdots & 0 & 1 \\ -a_0 & -a_1 & \cdots & -a_{n-2} & -a_{n-1} \end{bmatrix} \in \mathbb{R}^{n \times n} \tag{6.17a}$$

$$\boldsymbol{b}_{\mathrm{M}} = \begin{bmatrix} 0 & \cdots & 0 & \frac{1}{A} \end{bmatrix}^T \in \mathbb{R}^n \tag{6.17b}$$

$$(\boldsymbol{c}_{\mathrm{M}}^y)^T = \begin{bmatrix} b_0 - a_0 b_n & b_1 - a_1 b_n & \cdots & b_{n-1} - a_{n-1} b_n \end{bmatrix} \in \mathbb{R}^{1 \times n} \tag{6.17c}$$

$$d_{\mathrm{M}}^y = \frac{1}{A} b_n \tag{6.17d}$$

holds, where $u_\flat(t) = U(t)/A$ is used. Naturally, the output vector $(\boldsymbol{c}_{\mathrm{M}}^y)^T$ and the feedthrough d_{M}^y in (6.15b) result from the choice of the output $y(t)$ in (6.13). In contrast to that, the state $\tilde{\boldsymbol{X}}(t)$ as well as the matrices $\boldsymbol{A}_{\mathrm{M}}$ and $\boldsymbol{b}_{\mathrm{M}}$ are independent of this choice. For $\tilde{y}(t) \approx x_1(1,t) = Y(t)/(R_{\mathrm{s}} T_0)$, the scaled measurement

$$\tilde{y}(t) = (\boldsymbol{c}_{\mathrm{M}}^{\tilde{y}})^T \tilde{\boldsymbol{X}}(t) \tag{6.18}$$

is expressed in terms of $\tilde{\boldsymbol{X}}(t)$, where $Y(t)$ is defined in (2.51e).

Remark 6.3. Numerical studies indicate that the numerator and the denominator of $\tilde{G}_u^y(s)$ in (6.14) are coprime for any $\tilde{z}$ and m. Therefore, in the following, (6.15) is assumed to be a minimal realization. △

The approximation (6.13) can be utilized to derive an equation, relating the states $\boldsymbol{x}(z,t)$, $\xi(t)$ of the linear model (2.51) and the input $U(t)$ to the state $\tilde{\boldsymbol{X}}(t)$ of the finite-dimensional model (6.15). By evaluating (6.13) for, e.g., $i = 1$ and $\tilde{z} = z_1^j = 2j\Delta z$, $j = 0, \ldots, m$, as well as $i = 2$ and $\tilde{z} = z_2^j = (2j-1)\Delta z$, $j = 1, \ldots, m$, where $\Delta z = 1/(2m)$, the n linear equations

$$\boldsymbol{X}_{\mathrm{M}}(t) = \boldsymbol{C}_{\mathrm{M}} \tilde{\boldsymbol{X}}(t) + \boldsymbol{d}_{\mathrm{M}} U(t) \tag{6.19}$$

with

$$\boldsymbol{X}_{\mathrm{M}}(t) = \begin{bmatrix} x_1^0(t) & x_2^1(t) & x_1^1(t) & x_2^2(t) & x_1^2(t) & \cdots & x_2^m(t) & x_1^m(t) \end{bmatrix}^T$$

$$\boldsymbol{C}_{\mathrm{M}} = \begin{bmatrix} \boldsymbol{c}_{\mathrm{M}}^{x_1^0} & \boldsymbol{c}_{\mathrm{M}}^{x_2^1} & \boldsymbol{c}_{\mathrm{M}}^{x_1^1} & \boldsymbol{c}_{\mathrm{M}}^{x_2^2} & \boldsymbol{c}_{\mathrm{M}}^{x_1^2} & \cdots & \boldsymbol{c}_{\mathrm{M}}^{x_2^m} & \boldsymbol{c}_{\mathrm{M}}^{x_1^m} \end{bmatrix}^T$$

$$\boldsymbol{d}_{\mathrm{M}} = \begin{bmatrix} 0 & d_{\mathrm{M}}^{x_2^1} & 0 & d_{\mathrm{M}}^{x_2^2} & 0 & \cdots & d_{\mathrm{M}}^{x_2^m} & 0 \end{bmatrix}^T$$

follow from (6.15b), where $x_i^j(t) \approx x_i(z_i^j, t)$ is utilized. The state $\tilde{\boldsymbol{X}}(t)$ in (6.19) can be obtained from the known quantities $\boldsymbol{x}(z,t)$, $\xi(t)$, and $U(t)$ by solving the problem

$$\arg\min_{\tilde{\boldsymbol{X}}(t)} \left\| \boldsymbol{X}_{\mathrm{M}}(t) - \boldsymbol{C}_{\mathrm{M}} \tilde{\boldsymbol{X}}(t) - \boldsymbol{d}_{\mathrm{M}} U(t) \right\|_{\mathbb{R}^n}.$$

Thereby, for example, the lumped initial condition $\tilde{\boldsymbol{X}}(0)$ can be computed from $\boldsymbol{x}(z,0)$, $\xi(0)$.

Remark 6.4. In [RNM15], the proposed model with the approximation order $n = 3$ has the physically interpretable state $\tilde{\boldsymbol{X}}(t) \approx [\xi(t), x_2(1,t), x_1(1,t)]^T$, rendering (6.19) superfluous. In addition, the physical interpretability of the state allows to include a nonlinear friction term in the resulting model easily. However, a generalization to models with $n > 3$ does not seem trivial. △

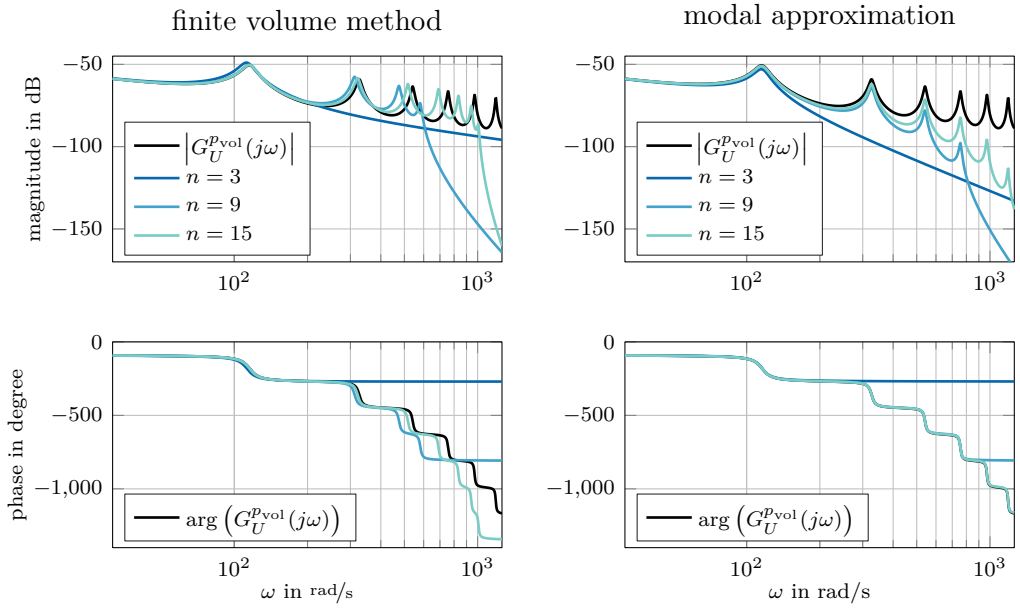

Figure 6.2: Bode plots for a tube with $L = 5\,\mathrm{m}$ as well as $D = 5.7\,\mathrm{mm}$

6.1.3 Comparison of the Lumped-Parameter Models

Next, the two lumped-parameter models (6.6) and (6.15), derived by the FVM and by the MA[5], respectively, are compared to the infinite-dimensional linear model (2.51) in terms of their input-to-output behavior. The input is the mass flow rate $U(t)$ through the valve and the output is the tank pressure $p_{\mathrm{vol}}(t)$. For that, first, the frequency responses and subsequently the time responses are investigated. The friction amplification factor is set to $k_{\mathrm{fric}} = 1$ for all three models.

Fig. 6.2 depicts the Bode plots of $G_U^{p_{\mathrm{vol}}}(s)$, $\bar{G}_U^{p_{\mathrm{vol}}}(s)$, and $\tilde{G}_U^{p_{\mathrm{vol}}}(s)$, where the standard test bench configuration in Tab. 3.1 is utilized. The transfer function $G_U^{p_{\mathrm{vol}}}(s)$ of the linear model follows from (6.9a) evaluated at $z = 0$, the transfer function $\bar{G}_U^{p_{\mathrm{vol}}}(s)$ of the FVM is obtained by

$$\bar{G}_U^{p_{\mathrm{vol}}}(s) = (\boldsymbol{c}_{\mathrm{F}}^{p_{\mathrm{vol}}})^T \, (s\boldsymbol{I} - \boldsymbol{A}_{\mathrm{F}})^{-1} \, \boldsymbol{b}_{\mathrm{F}},$$

and the transfer function $\tilde{G}_U^{p_{\mathrm{vol}}}(s)$ of the MA results from (6.12a) evaluated at $z = 0$. For both approximation approaches, the frequency responses for the orders $n = \{3, 9, 15\}$ are shown. As depicted in the left-hand Bode plot of Fig. 6.2, the transfer function $\bar{G}_U^{p_{\mathrm{vol}}}(s)$ does not preserve the first n poles of $G_U^{p_{\mathrm{vol}}}(s)$. Still, $|\bar{G}_U^{p_{\mathrm{vol}}}(j\omega)|$ and $|G_U^{p_{\mathrm{vol}}}(j\omega)|$ are of similar order up to the cutoff frequency, which depends on n. In the right Bode plot of Fig. 6.2, it can be seen that the poles of $\tilde{G}_U^{p_{\mathrm{vol}}}(s)$ match the first n poles of $G_U^{p_{\mathrm{vol}}}(s)$, resulting in an almost perfect fit of the phase up to the cutoff frequency. However, the magnitude $|\tilde{G}_U^{p_{\mathrm{vol}}}(j\omega)|$ decreases faster than the magnitude $|G_U^{p_{\mathrm{vol}}}(j\omega)|$. For both approaches, the corresponding mismatch is slightly improved by an increased order of approximation.

In order to compare the time responses of the models, a typical but highly dynamical input $U(t)$ is specified, illustrating the differences more clearly. It follows from the

[5]In the following, the abbreviations FVM and MA are used both for the methods themselves and the resulting models.

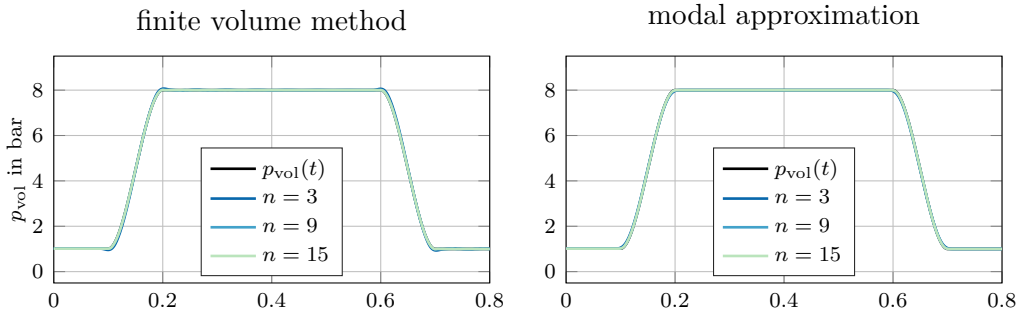

Figure 6.3: Simulation results for a tube with $L = 5\,\mathrm{m}$ as well as $D = 5.7\,\mathrm{mm}$

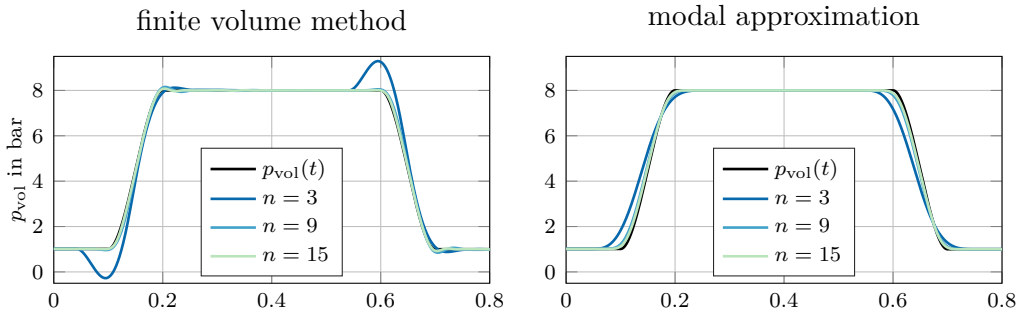

Figure 6.4: Simulation results for a tube with $L = 20\,\mathrm{m}$ as well as $D = 4\,\mathrm{mm}$

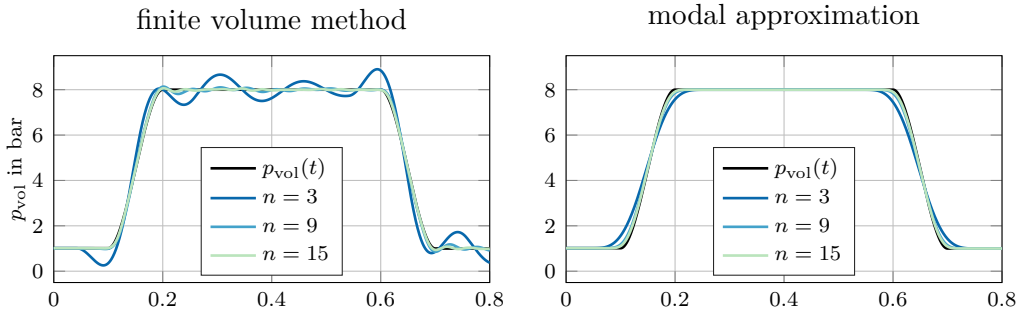

Figure 6.5: Simulation results for a tube with $L = 20\,\mathrm{m}$ as well as $D = 8\,\mathrm{mm}$

flatness-based parametrization (5.15b) at $z = 1$ by making use of the trajectory (3.11). The input $U(t)$ is fed to the linear model (2.51) as well as to the lumped-parameter models (6.6) and (6.15) with $n = \{3, 9, 15\}$. Thereby, the systems are charged from p_0 to approximately 8 bar in 0.1 s and back to p_0 at the same rate.

The tank pressure trajectories $p_{\mathrm{vol}}(t)$, resulting from the simulation of all models, are depicted in Figs. 6.3–6.5. The black line corresponds to the linear model and the blue lines to the approximated ones. As it can be seen in Fig. 6.3, both lumped-parameter models with $n = 3$ match the tank pressure of the linear model already almost perfectly for a tube with a length of $L = 5\,\mathrm{m}$ and a diameter of $D = 5.7\,\mathrm{mm}$. This observation is confirmed by quantifying the slight deviations in terms of the error measures in (2.42) and (2.43), where the tank pressure of the linear model serves as reference. The resulting error measures are stated in Tab. 6.1, where $L^1_{\mathrm{r,err,F}}$, $L^\infty_{\mathrm{err,F}}$ refers to the FVM and $L^1_{\mathrm{r,err,M}}$, $L^\infty_{\mathrm{r,err,M}}$ to the MA.

Table 6.1: Errors between the tank pressure of the linear model and of the approximated models for a tube with $L = 5\,\mathrm{m}$ as well as $D = 5.7\,\mathrm{mm}$

n	3	9	15
$L^1_{\mathrm{r,err,F}}$	0.886 %	0.123 %	0.050 %
$L^1_{\mathrm{r,err,M}}$	0.457 %	0.123 %	0.071 %
$L^\infty_{\mathrm{err,F}}$	0.122 bar	0.019 bar	0.008 bar
$L^\infty_{\mathrm{r,err,M}}$	0.078 bar	0.022 bar	0.012 bar

Table 6.2: Errors between the tank pressure of the linear model and of the approximated models for a tube with $L = 20\,\mathrm{m}$ as well as $D = 4\,\mathrm{mm}$

n	3	9	15
$L^1_{\mathrm{r,err,F}}$	11.880 %	1.611 %	0.607 %
$L^1_{\mathrm{r,err,M}}$	8.141 %	2.266 %	1.313 %
$L^\infty_{\mathrm{err,F}}$	1.290 bar	0.267 bar	0.110 bar
$L^\infty_{\mathrm{r,err,M}}$	1.259 bar	0.220 bar	0.224 bar

Table 6.3: Errors between the tank pressure of the linear model and of the approximated models for a tube with $L = 20\,\mathrm{m}$ as well as $D = 8\,\mathrm{mm}$

n	3	9	15
$L^1_{\mathrm{r,err,F}}$	14.025 %	2.036 %	0.768 %
$L^1_{\mathrm{r,err,M}}$	6.147 %	1.820 %	1.059 %
$L^\infty_{\mathrm{err,F}}$	0.901 bar	0.188 bar	0.086 bar
$L^\infty_{\mathrm{r,err,M}}$	0.774 bar	0.267 bar	0.163 bar

Fig. 6.4 and Fig. 6.5 display the simulation results for a tube with $L = 20\,\mathrm{m}$ and $D = 4\,\mathrm{mm}$ as well as $D = 8\,\mathrm{mm}$, respectively. The corresponding errors are given in Tab. 6.2 and Tab. 6.3. Interestingly, by comparing these results for the long tube in terms of $L^1_{\mathrm{r,err}}$, it can be seen that the accuracy of the FVM is higher for the smaller diameter of $D = 4\,\mathrm{mm}$ compared to $D = 8\,\mathrm{mm}$, while the opposite is true for the MA.

Summarizing the results in Tabs. 6.1–6.3, the following can be concluded from the simulation scenarios: The MA yields a slightly more accurate approximation of the linear model (2.51) compared to the FVM if an order of $n = 3$ is chosen. However, for larger values of n, the errors of the FVM converge faster to zero, rendering it more accurate for $n = 15$. Among other factors, the required order of approximation depends on the tube length. While $n = 3$ seems adequate for both approaches if a tube with a length of $L = 5\,\mathrm{m}$ is utilized (cf. Fig. 6.3), a tube length of $L = 20\,\mathrm{m}$ might require a higher approximation order (cf. Fig. 6.4 and Fig. 6.5). Naturally, in addition to the approximation order and the tube length, the accuracy of the approximated models depends on, e.g., the specified excitation. Regardless, the FVM may be beneficial for two reasons: First, the elements of the state $\bar{\boldsymbol{X}}(t)$ in (6.5) are a direct approximation of the conserved quantities ρ, ρv, facilitating the physical interpretability of the model. In addition, the approach can be applied directly to the semilinear model (2.35) and, after a straight-

forward extension, even to the isothermal model (2.50). Thereby, a relatively accurate finite-dimensional system description of the test bench could be obtained.

6.2 Output Feedback Tracking Controller

In the following, by making use of the lumped-parameter models (6.6) with (6.8) and (6.15) with (6.18), derived by the FVM and the MA, output feedback tracking controllers are derived, stabilizing the transition between desired pressure levels in the tank. Each controller comprises a flatness-based feedforward controller, a state feedback, and a state observer. While the state feedback is provided by a linear-quadratic regulator, the state observer is designed by pole placement.

6.2.1 Design of the Feedforward Controller

Finite Volume Method For the pair $(\boldsymbol{A}_\mathrm{F}, \boldsymbol{b}_\mathrm{F})$ in (6.6a), derived by the FVM, a flat output is given by

$$y_\mathrm{F}(t) = \frac{1}{k_4}\xi(t) + \frac{1}{2}\frac{1}{\kappa_1}\bar{X}_1^1(t). \tag{6.20}$$

This can be verified by differentiating (6.20) n times w.r.t. t and by making use of (6.6a). From that,

$$\begin{bmatrix} y_\mathrm{F}(t) \\ \dot{y}_\mathrm{F}(t) \\ \vdots \\ y_\mathrm{F}^{(n)}(t) \end{bmatrix} = \boldsymbol{M} \begin{bmatrix} \bar{\boldsymbol{X}}(t) \\ U(t) \end{bmatrix} \quad \text{with} \quad \boldsymbol{M} = \begin{bmatrix} \frac{1}{k_4} & 0 & \frac{1}{2}\frac{1}{\kappa_1} & 0 & \cdots & 0 \\ 0 & 1 & 0 & 0 & \ddots & \vdots \\ -\kappa_2 & -k_3 & \kappa_2 & \ddots & \ddots & 0 \\ * & * & * & m_4 & \ddots & 0 \\ * & * & * & * & \ddots & 0 \\ * & * & * & * & * & m_n \end{bmatrix}$$

is obtained. Therein, the elements m_k, $k = 4, \ldots, n$, are defined by

$$m_{2j} = \kappa_1^{j-2}\kappa_2^{j-1}\left(\kappa_1 + \frac{k_4}{2}\right), \quad m_{2(j+1)} = \kappa_1^{j-2}\kappa_2^{j}\left(\kappa_1 + \frac{k_4}{2}\right)$$

with $j = 2, \ldots, m$. Since

$$\det \boldsymbol{M} = \left(\frac{\kappa_2}{k_4} + \frac{1}{2}\frac{\kappa_2}{\kappa_1}\right)\prod_{k=4}^{n} m_k > 0$$

holds for all physically reasonable parameters in (6.7), the matrix $\boldsymbol{M}$ is invertible. As a result, the parametrization

$$\begin{bmatrix} \bar{\boldsymbol{X}}(t) \\ U(t) \end{bmatrix} = \boldsymbol{M}^{-1} \begin{bmatrix} y_\mathrm{F}(t) \\ \dot{y}_\mathrm{F}(t) \\ \vdots \\ y_\mathrm{F}^{(n)}(t) \end{bmatrix} \tag{6.21}$$

is obtained, and in particular

$$p_{\mathrm{vol}}(t) = R_{\mathrm{s}} T_0 \xi(t) = R_{\mathrm{s}} T_0 \left(\frac{2\kappa_1 k_4}{2\kappa_1 + k_4} y_{\mathrm{F}}(t) - \frac{k_3 k_4}{\kappa_2 (2\kappa_1 + k_4)} \dot{y}_{\mathrm{F}}(t) - \frac{k_4}{k_2 (2\kappa_1 + k_4)} \ddot{y}_{\mathrm{F}}(t) \right). \tag{6.22}$$

By choosing a reference trajectory $y_{\mathrm{F}}^{\mathrm{r}}(t)$ for the flat output, the corresponding reference state $\bar{\boldsymbol{X}}^{\mathrm{r}}(t)$ as well as the feedforward controller $U_{\mathrm{F}}^{\mathrm{r}}(t)$ directly follow from (6.21). Instead of $y_{\mathrm{F}}^{\mathrm{r}}(t)$, it would be referable to specify the desired reference trajectory $p_{\mathrm{vol}}^{\mathrm{r}}(t)$ for the tank pressure. However, p_{vol} is proportional to y_{F} in steady-state only (cf. (6.22)). Thus, while the feedforward controller enables the transition from an initial constant pressure level p_{b} to a desired constant pressure level p_{e}, the transition of $p_{\mathrm{vol}}(t)$ cannot be easily specified.

Modal Approximation Since the state-space representation (6.15), derived by the MA, is in controller form, a flat output of the pair $(\boldsymbol{A}_{\mathrm{M}}, \boldsymbol{b}_{\mathrm{M}})$ is defined by

$$y_{\mathrm{M}}(t) = \tilde{X}_1(t).$$

From that, the parametrization

$$\begin{bmatrix} \tilde{\boldsymbol{X}}(t) \\ U(t) \end{bmatrix} = \begin{bmatrix} y_{\mathrm{M}}(t) \\ \vdots \\ y_{\mathrm{M}}^{(n-1)}(t) \\ A \left(a_0 y_{\mathrm{M}}(t) + \cdots + a_{n-1} y_{\mathrm{M}}^{(n-1)}(t) + y_{\mathrm{M}}^{(n)}(t) \right) \end{bmatrix} \tag{6.23}$$

follows.

By choosing a reference trajectory $y_{\mathrm{M}}^{\mathrm{r}}(t)$ for the flat output, the reference state $\tilde{\boldsymbol{X}}^{\mathrm{r}}(t)$ and the feedforward controller $U_{\mathrm{M}}^{\mathrm{r}}(t)$ follow from (6.23). Evaluating the approximation (6.12a) at $z = 0$ yields $b_j = 0$, $j = 1, \ldots, n$, and

$$b_0 = \frac{k_1 k_4}{(k_4 + k_1) \tau_0^{2m}} \prod_{k=1}^{m} p_k^2$$

in the resulting transfer function (6.14). Therefore, with $\tilde{X}_1(t) = p_{\mathrm{vol}}(t)/(R_{\mathrm{s}} T_0)$, the tank pressure

$$p_{\mathrm{vol}}(t) = b_0 R_{\mathrm{s}} T_0 y_{\mathrm{M}}(t) \tag{6.24}$$

is proportional to the flat output. As a result, in contrast to (6.22), the feedforward controller is directly designed based on a desired reference trajectory $p_{\mathrm{vol}}^{\mathrm{r}}(t)$ for the tank pressure.

Trajectory Planning As a consequence of (6.21) and (6.23), in order for $U^{\mathrm{r}} \in C([0, \infty))$, the reference trajectory y^{r} has to be a $C^n([0, \infty))$ function. Since higher-degree polynomials can lead to numerical problems, the (smooth) Gevrey function

$$\bar{t} \mapsto y^{\mathrm{r}}(\bar{t}) = \begin{cases} y_{\mathrm{b}}, & \bar{t} \leq 0 \\ y_{\mathrm{b}} - \frac{1}{2}(y_{\mathrm{b}} - y_{\mathrm{e}}) \left(1 + \tanh \left(\frac{2(2\bar{t}-1)}{(4\bar{t}(1-\bar{t}))^{\mu}} \right) \right), & 0 < \bar{t} < 1 \\ y_{\mathrm{e}}, & \bar{t} \geq 1 \end{cases} \tag{6.25}$$

with $\mu \geq 1$ is chosen, e.g., [Rud03]. Therein, y_b, y_e, basically corresponding to the initial and desired pressure level in the tank, and $\bar{t}$ are defined in (3.11) and (3.10), respectively.

6.2.2 Design of the State Feedback

Since the parametrizations (6.21) and (6.23) in terms of the corresponding flat output uniquely exists, the systems (6.6) and (6.15) are differentially flat. This implies the controllability[6] of the pairs $(\boldsymbol{A}_\mathrm{F}, \boldsymbol{b}_\mathrm{F})$ as well as $(\boldsymbol{A}_\mathrm{M}, \boldsymbol{b}_\mathrm{M})$ and facilitates the subsequent controller design.

The state feedback[7]

$$U(t) = -\boldsymbol{k}^T \boldsymbol{X}(t), \tag{6.26}$$

where $\boldsymbol{k}^T \in \mathbb{R}^{1\times n}$, is designed in order to minimize the cost function[8]

$$J(U) = \int_0^\infty \left[q p_\mathrm{vol}^2(t) + U^2(t) \right] \mathrm{d}t, \tag{6.27}$$

subject to (6.1a), with the design parameter $q > 0$. By solving the associated Riccati equation

$$\boldsymbol{P}\boldsymbol{b}\boldsymbol{b}^T\boldsymbol{P} - \boldsymbol{P}\boldsymbol{A} - \boldsymbol{A}^T\boldsymbol{P} - \boldsymbol{Q} = \boldsymbol{0} \tag{6.28}$$

for the positive definite solution $\boldsymbol{P} \in \mathbb{R}^{n\times n}$, the gain

$$\boldsymbol{k}^T = \boldsymbol{b}^T\boldsymbol{P}$$

of the linear–quadratic regulator results, e.g., [Kir04]. The definition of the matrix $\boldsymbol{Q} \in \mathbb{R}^{n\times n}$ in (6.28) depends on whether the FVM or the MA is considered:

$$\boldsymbol{Q}_\mathrm{F} = \begin{bmatrix} q_\mathrm{F}(R_\mathrm{s}T_0)^2 & 0 & \cdots & 0 \\ 0 & 0 & \ddots & \vdots \\ \vdots & \ddots & \ddots & 0 \\ 0 & \cdots & 0 & 0 \end{bmatrix}, \quad \boldsymbol{Q}_\mathrm{M} = \begin{bmatrix} q_\mathrm{M}(b_0 R_\mathrm{s}T_0)^2 & 0 & \cdots & 0 \\ 0 & 0 & \ddots & \vdots \\ \vdots & \ddots & \ddots & 0 \\ 0 & \cdots & 0 & 0 \end{bmatrix},$$

where q_F and q_M, respectively, define q in (6.27). For the matrices $\boldsymbol{Q}_\mathrm{F}$ and $\boldsymbol{Q}_\mathrm{M}$, based on the pairs $(\boldsymbol{A}_\mathrm{F}, \boldsymbol{b}_\mathrm{F})$ and $(\boldsymbol{A}_\mathrm{M}, \boldsymbol{b}_\mathrm{M})$, the Riccati equation (6.28) has a corresponding unique positive definite solution[9] $\boldsymbol{P}$.

In contrast to a design based on pole placement, where n pole locations need to be specified, the proposed linear–quadratic regulator with the cost function (6.27) only requires the choice of q. The value of q is determined by trial and error, depending on the desired dynamical behavior of the tank pressure $p_\mathrm{vol}(t)$, i.e. the controlled variable.

For the computation of $\boldsymbol{k}^T$, the choice of q might not be arbitrary as the pair $(\boldsymbol{A}, \boldsymbol{b})$ can become numerically almost uncontrollable for high-order approximations, regardless of whether the FVM or the MA is utilized.

[6] For $(\boldsymbol{A}_\mathrm{M}, \boldsymbol{b}_\mathrm{M})$, this property is guaranteed by (6.15) being a minimal realization (cf. Rem. 6.3).

[7] The following linear-quadratic regulator is designed based on both, the model derived by the FVM and the MA.

[8] Therein, $p_\mathrm{vol}(t)$ is in Pa and $U(t)$ in $^\mathrm{kg}/_\mathrm{s}$.

[9] The model (6.15a), derived by the MA, is detectable via $p_\mathrm{vol}(t)$ as the latter is proportional to the flat output in (6.24), ensuring observability. In contrast, $p_\mathrm{vol}(t)$ is not a flat output of the model (6.6a), derived by the FVM (cf. (6.22)). However, based on the corresponding observability matrix w.r.t. $p_\mathrm{vol}(t)$, it can be shown that (6.6a) is observable via $p_\mathrm{vol}(t)$ and, thus, detectable.

Remark 6.5. Naturally, it is possible to scale the independent and dependent variables of the linear model (2.51), improving the numerical calculation of $\boldsymbol{k}^T$ to some extent. Since it is not necessary for the subsequently chosen approximation order n, this approach is not taken into account. △

6.2.3 Design of the State Observer

The implementation of the state feedback (6.26) at the test bench necessitates the knowledge of the state $\boldsymbol{X}(t)$. To provide an estimate $\hat{\boldsymbol{X}}(t)$ based on the measurement $Y(t)$, a state observer is designed in the following. For that, first, the observability of the systems (6.6) with (6.8) and (6.15) with (6.18) is investigated. For the pair $(\boldsymbol{A}_\mathrm{F}, (\boldsymbol{c}_\mathrm{F}^{\bar{y}})^T)$, the determinant of the observability matrix reads

$$\det \begin{bmatrix} (\boldsymbol{c}_\mathrm{F}^{\bar{y}})^T \\ (\boldsymbol{c}_\mathrm{F}^{\bar{y}})^T \boldsymbol{A}_\mathrm{F} \\ \vdots \\ (\boldsymbol{c}_\mathrm{F}^{\bar{y}})^T \boldsymbol{A}_\mathrm{F}^{n-1} \end{bmatrix} = \frac{a_{n+1}^2 \kappa_1^{\frac{n-1}{2}(\frac{n-1}{2}+1)-2} \kappa_2^{\frac{(n-1)^2}{4}} (2\kappa_1 + k_4)^2}{2^{n+1}},$$

where $a_{j+1} = 4a_j - a_{j-1}$, $j = 1, \ldots, n$ with $a_0 = 1$, $a_1 = 1$ [Slo]. Therefore, since the determinant is non-zero, the system is observable. The observability of the pair $(\boldsymbol{A}_\mathrm{M}, (\boldsymbol{c}_\mathrm{M}^{\bar{y}})^T)$ follows from the fact that the system (6.15) is a minimal realization (cf. Rem. 6.3).

Having discussed the observability of the systems, a Luenberger observer

$$\frac{\mathrm{d}}{\mathrm{d}t}\hat{\boldsymbol{X}}(t) = \boldsymbol{A}\hat{\boldsymbol{X}}(t) + \boldsymbol{b}U(t) + \boldsymbol{l}\left(Y(t) - \hat{Y}(t)\right) \tag{6.29a}$$

$$\hat{Y}(t) = \boldsymbol{c}^T \hat{\boldsymbol{X}}(t) \tag{6.29b}$$

is designed, based on the systems (6.6) with (6.8) and (6.15) with (6.18), respectively. The gain $\boldsymbol{l} \in \mathbb{R}^n$, rendering $\boldsymbol{A} - \boldsymbol{l}\boldsymbol{c}^T$ a Hurwitz matrix, is derived by pole placement, where the desired locations are specified by trial and error. For higher approximation orders, both, the FVM and the MA, may generate a pair $(\boldsymbol{A}, \boldsymbol{c}^T)$ which is numerically almost unobservable. This can cause ill-conditioned computational problems. Hence, some pole locations might not be feasible.

Remark 6.6. A state observer design dual to the state feedback design in Sec. 6.2.2, i.e. the Kalman-Bucy filter, is not pursued since it would require the determination of the process noise covariance, e.g., [WB06]. △

6.3 Simulation Studies

The controllers are discussed in simulations prior to their experimental validation. First, the state feedbacks, designed by making use of the FVM and the MA, respectively, are applied to the linear model (2.51) of the test bench. Next, each state feedback is combined with the corresponding state observer and augmented with the feedforward controller. The resulting two output feedback tracking controllers are applied to the linear model as well as to the plant model (2.48), where the parameters of the test bench configuration are stated in Tab. 3.1. The numerical solution of the finite-dimensional state observers (6.29) is described in Appx. B.1.2. The gains $\boldsymbol{k}^T$ and $\boldsymbol{l}$ are computed by the MATLAB commands `lqr()` and `place()`, respectively.

State Feedback Controller As it is desirable to stabilize a non-zero pressure level, the feedback law

$$U^{\mathrm{c}}(t) = -\boldsymbol{k}^T \left(\boldsymbol{X}(t) - \boldsymbol{X}^{\mathrm{r}} \right) \tag{6.30}$$

is introduced. Therein, $\boldsymbol{X}(t)$ is computed in each time step based on the states $\boldsymbol{x}(z,t)$, $\xi(t)$, resulting from the simulation of the linear model (2.51). While the state $\bar{\boldsymbol{X}}(t)$ of the FVM directly follows from (6.2), the state $\tilde{\boldsymbol{X}}(t)$ of the MA is obtained from the relation (6.19). These intermediate computations are only required in the context of simulations, where the state feedback is not based on the estimate of the state observer. The constant reference state $\boldsymbol{X}^{\mathrm{r}}$ results from the desired pressure level $p_{\mathrm{vol}}^{\mathrm{r}}$ by making use of (6.21), (6.22) and (6.23), (6.24), respectively. In order allow for a comparison between the early-lumping approach and the backstepping-based late-lumping approach, the design parameter q in (6.27) is chosen as follows: First, the settling time $t_{5\%} = 0.19\,\mathrm{s}$ of the backstepping-based state feedback in Fig. 4.10 is determined. This duration is defined by the time needed for $p_{\mathrm{vol}}(t)$ to reach and stay within a range of $\pm 5\,\%$ of the desired pressure level $p_{\mathrm{vol}}^{\mathrm{r}} = 3\,\mathrm{bar}$, e.g., [Oga10]. Next, the design parameter q is tuned in a simulation, where the early-lumping feedback controller (6.30) is applied to the corresponding finite-dimensional model (6.1) with $n = 7$ states[10], in order to achieve the same settling time. Thereby, $q_{\mathrm{F}} = 3.93 \cdot 10^{-5}\,\mathrm{kg^2/s^2 \cdot Pa^2}$ and $q_{\mathrm{M}} = 3.96 \cdot 10^{-5}\,\mathrm{kg^2/s^2 \cdot Pa^2}$ are obtained. As the state feedback is initially applied to the linear model, the friction amplification factor in (2.51a) is set to $k_{\mathrm{fric}} = 1$ in the simulations as well as for the computation of the corresponding gain $\boldsymbol{k}^T$ in (6.26).

Fig. 6.6 depicts the simulation results for the application of the state feedback $U_{\mathrm{F}}^{\mathrm{c}}(t)$, designed based on the FVM, to the linear model. For $t < t_{\mathrm{on}} = 0.05\,\mathrm{s}$, the system is in equilibrium with its surroundings, i.e. $\rho(z,0) = \rho_0$ and $(\rho v)(z,0) = 0$. At $t_{\mathrm{on}} = 0.05\,\mathrm{s}$, the controller is activated, trying to stabilize the desired pressure level $p_{\mathrm{vol}}^{\mathrm{r}} = 3\,\mathrm{bar}$. In the upper plot of Fig. 6.6, it can be seen that the tank pressure starts to rise shortly after t_{on}, slightly oscillating. These lower frequency oscillations are superimposed with higher frequencies, destabilizing the system. Similar effects can be observed in Fig. 6.7, where the simulation data, resulting from the application of the state feedback $U_{\mathrm{M}}^{\mathrm{c}}(t)$ designed based on the MA to the linear model, is depicted. It can be seen that the higher frequency oscillations in the tank pressure are not as dominant as in Fig. 6.6. Still, as shown in in Fig. 6.8, the distributed pressure $p(z,t)$ along the tube oscillates heavily. Thus, the system does not converge to a steady state, neither.

The lower frequency oscillations shortly after t_{on} in Fig. 6.6 and Fig. 6.7 result from the $n-1$ complex eigenvalues of the corresponding matrix $\boldsymbol{A} - \boldsymbol{b}\boldsymbol{k}^T$. In contrast to that, the higher frequency oscillations can be attributed to the spillover effect, which prevents the system from converging to the desired constant pressure level. The spillover is caused by the fact that the approximation cannot fully capture the effects inherent to hyperbolic systems, e.g., discontinuities in the solution as well as the propagation of waves with finite speed. Thereby, such an inferior control performance as depicted in Fig. 6.6 and Fig. 6.7 can result. The amplitude of the higher frequency oscillations mainly depends on the chosen design parameter q and the approximation order[11] n. A lower value of the weight q and/or a larger value of n might decrease the higher frequency oscillations. However, if the state feedback is combined with the state observer (6.29), an adjustment

[10] The choice of the approximation order is discussed in the following.

[11] Naturally, the choice of the discretization scheme, stated in Appx. B.1 and required for the numerical simulation of the linear model (2.51), can effect the amplitude of the higher frequency oscillations, too.

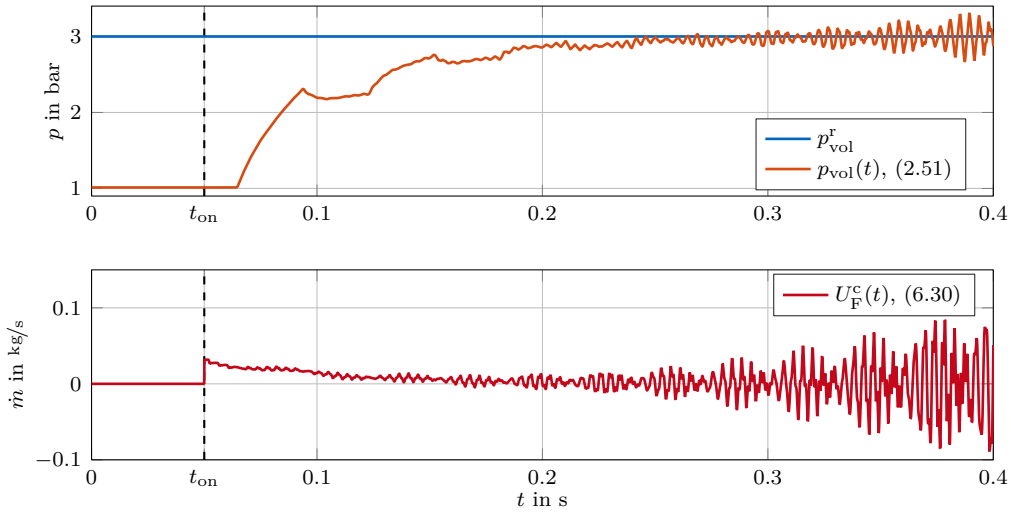

Figure 6.6: Application of the feedback controller (6.30), designed based on the FVM in Sec. 6.1.1, to the linear model (2.51): Reference pressure p^{r}_{vol} and tank pressure $p_{vol}(t)$ as well as corresponding control input $U^{c}_{F}(t)$

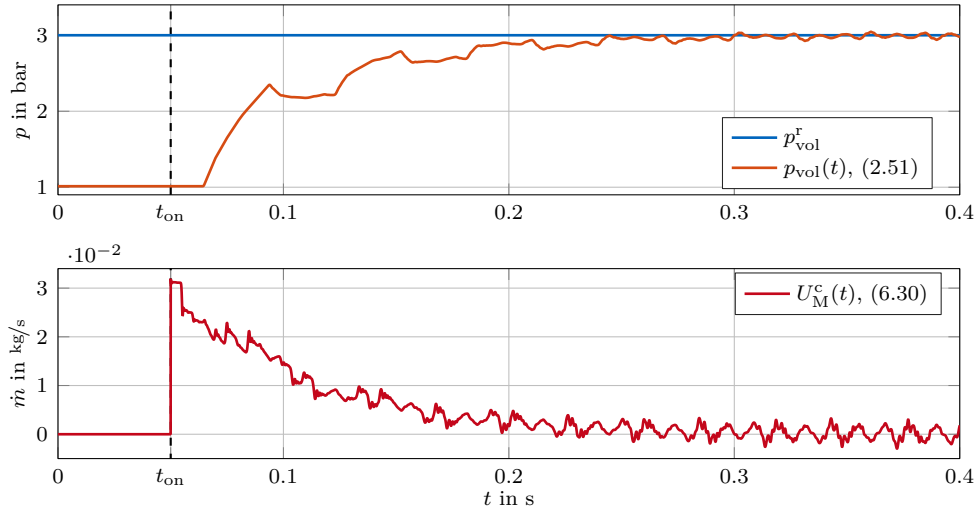

Figure 6.7: Application of the feedback controller (6.30), designed based on the MA in Sec. 6.1.2, to the linear model (2.51): Reference pressure p^{r}_{vol} and tank pressure $p_{vol}(t)$ as well as corresponding control input $U^{c}_{M}(t)$

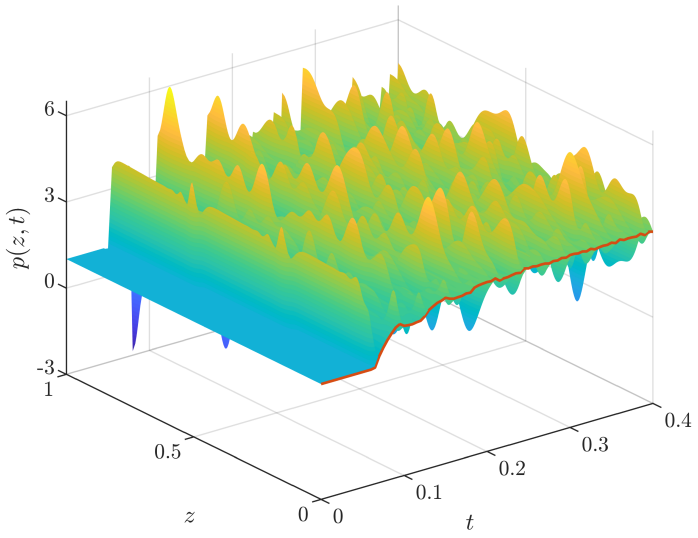

Figure 6.8: Distributed pressure $p(z,t)$ along the tube and the tank pressure $p_{\mathrm{vol}}(t)$ (orange line) in bar

of q or n is unnecessary as the use of the resulting output feedback controller significantly reduces the oscillations. Such a scenario is investigated in the following.

Output Feedback Tracking Controller In the following, the output feedback tracking controller

$$U(t) = U^{\mathrm{r}}(t) + U^{\mathrm{c}}(t), \tag{6.31}$$

where

$$U^{\mathrm{c}}(t) = -\boldsymbol{k}^T \left(\hat{\boldsymbol{X}}(t) - \boldsymbol{X}^{\mathrm{r}}(t) \right), \tag{6.32}$$

is applied to the linear model. It is obtained from combining the state feedback (6.30), based on the estimate $\hat{\boldsymbol{X}}(t)$ of the state observer (6.29), with the corresponding feedforward controller in Sec. 6.2.1, where μ in (6.25) is set to $\mu = 0.4$. The desired pressure levels and the rate of the transitions are equal to those of the standard reference trajectory depicted in Fig. 3.2. Since $y^{\mathrm{r}}(t)$ is based on the Gevrey function in (6.25) instead of on the polynomial in (3.11), the resulting reference trajectory slightly differs from the one depicted in Fig. 3.2. In addition, $p^{\mathrm{r}}_{\mathrm{vol}}(t)$ in (6.22) is not proportional to $y^{\mathrm{r}}_{\mathrm{F}}(t)$ during the transitions. However, since the deviations between $\xi(t)$ and $\bar{X}^1_1(t)$ in (6.5) are marginal for the chosen reference trajectory, the deviations between $(2\kappa_1 + k_4) R_{\mathrm{s}} T_0 y^{\mathrm{r}}_{\mathrm{F}}(t)$ and $p^{\mathrm{r}}_{\mathrm{vol}}(t)$ are small, too (cf. (6.20)).

The observer eigenvalues β_i, $i = 1, \ldots, 7$, of the matrix $\boldsymbol{A} - \boldsymbol{l}\boldsymbol{c}^T$ are determined by an approach comparable to the previously considered one for the determination of the gain $\boldsymbol{k}^T$ in (6.30): First, the backstepping-based state observer (4.38) is simulated, where the parameters corresponding to Fig. 4.13 are utilized. The initial conditions of the state observer read $\hat{x}_1(z,0) = 3\rho_0$, $\hat{x}_2(z,0) = 0$. In contrast to that, the system is in equilibrium with its surroundings for all t. Hence, the input $U(t)$ is zero and the

measurement $Y(t) = \rho_0 R_s T_0$, fed to the observer, is constant. From this simulation, the settling time $t_{5\%} = 0.20\,\mathrm{s}$ is obtained for the backstepping-based state observer, i.e. the time needed for the estimated tank pressure $\hat{p}_{\mathrm{vol}}(t)$ to reach and stay within a $\pm 5\,\%$ range of the measurement $Y(t)$. Subsequently, simulations of the corresponding finite-dimensional state observer (6.29) are performed, where the real parts of the eigenvalues

$$\beta_i = \alpha \mathrm{Re}(\lambda_{\min}) + j\mathrm{Im}(\lambda_i) \tag{6.33}$$

of $\boldsymbol{A} - \boldsymbol{l}\boldsymbol{c}^T$ are varied by tuning $\alpha > 0$ in order to achieve the settling time $t_{5\%} = 0.20\,\mathrm{s}$. The minimum eigenvalue $\lambda_{\min}$ is defined by

$$\lambda_{\min} = -\arg\max_{\lambda_i} |\mathrm{Re}(\lambda_i)|\,,$$

where λ_i are the eigenvalues of the corresponding matrix $\boldsymbol{A}$ in (6.6) and (6.15), respectively. From that, $\alpha = 2.53$ is obtained for both approximation approaches, defining the respective observer gain $\boldsymbol{l}$ in (6.29).

In Fig. 6.9 and Fig. 6.11, the simulation data for the application of $U(t)$ in (6.31), resulting from the FVM and the MA, respectively, to the linear model (2.51) is depicted. While the system is initially in equilibrium with its surroundings, the state observers (6.29) are initialized with

$$\hat{\boldsymbol{X}}(0) = 3\boldsymbol{X}(0),$$

where $\boldsymbol{X}(0)$ follows from $\boldsymbol{x}(z,0)$, $\xi(0)$ by making use of the relations in (6.2) and (6.19), respectively. In the upper plots of Fig. 6.9 and Fig. 6.11, it can be seen that the tank pressures $p_{\mathrm{vol}}(t)$ start to deviate from the reference pressures $p^{\mathrm{r}}_{\mathrm{vol}}(t)$, caused by the initial mismatch between the respective observer state and the state of the linear model. For approximately $t > 0.4\,\mathrm{s}$, as shown in Fig. 6.10 and Fig. 6.12, the deviations $\Delta p(t)$ between the reference pressures $p^{\mathrm{r}}_{\mathrm{vol}}(t)$, the estimated pressures $\hat{p}_{\mathrm{vol}}(t)$, and the tank pressures $p_{\mathrm{vol}}(t)$ become virtually zero. Consequently, the systems are steered by the feedforward controllers $U^{\mathrm{r}}_{\mathrm{F}}(t)$ and $U^{\mathrm{r}}_{\mathrm{M}}(t)$, respectively, only.

By comparing Fig. 6.10 and Fig. 6.12, it can be concluded that both early-lumping controllers have a very similar performance. Furthermore, in contrast to the simulations in Fig. 6.6 and Fig. 6.7, where the corresponding state feedback (6.30) is based on the actual state $\boldsymbol{x}(z,t)$, $\xi(t)$ of the system, the higher frequency oscillations are virtually nonexistent in Fig. 6.10 and Fig. 6.12. The reason for this is the fact that the state feedback (6.32) in the output feedback tracking controller (6.31) is based on the estimate of the state observer (6.29), by which the higher frequency oscillations are significantly reduced. The lower frequency oscillations still visible can be attributed to the complex eigenvalues of the closed-loop system. An increase of the approximation order n would basically result in the same performance of the output feedback tracking controller. This is confirmed by [RNM16; AF16; Fal17; TU18], where $n < 7$ is verified to be sufficient.

Before each output feedback tracking controller is tested in experiments, it is applied to the plant model (2.48). Both, the system and the state observer, are initially in equilibrium with the surroundings. In order to compensate the turbulent friction effects, the friction amplification factor in (2.51a) is set to $k_{\mathrm{fric}} = 4$ for the computation of the feedback and observer gain $\boldsymbol{k}^T$ and $\boldsymbol{l}$ in (6.26) and (6.29), respectively. Fig. 6.13 shows the simulation data for the FVM and the corresponding errors[12] can be seen in Fig. 6.14.

[12] As already mentioned, the deviations of all essential simulations are quantified in terms of the error measures $L^1_{\mathrm{r,err}}$ and L^∞_{err} in (2.42) and (2.43), respectively, and can be found in Chap. 7.

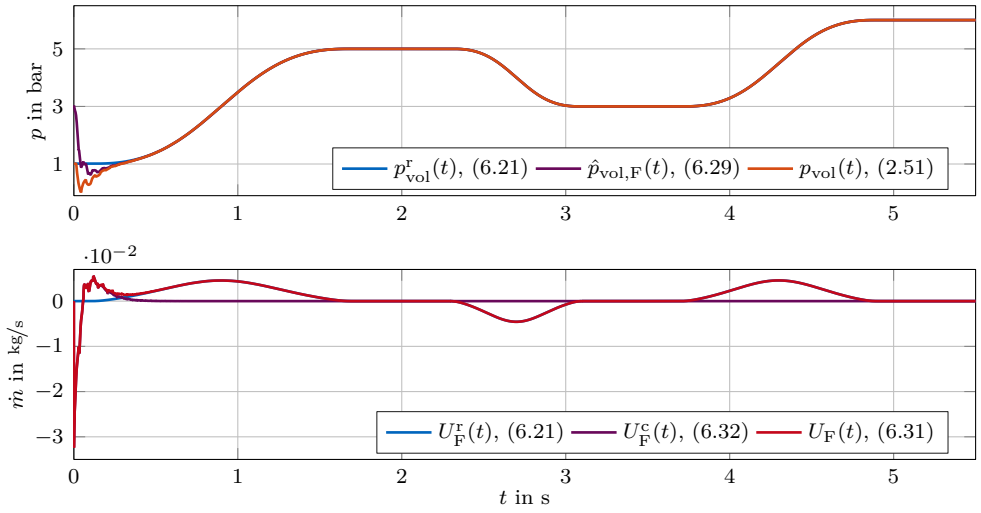

Figure 6.9: Application of the output feedback tracking controller (6.31), designed based on the FVM in Sec. 6.1.1, to the linear model (2.51): Reference pressure $p^{\mathrm{r}}_{\mathrm{vol}}(t)$, estimated pressure $\hat{p}_{\mathrm{vol,F}}(t)$, and tank pressure $p_{\mathrm{vol}}(t)$ as well as corresponding control input $U_{\mathrm{F}}(t)$ with feedforward part $U^{\mathrm{r}}_{\mathrm{F}}(t)$ and feedback part $U^{\mathrm{c}}_{\mathrm{F}}(t)$

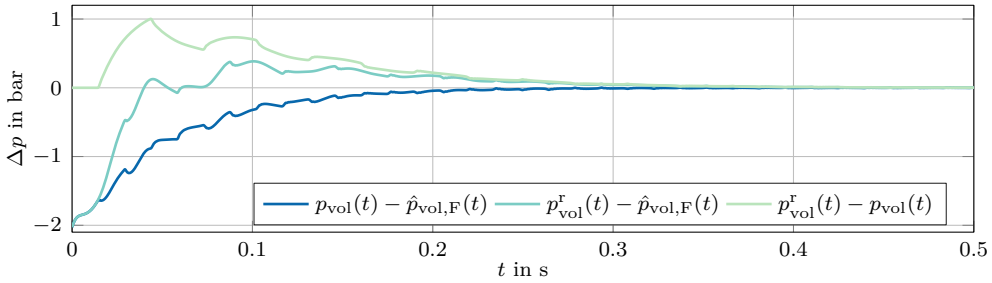

Figure 6.10: Deviations between the reference pressure $p^{\mathrm{r}}_{\mathrm{vol}}(t)$, the estimated pressure $\hat{p}_{\mathrm{vol,F}}(t)$, and the tank pressure $p_{\mathrm{vol}}(t)$ in Fig. 6.9

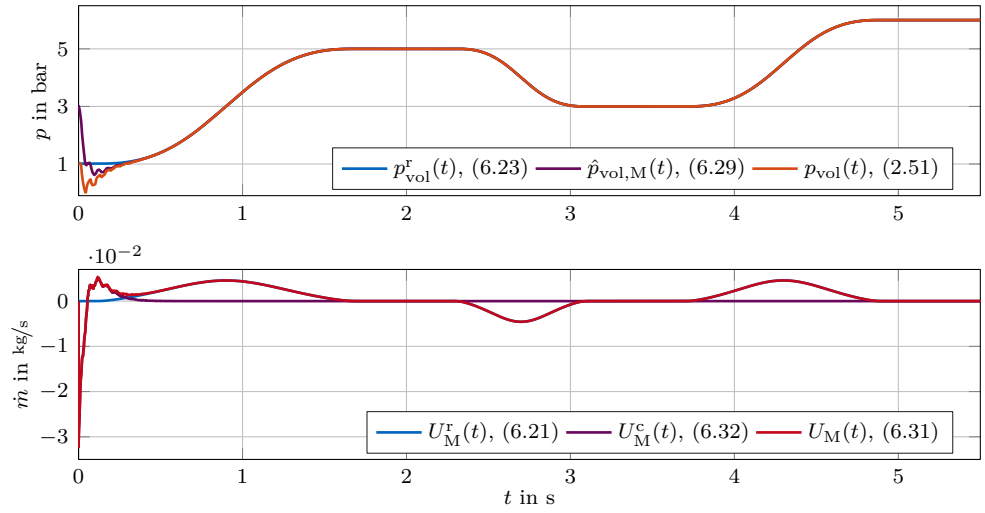

Figure 6.11: Application of the output feedback tracking controller (6.31), designed based on the MA in Sec. 6.1.2, to the linear model (2.51): Reference pressure $p^{\mathrm{r}}_{\mathrm{vol}}(t)$, estimated pressure $\hat{p}_{\mathrm{vol,M}}(t)$, and tank pressure $p_{\mathrm{vol}}(t)$ as well as corresponding control input $U_{\mathrm{M}}(t)$ with feedforward part $U^{\mathrm{r}}_{\mathrm{M}}(t)$ and feedback part $U^{\mathrm{c}}_{\mathrm{M}}(t)$

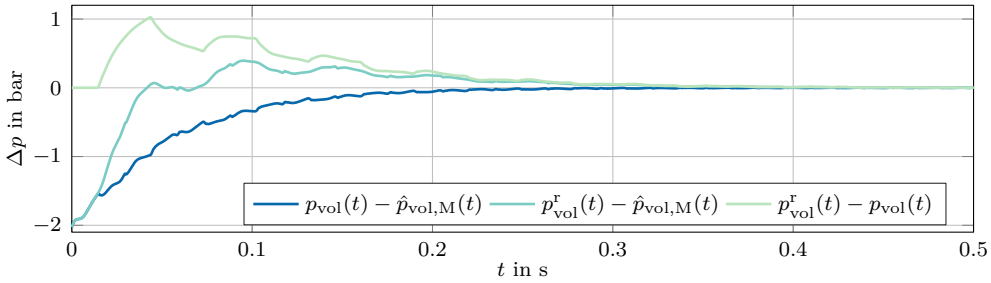

Figure 6.12: Deviations between the reference pressure $p^{\mathrm{r}}_{\mathrm{vol}}(t)$, the estimated pressure $\hat{p}_{\mathrm{vol,M}}(t)$, and the tank pressure $p_{\mathrm{vol}}(t)$ in Fig. 6.11

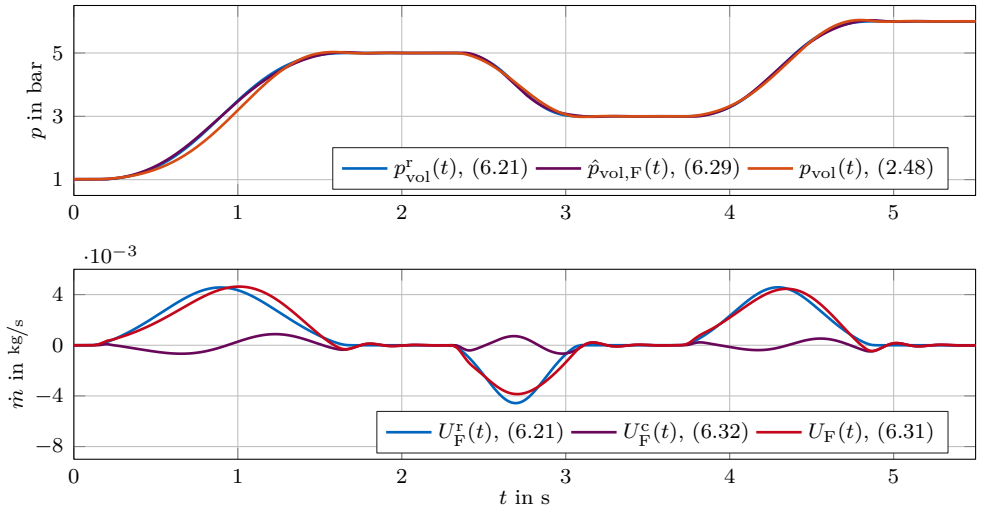

Figure 6.13: Application of the output feedback tracking controller (6.31), designed based on the FVM in Sec. 6.1.1, to the plant model (2.48): Reference pressure $p^{\mathrm{r}}_{\mathrm{vol}}(t)$, estimated pressure $\hat{p}_{\mathrm{vol,F}}(t)$, and tank pressure $p_{\mathrm{vol}}(t)$ as well as corresponding control input $U_{\mathrm{F}}(t)$ with feedforward part $U^{\mathrm{r}}_{\mathrm{F}}(t)$ and feedback part $U^{\mathrm{c}}_{\mathrm{F}}(t)$

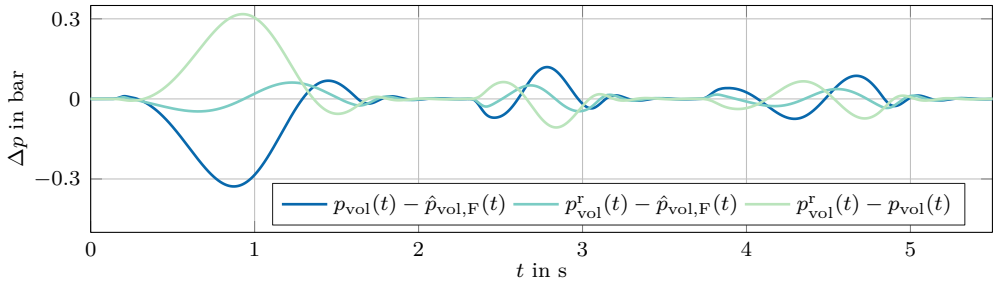

Figure 6.14: Deviations between the reference pressure $p^{\mathrm{r}}_{\mathrm{vol}}(t)$, the estimated pressure $\hat{p}_{\mathrm{vol,F}}(t)$, and the tank pressure $p_{\mathrm{vol}}(t)$ in Fig. 6.13

While there are deviations during the transitions, steady-state accuracy is achieved. As the simulation data for the FVM and the MA are again very similar, the results for the MA are not explicitly depicted.

6.4 Experimental Results

In order to implement the output feedback tracking controller (6.31) at the test bench with the configuration in Tab. 3.1, the respective state-space representation (6.1) with $k_{\mathrm{fric}} = 4$ is discretized[13] w.r.t. t by means of the zero-order hold method. Based on this discrete-time model with the sample time $\Delta t = 5 \cdot 10^{-4}\,\mathrm{s}$ of the test bench, the gains $\boldsymbol{k}_{\mathrm{d}}^T$ and $\boldsymbol{l}_{\mathrm{d}}$ are designed by making use of the MATLAB commands `lqrd()` and `place()`. The design parameters q_{F}, q_{M} and the dynamics of the discrete state observers with the eigenvalues $\beta_{\mathrm{d},i} = \mathrm{e}^{\beta_i \Delta t}$ are chosen as in the previous section. Subsequently, similar to the implementation of the backstepping-based controller in Sec. 4.7, the resulting two output feedback tracking controller are implemented in Simulink and integrated in the software framework of the test bench.

Fig. 6.15 and Fig. 6.17 display the experimental data resulting from the application of the output feedback tracking controllers, designed based on the FVM and the MA, respectively, to the test bench. The corresponding pressure deviations are shown in Fig. 6.16 and Fig. 6.18. It can be seen that the experimental data is relatively similar to the simulation data in Fig. 6.13 and Fig. 6.14. However, measurement noise and higher frequency oscillations are present in the experiment, even if the system should be in a steady state. The oscillations depend on the pressure level and result from the slightly inaccurate inverse mass flow rate model (2.19) of the valve. As these inaccuracies are somewhat amplified by the output feedback tracking controllers, experiments confirm that choosing a slower closed-loop dynamics will decrease the amplitude of the oscillations. Furthermore, comparable to the previous simulation studies, both controllers achieve a relatively similar performance in the experiments presented in Fig. 6.15 and Fig. 6.17.

In the following scenario, a reference trajectory is chosen which partially exceeds the test bench capabilities. For that, the pressure levels and the rate of the transitions are defined as in Fig. 4.20. To avoid peaks in the reference input $U^{\mathrm{r}}(t)$, resulting from the involved higher-order time derivatives of the highly dynamic reference trajectory $y^{\mathrm{r}}(t)$ (cf. (6.23) and (6.21)), $U^{\mathrm{r}}(t)$ is smoothed by a low-pass filter. Since the experimental data for both approximation approaches is again relatively similar, only the results of the FVM are shown in Fig. 6.19. Therein, the bounded input $U_\nu(t)$ in (4.79) is depicted instead of $U(t)$. The corresponding pressure deviations are shown in Fig. 6.20.

It can be seen that the controller is not able to track the reference pressure satisfactorily during the first transitions, where relatively large deviations occur. These mostly originate from the highly dynamic reference trajectory, which causes high flow velocities in the tube. The latter violate the assumptions imposed on the linear model (2.51). As the output feedback tracking controller is designed based on this model, the tracking perfor-

[13] In Sec. 6.3, the continuous-time formulation of the state-space representation is used for the design of the feedback and observer gains $\boldsymbol{k}^T$ and $\boldsymbol{l}$ in (6.26) and (6.29), respectively. The reason for this is the fact that the (possibly non-constant) time step $\Delta t_m \approx 4.95 \cdot 10^{-5}\,\mathrm{s}$ is sufficiently small compared to the bandwidth of the closed-loop system. Thus, the continuous-time formulation is appropriate (cf. Appx. B.1 and [Oga95]).

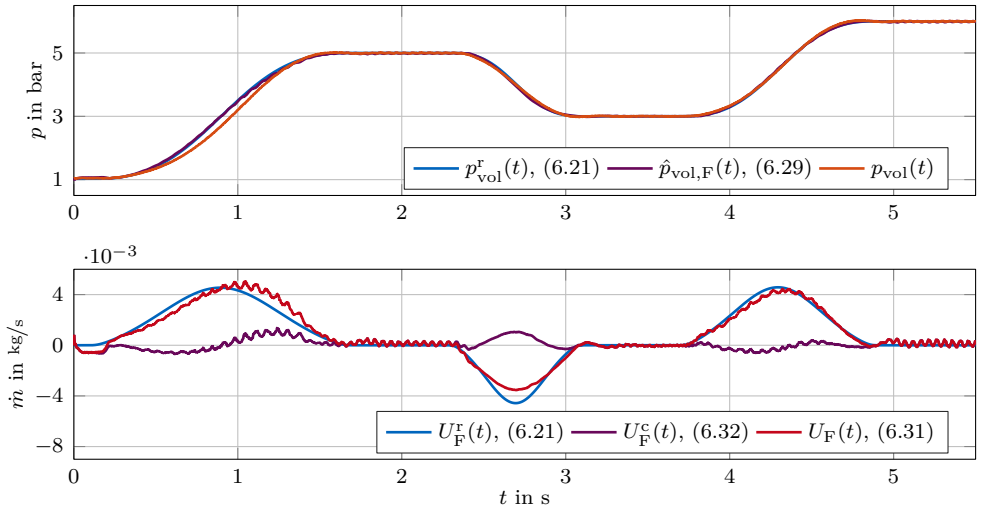

Figure 6.15: Application of the output feedback tracking controller (6.31), designed based on the FVM in Sec. 6.1.1, to the test bench: Reference pressure $p^{\mathrm{r}}_{\mathrm{vol}}(t)$, estimated pressure $\hat{p}_{\mathrm{vol,F}}(t)$, and measured tank pressure $p_{\mathrm{vol}}(t)$ as well as corresponding control input $U_{\mathrm{F}}(t)$ with feedforward part $U^{\mathrm{r}}_{\mathrm{F}}(t)$ and feedback part $U^{\mathrm{c}}_{\mathrm{F}}(t)$

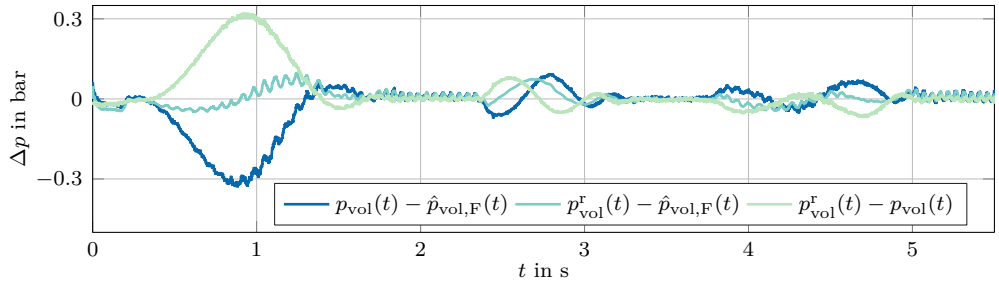

Figure 6.16: Deviations between the reference pressure $p^{\mathrm{r}}_{\mathrm{vol}}(t)$, the estimated pressure $\hat{p}_{\mathrm{vol,F}}(t)$, and the measured tank pressure $p_{\mathrm{vol}}(t)$ in Fig. 6.15

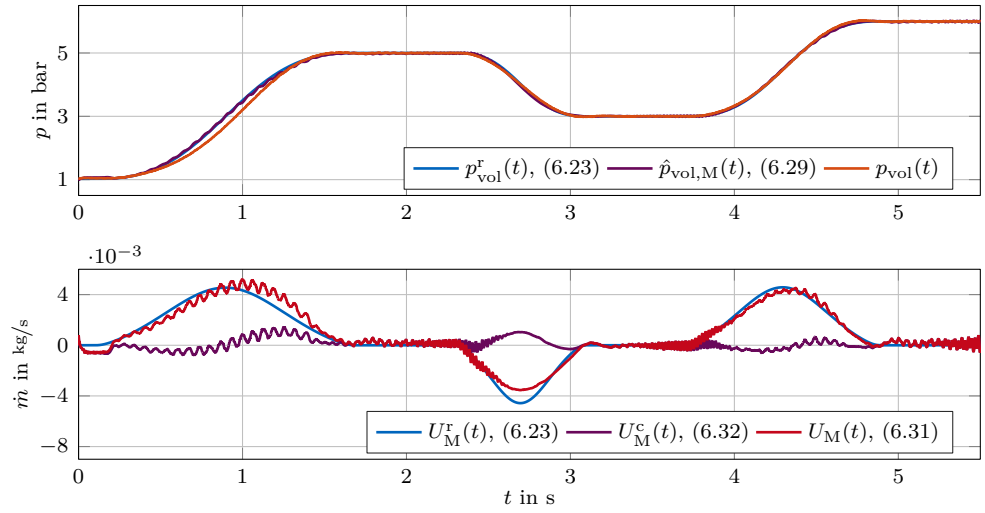

Figure 6.17: Application of the output feedback tracking controller (6.31), designed based on the MA in Sec. 6.1.2, to the test bench: Reference pressure $p^{\mathrm{r}}_{\mathrm{vol}}(t)$, estimated pressure $\hat{p}_{\mathrm{vol,M}}(t)$, and measured tank pressure $p_{\mathrm{vol}}(t)$ as well as corresponding control input $U_{\mathrm{M}}(t)$ with feedforward part $U^{\mathrm{r}}_{\mathrm{M}}(t)$ and feedback part $U^{\mathrm{c}}_{\mathrm{M}}(t)$

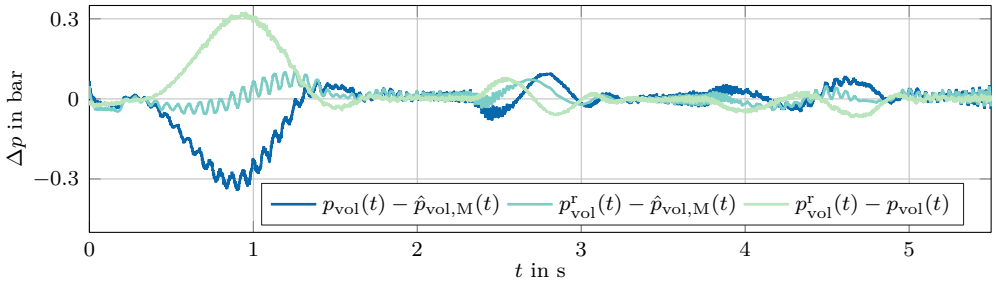

Figure 6.18: Deviations between the reference pressure $p^{\mathrm{r}}_{\mathrm{vol}}(t)$, the estimated pressure $\hat{p}_{\mathrm{vol,M}}(t)$, and the measured tank pressure $p_{\mathrm{vol}}(t)$ in Fig. 6.17

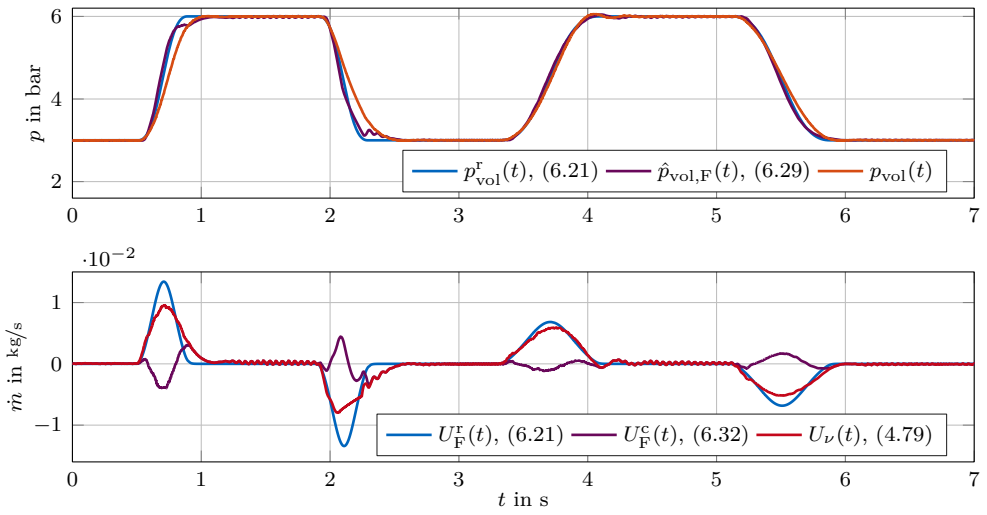

Figure 6.19: Application of the output feedback tracking controller (6.31), designed based on the FVM in Sec. 6.1.1, to the test bench with faster transitions: Reference pressure $p^{\mathrm{r}}_{\mathrm{vol}}(t)$, estimated pressure $\hat{p}_{\mathrm{vol,F}}(t)$, and measured tank pressure $p_{\mathrm{vol}}(t)$ as well as corresponding bounded control input $U_\nu(t)$ with feedforward part $U^{\mathrm{r}}_{\mathrm{F}}(t)$ and feedback part $U^{\mathrm{c}}_{\mathrm{F}}(t)$

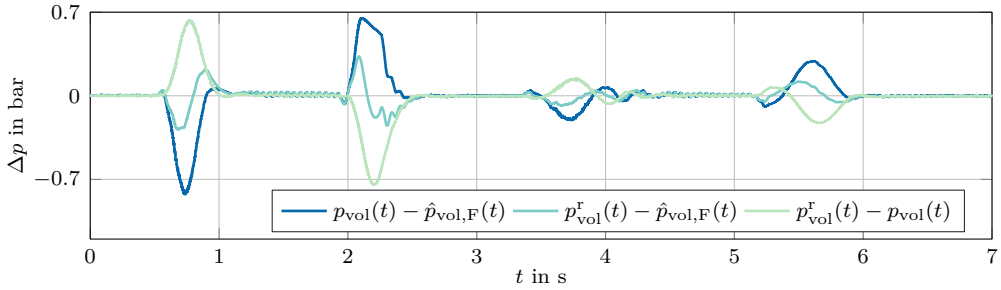

Figure 6.20: Deviations between the reference pressure $p^{\mathrm{r}}_{\mathrm{vol}}(t)$, the estimated pressure $\hat{p}_{\mathrm{vol}}(t)$, and the measured tank pressure $p_{\mathrm{vol}}(t)$ in Fig. 6.19

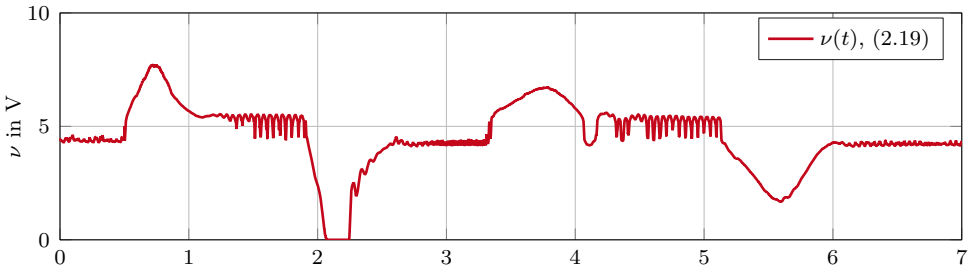

Figure 6.21: The voltage $\nu(t)$, resulting from the inverse mass flow rate model (2.19) and fed to the valve for the experiment in Fig. 6.19

mance is significantly degraded (cf. Sec. 2.7). Furthermore, the highly dynamic reference trajectory partially exceeds the test bench capabilities during the first discharge process. Fig. 6.21 shows the corresponding voltage, fed to the valve. Since $\nu(t) = 0$ holds for $t \in [2.08\,\mathrm{s}, 2.23\,\mathrm{s}]$, the test bench is discharged at its fastest rate. In contrast to that, the controller is able to track the latter transitions in Fig. 6.19 with a relatively high precision and the desired pressure levels are reached without significant delays. The capabilities of valve are respected since $0 < \nu(t) < 10\,\mathrm{V}$ holds. However, especially for $U_\nu(t) = 0$, oscillations are present in $\nu(t)$. These can be related to the oscillations in $p_{\mathrm{vol}}(t)$ in Fig. 6.19 and, as discussed in the context of Fig. 6.15 and Fig. 6.17, mostly originate from the slightly inaccurate inverse mass flow rate model (2.19) of the valve.

6.5 Chapter Highlights

This chapter made use of the early-lumping method to design two output feedback tracking controllers. For the approximation of the linear model, two approaches were utilized: the FVM and the MA. While the presented FVM follows [KS13] relatively closely, the MA in this thesis somewhat differs from [RNM15]. The input-to-output behavior of the finite-dimensional models was compared and discussed with respect to the infinite-dimensional linear model. Finally, output feedback tracking controllers were designed and investigated in simulations and experiments.

The discussion of the approximation approaches might facilitate the choice of one of them, depending on the intended application. In addition, the results in this chapter allow to compare the novel late-lumping controllers in this thesis with state-of-the-art early-lumping controller designs.

The supervised student theses [Her16; Mei17; Ame17] have contributed to the development of this chapter's results.

Chapter 7

Conclusion

In this chapter, the late-lumping and early-lumping approaches are summarized and discussed in terms of their theoretical and implementation aspects. Furthermore, their performance is compared by evaluating the presented simulation and experimental data. Finally, the highlights of this thesis are outlined and an outlook for potential further research is given.

7.1 Comparative Analysis of the Design Approaches

General Aspects The flatness-based feedforward controller in Chap. 3 is designed based on the isothermal model (2.50) of the test bench. Parametrizing the boundary system at the unactuated boundary in terms of a flat output results in a Cauchy problem w.r.t. space. Based on a desired reference trajectory of the flat output, the solution of the Cauchy problem yields the reference states and, hence, the feedforward controller. Both can be easily transformed into the conservative variables $\rho(z,t)$, $(\rho v)(z,t)$.

The design of the backstepping-based state feedback and observer in Chap. 4 is based on the linear model (2.51). For the derivation of the state feedback, the original system is transformed into a target system with the desired dynamics. From that, the control law is obtained. In a similar manner, the state observer is derived by transforming the dynamics of the observer error into a desired target system. The state feedback and observer are combined to the output feedback controller, which can be explicitly expressed in terms of the conservative variables.

The flatness-based state feedback and observer in Chap. 5 are derived from the linear model, too. For the design of the state feedback, the solution of the original system is parametrized in terms of the flat coordinates by making use of a flat output. A Volterra integral equation defines the transformation of the conservative variables into the flat coordinates. The control law essentially follows by prescribing a desired dynamics for the flat output. To design the observer, the system dynamics is written in terms of the input and the measured output. Thereby, the system in HOF is obtained. Based on this system description and a desired dynamics for the observation error, the state observer results. Currently, the transformation between the original and the observer coordinates is unknown, preventing the derivation of an output feedback controller.

For the early-lumping approach in Chap. 6, first, the infinite-dimensional linear model (2.51) of the test bench is approximately described by ODEs, resulting in a finite-

dimensional model. For that, two methods are applied, the FVM and the MA. The FVM is a time-domain approach, where the lumped state of the finite-dimensional model is a direct approximation of the distributed state. In contrast to that, the MA is carried out in the operational domain and the resulting lumped state does not allow for a straightforward physical interpretation. The subsequently designed output feedback tracking controllers each comprise a flatness-based feedforward controller, a linear-quadratic regulator, and a state observer, derived by pole placement.

Design Parameters The design of the flatness-based feedforward controller (3.14) allows for the choice of a reference trajectory $y^{\mathrm{r}}(t)$ of the flat output $y(t)$. Since $y(t)$ is proportional to the tank pressure $p_{\mathrm{vol}}(t)$, equivalently, a desired reference trajectory $p_{\mathrm{vol}}^{\mathrm{r}}(t)$ can be chosen. As the tank is modeled by a first-order ODE, the reference trajectory y^{r} has to be a $C^1([0,\infty))$ function. The duration of the transition from the initial to the desired pressure level is defined by the sum of the minimum transition time and the duration of the pressure change in the tank. The latter is a design parameter, which has to be selected carefully in order to respect the capabilities of the pneumatic system.

To design the backstepping-based feedback gains k_η, $\boldsymbol{k}_w^T(z)$ in (4.28), the parameter k has to be chosen. Thereby, the desired convergence rate of the state of the closed-loop system to zero is defined. The design parameter of the observer gains l_η, $\boldsymbol{l}(z)$ in (4.60) is given by ℓ. Its choice specifies the convergence rate of the observer error.

The computation of the gains k_0, k_1, k^+, k^-, and $k(\tau)$ in the flatness-based state feedback (5.19) requires the specification of the design parameters κ_{c} and γ_{c}, where $\gamma_{\mathrm{c}} = 0$ is chosen in this context (cf. Rem. 5.1). The choice of κ_{c} defines the convergence rate of the flat output and, hence, of the state of the closed-loop system. For the flatness-based state observer (5.38), the design parameters are given by κ_{o} and γ_{o}, where γ_{o} is set to $\gamma_{\mathrm{o}} = 0$. The convergence rate of the observation error is specified by κ_{o}.

If the early-lumping approach is applied, the approximation method and the desired order n have to be chosen, depending on the desired accuracy of the approximation. The feedback gain $\boldsymbol{k}^T$ in (6.26) follows from the choice of the design parameter q in the simplified cost function (6.27). Similarly, the n observer eigenvalues are defined by the tuning parameter α in (6.33). From that, the observer gain $\boldsymbol{l}$ in (6.29) is obtained. The flatness-based feedforward controllers in (6.21) and (6.23), respectively, follow from a desired reference trajectory $y^{\mathrm{r}}(t)$ for the flat output. While $y^{\mathrm{r}}(t)$ is proportional to $p_{\mathrm{vol}}^{\mathrm{r}}(t)$ if the MA is applied, this relation only holds in steady state if the FVM is utilized. Based on the order n, the reference trajectory y^{r} is chosen as a $C^n([0,\infty))$ function.

Stability The stability of the system (4.9), i.e. the system (4.1) in standard backstepping form controlled by the backstepping-based state feedback (4.8), follows from the stability of the target system (4.21). For $t > t_{\mathrm{c}}$, the closed-loop solution is explicitly given in (4.37). From that, the exponential convergence of the L^∞-norm of the distributed state follows. The stability of the observer error dynamics (4.40) is shown in a similar manner. For $t > t_{\mathrm{o}}$, the explicit solution (4.63), (4.64) of the observer error is obtained, where the convergence rate is exponential, too. By making use of these results, for $t > t_{\mathrm{o}} + t_{\mathrm{c}}$, the exponential stability of the closed-loop system (4.66), i.e. the system (4.1) in standard backstepping form controlled by the output feedback controller (4.65), follows from (4.73).

The flatness-based[1] state feedback (5.19) stabilizes the linear model (2.51) since it imposes the desired dynamics (5.18) of the flat output. For $t > 2\tau_0$, the explicit solution of the closed-loop system is stated in (5.26). Thereby, it can be easily shown that the convergence of the L^∞-norm of the distributed state is exponential. Similar to that, the observer error dynamics (5.36) are stable as, for $t > 2\tau_0$, the explicit solution (5.39), (5.40) of the observer error in HOF converges exponentially to zero. Since $t_\mathrm{c} = t_\mathrm{o} = 2\tau_0$ holds, the results for the stability of the closed-loop system and the observer error are similar to those of the backstepping approach.

In the context of the early-lumping approach, the exponential stability of the closed-loop system, i.e. the finite-dimensional system (6.1) controlled by the state feedback (6.26), and the exponential stability of the observer error dynamics follow from $\boldsymbol{A} - \boldsymbol{b}\boldsymbol{k}^T$ and $\boldsymbol{A} - \boldsymbol{l}\boldsymbol{c}^T$ being Hurwitz matrices.

Implementation The flatness-based feedforward controller (3.14) and the reference states result from the offline solution of the Cauchy problem (3.1), (3.13), where the initial data in (3.1) is parametrized in terms of $y^\mathrm{r}(t)$ and $\dot{y}^\mathrm{r}(t)$. The Cauchy problem is solved numerically by making use of the approximation scheme in Appx. B.2.

The gains k_η and $\boldsymbol{k}_w^T(z)$ of the backstepping-based state feedback (4.74) necessitate the calculation of $\boldsymbol{e}_2^T\boldsymbol{K}(z,\zeta)$, $\boldsymbol{e}_2^T\boldsymbol{n}(z)$, and $\boldsymbol{e}_2^T\boldsymbol{P}(z,\zeta)$. While $\boldsymbol{e}_2^T\boldsymbol{K}(z,\zeta)$ is obtained explicitly by (4.16) and (4.17), $\boldsymbol{e}_2^T\boldsymbol{n}(z)$ and $\boldsymbol{e}_2^T\boldsymbol{P}(z,\zeta)$ result from the numerical solution of the Volterra integral equation (4.33). This solution can be efficiently computed, e.g., by making use of a truncated fixed-point iteration. The observer gains l_η and $\boldsymbol{l}(z)$ result from $\boldsymbol{J}_I(z,\zeta)\boldsymbol{e}_1$, $\boldsymbol{e}_1^T\boldsymbol{r}(z)$, and $\boldsymbol{\Omega}_I(z,\zeta)\boldsymbol{e}_1$. While $\boldsymbol{J}_I(z,\zeta)\boldsymbol{e}_1$ and $\boldsymbol{e}_1^T\boldsymbol{r}(z)$ are obtained explicitly by (4.47) and (4.52), respectively, $\boldsymbol{\Omega}_I(z,\zeta)\boldsymbol{e}_1$ follows from the numerical solution of the Volterra integral equation (4.59). To implement the output feedback controller (4.65), the integral in the state feedback (4.74) is approximated by the trapezoidal rule and the state observer (4.38) is discretized with respect to time and space by applying the methods in Appx. B.1. During the run time, the resulting discretized output feedback controller is computed in each time step.

The gains k_0, k_1, k^+, k^-, and $k(\tau)$ of the flatness-based state feedback (5.19) in flat coordinates are defined explicitly in (5.20) and the coefficients of the state observer (5.38) in HOF are given in (5.32). The integral in the state feedback is approximated by the trapezoidal rule and the state observer is discretized by the methods in Appx. B.1. Assuming that an estimate of the state in conservative variables were available, the flatness-based state feedback (5.19) in flat coordinates could be applied to the test bench. To evaluate such a control law, the Volterra integral equation (5.23) needs to be solved online in each time step. Therein, the matrices $\boldsymbol{D}(\tau)$ and $\boldsymbol{H}(z,\tau)$ are computed offline. By making use of a truncated fixed-point iteration, where the iteration in the actual time step is initialized with the solution of the last time step, the required computational time to solve the Volterra integral equation (5.23) is kept within limits.

To implement the early-lumping approach at the test bench, the respective state-space representation is discretized w.r.t. t by means of the zero-order hold method. The gains $\boldsymbol{k}_\mathrm{d}^T$ and $\boldsymbol{l}_\mathrm{d}$ are obtained by making use of the MATLAB commands `lqrd()` and `place()`. For the computation of the feedforward controllers and the reference states, defined in (6.21) and (6.23), respectively, $y^\mathrm{r}(t)$ is differentiated n times. During the experiment,

[1] It is assumed that $\gamma_\mathrm{c} = \gamma_\mathrm{o} = 0$ holds (cf. Rem. 5.1 and Rem. 5.4).

Table 7.1: Errors as well as control efforts: The state feedbacks are applied to the linear model in a simulation

design	Fig.	$L^1_{\mathrm{r,err}}$	L^1_{eff}
backstepping	4.10	10.675 %	1.819 g
flatness-based	5.2	10.675 %	1.818 g
FVM	6.6	10.787 %	3.513 g
MA	6.7	10.098 %	1.870 g

the discretized output feedback controllers, following from (6.26) and (6.29), have to be evaluated in each time step.

Simulation and Experiment The performance of the presented controllers is compared in terms of the deviation between the reference pressure $p^{\mathrm{r}}_{\mathrm{vol}}(t)$ and the tank pressure $p_{\mathrm{vol}}(t)$, quantified by the error measures $L^1_{\mathrm{r,err}}$ and L^∞_{err} in (2.42) and (2.43), respectively. In addition to $L^1_{\mathrm{r,err}}$ and L^∞_{err}, a further measure is introduced:

$$L^1_{\mathrm{eff}} = \int_0^{t_{\mathrm{f}}} \max\{0, U_\nu(t)\}\,\mathrm{d}t, \tag{7.1}$$

where $U_\nu(t)$ is defined in (4.79) and t_{f} denotes the duration of the simulation or the experiment. Thereby, the necessary control effort, i.e. the amount of compressed air consumed, is quantified.

Remark 7.1. Naturally, the performance of the controllers depends on several factors such as the test bench configuration, the reference pressure trajectory as well as the chosen design parameters. It could be improved by, e.g., an optimization-based tuning of the design parameters. △

The first comparison is based on the simulations, where the state feedbacks are applied to the linear model (2.51). Tab. 7.1 lists the corresponding error measures[2] $L^1_{\mathrm{r,err}}$, where the lower limit of the integration in (2.42) is replaced by t_{on}, and the control efforts L^1_{eff}. By comparing the simulation results of the backstepping- and flatness-based state feedbacks in Fig. 4.10 and Fig. 5.2, respectively, it can be seen that both late-lumping approaches virtually lead to the same closed-loop dynamics. The negligible deviations between the two inputs $U^{\mathrm{c}}(t)$ around t_{on} and t_2 most probably result from numerical inaccuracies. The application of the early-lumping state feedbacks to the linear model, depicted in Fig. 6.6 and Fig. 6.7, induces high frequency oscillations in the closed-loop system. In contrast to the late-lumping approaches, where the tank pressure converges to the desired pressure with the specified convergence rate, steady-state accuracy is not achieved. As it can be seen in the lower plot of Fig. 4.10 and Fig. 5.2, the infinite-dimensional control laws take the hyperbolic character of the system into account by compensating the reflected pressure wave at t_2. Since this is not the case for the early-lumping controllers, the lower frequency oscillations depicted in Fig. 6.6 and Fig. 6.7 result. Furthermore, as stated in Tab. 7.1, the early-lumping controllers consume more compressed air, especially if the design is based on the FVM.

[2] For all state feedbacks, $L^\infty_{\mathrm{err}} = p^{\mathrm{r}}_{\mathrm{vol}} - p_0 = 1.987\,\mathrm{bar}$ results.

Table 7.2: Errors as well as control efforts: The output feedback tracking controllers are applied to the plant model in a simulation

design	Fig.	$L^1_{\mathrm{r,err}}$	L^∞_{err}	L^1_{eff}
backstepping	4.15	1.021 %	0.155 bar	6.521 g
FVM	6.13	1.633 %	0.318 bar	6.516 g
MA	not depicted	1.639 %	0.319 bar	6.518 g

Next, the simulations, where the output feedback tracking controllers are applied to the plant model (2.48), are discussed[3]. It can be seen in Fig. 4.15 that the backstepping-based output feedback controller, combined with the flatness-based feedforward controller[4], tracks the reference pressure trajectory almost perfectly. While still being adequate, the performance of the early-lumping controller in Fig. 6.13, derived by the FVM, is slightly inferior. The diminished performance of the early-lumping approach is also apparent from the error measures in Tab. 7.2: Compared to the backstepping-based controller, the measures $L^1_{\mathrm{r,err}}$, L^∞_{err} of the early-lumping controllers, derived by the FVM and the MA, are increased by approximately 60 %, 105 % and 61 %, 106 %, respectively, while almost the same amount of compressed air is consumed. It can be concluded that the choice of the approximation method has no significant effect on the resulting controller performance.

Remark 7.2. For a comparison, the backstepping-based output feedback controller (4.65) is augmented by a feedforward controller based on the linear model by making use of (5.15b) evaluated at $z = 1$. Thus, similar to the early-lumping approaches, the feedforward and the feedback part are derived from the same system description. A simulation similar to Fig. 4.15, where the resulting (linear) output feedback tracking controller is applied to the plant model, yields the error measures $L^1_{\mathrm{r,err}} = 1.275\,\%$ as well as $L^\infty_{\mathrm{err}} = 0.188\,\mathrm{bar}$ and the control effort $L^1_{\mathrm{eff}} = 6.547\,\mathrm{g}$. By comparing these values with the ones of the early-lumping controllers in Tab. 7.2, it can be concluded that the excellent performance of the backstepping-based controller is not solely caused by the superior feedforward part. △

The experimental results depicted in Fig. 4.18, Fig. 6.15, and Fig. 6.17 support that the backstepping-based controller may be advantageous in industrial applications: As stated in Tab. 7.3, the errors $L^1_{\mathrm{r,err}}$, L^∞_{err}, resulting from the early-lumping controllers, are about 38 %, 85 % and 37 %, 86 %, respectively, larger than those of the backstepping-based controller. At the same time, the early-lumping controllers consume more compressed air. Again, both approximation approaches lead to a similar performance. Overall, the experimental results confirm the validity of the simulation studies (cf. Tab. 7.2 and Tab. 7.3).

The experimental data shown in Fig. 4.20 and Fig. 6.20, where fast pressure changes are executed, also demonstrates the excellent performance of the backstepping-based controller. By comparing the measures in Tab. 7.4, it can be seen that the errors $L^1_{\mathrm{r,err}}$, L^∞_{err} of the early-lumping controllers are enlarged by 73 %, 106 % and 79 %, 107 %, respectively, w.r.t. the errors of the backstepping-based controller. Hence, the latter appears to be even more powerful if very fast transitions are intended.

[3] As mentioned before, no such controller exists for the flatness-based approach.

[4] In the following, it is called the backstepping-based controller for the sake of brevity.

Table 7.3: Errors as well as control efforts: The output feedback tracking controllers are applied to the test bench in an experiment

design	Fig.	$L^1_{\mathrm{r,err}}$	L^∞_{err}	L^1_{eff}
backstepping	4.18	1.122 %	0.175 bar	6.658 g
FVM	6.15	1.543 %	0.324 bar	6.635 g
MA	6.17	1.541 %	0.326 bar	6.809 g

Table 7.4: Errors as well as control efforts: The output feedback tracking controllers are applied to the test bench in an experiment with fast pressure changes

design	Fig.	$L^1_{\mathrm{r,err}}$	L^∞_{err}	L^1_{eff}
backstepping	4.20	0.842 %	0.364 bar	5.718 g
FVM	6.19	1.456 %	0.750 bar	5.638 g
MA	not depicted	1.503 %	0.752 bar	5.947 g

Remark 7.3. While this thesis focuses on the test bench configuration in Tab. 3.1, where a tube with a length of $L = 5\,\mathrm{m}$ is considered, the experimental validation of the backstepping-based controller for a tube with $L = 20\,\mathrm{m}$ can be found in [Ker19] as well as in Appx. C. Furthermore, the student theses [Her16; Mei17; Mei18] experimentally validate late-lumping and early-lumping controllers for tubes ranging between $L = 5\,\mathrm{m}$ and $L = 20\,\mathrm{m}$. △

7.2 Concluding Remarks and Outlook

This thesis presented the design and experimental validation of output feedback tracking controllers for a pneumatic system with distributed parameters. The system basically comprises a valve and a tank, connected via a long tube. The valve is characterized by static relations and the tank is modeled by ODEs. In contrast to that, the tube is described by PDEs. Thereby, the spatially distributed character of the tube dynamics was explicitly considered in the model-based controller designs.

Five different test bench models with successively decreasing complexity were presented in Chap. 2. They are described by PDE-ODE systems and range from the very accurate plant model (2.48) to the simplified linear model (2.51). All assumptions involved in the derivation of the models were clearly stated and the resulting system descriptions compared to each other and with measurements. By that, the choice of a suitable model is facilitated, whereby its use is not limited to the context of controller design: The modular model structure allows to, e.g., utilize the tube dynamics of the semilinear model (2.35) in a simulation of a large pneumatic network or of a heavy truck air brake system. In addition, the tank model (2.22) can be easily extended to account for a varying volume. Thereby, for example, the pressure chamber of a pneumatic cylinder can be described. Further research could focus on the development of different dynamic valve models with preferably decreasing complexity. The resulting mathematical description of the test bench would thus belong to the class of ODE-PDE-ODE systems.

To facilitate specified transitions between constant tank pressure levels in finite time, a feedforward controller was designed in Chap. 3. It was demonstrated that the flatness-based approach in [Knü15] can be applied to the isothermal model (2.50) of the test bench in a straightforward manner.

The flatness-based feedforward controller was combined with the backstepping-based state feedback and the state observer, designed in Chap. 4. By that, the infinite-dimensional output feedback tracking controller was derived. As the state observer is based on a collocated measurement, no sensor is required in the tank. Thereby, the wiring costs are reduced and the tank can be installed in environments, where the use of electrical devices and/or metallic materials is limited. The computation of the feedback and observer gains is relatively simple since the presented two-step approach eases the necessary calculations and only two Volterra integral equations have to be solved numerically. Beyond this thesis, the approach in [Aur+18] could be applied to the linear model (2.51) of the test bench. Thereby, a delay-robust backstepping-based state feedback would be obtained, which may be advantageous in an industrial application. In addition, if the valve is modeled by a linear ODE system in order to better capture the valve dynamics, an output feedback tracking controller could be designed for the resulting ODE-PDE-ODE model. Since the approaches in [Knü15] and [DGK18] are suitable for this class of systems, assuming the prerequisites regarding the system properties therein are met, such a controller could be derived by extending the results of this thesis. To improve the tracking performance even further, the following is suggested: First, the isothermal model (2.50) of the test bench is linearized along a desired trajectory, resulting in a linear time-variant PDE-ODE system. This model necessitates the development of a new backstepping-based state feedback and observer design. For that, the approach in [DJK16] might be helpful. Therein, a backstepping-based observer design for a class of distributed-parameter systems, described by linear time-varying hyperbolic partial integro-differential equations, is presented. Furthermore, regarding the implementation of the backstepping-based (and the early-lumping) controller, the minimum approximation order, stabilizing the closed-loop system, could be investigated. For several distributed-parameter systems, such a discussion can be found in [AMD19].

Another late-lumping state feedback and observer design was presented in Chap. 5 by making use of the notion of flatness. The stability analysis and the simulation results indicated that the backstepping-based and the flatness-based designs are related. This relation is an ongoing research topic in a more general context and should be investigated further. Moreover, the unknown coordinate transformation, preventing the implementation of the controller at the test bench, requires additional studies. Meanwhile, the approach in [WRE17; RW18], which is a combination of early- and late-lumping, suggests that this transformation might not be necessary. An output feedback controller, derived based on this method, is currently being investigated. First experimental results for the pneumatic test bench in this thesis are already very promising.

In order to compare the proposed infinite-dimensional backstepping-based controller to state-of-the-art controller designs by early-lumping, finite-dimensional output feedback tracking controllers were designed in Chap. 6. For that, two established approximation approaches were applied to the linear model. Future research could also consider a nonlinear finite-dimensional model, which can be derived by, e.g., applying the FVM to the semilinear model (2.35) of the test bench. Based on this approximation, nonlinear finite-dimensional controllers could be designed and compared to the presented late-

lumping controllers. First results for a nonlinear model predictive control design can be found in the student theses [Mei17] and [Ame17].

The late-lumping and early-lumping controller designs were discussed in a comparative analysis. Thereby, considering theoretical and implementation aspects, the differences and similarities of the approaches were pointed out. While the use of an infinite-dimensional output feedback controller might be unusual for its perceived purely theoretical value, it was shown that such a controller can be obtained in a relatively straightforward manner by making use of the two-step backstepping approach. Furthermore, based on the presented simulation and experimental data, it was demonstrated that the backstepping-based output feedback controller, combined with the flatness-based feedforward controller, yields a high-performance control law. It accurately executes fast pressure changes in the tank and, hence, in the system. At the same time, the control effort is kept low, limiting the amount of compressed air consumed. Thus, a controller was presented that allows for the efficient operation of pneumatic systems, where long tubes are involved.

Appendix A

Components of the Test Bench

The main components of the test bench can be classified into five categories: the tubes and tanks, the sensors, the actuators, the real-time system, and the auxiliary components. Tab. A.1 lists the polyurethane tubes and high-alloy stainless steel tanks used in the experiments in this thesis. The volume of each tank is determined by measuring the mass of water that fits into the tank. The sensors are listed in Tab. A.2. While the SPTE pressure sensor is less accurate compared to the SPTW pressure sensor, the former has a shorter rise time, rendering it more suitable for the measurement of transient pressure trajectories. Hence, the SPTW sensor, depicted in Fig. A.1, measures a reference pressure in steady state which is used to calibrate the SPTE pressure sensors prior to an experiment. Tab. A.3 summarizes the actuators at the test bench. If the test bench is operated in the standard configuration in Fig. 2.1, the VPPM proportional pressure regulator valve as well as the SFAB mass flow rate sensor and the Pt1000 temperature sensor are not installed. These components are only used to obtain the inverse mass flow rate and temperature model of the valve in (2.19) and (2.20), respectively (cf. Sec. 2.3). The components of the real-time system are listed in Tab. A.4. During the experiments, all computations are performed on the real-time target machine. It is connected to the actuators and sensors via the IO116 module. The auxiliary components are stated in Tab. A.5. As depicted in Fig. A.1, a filter regulator is installed between the compressed air supply and an air reservoir. It filters the compressed air to avoid particles in the valve and allows to reduce the supply pressure. The air reservoir, connected to the MPYE proportional directional control valve, stores the compressed air, reducing fluctuations in the supply pressure.

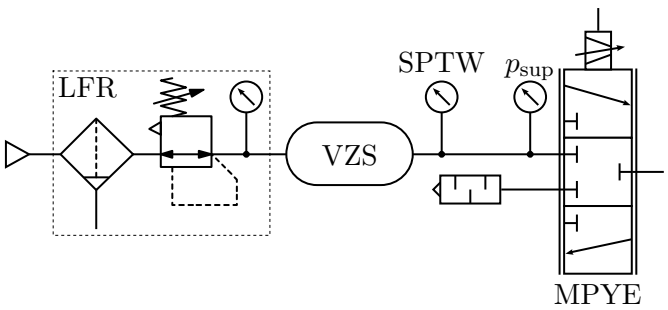

Figure A.1: Auxiliary components between the compressed air supply and the MPYE valve

Table A.1: Polyurethane tubes and high-alloy stainless steel tanks

component	manufacturer	product	properties
tube	Festo	PUN-6×1-SW	$D = 4\,\mathrm{mm}$
tube	Festo	PUN-12×1.25-SW	$D = 5.7\,\mathrm{mm}$
tube	Festo	PUN-12×2-SW	$D = 8\,\mathrm{mm}$
tank	Festo	CRVZS-0.1	$V_{\mathrm{vol}} = 0.10 \cdot 10^{-3}\,\mathrm{m}^3$
tank	Festo	CRVZS-0.75	$V_{\mathrm{vol}} = 0.64 \cdot 10^{-3}\,\mathrm{m}^3$

Table A.2: Sensors

sensor	manufacturer	product	accuracy
pressure	Festo	SPTE-P10R-S6-B-2.5K	$\pm 0.3\,\mathrm{bar}$
pressure	Festo	SPTW-P10R-G14-A-M12	$\pm 0.1\,\mathrm{bar}$
mass flow rate	Festo	SFAB-1000U-HQ12-2SA-M12-EX2	$\pm 0.65 \cdot 10^{-3}\,\mathrm{kg/s}$
temperature	B+B Thermo-Technik	Pt1000 A	$\pm\left(0.15 + 0.002\lvert T\rvert\right)\,°\mathrm{C}$

Table A.3: Actuators

actuator	manufacturer	product
proportional directional control valve	Festo	MPYE MPYE-5-1/8-LF-10-B
proportional pressure regulator valve	Festo	VPPM-8F-L-1-0L10H-V1P-S1

Table A.4: Components of the real-time system

component	manufacturer	product	specifications
computer	Speedgoat	performance real-time target machine	CPU: i7-6700K 4.0 GHz RAM: 4096 MB
I/O module	Speedgoat	IO116	resolution: 16 bit model sample rate

Table A.5: Auxiliary components

component	manufacturer	product
filter regulator	Festo	LFR-1/4-D-5M-MIDI
air reservoir	Festo	VZS-20-B

Appendix B

Numerical Approximation Schemes

In the following, the numerical approximation schemes, used to solve the PDEs and ODEs in this thesis, are stated. As for all other computations, these are implemented in MATLAB R2018a.

B.1 Implementation of the Systems

The systems in this thesis are mostly composed of a PDE subsystem coupled to an ODE subsystem. In order to solve these numerically, finite difference methods are chosen to discretize the continuous system description, e.g., for simulations involving the test bench models or for the experimental validation of the backstepping-based output feedback tracking controller.

B.1.1 Approximation of PDEs

To numerically solve the hyperbolic PDE (2.1), first, the normalized spatial variable $z \in [0,1]$ is discretized by choosing N_z points in space at the positions $z^n = (n-1)\Delta z$, $n = 1, \ldots, N_z$, where the constant spatial step size reads $\Delta z = 1/(N_z - 1)$. The discrete points in time $t \in [0, t_\mathrm{f}]$, where t_f denotes the duration of the simulation or the experiment, are specified by $t_m = m\Delta t_m$, $m = 0, \ldots, N_t$. If the PDE is quasilinear, the time step size Δt_m is non-constant and, hence, the number of time steps N_t not known a priori.

Next, in order to obtain an approximation $\boldsymbol{X}_m^n \approx \boldsymbol{x}(z^n, t_m) \in \mathbb{R}^k$ of the state $\boldsymbol{x}(z,t)$ of the PDE (2.1) at appropriate grid points (z^n, t_m), a suitable numerical scheme has to be chosen. This thesis makes use of the two-step MacCormack method for hyperbolic systems with a source term since it is easy to implement and often yields results with perfectly sufficient accuracy, e.g., [Hir90; And95]. Applying this scheme to the PDE (2.1) yields two algebraic equations:

$$\boldsymbol{X}_*^n = \boldsymbol{X}_m^n - \frac{\Delta t_m}{\Delta z}\left[\boldsymbol{g}\left(\boldsymbol{X}_m^{n+1}\right) - \boldsymbol{g}\left(\boldsymbol{X}_m^n\right)\right] + \Delta t_m \boldsymbol{c}\left(\boldsymbol{X}_m^n\right) \tag{B.1a}$$

$$\boldsymbol{X}_{m+1}^n = \frac{1}{2}\left[\boldsymbol{X}_m^n + \boldsymbol{X}_*^n\right] - \frac{\Delta t_m}{2\Delta z}\left[\boldsymbol{g}\left(\boldsymbol{X}_*^n\right) - \boldsymbol{g}\left(\boldsymbol{X}_*^{n-1}\right)\right] + \frac{\Delta t_m}{2}\boldsymbol{c}\left(\boldsymbol{X}_*^n\right), \tag{B.1b}$$

where (B.1a) is defined for $n = 1, \ldots, N_z - 1$ and (B.1b) for $n = 2, \ldots, N_z - 1$. First, the predictor step (B.1a) is evaluated, resulting in $\boldsymbol{X}_*^n \in \mathbb{R}^k$. Subsequently, the approximation $\boldsymbol{X}_{m+1}^n$ of the state $\boldsymbol{x}(z^n, t_{m+1})$ in the new time step is obtained from the corrector step (B.1b).

The values of $\boldsymbol{X}_{m+1}^1$ at $z = 0$ and $\boldsymbol{X}_{m+1}^{N_z}$ at $z = 1$ are undefined in (B.1b) but follow from the boundary conditions of (2.1). Usually, there exist k physical boundary conditions, necessitating k additional numerical boundary conditions, e.g., [Hir90]. In this thesis, the numerical boundary conditions are determined by the first-order extrapolations

$$\begin{aligned} X_{m+1}^1 &= 2X_{m+1}^2 - X_{m+1}^3 \\ X_{m+1}^{N_z} &= 2X_{m+1}^{N_z-1} - X_{m+1}^{N_z-2}, \end{aligned}$$

where X_{m+1}^1 and $X_{m+1}^{N_z}$ are the quantities which are not specified by physical boundary conditions.

The variable time step size Δt_m in (B.1) follows from

$$\Delta t_m = \frac{C_{\mathrm{CFL}} \Delta z}{\lambda_{\max}} \quad \text{with} \quad \lambda_{\max} = \max_{i,n} \left| \lambda_i(\boldsymbol{X}_m^n) \right|, \tag{B.2}$$

where $i = 1, \ldots, k$, e.g., [Tor09]. Therein, $\lambda_i(\boldsymbol{X}_m^n)$ denotes the eigenvalues[1] of $\boldsymbol{B}(\boldsymbol{X}_m^n) \in \mathbb{R}^{k \times k}$, where $\boldsymbol{B}(\boldsymbol{x})$ is defined in (2.49). To satisfy the so-called Courant–Friedrichs–Lewy (CFL) condition, necessary for numerical stability, the coefficient C_{CFL} has to be chosen as $0 < C_{\mathrm{CFL}} \leq 1$, e.g., [Tor09]. Since this choice alters the dispersion and diffusion errors of the approximation scheme, the numerical solution of (2.1) slightly depends on C_{CFL}, especially if discontinuities are present, e.g., [Hir07]. According to [Tor09], an adequate choice is $C_{\mathrm{CFL}} = 0.9$, assuming that $\lambda_{\max}$ can be predicted relatively accurately. If $\lambda_{\max}$ can only be roughly estimated, a smaller value of C_{CFL} has to be chosen.

The approach is summarized in Alg. B.1. Therein, t_{f} defines N_t based on the condition $t_m < t_{\mathrm{f}}$.

Throughout this thesis, $N_z = 201$ and $C_{\mathrm{CFL}} = 0.7$ are chosen for the simulations. In contrast to that, in experiments, the number of points in space is set to $N_z = 21$ and C_{CFL} results from the time step Δt_m, which is in turn defined by the fixed sample time $\Delta t_m = \Delta t = 5 \cdot 10^{-4}\,\mathrm{s}$ of the test bench. The chosen value of N_z guarantees the on-time execution of all necessary computations, such as the evaluation of the output feedback tracking controller, on the real-time target machine, given in Tab. A.4. A refinement of the grid, e.g., by increasing N_z, would not improve the respective results significantly.

B.1.2 Approximation of ODEs

In general, the ODEs in this thesis can be stated as

$$\frac{\mathrm{d}}{\mathrm{d}t} \boldsymbol{X}(t) = \boldsymbol{f}(\boldsymbol{X}(t), \boldsymbol{U}(t)). \tag{B.3}$$

In simulations, the ODEs are solved by the MATLAB function `ode45()` if (B.3) is nonlinear, the standard method for non-stiff ODEs, e.g., [WSV14]. If (B.3) is linear, the MATLAB function `lsim()` is used, the standard method for linear ODEs, e.g., [Oga10].

[1] For semilinear and linear hyperbolic systems, $\boldsymbol{B}$ is constant. Hence, $\lambda_{\max}$ is constant and known a priori, rendering Δt_m constant, too.

Algorithm B.1: Numerical solution of the PDE (2.1)

```
for n = 1 : 1 : N_z do
    initialize X_0^n = x(z^n, 0);
m = 0;
while true do
    evaluate (B.2) to calculate Δt_m;
    if t_m ≥ t_f then
        break;
    for n = 1 : 1 : N_z − 1 do
        evaluate (B.1a) to calculate X_*^n;
    for n = 2 : 1 : N_z − 1 do
        evaluate (B.1b) to calculate X_{m+1}^n;
    evaluate the physical and the numerical boundary conditions at z = 0 and z = 1;
    m = m + 1;
N_t = m;
```

To perform real-time experiments, C/C++ code is generated from the Simulink models. In this case, the use of `ode45()` is limited and `lsim()` is not supported. Thus, the explicit Euler method is utilized to solve (B.3), resulting in

$$\boldsymbol{X}_{m+1} = \boldsymbol{X}_m + \Delta t \boldsymbol{f}(\boldsymbol{X}_m, \boldsymbol{U}_m),$$

e.g., [Tor09]. Therein, $\boldsymbol{X}_m \approx \boldsymbol{X}(t_m)$ as well as $\boldsymbol{U}_m = \boldsymbol{U}(t_m)$ holds and Δt is the fixed sample time $\Delta t = 5 \cdot 10^{-4}\,\mathrm{s}$ of the test bench.

B.2 Numerical Application of the Method of Characteristics

To calculate the feedforward controller $U^{\mathrm{r}}(t)$ with the corresponding reference[2] state $\bar{\boldsymbol{w}}^{\mathrm{r}}(z,t) \in \mathbb{R}^2$ in the diagonal form (3.2) (cf. Chap. 3), the Cauchy problem, consisting of the ODEs (3.13), subject to the initial data (3.1) at $z = 0$, is solved numerically.

For that, the spatial coordinate z as well as the time t are discretized. Thereby, a grid with the points (z^n, t_m) results, defined as in Sec. B.1.1 but with a fixed time step size $\Delta t_m = \Delta t$. The value of Δt, specified a priori, is constant in order to obtain the approximation $\bar{\boldsymbol{W}}_m^n = [\bar{W}_{1,m}^n, \bar{W}_{2,m}^n]^T \approx \bar{\boldsymbol{w}}(n\Delta z, m\Delta t)$ on an uniformly spaced grid, simplifying the implementation.

Remark B.1. The a priori defined step sizes Δz and Δt have to be chosen in order to fulfill the CFL condition

$$C_{\mathrm{CFL}} = \frac{\Delta t}{\Delta z}\bar{\lambda}_{\max} \leq 1 \quad \text{with} \quad \bar{\lambda}_{\max} = \max_{i,n,m}\left|\bar{\lambda}_i(\bar{\boldsymbol{W}}_m^n)\right|,$$

[2] In the following, the superscript r is neglected, simplifying the notation.

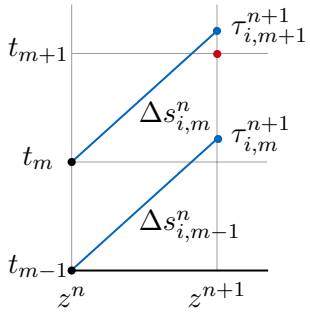

Figure B.1: Integration along the characteristic curves and subsequent interpolation

necessary for numerical stability, e.g., [Tor09]. Therein, $\bar{\lambda}_i(\bar{\boldsymbol{W}}_m^n)$, $i = 1, 2$, is defined in (3.7a). △

Next, the numerical scheme to compute the approximation $\breve{W}_{i,m}^n \approx \breve{w}_i(s_{i,m}^n)$, $i = 1, 2$, at $\zeta_{i,m}^n = \zeta_i(s_{i,m}^n)$ and $\tau_{i,m}^n = \tau_i(s_{i,m}^n)$, where $\breve{w}_i(s_{i,m}^n) = \bar{w}_i(\zeta_i(s_{i,m}^n), \tau_i(s_{i,m}^n))$ and $\zeta_{i,m}^n = z^n$ hold, is presented. The quantities $\zeta_i(s)$, $\tau_i(s)$, and $\breve{w}_i(s)$ are defined in (3.13) and $s_{i,m}^n$ denotes the discrete value of s at $\zeta_{i,m}^n$ and $\tau_{i,m}^n$. To discretize the ODEs (3.13), derived by the method of characteristics, the explicit Euler method is applied. Thereby, the solution

$$\breve{W}_{i,m+1}^{n+1} = \breve{W}_{i,m}^n + \Delta s_{i,m}^n \bar{c}(\breve{\boldsymbol{W}}_m^n) \tag{B.4}$$

in the next step at $(\zeta_{i,m+1}^{n+1}, \tau_{i,m+1}^{n+1})$ results from (3.13c), where $\breve{\boldsymbol{W}}_m^n = [\breve{W}_{1,m}^n, \breve{W}_{2,m}^n]^T$. The non-constant step size $\Delta s_{i,m}^n = s_{i,m+1}^{n+1} - s_{i,m}^n$ along a characteristic curve follows from the discretization of (3.13a), i.e.

$$\zeta_{i,m+1}^{n+1} = \zeta_{i,m}^n - \Delta s_{i,m}^n \bar{\lambda}(\breve{\boldsymbol{W}}_m^n). \tag{B.5}$$

Solving (B.5) for $\Delta s_{i,m}^n$ yields

$$\Delta s_{i,m}^n = -\frac{\Delta \zeta_{i,m}^n}{\bar{\lambda}(\breve{\boldsymbol{W}}_m^n)}, \tag{B.6}$$

where $\Delta \zeta_{i,m}^n = \zeta_{i,m+1}^{n+1} - \zeta_{i,m}^n = z^{n+1} - z^n = \Delta z$ is the fixed spatial step. From (3.13b), the time

$$\tau_{i,m+1}^{n+1} = \tau_{i,m}^n + \Delta s_{i,m}^n \tag{B.7}$$

is obtained.

While $\zeta_{i,m+1}^{n+1} = z^{n+1}$ holds, $\tau_{i,m+1}^{n+1} \neq t_{m+1}$ may result as the characteristic curves of quasi-linear systems are not necessarily linear and/or if $C_{\mathrm{CFL}} < 1$ is considered (cf. Rem. B.1). To obtain the quantities $\bar{W}_{i,m+1}^{n+1}$ at (z^{n+1}, t_{m+1}), a linear interpolation is performed between the values of $\breve{W}_{i,m}^{n+1}$ and $\breve{W}_{i,m+1}^{n+1}$ at $(z^{n+1}, \tau_{i,m}^{n+1})$ and $(z^{n+1}, \tau_{i,m+1}^{n+1})$, respectively. Fig. B.1 exemplarily depicts this procedure for the calculation of $\bar{W}_{i,m+1}^{n+1}$: The values for $\bar{W}_{i,m-1}^n$ and $\bar{W}_{i,m}^n$ (black dots) are given at (z^n, t_{m-1}) and (z^n, t_m), respectively. Integrating along the characteristic curves (blue lines) with the step sizes $\Delta s_{i,m-1}^n$ and $\Delta s_{i,m}^n$ yields $\breve{W}_{i,m}^{n+1}$ and $\breve{W}_{i,m+1}^{n+1}$ (blue dots) at $(z^{n+1}, \tau_{i,m}^{n+1})$ and $(z^{n+1}, \tau_{i,m+1}^{n+1})$, respectively. From an interpolation, $\bar{W}_{i,m+1}^{n+1}$ (red dot) at (z^{n+1}, t_{m+1}) results. Hence, to be precise, $\breve{W}_{i,m}^n$ in (B.4)–(B.6) needs to be replaced by $\bar{W}_{i,m}^n$

Obviously, to solve (3.13) with the above stated scheme, the initial data $\bar{W}^1_{i,m}$ at $(\zeta^1_{i,m}, \tau^1_{i,m}) = (0, t_m)$ needs to be specified first. By making use of the flatness-based parametrization of $\bar{\boldsymbol{w}}(0, t_m)$ in (3.1), $\bar{W}^1_{i,m}$ follows. Furthermore, since the flow is assumed to be subsonic with $Ma < 1$ (cf. Sec. 2.5), $\bar{\lambda}_1(\bar{\boldsymbol{W}}^n_m) < 0$ and $\bar{\lambda}_2(\bar{\boldsymbol{W}}^n_m) > 0$ holds in (B.5) and (B.6). Therefore, as $\Delta\tau^n_{1,m} > 0$ and $\Delta\tau^n_{2,m} < 0$, where $\Delta\tau^n_{i,m} = \tau^{n+1}_{i,m+1} - \tau^n_{i,m}$ results from (B.7), the integration along the characteristic curves to calculate $\breve{W}^{n+1}_{1,m+1}$ and $\breve{W}^{n+1}_{2,m+1}$ is forward and backward in time, respectively.

Remark B.2. For each next step at z^{n+1}, $2N_t$ new characteristic curves enter the grid from the boundaries at $t = 0$ as well as $t = t_\mathrm{f}$ and have to be taken into account. These are defined by the steady-states $\bar{\boldsymbol{w}}_\mathrm{b}(z)$ and $\bar{\boldsymbol{w}}_\mathrm{e}(z)$, respectively (cf. Sec. 3.2). Simultaneously, the same number of characteristic curves is discarded since they exceed one of these boundaries. △

Algorithm B.2 summarizes the numerical integration scheme.

Algorithm B.2: Numerical integration along the characteristic curves

```
initialize W̄^1_{i,m} = w̄_i(0, t_m) for i = 1, 2;
for n = 1 : 1 : N_z − 1 do
    for m = 1 : 1 : N_t do
        integrate along the characteristic curves to calculate W̆^{n+1}_{i,m+1} at (ζ^{n+1}_{i,m+1}, τ^{n+1}_{i,m+1});
        calculate W̄^{n+1}_{i,m+1} at (z^{n+1}, t_{m+1}) by interpolating between W̆^{n+1}_{i,m} and W̆^{n+1}_{i,m+1};
    replace the characteristic curves at t = 0 and t = t_f;
```

Appendix C

Nonlinear State Observer

For some test bench configurations, e.g., with a very long tube and/or highly dynamic pressure changes, the tracking performance of the backstepping-based output feedback tracking controller in Chap. 4 may not be adequate. Such a scenario is considered in the following. For that, the standard configuration in Tab. 3.1 is adapted and a very long tube with $L = 20\,\mathrm{m}$ as well as $D = 5.7\,\mathrm{mm}$ installed at the test bench.

To motivate the design of the nonlinear state observer, the output feedback tracking controller (4.77) with the linear state observer is applied to the plant model (2.48) with the very long tube in a simulation. While the design parameters k and ℓ are chosen as in Sec. 4.6, i.e. such that $a - bk = -20$ and $a - \ell c = -20$ hold in (4.21d) and (4.49d), respectively, the increased tube length necessitates two adjustments: First, the transitions of the standard reference pressure trajectory in Fig. 3.2 are reduced to a rate of $2\,{}^{\mathrm{bar}}/_{\mathrm{s}}$ in order to respect the physical limits of the valve. Second, for the design of the state feedback and observer, the friction amplification factor is set to $k_{\mathrm{fric}} = 1$. Although this choice underestimates friction effects in turbulent flow with high velocities, it is more accurate for laminar flow with low velocities. Naturally, the tracking performance during the transitions, where the flow is turbulent, will be degraded. However, a controller with $k_{\mathrm{fric}} = 1$ achieves steady-state accuracy, where the flow is laminar and the velocity tends to zero. In contrast to that, a design with $k_{\mathrm{fric}} = 4$ leads to undesired oscillations and does not guarantee steady-state accuracy.

The results of this simulation are depicted in Fig. C.1 and the corresponding deviations in Fig. C.2. It can be seen that the estimated tank pressure $\hat{p}_{\mathrm{vol}}(t)$ significantly deviates from the actual tank pressure $p_{\mathrm{vol}}(t)$ during the transitions. This mismatch occurs from the relatively large observer error, caused by the increased length of the tube. As a consequence, the transient tank pressure $p_{\mathrm{vol}}(t)$ does not match the desired reference pressure $p_{\mathrm{vol}}^{\mathrm{r}}(t)$.

An approach to tackle this unsatisfactory controller performance is presented in [RNM16]. Therein, without proof of stability, a nonlinear finite-dimensional state observer is designed for a pneumatic system similar to the test bench in Fig. 1.3. For that, first, the observer gain is derived based on a linear lumped-parameter model. Subsequently, this model is augmented by a nonlinear friction term. By injecting the measurement error, multiplied by the gain previously designed, into a copy of the augmented model, the nonlinear state observer follows. Its excellent performance is validated in experiments. Similar results are also obtained in [Fal17] (in German), where the design of this nonlinear state observer is slightly modified for a varying volume.

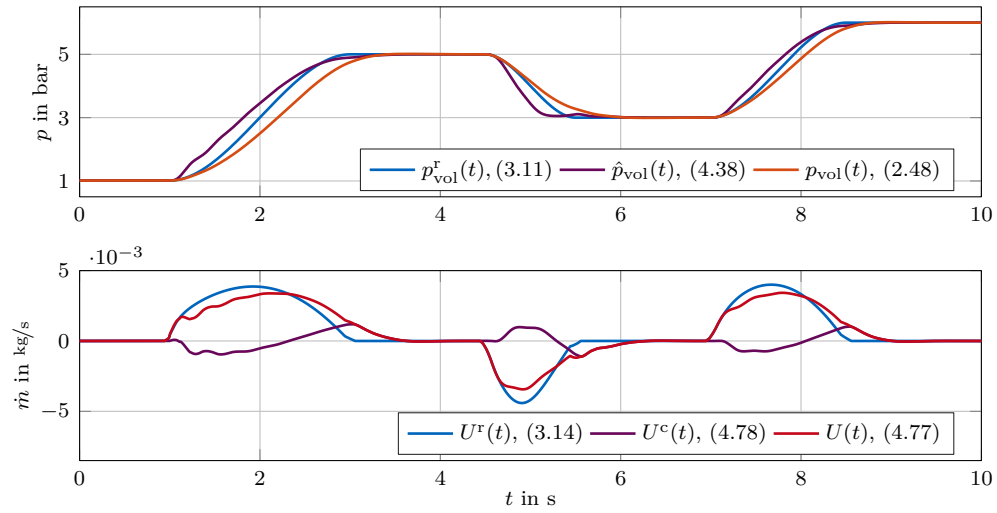

Figure C.1: Application of the output feedback tracking controller (4.77) to the plant model (2.48) with a tube of $L = 20\,\mathrm{m}$: Reference pressure $p^{\mathrm{r}}_{\mathrm{vol}}(t)$, estimated pressure $\hat{p}_{\mathrm{vol}}(t)$, and tank pressure $p_{\mathrm{vol}}(t)$ as well as corresponding control input $U(t)$ with feedforward part $U^{\mathrm{r}}(t)$ and feedback part $U^{\mathrm{c}}(t)$

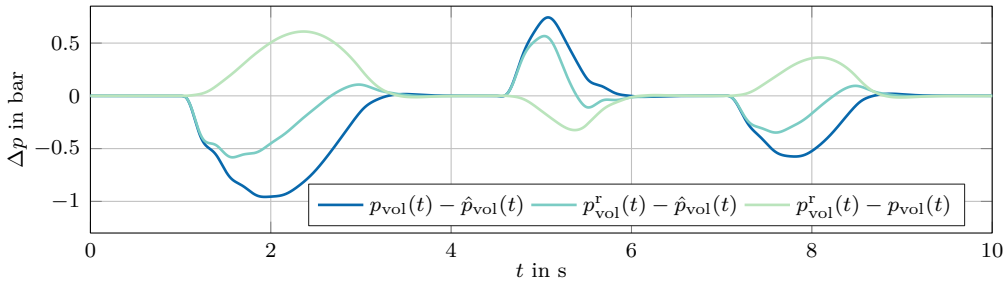

Figure C.2: Deviations between the reference pressure $p^{\mathrm{r}}_{\mathrm{vol}}(t)$, the estimated pressure $\hat{p}_{\mathrm{vol}}(t)$, and the tank pressure $p_{\mathrm{vol}}(t)$ in Fig. C.1

C.1 Design of the Nonlinear State Observer

Here, the idea in [RNM16] is utilized to design a nonlinear infinite-dimensional state observer based on the plant model since it is the most accurate description of the test bench. For that, first, the linear backstepping-based state observer (4.38), derived from the standard backstepping form (4.1), is rewritten in conservative form by applying the inverse transformations of (4.2) and (4.5). From that,

$$\frac{\partial}{\partial t}\hat{\boldsymbol{x}} = \boldsymbol{B}\frac{\partial}{\partial z}\hat{\boldsymbol{x}} + \boldsymbol{C}\hat{\boldsymbol{x}} + \bar{\boldsymbol{l}}\left(\frac{1}{R_\mathrm{s}T_0}Y - \hat{x}_1(1)\right) \tag{C.1a}$$

$$\hat{x}_1(0,t) = \hat{\xi}(t) \tag{C.1b}$$

$$\hat{x}_2(1,t) = \frac{1}{A}U(t) + a_\mathrm{iso}\left(\frac{1}{R_\mathrm{s}T_0}Y(t) - \hat{x}_1(1,t)\right) \tag{C.1c}$$

$$\frac{\mathrm{d}}{\mathrm{d}t}\hat{\xi}(t) = \frac{A}{V_\mathrm{vol}}\hat{x}_2(0,t) + \bar{l}_\xi\left(\frac{1}{R_\mathrm{s}T_0}Y(t) - \hat{x}_1(1,t)\right) \tag{C.1d}$$

is obtained. Therein, $\boldsymbol{B}$ and $\boldsymbol{C}$ are defined in (2.51). The observer gains

$$\bar{\boldsymbol{l}}(z) = \begin{bmatrix} \mathrm{e}^{\alpha\tau_0(1-z)} & -\mathrm{e}^{\alpha\tau_0(1+z)} \\ -a_\mathrm{iso}\mathrm{e}^{\alpha\tau_0(1-z)} & -a_\mathrm{iso}\mathrm{e}^{\alpha\tau_0(1+z)} \end{bmatrix}\boldsymbol{l}(z) \tag{C.2a}$$

$$\bar{l}_\xi = -\mathrm{e}^{\alpha\tau_0}l_\eta \tag{C.2b}$$

in conservative form, where $\bar{\boldsymbol{l}}(z) = [\bar{l}_1(z), \bar{l}_2(z)]^T \in \mathbb{R}^2$, follow from the gains $\boldsymbol{l}(z)$, l_η in (4.60).

Next, based on the error injections in the state observer (C.1), the error $Y(t)/(R_\mathrm{s}T_0) - \hat{\rho}(1,t)$ with the corresponding gain is injected into a copy of the plant model (2.48). By that, the nonlinear infinite-dimensional state observer[1]

$$\frac{\partial}{\partial t}\hat{\rho} = \frac{1}{L}\frac{\partial}{\partial z}(\hat{\rho}\hat{v}) + \bar{l}_1\left(\frac{1}{R_\mathrm{s}T_0}Y - \hat{\rho}(1)\right) \tag{C.3a}$$

$$\frac{\partial}{\partial t}(\hat{\rho}\hat{v}) = \frac{1}{L}\frac{\partial}{\partial z}(\hat{\rho}\hat{v}^2 + \hat{p}) - f_\mathrm{c}\frac{\hat{\rho}\hat{v}|\hat{v}|}{2D} + \bar{l}_2\left(\frac{1}{R_\mathrm{s}T_0}Y - \hat{\rho}(1)\right) \tag{C.3b}$$

$$\frac{\partial}{\partial t}(\hat{\rho}\hat{e}) = \frac{1}{L}\frac{\partial}{\partial z}(\hat{v}(\hat{\rho}\hat{e} + \hat{p})) + \frac{4}{D}\alpha(T_0 - \hat{T}) - f_\mathrm{c}\frac{\hat{\rho}\hat{v}^2|\hat{v}|}{2D} \tag{C.3c}$$

$$\hat{\rho}(0,t) = \begin{cases} \hat{\rho}_\mathrm{vol}(t), & (\hat{\rho}\hat{v})(0,t) \le 0 \\ \hat{\rho}(0,t), & (\hat{\rho}\hat{v})(0,t) > 0 \end{cases} \tag{C.3d}$$

$$(\hat{\rho}\hat{e})(0,t) = \begin{cases} \frac{1}{2}\hat{\rho}_\mathrm{vol}(t)\hat{v}^2(0,t) + \frac{1}{\gamma-1}\hat{p}_\mathrm{vol}(t), & (\hat{\rho}\hat{v})(0,t) \le 0 \\ \frac{1}{2}(\hat{\rho}\hat{v}^2)(0,t) + \frac{1}{\gamma-1}\hat{p}_\mathrm{vol}(t), & (\hat{\rho}\hat{v})(0,t) > 0 \end{cases} \tag{C.3e}$$

$$\hat{\rho}(1,t) = \begin{cases} \rho_\mathrm{in}(t), & (\hat{\rho}\hat{v})(1,t) \ge 0 \\ \hat{\rho}(1,t), & (\hat{\rho}\hat{v})(1,t) < 0 \end{cases} \tag{C.3f}$$

$$(\hat{\rho}\hat{v})(1,t) = \frac{1}{A}U(t) + a_\mathrm{iso}\left(\frac{1}{R_\mathrm{s}T_0}Y(t) - \hat{\rho}(1,t)\right) \tag{C.3g}$$

$$\frac{\mathrm{d}}{\mathrm{d}t}\hat{\rho}_\mathrm{vol}(t) = \frac{A}{V_\mathrm{vol}}(\hat{\rho}\hat{v})(0,t) + \bar{l}_\rho\left(\frac{1}{R_\mathrm{s}T_0}Y(t) - \hat{\rho}(1,t)\right) \tag{C.3h}$$

[1] In fact, $\hat{\rho}\hat{v}$ and $\hat{\rho}\hat{e}$ should be replaced by $\hat{\rho v}$ and $\hat{\rho e}$, respectively. This imprecision is accepted here since it avoids expressions such as $\hat{\rho v}/\hat{\rho}$ instead of $\hat{v}$, which increases the readability.

$$\frac{\mathrm{d}}{\mathrm{d}t}\hat{p}_{\mathrm{vol}}(t) = A\frac{\gamma-1}{V_{\mathrm{vol}}}\left[\frac{1}{2}(\hat{\rho}\hat{v}^3)(0,t) + \frac{\gamma}{\gamma-1}\hat{p}_{\mathrm{vol}}(t)\hat{v}(0,t) + \frac{1}{AR_{\mathrm{vol}}}\left(T_0 - \frac{\hat{p}_{\mathrm{vol}}(t)}{R_{\mathrm{s}}\hat{\rho}_{\mathrm{vol}}(t)}\right)\right] \tag{C.3i}$$

is obtained.

C.2 Simulation Study

The output feedback tracking controller

$$U(t) = U^{\mathrm{r}}(t) + U^{\mathrm{c}}(t) \tag{C.4}$$

follows from (4.77) by replacing the estimates in the error states $\tilde{\boldsymbol{w}}(z,t) = \hat{\boldsymbol{w}}(z,t) - \boldsymbol{w}^{\mathrm{r}}(z,t)$, $\tilde{\eta}(t) = \hat{\eta}(t) - \eta^{\mathrm{r}}(t)$ in the feedback part

$$U^{\mathrm{c}}(t) = A\left(\mathrm{e}^{-\alpha\tau_0}\tilde{w}_1(1,t) + \mathrm{e}^{\alpha\tau_0}\mathcal{K}[\tilde{\eta}(t), \tilde{\boldsymbol{w}}(t)]\right), \tag{C.5}$$

defined in (4.78), by the states $\hat{\rho}(z,t)$, $(\hat{\rho}\hat{v})(z,t)$, $(\hat{\rho}\hat{e})(z,t)$, $\hat{\rho}_{\mathrm{vol}}(t)$, $\hat{p}_{\mathrm{vol}}(t)$ of the nonlinear state observer (C.3).

To show the excellent performance of the output feedback tracking controller (C.4), it is applied to the plant model (2.48) in a simulation. The results are depicted in Fig. C.3 and the deviations in Fig. C.4. It can be seen that the controller tracks the reference trajectory almost perfectly. Compared to the same scenario with the linear state observer in Fig. C.1, the errors are significantly decreased. The improved tracking behavior also becomes apparent by making use of the error measures in (2.42) and (2.43), quantifying the deviations. From that, $\mathrm{L}^1_{\mathrm{r,err}} = 3.533\,\%$, $L^\infty_{\mathrm{err}} = 0.610\,\mathrm{bar}$ and $\mathrm{L}^1_{\mathrm{r,err}} = 1.298\,\%$, $L^\infty_{\mathrm{err}} = 0.194\,\mathrm{bar}$ result from the simulation depicted in Fig. C.1 and Fig. C.3, respectively.

C.3 Experimental Results

In addition to the previous simulation study, the controller (C.4) is validated experimentally at the test bench with the very long tube. The results are depicted in Fig. C.5 and the corresponding deviations in Fig. C.6. The errors are quantified by $\mathrm{L}^1_{\mathrm{r,err}} = 1.415\,\%$ and $L^\infty_{\mathrm{err}} = 0.241\,\mathrm{bar}$. Obviously, the experimental data is almost identical to the simulation data in Fig. C.3 and Fig. C.4. The excellent tracking performance proves the effectiveness of the nonlinear state observer.

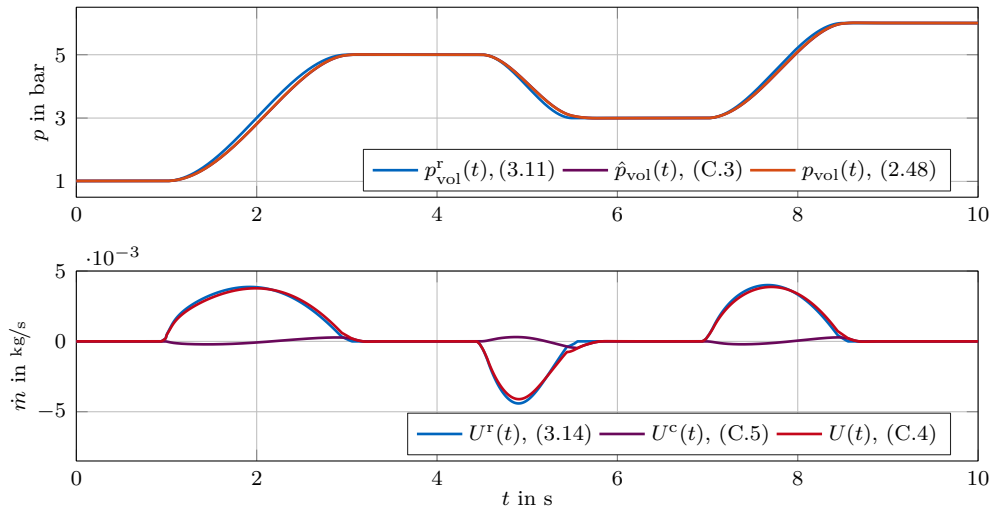

Figure C.3: Application of the output feedback tracking controller (4.77) to the plant model (2.48) with a tube of $L = 20\,\mathrm{m}$: Reference pressure $p^{\mathrm{r}}_{\mathrm{vol}}(t)$, estimated pressure $\hat{p}_{\mathrm{vol}}(t)$, and tank pressure $p_{\mathrm{vol}}(t)$ as well as corresponding control input $U(t)$ with feedforward part $U^{\mathrm{r}}(t)$ and feedback part $U^{\mathrm{c}}(t)$

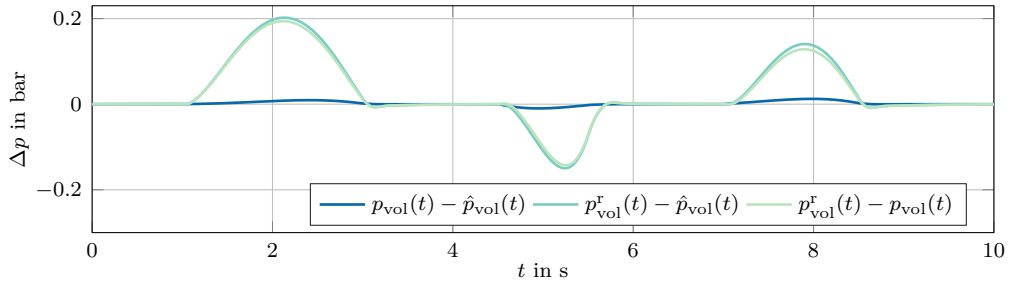

Figure C.4: Deviations between the reference pressure $p^{\mathrm{r}}_{\mathrm{vol}}(t)$, the estimated pressure $\hat{p}_{\mathrm{vol}}(t)$, and tank pressure $p_{\mathrm{vol}}(t)$ in Fig. C.3

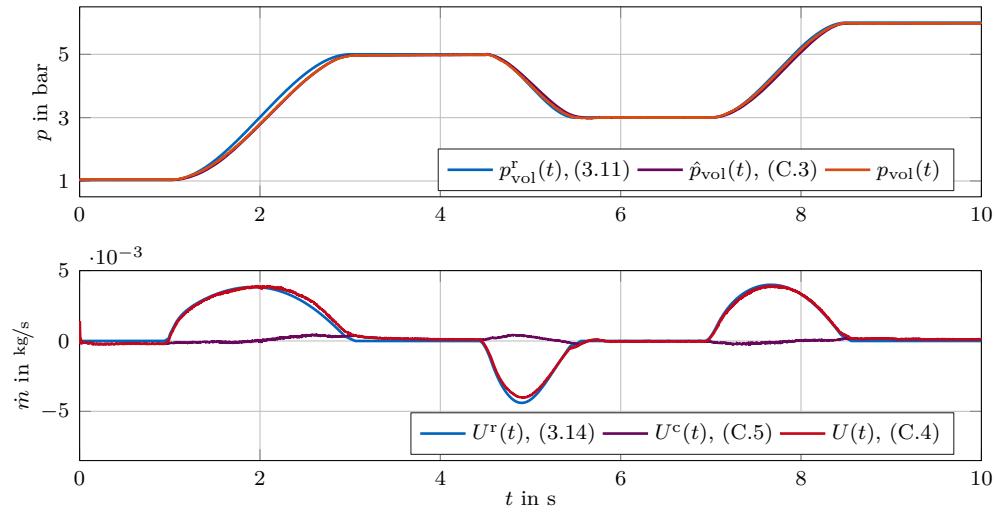

Figure C.5: Application of the output feedback tracking controller (4.77) to the test bench with a tube of $L = 20\,\mathrm{m}$: Reference pressure $p^{\mathrm{r}}_{\mathrm{vol}}(t)$, estimated pressure $\hat{p}_{\mathrm{vol}}(t)$, and measured tank pressure $p_{\mathrm{vol}}(t)$ as well as corresponding control input $U(t)$ with feedforward part $U^{\mathrm{r}}(t)$ and feedback part $U^{\mathrm{c}}(t)$

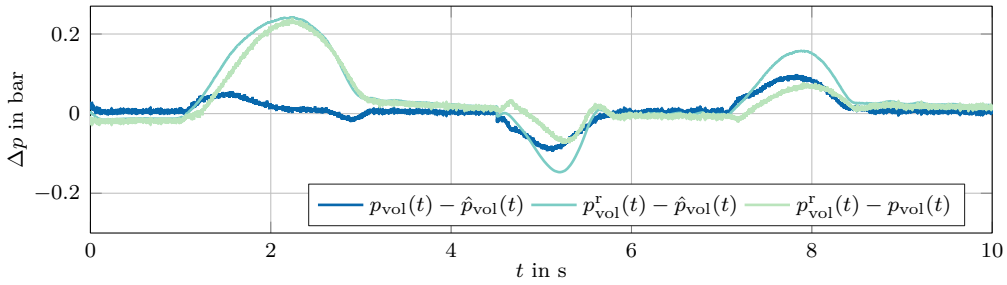

Figure C.6: Deviations between the reference pressure $p^{\mathrm{r}}_{\mathrm{vol}}(t)$, the estimated pressure $\hat{p}_{\mathrm{vol}}(t)$, and the measured pressure $p_{\mathrm{vol}}(t)$ in Fig. C.5

Appendix D

Two-Sided Laplace Transform

Chap. 5 makes use of the two-sided Laplace transform to derive the solutions (5.15) and (5.29). Following [vB55], the definition of the two-sided Laplace transform and a transformation as well as some properties, required for the calculations in Chap. 5, are restated.

Remark D.1. In this thesis, the two-sided Laplace transform is a tool of convenience. Thus, it is not employed with strict mathematical rigor. Further information on, for example, the strip of convergence can be found in [vB55]. △

D.1 Definition

The two-sided Laplace transform and its inverse are defined as

$$\hat{f}(s) = \mathcal{L}_{II}\left[f\right](s) = s\int_{-\infty}^{\infty} \mathrm{e}^{-st} f(t)\,\mathrm{d}t \tag{D.1a}$$

$$f(t) = \mathcal{L}_{II}^{-1}\left[\hat{f}\right](t) = \frac{1}{2\pi j}\int_{c-j\infty}^{c+j\infty} \mathrm{e}^{st}\frac{\hat{f}(s)}{s}\,\mathrm{d}s, \tag{D.1b}$$

respectively, where $s \in \mathbb{C}$ is a complex variable.

D.2 A Selected Transformation

This thesis makes use of the transformation in Tab. D.1. Therein, $I_0(z)$ is the modified Bessel function of the first kind of zeroth order and $h(z)$ the Heaviside step function, defined in (4.35).

Table D.1: Selected transformation

time domain	operational domain	comment
$h(t-\sigma)I_0\left(\sqrt{t^2-\sigma^2}\right)$	$\frac{s}{\sqrt{s^2-1}}\mathrm{e}^{-\sigma\sqrt{s^2-1}}$	$\sigma \in \mathbb{R}$

D.3 Selected Properties

Tab. D.2 summarizes selected properties of the two-sided Laplace transform.

Table D.2: Selected properties

property	time domain	operational domain	comment
differentiation	$\frac{\mathrm{d}}{\mathrm{d}t} f(t)$	$s\hat{f}(s)$	
shift	$f(t+\sigma)$	$\mathrm{e}^{\sigma s}\hat{f}(s)$	$\sigma \in \mathbb{R}$
similarity	$f(\sigma t)$	$f\left(\frac{s}{\sigma}\right)$	$\sigma > 0$
	$f(\sigma t)$	$-f\left(\frac{s}{\sigma}\right)$	$\sigma < 0$
attenuation	$\mathrm{e}^{-\sigma t} f(t)$	$\frac{s}{s+\sigma}\hat{f}(s+\sigma)$	$\sigma \in \mathbb{C}$
convolution	$\int_{-\infty}^{\infty} f_1(\tau) f_2(t-\tau)\,\mathrm{d}\tau$	$\frac{1}{s}\hat{f}_1(s)\hat{f}_2(s)$	

Bibliography

[Aam13] O. M. Aamo. "Disturbance rejection in 2×2 linear hyperbolic systems". In: *IEEE Trans. Automat. Contr.* 58.5 (2013), pp. 1095–1106.

[AC08] M. Abbaspour and K. S. Chapman. "Nonisothermal transient flow in natural gas pipeline". In: *J. Appl. Mech.* 75.3 (2008), pp. 031018-1–031018-8.

[AF16] O. Alaya and M. Fiedler. "Optimal pressure control using switching solenoid valves". In: *Proc. 10th International Fluid Power Conference*. Dresden, Germany, 2016, pp. 281–292.

[AMD19] J. Auriol, K. A. Morris, and F. Di Meglio. "Late-lumping backstepping control of partial differential equations". In: *Automatica* 100 (2019), pp. 247–259.

[And03] J. D. Anderson. *Modern Compressible Flow: With Historical Perspective*. New York: McGraw-Hill, 2003.

[And11] J. D. Anderson. *Fundamentals of Aerodynamics*. New York: McGraw-Hill, 2011.

[And95] J. D. Anderson. *Computational Fluid Dynamics: The Basics with Applications*. New York: McGraw-Hill, 1995.

[Aur+18] J. Auriol, F. Bribiesca-Argomedo, D. Bou Saba, M. Di Loreto, and F. Di Meglio. "Delay-robust stabilization of a hyperbolic PDE–ODE system". In: *Automatica* 95 (2018), pp. 494–502.

[Bal78] M. J. Balas. "Active control of flexible systems". In: *J. Optim. Theor. Appl.* 25.3 (1978), pp. 415–436.

[BC16] G. Bastin and J.-M. Coron. *Stability and Boundary Stabilization of 1-D Hyperbolic Systems*. Progress in Nonlinear Differential Equations and Their Applications. 2016.

[BC63] R. Bellman and K. Cooke. *Differential-Difference Equations*. Vol. 6. Mathematics in Science and Engineering. New York: Academic Press, 1963.

[Bea07] P. Beater. *Pneumatic Drives: System Design, Modelling and Control*. Berlin: Springer, 2007.

[BK01] A. Balogh and M. Krstic. "Infinite-step backstepping for a heat equation-like PDE with arbitrarily many unstable eigenvalues". In: *Proc. 2001 American Control Conference*. Arlington, USA, 2001, pp. 2480–2485.

[BK02] A. Balogh and M. Krstic. "Infinite dimensional backstepping-style feedback transformations for a heat equation with an arbitrary level of instability". In: *Eur. J. Contr.* 8.2 (2002), pp. 165–175.

[BKL01] D. M. Boskovic, M. Krstic, and W. Liu. “Boundary control of an unstable heat equation via measurement of domain-averaged temperature”. In: *IEEE Trans. Automat. Contr.* 46.12 (2001), pp. 2022–2028.

[BM98] J. E. Bobrow and B. W. McDonell. “Modeling, identification, and control of a pneumatically actuated, force controllable robot”. In: *IEEE Trans. Robot. Autom.* 14.5 (1998), pp. 732–742.

[Bru+99] X. Brun, M. Belgharbi, S. Sesmat, D. Thomasset, and S. Scavarda. “Control of an electropneumatic actuator: Comparison between some linear and non-linear control laws”. In: *Proc. IME J. Syst. Contr. Eng.* 213.5 (1999), pp. 387–406.

[CD98] P. D. Christofides and P. Daoutidis. “Robust control of hyperbolic PDE systems”. In: *Chem. Eng. Sci.* 53.1 (1998), pp. 85–105.

[Cha10] M. Chaczykowski. “Transient flow in natural gas pipeline–the effect of pipeline thermal model”. In: *Appl. Math. Model.* 34.4 (2010), pp. 1051–1067.

[Chr01] P. D. Christofides. *Nonlinear and Robust Control of PDE Systems: Methods and Applications to Transport-Reaction Processes*. Systems & Control. Boston: Birkhäuser Boston, 2001.

[CM09] R. Curtain and K. Morris. “Transfer functions of distributed parameter systems: A tutorial”. In: *Automatica* 45.5 (2009), pp. 1101–1116.

[Cor+13] J.-M. Coron, R. Vazquez, M. Krstic, and G. Bastin. “Local exponential H^2 stabilization of a 2×2 quasilinear hyperbolic system using backstepping”. In: *SIAM J. Control Optim.* 51.3 (2013), pp. 2005–2035.

[Dan76] H. Daneshyar. *One-dimensional Compressible Flow*. Oxford: Pergamon Press, 1976.

[Deb12] L. Debnath. *Nonlinear Partial Differential Equations*. Basel: Birkhäuser, 2012.

[DGK17] J. Deutscher, N. Gehring, and R. Kern. “Backstepping control of linear 2×2 hyperbolic systems with dynamic boundary conditions”. In: *Proc. 20th IFAC World Congress*. Toulouse, France, 2017, pp. 4608–4613.

[DGK18] J. Deutscher, N. Gehring, and R. Kern. “Output feedback control of general linear heterodirectional hyperbolic ODE-PDE-ODE systems”. In: *Automatica* 95 (2018), pp. 472–480.

[DGK19] J. Deutscher, N. Gehring, and R. Kern. “Output feedback control of general linear heterodirectional hyperbolic PDE-ODE systems with spatially-varying coefficients”. In: *Int. J. Contr.* 92.10 (2019), pp. 2274–2290.

[Di +18] F. Di Meglio, F. B. Argomedo, L. Hu, and M. Krstic. “Stabilization of coupled linear heterodirectional hyperbolic PDE-ODE systems”. In: *Automatica* 87 (2018), pp. 281–289.

[DJK16] A. Deutschmann, L. Jadachowski, and A. Kugi. “Backstepping-based boundary observer for a class of time-varying linear hyperbolic PIDEs”. In: *Automatica* 68 (2016), pp. 369–377.

[Doe56] G. Doetsch. *Handbuch der Laplace-Transformation: Band III: Anwendungen der Laplace-Transformation*. Vol. 19. Lehrbücher und Monographien aus dem Gebiete der Exakten Wissenschaften. Basel: Springer Basel, 1956.

[ETO03] H. Elmqvist, H. Tummescheit, and M. Otter. "Object-oriented modeling of thermo-fluid systems". In: *Proc. 3rd International Modelica Conference*. Linköping, Sweden, 2003, pp. 269–286.

[Fal17] V. Falkenhahn. *Modellierung und modellbasierte Regelung von Kontinuum-Manipulatoren*. Vol. 32. Berichte aus dem Institut für Systemdynamik Universität Stuttgart. Aachen: Shaker, 2017.

[Fes18] Festo AG & Co. KG. *Datasheet of proportional directional control valves MPYE*. Tech. rep. Esslingen, 2018. URL: `https://www.festo.com/cat/en_gb/data/doc_engb/PDF/EN/MPYE_EN.PDF` (visited on 05/24/2019).

[FG11] J. Falcão Carneiro and F. Gomes de Almeida. "Pneumatic servo valve models based on artificial neural networks". In: *Proc. IME J. Syst. Contr. Eng.* 225.3 (2011), pp. 393–411.

[Fli+95] M. Fliess, J. Lévine, P. Martin, and P. Rouchon. "Flatness and defect of non-linear systems: Introductory theory and examples". In: *Int. J. Contr.* 61.6 (1995), pp. 1327–1361.

[Fod65] G. Fodor. *Laplace Transforms in Engineering*. Budapest: Akadémiai Kiadó, 1965.

[Föl72] O. Föllinger. *Regelungstechnik: Einführung in die Methoden und ihre Anwendung*. Berlin: Elitera, 1972.

[Geh18] N. Gehring. *Applying flatness-based methods to a pneumatic transmission line*. Tech. rep. 2018.

[Gio+08] R. de Giorgi, N. Kobbi, S. Sesmat, and E. Bideaux. "Thermal model of a tank for simulation and mass flow rate characterization purposes". In: *Proc. 7th JFPS International Symposium on Fluid Power*. Toyama, Japan, 2008, pp. 225–230.

[GK18] N. Gehring and R. Kern. "Flatness-based tracking control for a pneumatic system with distributed parameters". In: *Proc. 9th Vienna International Conference on Mathematical Modelling*. Vienna, Austria, 2018, pp. 487–492.

[GK68] M. S. Ghausi and J. J. Kelly. *Introduction to Distributed-Parameter Networks: With Application to Integrated Circuits*. Holt, Rinehart and Winston series in electrical engineering, electronics and systems. New York: Holt, Rinehart and Winston, 1968.

[GL72] R. E. Goodson and R. G. Leonard. "A survey of modeling techniques for fluid line transients". In: *J. Basic Eng.* 94.2 (1972), pp. 474–482.

[Goo70] R. E. Goodson. "Distributed system simulation using infinite product expansions". In: *SIMULATION* 15.6 (1970), pp. 255–263.

[Hir07] C. Hirsch. *Numerical Computation of Internal and External Flows: The Fundamentals of Computational Fluid Dynamics*. Oxford: Butterworth-Heinemann, 2007.

[Hir90] C. Hirsch. *Numerical Computation of Internal and External Flows: Computational Methods for Inviscid and Viscous Flows*. Chichester: John Wiley & Sons Ltd., 1990.

[HK06] R. J. Hyndman and A. B. Koehler. "Another look at measures of forecast accuracy". In: *Int. J. Forecast.* 22.4 (2006), pp. 679–688.

[HMS09] M. Herty, J. Mohring, and V. Sachers. “A new model for gas flow in pipe networks”. In: *Math. Meth. Appl. Sci.* 33.7 (2009), pp. 845–855.

[Ide94] I. E. Idel’chik. *Handbook of Hydraulic Resistance*. Boca Raton: CRC Press, 1994.

[IG81] J. V. Iribarne and W. L. Godson. *Atmospheric Thermodynamics*. Dordrecht: Springer, 1981.

[Int12] International Organization for Standardization. *ISO 1219-1:2012. Fluid power systems and components – Graphical symbols and circuit diagrams*. Tech. rep. Geneva, 2012.

[Int13] International Organization for Standardization. *ISO 6358-1:2013. Pneumatic fluid power – Determination of flow-rate characteristics of components using compressible fluids*. Tech. rep. Geneva, 2013.

[JK03] M. Jelali and A. Kroll. *Hydraulic Servo-Systems: Modelling, Identification and Control*. Advances in Industrial Control. Berlin: Springer, 2003.

[Kam17] Z. Kamiński. “A simplified lumped parameter model for pneumatic tubes”. In: *Math. Comput. Model. Dyn. Syst.* 23.5 (2017), pp. 523–535.

[Ker+18a] R. Kern, N. Gehring, J. Deutscher, and M. Meißner. “Design and experimental validation of an output feedback controller for a pneumatic system with distributed parameters”. In: *Proc. 18th International Conference on Control, Automation and Systems*. PyeongChang, South Korea, 2018, pp. 1391–1396.

[Ker17] R. Kern. “Physical modelling of a long pneumatic transmission line: models of successively decreasing complexity and their experimental validation”. In: *Math. Comput. Model. Dyn. Syst.* 23.5 (2017), pp. 536–553.

[KG17] R. Kern and N. Gehring. “Tracking control for a long pneumatic transmission line”. In: *Proc. 22nd International Conference on Methods and Models in Automation and Robotics*. Międzyzdroje, Poland, 2017, pp. 180–185.

[Kha02] H. K. Khalil. *Nonlinear Systems*. Upper Saddle River: Prentice Hall, 2002.

[Kir04] D. E. Kirk. *Optimal Control Theory: An Introduction*. Dover Books on Electrical Engineering. Mineola: Dover Publications, 2004.

[Knü15] T. Knüppel. *Beiträge zum flachheitsbasierten Steuerungsentwurf für quasilineare hyperbolische Systeme*. Dresden: TUDpress, 2015.

[Krs09a] M. Krstic. “Compensating a string PDE in the actuation or sensing path of an unstable ODE”. In: *IEEE Trans. Circ. Syst.* 54.6 (2009), pp. 1362–1368.

[Krs09b] M. Krstic. “Compensating actuator and sensor dynamics governed by diffusion PDEs”. In: *Syst. Contr. Lett.* 58.5 (2009), pp. 372–377.

[KS08a] M. Krstic and A. Smyshlyaev. “Backstepping boundary control for first-order hyperbolic PDEs and application to systems with actuator and sensor delays”. In: *Syst. Contr. Lett.* 57.9 (2008), pp. 750–758.

[KS08b] M. Krstic and A. Smyshlyaev. *Boundary Control of PDEs: A Course on Backstepping Designs*. Philadelphia: SIAM, 2008.

[KS11] S. V. Krichel and O. Sawodny. “Dynamic modeling of pneumatic transmission lines in Matlab/Simulink”. In: *Proc. 2011 International Conference on Fluid Power and Mechatronics*. Beijing, China, 2011, pp. 24–29.

[KS13] S. V. Krichel and O. Sawodny. “Non-linear friction modelling and simulation of long pneumatic transmission lines”. In: *Math. Comput. Model. Dyn. Syst.* 20.1 (2013), pp. 23–44.

[KW15] T. Knüppel and F. Woittennek. “Control design for quasi-linear hyperbolic systems with an application to the heavy rope”. In: *IEEE Trans. Automat. Contr.* 60.1 (2015), pp. 5–18.

[LB88] S. Liu and J. E. Bobrow. “An analysis of a pneumatic servo system and its application to a computer-controlled robot”. In: *J. Dyn. Syst. Meas. Contr.* 110.3 (1988), pp. 228–235.

[LeV02] R. J. LeVeque. *Finite Volume Methods for Hyperbolic Problems*. Cambridge texts in applied mathematics. Cambridge: Cambridge University Press, 2002.

[LeV92] R. J. LeVeque. *Numerical Methods for Conservation Laws*. Basel: Springer Basel AG, 1992.

[Lin85] P. Linz. *Analytical and Numerical Methods for Volterra Equations*. Philadelphia: SIAM, 1985.

[Meu13] T. Meurer. *Control of Higher-Dimensional PDEs: Flatness and Backstepping Designs*. Communications and Control Engineering. Berlin: Springer, 2013.

[MK19] M. Meißner and R. Kern. *Quick start pneumatic test bench: User guide*. Tech. rep. 2019.

[MKK14] S. Mousavi, S. Kara, and B. Kornfeld. “Energy efficiency of compressed air systems”. In: *Procedia CIRP* 15 (2014), pp. 313–318.

[MPE00] J. Mäkinen, R. Piché, and A. Ellman. “Fluid transmission line modeling using a variational method”. In: *J. Dyn. Syst. Meas. Contr.* 122.1 (2000), pp. 153–162.

[Mun13] B. R. Munson. *Fundamentals of Fluid Mechanics*. Hoboken: Wiley, 2013.

[Nik94] N. V. Nikitin. “Direct numerical modeling of three-dimensional turbulent flows in pipes of circular cross section”. In: *Fluid. Dynam.* 29.6 (1994), pp. 749–758.

[OC01] A. J. Osiadacz and M. Chaczykowski. “Comparison of isothermal and non-isothermal pipeline gas flow models”. In: *Chem. Eng. J.* 81.1–3 (2001), pp. 41–51.

[OG64] R. Oldenburger and R. E. Goodson. “Simplification of hydraulic line dynamics by use of infinite products”. In: *J. Basic Eng.* 86.1 (1964), pp. 1–8.

[Oga10] K. Ogata. *Modern Control Engineering*. Upper Saddle River: Prentice Hall, 2010.

[Oga95] K. Ogata. *Discrete-Time Control Systems*. Englewood Cliffs: Prentice-Hall International, 1995.

[Ola+05] O. Olaby, X. Brun, S. Sesmat, T. Redarce, and E. Bideaux. “Characterization and Modeling of a proportional valve for control synthesis”. In: *Proc. 6th JFPS International Symposium on Fluid Power*. Tsukuba, Japan, 2005, pp. 771–776.

[Pat80] S. V. Patankar. *Numerical Heat Transfer and Fluid Flow*. Series in computational methods in mechanics and thermal sciences. Washington: Hemisphere, 1980.

[Pfe18] A. Pfeffer. *Modelling, Estimation and Control Concepts for Pneumatic Systems*. Vol. 40. Modellierung und Regelung komplexer dynamischer Systeme. Aachen: Shaker, 2018.

[PKS91] G. H. Pfreundschuh, V. Kumar, and T. G. Sugar. "Design and control of a 3-DOF in-parallel actuated manipulator". In: *Proc. 1991 IEEE International Conference on Robotics and Automation*. Sacramento, USA, 1991, pp. 1659–1664.

[PR01] N. Petit and P. Rouchon. "Flatness of heavy chain systems". In: *SIAM J. Contr. Optim.* 40.2 (2001), pp. 475–495.

[PWB08] C. Prieur, J. Winkin, and G. Bastin. "Robust boundary control of systems of conservation laws". In: *Math. Control Signals Syst.* 20.2 (2008), pp. 173–197.

[Rad01] P. Radgen, ed. *Compressed Air Systems in the European Union: Energy, Emissions, Savings Potential and Policy Actions*. Stuttgart: LOG_X, 2001.

[RH00a] E. Richer and Y. Hurmuzlu. "A high performance pneumatic force actuator system: part I-nonlinear mathematical model". In: *J. Dyn. Syst. Meas. Contr.* 122.3 (2000), pp. 416–425.

[RH00b] E. Richer and Y. Hurmuzlu. "A high performance pneumatic force actuator system: part II–nonlinear controller design". In: *J. Dyn. Syst. Meas. Contr.* 122.3 (2000), pp. 426–434.

[RHC98] W. M. Rohsenow, J. P. Hartnett, and Y. I. Cho, eds. *Handbook of Heat Transfer*. New York: McGraw-Hill, 1998.

[RNM15] D. Rager, R. Neumann, and H. Murrenhoff. "Simplified fluid transmission line model for pneumatic control applications". In: *Proc. 14th Scandinavian International Conference on Fluid Power*. Tampere, Finland, 2015.

[RNM16] D. Rager, R. Neumann, and H. Murrenhoff. "Remote pressure control – considering pneumatic tubes in controller design". In: *Proc. 10th International Fluid Power Conference*. Dresden, Germany, 2016, pp. 239–254.

[Rud03] J. Rudolph. *Flatness Based Control of Distributed Parameter Systems*. Berichte aus der Steuerungs- und Regelungstechnik. Aachen: Shaker, 2003.

[Rus73] D. L. Russell. "A unified boundary controllability theory for hyperbolic and parabolic partial differential equations". In: *Stud. Appl. Math.* 52.3 (1973), pp. 189–211.

[RW18] M. Riesmeier and F. Woittennek. "On approximation of backstepping observers for parabolic systems with Robin boundary conditions". In: *Proc. 2018 IEEE Conference on Decision and Control*. Miami Beach, USA, 2018, pp. 4601–4606.

[SA04] H. Sira-Ramírez and S. K. Agrawal. *Differentially Flat Systems*. Vol. 17. Control Engineering. New York: Marcel Dekker, 2004.

[SB59] C. B. Schuder and R. C. Binder. "The response of pneumatic transmission lines to step inputs". In: *Trans. ASME. J. Basic Eng.* 81.12 (1959), pp. 578–584.

[SD86a] J. S. Stecki and D. C. Davis. “Fluid transmission lines—distributed parameter models part 1: A review of the state of the art”. In: *Proc. IME J. Power Energ.* 200.41 (1986), pp. 215–228.

[SD86b] J. S. Stecki and D. C. Davis. “Fluid transmission lines—distributed parameter models part 2: Comparison of models”. In: *Proc. IME J. Power Energ.* 200.41 (1986), pp. 229–236.

[Slo] N. J. A. Sloane, ed. *The On-Line Encyclopedia of Integer Sequences*. URL: `https://oeis.org/A046184` (visited on 03/27/2019).

[Sou+05] M. Soumelidis, D. N. Johnston, K. A. Edge, and D. G. Tilley. “A comparative study of modelling techniques for laminar flow transients in hydraulic pipelines”. In: *Proc. 6th JFPS International Symposium on Fluid Power*. Tsukuba, Japan, 2005, pp. 100–105.

[SRH10] R. Saidur, N. A. Rahim, and M. Hasanuzzaman. “A review on compressed-air energy use and energy savings”. In: *Renew. Sustain. Energ. Rev.* 14.4 (2010), pp. 1135–1153.

[Tan92] W. Y. Tan. *Shallow Water Hydrodynamics: Mathematical Theory and Numerical Solution for a Two-Dimensional System of Shallow-Water Equations*. Vol. 55. Oceanography. Amsterdam: Elsevier Science Publishers, 1992.

[Tho99] P. Thomas. *Simulation of Industrial Processes for Control Engineers*. Oxford: Butterworth-Heinemann, 1999.

[Tor09] E. F. Toro. *Riemann Solvers and Numerical Methods for Fluid Dynamics: A Practical Introduction*. Berlin: Springer, 2009.

[TRB01] I. Tunay, E. Y. Rodin, and A. A. Beck. “Modeling and robust control design for aircraft brake hydraulics”. In: *IEEE Trans. Contr. Syst. Tech.* 9.2 (2001), pp. 319–329.

[TU17] M. Turkseven and J. Ueda. “Control of pneumatic actuators with long transmission lines for rehabilitation in MRI”. In: *2016 International Symposium on Experimental Robotics*. Ed. by D. Kulić, Y. Nakamura, O. Khatib, and G. Venture. Springer Proceedings in Advanced Robotics. Cham: Springer International Publishing, 2017, pp. 84–91.

[TU18] M. Turkseven and J. Ueda. “Model-based force control of pneumatic actuators with long transmission lines”. In: *IEEE ASME Trans. Mechatron.* 23.3 (2018), pp. 1292–1302.

[TX11] S. Tang and C. Xie. “State and output feedback boundary control for a coupled PDE–ODE system”. In: *Syst. Contr. Lett.* 60.8 (2011), pp. 540–545.

[vB55] B. van der Pol and H. Bremmer. *Operational Calculus: Based on the Two-Sided Laplace Integral*. Cambridge: Cambridge University Press, 1955.

[VDI10] VDI-Gesellschaft Verfahrenstechnik und Chemieingenieurwesen, ed. *VDI Heat Atlas*. Berlin: Springer, 2010.

[VK14] R. Vazquez and M. Krstic. “Marcum Q-functions and explicit kernels for stabilization of linear hyperbolic systems with constant coefficients”. In: *Syst. Contr. Lett.* 68 (2014), pp. 33–42.

[WB06] G. Welch and G. Bishop. *An introduction to the Kalman filter: TR 95-041*. Tech. rep. Chapel Hill: Department of Computer Science, University of North Carolina at Chapel Hill, 2006.

[WM10] F. Woittennek and H. Mounier. "Flachheit und Steuerbarkeit einer Klasse von Netzwerken örtlich verteilter Systeme". In: *at – Automatisierungstechnik* 58.3 (2010), pp. 139–150.

[Woi11] F. Woittennek. "On flatness and controllability of simple hyperbolic distributed parameter systems". In: *Proc. 18th IFAC World Congress*. Milan, Italy, 2011, pp. 14452–14457.

[Woi12] F. Woittennek. "Beobachterbasierte Zustandsrückführungen für hyperbolische verteiltparametrische Systeme". In: *at – Automatisierungstechnik* 60.8 (2012), pp. 462–475.

[Woi13a] F. Woittennek. "Flatness based feedback design for hyperbolic distributed parameter systems with spatially varying coefficients". In: *Proc. 1st IFAC Workshop on Control of Systems Governed by Partial Differential Equations*. Vol. 46. Paris, France, 2013, pp. 37–42.

[Woi13b] F. Woittennek. "On the hyperbolic observer canonical form". In: *Proc. 8th International Workshop on Multidimensional Systems*. Erlangen, Germany, 2013, pp. 57–62.

[WR12] F. Woittennek and J. Rudolph. "Controller canonical forms and flatness based state feedback for 1D hyperbolic systems". In: *Proc. 7th Vienna International Conference on Mathematical Modelling*. Vienna, Austria, 2012, pp. 792–797.

[WRB09] E. T. Wolbrecht, D. J. Reinkensmeyer, and J. E. Bobrow. "Pneumatic control of robots for rehabilitation". In: *Int. J. Robot. Res.* 29.1 (2009), pp. 23–38.

[WRE17] F. Woittennek, M. Riesmeier, and S. Ecklebe. "On approximation and implementation of transformation based feedback laws for distributed parameter systems". In: *Proc. 20th IFAC World Congress*. Toulouse, France, 2017, pp. 6786–6792.

[WSV14] V. A. Wouwer, P. Saucez, and C. Vilas. *Simulation of ODE/PDE Models with MATLAB®, OCTAVE and SCILAB: Scientific and Engineering Applications*. Cham: Springer, 2014.

[WT88] J. Watton and M. J. Tadmori. "A comparison of techniques for the analysis of transmission line dynamics in electrohydraulic control systems". In: *Appl. Math. Model.* 12.5 (1988), pp. 457–466.

[XW04] F. Xiang and J. Wikander. "Block-oriented approximate feedback linearization for control of pneumatic actuator system". In: *Contr. Eng. Pract.* 12.4 (2004), pp. 387–399.

[Yan+11] B. Yang, T. U-Xuan, A. McMillan, R. Gullapalli, and J. P. Desai. "Design and control of a 1-DOF MRI compatible pneumatically actuated robot with long transmission lines". In: *IEEE ASME Trans. Mechatron.* 16.6 (2011), pp. 1040–1048.

[Yos95] K. Yosida. *Functional Analysis*. Berlin: Springer, 1995.

[Yu+08] N. Yu, C. Hollnagel, A. Blickenstorfer, S. S. Kollias, and R. Riener. “Comparison of MRI-compatible mechatronic systems with hydrodynamic and pneumatic actuation”. In: *IEEE ASME Trans. Mechatron.* 13.3 (2008), pp. 268–277.

[ZT12] Z. Zhou and S. Tang. “Boundary stabilization of a coupled wave-ODE system with internal anti-damping”. In: *Int. J. Contr.* 85.11 (2012), pp. 1683–1693.

Talks

[GK17] N. Gehring and R. Kern. *Trajektorienfolgeregelung für ein verteilt-parametrisches, pneumatisches System.* GMA-Fachausschuss 1.40 "Theoretische Verfahren der Regelungstechnik", Anif, Austria, 2017.

[Ker+18b] R. Kern, N. Gehring, J. Deutscher, and M. Meißner. *Experimentelle Validierung eines verteilt-parametrischen, backsteppingbasierten Ausgangsfolgereglers.* GMA-Fachausschuss 1.40 "Systemtheorie und Regelungstechnik", Anif, Austria, 2018.

[Ker15] R. Kern. *Dynamische Modellierung und Simulation einer langen pneumatischen Leitung.* Regelungstechnischer Workshop, Beilngries, Germany, 2015.

[Ker16] R. Kern. *Physikalische Beschreibung und Vergleich sukzessiv vereinfachter Modelle einer langen pneumatischen Leitung.* GMA-Fachausschuss 1.30 "Modellbildung, Identifikation und Simulation in der Automatisierungstechnik", Anif, Austria, 2016.

[Ker19] R. Kern. *Regelung eines pneumatischen Systems mit verteilten Parametern.* 53. Regelungstechnisches Kolloquium, Boppard, Germany, 2019.

Student Theses

[Ame17] A. Amerio. “Highly nonlinear model predictive control of a pneumatic distributed parameter system”. Master’s thesis. Technical University of Munich, 2017.

[Fri18] L. Fritz. “Flachheitsbasierter Beobachterentwurf für eine lange pneumatische Leitung”. Term paper. Technical University of Munich, 2018.

[Gra18] D. Grassinger. “Thermische und pneumatische Modellierung eines Ventils”. Bachelor’s thesis. Technical University of Munich, 2018.

[Gün16] P. Günzel. “Modellierung der Dynamik einer langen pneumatischen Leitung”. Bachelor’s thesis. Technical University of Munich, 2016.

[Her16] A. Herdt. “Vergleichsstudien zu unterschiedlichen Regelungskonzepten für eine lange pneumatische Leitung”. Term paper. Technical University of Munich, 2016.

[Mei17] V. Meidinger. “Nichtlineare modellbasierte prädiktive Regelung für eine lange pneumatische Leitung”. Term paper. Technical University of Munich, 2017.

[Mei18] M. Meißner. “Verteilt-parametrische Regelung für eine lange pneumatische Leitung mit experimenteller Validierung”. Term paper. Technical University of Munich, 2018.

[Mey16] L. Meyer. “Distributed parameter control of a long pneumatic transmission line”. Term paper. Technical University of Munich, 2016.

[Ngu17] D. Nguyen. “Modeling of a pneumatic valve”. Master’s thesis. Technical University of Munich, 2017.

[Rot18] J. Rothe. “Realisierung eines backsteppingbasierten Beobachters für eine lange pneumatische Leitung”. Bachelor’s thesis. Technical University of Munich, 2018.

[Sch17] T. Scheuermann. “Flachheitsbasierte Trajektorienplanung für eine lange pneumatische Leitung”. Master’s thesis. Technical University of Munich, 2017.

[Sei15] S. Seidel. “Auslegung und Inbetriebnahme des Prüfstands „Pneumatische Leitung“”. Term paper. Technical University of Munich, 2015.

[Zah16] F. Zahn. “Dynamische Simulation einer langen pneumatischen Leitung mit Reibung”. Bachelor’s thesis. Technical University of Munich, 2016.

[Zof17] P. Zofer. “Flachheitsbasierte Regelung einer langen pneumatischen Leitung”. Term paper. Technical University of Munich, 2017.